



# Effects of Nano- and Micro-surface Treatments on Boiling Heat Transfer

Hai Trieu Phan

## ► To cite this version:

Hai Trieu Phan. Effects of Nano- and Micro-surface Treatments on Boiling Heat Transfer. Electric power. Institut National Polytechnique de Grenoble - INPG, 2010. English. NNT: . tel-00574573

**HAL Id: tel-00574573**

**<https://theses.hal.science/tel-00574573>**

Submitted on 8 Mar 2011

**HAL** is a multi-disciplinary open access archive for the deposit and dissemination of scientific research documents, whether they are published or not. The documents may come from teaching and research institutions in France or abroad, or from public or private research centers.

L'archive ouverte pluridisciplinaire **HAL**, est destinée au dépôt et à la diffusion de documents scientifiques de niveau recherche, publiés ou non, émanant des établissements d'enseignement et de recherche français ou étrangers, des laboratoires publics ou privés.

UNIVERSITE DE GRENOBLE

N° attribué par la bibliothèque

□□□□□□□□□□

**T H E S E**

pour obtenir le grade de

**DOCTEUR DE L'UNIVERSITE DE GRENOBLE**

Spécialité : **Mécanique des fluides, Energétique, Procédés**

préparée au laboratoire LEGI/LETH  
dans le cadre de l'Ecole Doctorale I-MEP2

présentée et soutenue publiquement

par

**Hai Trieu PHAN**

Le 14 septembre 2010

Intitulée :

**EFFETS DES NANO- ET MICRO-STRUCTURATIONS DE SURFACE SUR LE  
TRANSFERT THERMIQUE EN EBULLITION**

*Effects of Nano- and Micro-surface Treatments on Boiling Heat Transfer*

Thèse dirigée par Philippe MARTY et Nadia CANEY

**JURY**

Prof. BONJOUR, J.	INSA, Lyon	Président
Prof. TADRIST, L.	Polytech, Marseille	Rapporteur
Prof. COLIN, C.	INP, Toulouse	Rapporteur
Prof. MARTY, P.	UJF, Grenoble	Directeur de thèse
Dr. CANEY, N.	UJF, Grenoble	Co-directeur de thèse
Prof. PALM, B.	KTH, Stockholm	Examineur
Dr. WEN, D.	QMUL, London	Examineur
Dr. GAVILLET, J.	CEA, Grenoble	Examineur



## Acknowledgments

This work has been carried out at Laboratory of Heat Exchangers (LITEN/LETH), Atomic Energy Commissariat (CEA de Grenoble), under the supervisions of Prof. Philippe Marty and Ms. Nadia Caney. The project has been supported by the Atomic Energy Commissariat, who is gratefully acknowledged.

Foremost, I would like to express profound gratitude to my supervisors, Philippe Marty, Nadia Caney, Stéphane Colasson and Jérôme Gavillet, for their guidance and encouragement throughout this work. In particular, I was inspired by Philippe Marty who gave me the passion of questioning about daily observations and of giving explanations to them. I learnt from Nadia Caney the rigorous approach to research and the methods needed to be competent at synthesising information. Stéphane Colasson was always available for discussions about any research topics. The collaboration with Jérôme Gavillet enriched my project-management methodologies and inspired in me the passion for innovative technologies.

I would like also to thank Pierre Mercier and Patrice Tochon for giving me the opportunity to carry out my thesis in LETH laboratory.

I gratefully acknowledge Prof. Lounès Tadrist and Prof. Catherine Colin for their careful reading of this manuscript.

It is a pleasure to record my gratitude to Antoine Gruss, André Bontemps and Arnaud Bruch for the deep scientific discussions we had everyday and for their suggestions for my writing. I would like also to acknowledge Jean-François Fourmigue and Tristan Desrue for their help in numerical calculations.

I really appreciate the participation of Olivier Soriano, Jérôme Bentivoglio and Martin Gérard for the successful construction of the experimental facilities.

I would like to express my deep thanks to Thierry Krebs, Stéphanie Thollon, Olivier Dellea and Anne-Laure Seiler for sample-surface production; Olivier Poncelet and Olivier Renard for nanofluid preparation; Fabrice Emieux and Alexandre Montani for technical support on scanning-electronic microscopic; as well as Muriel Marchand and Jean-Pierre Berlandis for their help on experimental equipments.

I am also grateful to Quynh-Trang Pham, Ken Delbos-Corfield and Pierre-Emmanuel Beliard for their kind help during the thesis writing.

I would like to thank my parents, my brother and sisters for their love, support and encouragement all along of my residence in France.

Finally, I sincerely would like to thank every individual in LETH laboratory, for being so helpful and supportive.



# Effects of Nano- and Micro-surface Treatments on Boiling Heat Transfer

**Abstract** – This work investigates the flow boiling heat transfer in microchannels with the aim of developing compact cooling systems which can be adapted to miniaturized power components. Nano and micro-surface treatments were used as innovative techniques to improve the heat transfer performance as well as to delay the intermittent dryout. Initially, pool-boiling experiments were performed to highlight the impact of nanocoatings on nucleate-boiling mechanisms. It was observed that the surface wettability modified by nanoparticle deposition had significant effects on the boiling processes. Afterwards, a second experimental campaign was conducted to investigate the flow boiling in a microchannel with nanocoated and microstructured samples. These studies highlighted the impacts of surface wettability and of micro-patterning on two-phase flow patterns, pressure drop and heat transfer coefficient. In particular, significant enhancements in heat transfer coefficient and in intermittent dryout were obtained with micro-structured samples.

**Keywords:** boiling, contact angle, heat transfer, microchannel, micro-patterning, nanocoating, surface wettability.

---

**Résumé** – Ce travail concerne l'étude du transfert thermique par ébullition dans des microcanaux avec l'objectif de développer des systèmes thermiques compacts adaptés aux composants de puissance miniaturisés. Les techniques de nano- et micro-structurations de surface ont été utilisées comme des méthodes novatrices pour améliorer les performances de transfert thermique ainsi que pour retarder l'assèchement intermittent qui apparaît dans les microcanaux. Dans un premier temps, des expériences d'ébullition en vase ont été réalisées afin de mettre en évidence l'impact d'un revêtement à l'échelle nanométrique sur les mécanismes d'ébullition nucléée. Il a été observé que la mouillabilité de surface, qui est modifiée par le dépôt de nanoparticules, a des effets significatifs sur les processus d'ébullition. Dans un deuxième temps, une campagne expérimentale a été réalisée pour étudier l'ébullition convective dans un microcanal avec des échantillons nano- et micro-structurés. Ces études ont mis en évidence les effets de la mouillabilité et de la micro-structuration de surface sur les régimes d'écoulement, les pertes de charge et le coefficient de transfert thermique. En particulier, de fortes améliorations du coefficient de transfert thermique et le retard d'assèchement intermittent ont été obtenus avec des surfaces micro-structurées.

**Mots-clefs :** angle de contact, ébullition, microcanal, micro-motif, mouillabilité de surface, nano-revêtement, transfert thermique.

Thèse préparée au  
CEA de Grenoble, LITEN/DRT, équipeLEGI-LETh  
Laboratoire des Echangeurs Thermiques (LETH)  
17 rue des Martyrs, 38054 Grenoble



# Table of contents

<b>NOMENCLATURE.....</b>	<b>IX</b>
<b>INTRODUCTION.....</b>	<b>1</b>
<b>PART 1 - STATE OF THE ART .....</b>	<b>3</b>
<b>CHAPTER 1: INTRODUCTION TO HETEROGENEOUS BOILING.....</b>	<b>5</b>
1.1 POOL BOILING.....	5
1.1.1 Heterogeneous nucleation.....	5
1.1.2 Bubble growth and detachment.....	7
1.1.3 Regimes of pool boiling.....	8
1.1.4 Heat transfer models for nucleate boiling.....	10
1.2 FLOW BOILING .....	11
1.2.1 Characteristic parameters.....	11
1.2.2 Regimes of flow boiling in conventional (macro) channels.....	13
1.2.3 Flow boiling in microchannels.....	13
1.3 WETTING PHENOMENA .....	16
1.3.1 Classical laws of wetting.....	16
1.3.2 Theories of solid surface tension.....	18
1.3.3 Effect of surface roughness on wetting.....	20
1.4 BOILING ON ENHANCED SURFACES .....	22
1.4.1 Boiling on conventional enhanced surfaces.....	22
1.4.2 Boiling on surfaces structured at micro- and nanoscale.....	24
1.4.3 Effects of surface wettability on boiling heat transfer.....	26
1.5 REFERENCES .....	27
<b>CHAPTER 2: TECHNIQUES FOR SURFACE TREATMENT AND CHARACTERIZATION .....</b>	<b>33</b>
2.1 SURFACE TREATMENT.....	33
2.1.1 Physical vapour deposition.....	34
2.1.2 Chemical vapour deposition.....	35
2.1.3 Laser ablation .....	38
2.2 SURFACE CHARACTERIZATION.....	39
2.2.1 Scanning electron microscope.....	39
2.2.2 Atomic force microscopic.....	41
2.2.3 Contact angle measurement.....	42
2.2.4 Surface temperature measurement.....	44
2.3 REFERENCES .....	48
<b>PART 2 - POOL BOILING EXPERIMENTS.....</b>	<b>49</b>
<b>CHAPTER 3: EFFECTS OF SURFACE COATING BY NANOFLUID BOILING.....</b>	<b>51</b>
3.1 SAMPLE-SURFACE COATING BY NANOFLUID BOILING .....	51
3.1.1 Nanofluid preparation.....	51
3.1.2 Coating apparatus and procedure .....	52
3.1.3 Coating results. ....	53
3.2 POOL BOILING EXPERIMENTAL SETUP .....	56
3.3 EXPERIMENTAL RESULTS .....	57
3.4 DISCUSSION .....	58
3.5 CONCLUSION .....	62
3.6 REFERENCES .....	63
<b>CHAPTER 4: EFFECTS OF SURFACE WETTABILITY MODIFIED BY NANOCOATINGS.....</b>	<b>65</b>
4.1 SAMPLE PREPARATION.....	65
4.1.1 Coating process.....	65
4.1.2 Surface characterization .....	66
4.2 EXPERIMENTAL SETUP AND RESULTS .....	67
4.2.1 Experimental setup.....	67
4.2.2 Experimental results.....	68



4.3	MODEL OF BUBBLE GROWTH .....	72
4.3.1	Dynamic contact angle approach for nucleation .....	72
4.3.2	Concept of macro- and micro-contact angles .....	73
4.4	MODEL OF BUBBLE DEPARTURE DIAMETER .....	76
4.4.1	New correlation of bubble departure diameter .....	76
4.4.2	New theoretical model of bubble departure diameter .....	78
4.5	MODEL OF HEAT TRANSFER COEFFICIENT .....	84
4.5.1	Discussion about heat transfer on hydrophobic surfaces .....	84
4.5.2	Correlation of nucleate boiling heat transfer .....	84
4.6	MODEL OF CRITICAL HEAT FLUX .....	88
4.6.1	Introduction .....	88
4.6.2	Development of the model .....	89
4.7	CONCLUSION .....	92
4.8	REFERENCES .....	92
<b>PART 3 - FLOW BOILING EXPERIMENTS .....</b>		<b>95</b>
<b>CHAPTER 5: EXPERIMENTAL SETUP, PROCEDURE AND VALIDATION .....</b>		<b>97</b>
5.1	SAMPLE SURFACE FABRICATION .....	97
5.1.1	Fabrication processes .....	97
5.1.2	Electrical connexions .....	99
5.1.3	FEG-SEM images .....	101
5.1.4	R/T curves of titanium surface .....	103
5.2	TEST SECTION .....	104
5.2.1	Test section setup .....	104
5.2.2	End effects .....	104
5.3	EXPERIMENTAL APPARATUS AND PROCEDURE .....	105
5.3.1	Experimental apparatus .....	105
5.3.2	Experimental procedure .....	105
5.4	SINGLE-PHASE FLOW VALIDATION TESTS .....	106
5.4.1	Heat loss .....	106
5.4.2	Single-phase pressure drops .....	108
5.4.3	Single-phase heat transfer .....	111
5.5	CONCLUSION .....	114
5.6	REFERENCE .....	114
<b>CHAPTER 6: DATA REDUCTION AND EXPERIMENTAL RESULTS .....</b>		<b>115</b>
6.1	DATA REDUCTION .....	115
6.1.1	Heat flux .....	115
6.1.2	Subcooled conditions .....	115
6.1.3	Two-phase length .....	116
6.1.4	Boiling conditions .....	117
6.1.5	Vapour quality .....	118
6.1.6	Average parameters .....	118
6.1.7	Operating conditions .....	118
6.2	SMOOTH SURFACES .....	119
6.2.1	Contact angle .....	119
6.2.2	Pressure drop .....	119
6.2.3	Flow patterns visualisation .....	120
6.2.4	Heat transfer .....	125
6.2.5	Analytical approaches .....	129
6.3	MICRO-STRUCTURED SURFACES .....	139
6.3.1	Contact angle .....	139
6.3.2	Pressure drop .....	140
6.3.3	Flow patterns visualization .....	141
6.3.4	Heat transfer .....	142
6.4	CONCLUSION .....	146
6.5	REFERENCE .....	146
<b>GENERAL CONCLUSIONS AND PERSPECTIVES .....</b>		<b>149</b>
<b>LIST OF FIGURES .....</b>		<b>A</b>

LIST OF TABLES .....	E
APPENDIX – PROPAGATION OF UNCERTAINTY .....	F
INDEX.....	G



## Nomenclature

$A_c$	cross-section area, m <sup>2</sup>
$A_e$	electrical cross-section area, m <sup>2</sup>
$A_h$	heat exchange area, m <sup>2</sup>
$C_p$	specific heat or liquid specific heat if no subscript is mentioned, J/kg K
$D$	diameter, m
$D^*$	maximum diameter, m
$D_h$	hydraudynamic diameter, m
$D_x$	diameter of the heat-exchange area between a heated surface and a bubble, m
$E$	energy, J
$\dot{E}$	power, W
$f$	bubble emission frequency, Hz
$f_p$	single-phase frictional factor, Po/ Re , -
$f(\theta)$	energy factor, $(2 + 3 \cos \theta - \cos^3 \theta) / 4$ , -
$F_{cp}$	contact pressure force, N
$F_d$	dynamic force, N
$F_g$	buoyancy, N
$F_\sigma$	surface tension force, N
$F_{\sigma,h}$	horizontal component of $F_\sigma$ , N
$F_{\sigma,v}$	vertical component of $F_\sigma$ , N
$g$	gravity, m/s <sup>2</sup>
$G$	mass flux, kg/m <sup>2</sup> s
$\Delta G_e$	formation energy, J
$h$	heat transfer coefficient, W/m <sup>2</sup> K
$h_f$	heat transfer coefficient depending on the bubble emission frequency, W/m <sup>2</sup> K
$h_o$	heat transfer coefficient independent of the contact angle, W/m <sup>2</sup> K
$h_\delta$	heat transfer coefficient by conduction through the liquid microlayer, W/m <sup>2</sup> K
$H$	height, m
$H_{lv}$	evaporation latent heat, J/kg
$I$	current, A
$j$	superficial velocity, m/s
$L$	length, m
$L_c$	capillary length, $\left( \frac{\sigma_{lv}}{g(\rho_l - \rho_v)} \right)^{1/2}$ , m
$L_{th}$	thermal entrance length, m
$\dot{m}$	mass flow rate, kg/s
$M$	molecular weight, g/mol
MAE	mean average error, $\frac{1}{N} \sum_1^N \left  \frac{\text{Predicted value} - \text{exp. value}}{\text{exp. value}} \right  \times 100\%$ , %
MRE	mean relative error, $\frac{1}{N} \sum_1^N \left( \frac{\text{Predicted value} - \text{exp. value}}{\text{exp. value}} \right) \times 100\%$ , %
$n$	indice,-
$N$	number, -
$p^*$	reduced pressure, -
$P$	pressure, Pa

$\Delta P$	pressure drop, Pa
$q$	heat flux, W/m <sup>2</sup>
$q_{CHF}$	critical heat flux, W/m <sup>2</sup>
$q_{CHF, 45^\circ}$	critical heat flux for a contact angle of 45°, W/m <sup>2</sup>
$\bar{q}$	average heat flux, W/m <sup>2</sup>
$\bar{q}_{loss}^o$	average heat loss flux before generation of electrical power, W/m <sup>2</sup>
$Q_{d,loss}$	electrical power loss by conduction through a Pyrex wafer, W
$Q_{e,f}$	electrical power towards a fluid, W
$Q_e$	electrical power, W
$Q_{loss}^o$	heat loss before generation of electrical power due to air convection and radiation, W
$Q_{loss}$	overall heat loss due to electrical power generation, $Q_{loss} = Q_{d,loss} + Q_{u,loss}$ , W
$Q_{u,loss}$	part of $Q_{e,f}$ dissipated to the ambient, W
$r$	roughness factor, -
$R$	radius, m
$R_1$	curvature radius, m
$R_2$	curvature radius, m
$R_a$	average roughness, $\mu\text{m}$
$R_e$	electrical resistance, $\Omega$
$R_p$	maximum roughness, $\mu\text{m}$
$S$	slip ratio, $U_v/U_l$ , -
$S_p$	particle size, $\mu\text{m}$
$t$	time, s
$t_\infty$	time needed to evaporate all liquid in a pool, s
$T$	temperature, K
$T_\infty$	bulk temperature, K
$\bar{T}$	average temperature, °C or K
$\Delta T_{ls}$	liquid superheat, K
$\Delta T_{wf, ONB}$	wall superheat for onset of nucleate boiling, K
$U$	velocity, m/s
$V$	tension, V
$V_b$	bubble volume, m <sup>3</sup>
$V_b^*$	maximum bubble volume, m <sup>3</sup>
$V_l$	liquid volume, m <sup>3</sup>
$V_l^*$	volume of liquid evaporated in the microlayer beneath a bubble, m <sup>3</sup>
$W$	width, m
$W^a$	adhesion energy, $\sigma_{sv} + \sigma_{lv} - \sigma_{sl}$ , N/m
$x$	vapour quality, -
$\Delta x$	variation of vapour quality, -
$z$	$z$ coordinate, m

### Greek symbols

$\alpha_e$	temperature coefficient of resistivity, 1/K
$\delta$	thickness, m
$\dot{\delta}$	growth rate, m/s
$\varepsilon$	void fraction, -

$\varepsilon_h$	void fraction given by a homogeneous model, -
$\varepsilon_{sf}$	void fraction given by a separated-flow model, -
$\zeta$	ratio of the channel height to the channel width, -
$\theta$	contact angle, ° or rad
$\theta^\circ$	contact angle measured at room temperature, ° or rad
$\theta_\mu$	micro-contact angle, ° or rad
$\Delta\theta$	contact angle hysteresis, ° or rad
$\kappa$	surface dependant parameter, -
$\lambda$	thermal conductivity, W/m K
$\mu$	dynamic viscosity, Pa.s
$\rho$	density, kg/m <sup>3</sup>
$\rho_e$	electrical resistivity, $\Omega$ .m
$\sigma$	surface tension or liquid-vapour surface tension if no subscript is given, N/m
$\sigma^D$	dispersive component of the surface tension, N/m
$\sigma^P$	polar component of the surface tension, N/m
$\tau$	period, s
$\phi$	heater orientation angle relative to horizontal, ° or rad
$\Phi_s$	fraction of the solid in contact with the liquid, -
$\varphi$	volumetric concentration, %v

### Subscripts

0	reference
a	advancing
ac	acceleration
as	active-sites
b	bubble
backflow	backflow
c	capillary
cl	contact line
cr	critical
d	bubble-departure
e	equilibrium
eva	evaporation
exp	experimental
f	fluid
frict	frictional
g	gas
gt	growth time
i	portion of the sample surface
in	at the inlet
l	liquid
loss	lost
lv	liquid-vapour
m	microlayer
ms	micro-cavities
o	initial
onb	onset of nucleate boiling
out	at the outlet
PTFE	poly(tetrafluoroethylene) surface

pyrex	pyrex-surface
r	receding
s	saturation
sing	singular
sl	solid-liquid
smooth	smooth-surface
static	static
sv	solid-vapour
Ti	titanium-surface
tp	two-phase
v	vapour
w	wall
wt	waiting time
$\theta$	wetting

### Dimensionless numbers

Bi	Biot number, $\text{Bi} = \frac{h\delta}{\lambda}$
Co	confinement number, $L_c / D_h$
Ja	Jakob number, $\frac{\rho_l C_p \Delta T_{wf, ONB}}{\rho_v H_{lv}}$
$L_{th}^+$	dimensionless number of thermal entrance length, $L_{th}^+ = L_{th} / D_h \text{RePr}$
Mi	New dimensionless number, $\frac{D_d}{L_c} \left( 6\sqrt{\frac{3}{2}} \right)^{-1/3} \left( \frac{\rho_l}{\rho_v} \right)^{1/2} \left( \frac{\rho_l}{\rho_v} - 1 \right)^{-1/3}$
Nu	Nusselt number, $hD_h / \lambda$
$\text{Nu}_\infty$	Nusselt number for thermally fully-developed flow
Pr	Prandtl number, $\mu C_p / \lambda$
Re	Reynolds number, $GD_h / \mu_l$
$z^+$	reduced length, $z / D_h \text{RePr}$

### Mathematical functions

$h_1$	Eq. (6-47)
$h_2$	Eq. (6-53)
$h_3$	Eq. (6-54)
$K_0$	Eq. (2-6)
$K_1$	Eq. (2-5)
$K_a$	Eq. (4-45)
$K_d$	Eq. (4-44)
$K_f$	Eq. (4-43)
$K_{frict}$	Eq. (5-14)
$K_{sing}$	Eq. (5-15)
$K_\theta$	Eq. (6-37)
$X$	Eq. (1-35)
$Y$	Eq. (1-34)
$\Psi(\theta)$	Eq. (4-36)

**Abbreviations**

AF	Annular Flow
AFM	Atomic Force Microscope
BF	Bubbly Flow
CBF	Confined-Bubbly Flow
CF	Churn Flow
CHF	Critical Heat Flux
CVD	Chemical Vapour Deposition
DLC	Diamond-Like Carbon
FB	Film Boiling
FEG	Field-Emission Gun
HTC	Heat Transfer Coefficient
MOCVD	Metalorganic Chemical Vapour Deposition
NB	Nucleate Boiling
NC	Natural Convection
NNDB	Nanofluid Nucleate Boiling Deposition
ONB	Onset of Nucleate Boiling
PECVD	Plasma enhanced chemical vapour deposition
PVD	Physical Vapour Deposition
SAF	Slug-Annular Flow
SEM	Scanning Electron Microscope
SF	Slug Flow
STM	Scanning Tunnelling Microscope
TB	Transion Boiling
TCL	Triple Contact Line





## Introduction

Power systems, such as electronic components or fuel cells, are dissipating more and more heat due to progressively increasing power densities associated with continuous advances in their miniaturization. In order to prevent damages to their components, this generated heat must be efficiently removed. Various cooling modes can be applied, such as air convection or liquid and boiling flows.

Air convection is the most widely-used method because of its easy implementation. However, this mode exhibits a poor heat transfer performance and its operational limits have been already reached. As a consequence, cooling systems by liquid and boiling flows have been increasingly developed. Flow boiling is the most efficient mode as it provides better heat transfer efficiencies. Indeed, for this cooling mode, a part of heat is transferred into the latent heat during liquid-vapour phase change in addition to convective effects.

In the present study, flow boiling was generated inside the systems called mini-and microchannels, which are channels of small size with hydraulic diameters of less than 3 mm. Over the last decade, mini- and microchannels have attracted the attention of researchers in the field of heat and mass transfer, because they enable the development of compact cooling systems which can be adapted to miniaturized power components.

However, the physics of boiling heat transfer in mini-and microchannels is not yet fully understood. A number of investigations showed that the classical laws established for macroscale could not provide good predictions for boiling processes at microscale. This can be related to the capillary effects, which were neglected in classical studies, but become dominant in small-size channels. For instance, recent studies in our laboratory showed that dryout occurs at lower vapour qualities in mini- and microchannels than in traditional macrochannels. This phenomenon was also observed by many other research groups worldwide, and is now commonly called "intermittent dryout" or "partial dryout". Therefore, when increasing the heat transfer efficiency of flow boiling in mini- and microchannels, methods to limit intermittent dryout should be also investigated.

Potential methods to achieve the above targets are nano- and micro-surface treatments, inspired by the emergence of nanofluids, which are fluids containing particles of sizes less than 100 nm. These particles are referred to as "nanoparticles". Recent investigations have shown that during boiling of nanofluids, nanoparticles deposit along the heated surface, modifying the surface properties. Particularly, this leads to a modification in the surface wettability, which is considered as the main cause of change in the bubble growth processes. Another field of interest is that nanoparticle deposition results in significant enhancements of critical heat flux in pool boiling conditions. However, its effects on heat transfer coefficient still remain complex and further works is required for a better understanding of the involved mechanisms.

In the present study, surface treatments at nano- and microscales were used as innovative techniques to improve the heat transfer performance of flow boiling in mini- and microchannels, as well as to delay the associated intermittent dryout. As a first step, pool-boiling experiments were performed in order to highlight the impact of surface wettability on nucleate boiling processes, especially on bubble growth mechanisms. The conclusion from

## 2 INTRODUCTION

this work enabled the development of several processes for sample fabrication and of an experimental setup to study flow boiling in microchannels.

The manuscript is divided into three parts. In the first part (Chapters 1 and 2), the state of the art and the techniques of surface treatment and characterization will be introduced. The second part (Chapters 3 and 4) is devoted to the description of the pool-boiling experiments. The experimental setup and results for flow boiling heat transfer in a microchannel will be presented and discussed in the last part (Chapter 5 and 6). The details of the different chapters are given below.

In **Chapter 1**, boiling and wetting fundamentals will be briefly introduced and described for a better understanding of the concepts used throughout this manuscript. In addition, this chapter is also devoted to the state of the art of boiling with coated and structured surfaces.

**Chapter 2** describes the techniques of surface treatment used in the present work. These techniques consist of chemical and physical vapour depositions as well as laser etching. The methods used for surface characterization will be also presented. These methods enable determination of surface parameters such as roughness, topography, wettability and temperature.

**Chapter 3** presents and discusses the experimental results on boiling of nanofluids. In particular, the mechanism of nanoparticle deposition and its impact on nucleate boiling heat transfer will be highlighted.

Another pool boiling experiment is presented in **Chapter 4**. Several samples with various contact angles between  $22^\circ$  and  $110^\circ$  were used to study the effects of surface wettability on nucleate boiling.

**Chapters 5 and 6** are devoted to describing the experimental setup and results of flow boiling in a microchannel, respectively. It is shown in the last chapter that the surfaces developed in this work allow significant improvements of two-phase heat transfer and are able to delay the intermittent dryout phenomenon.

This thesis has given birth to 6 patents (published and accepted), 5 journal articles (published and accepted) and 8 conference papers.

## **PART 1 - STATE OF THE ART**

This part introduces some boiling and wetting fundamentals as well as the state of the art of boiling with coated and structured surfaces. For easy reading, only key concepts which are necessary to understand the present work will be presented. The reader should consult the literature cited for a more complete understanding of the specific theories or processes discussed. This part also describes the techniques of surface treatment and characterization used in the present work.



## Chapter 1: Introduction to heterogeneous boiling

Heterogeneous boiling is the rapid vaporisation of a liquid associated with bubble formation on a solid surface. Heat transfer by heterogeneous boiling occupies an important place in engineering disciplines. Compared to single-phase processes, this process enables exchanging more energy with a relatively lower jump of temperature at the wall. It may be analysed under two categories, namely: pool boiling and flow boiling, where the latter is also referred to as convective boiling in the literature. Heterogeneous boiling is significantly affected by interactions at the solid-liquid interface, of which two main parameters are surface wettability and topography. This chapter begins with introduction to pool boiling and flow boiling. Classical laws of wetting are also discussed. The final paragraph concerns a review of study on boiling with enhanced surfaces at different scales (from nano- to macroscale).

### 1.1 Pool boiling

Pool boiling is the process in which the heated surface is submerged in a large body of stagnant liquid. The relative motion of fluid near the heated surface is primarily due to buoyancy effect. If enough heat is added to the system, the liquid near the wall may reach and slightly exceed the equilibrium saturation temperature. Heterogeneous nucleation occurs when vapour embryo is formed at the heated surface.

#### 1.1.1 Heterogeneous nucleation

In general, the shape of a vapour embryo is dictated by the contact angle and the interfacial tension, together with the shape of the surface itself. Assuming that the solid surface is flat, the vapour embryo will have a profile shape like the one shown in Figure 1-1. The formation of such an embryo occurs in a system held at constant liquid temperature and pressure.

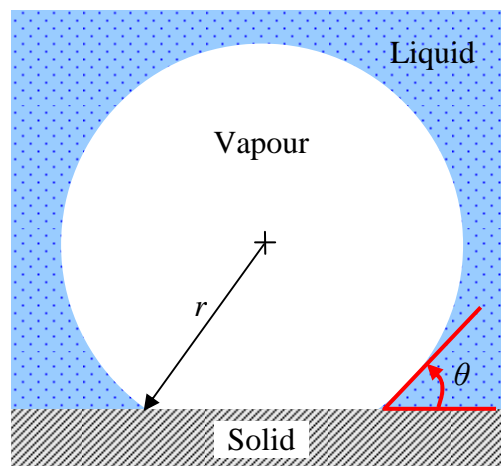


Figure 1-1. A vapour embryo formed at the solid surface with a contact angle  $\theta$ .

#### Factor energy

If the embryo shape is idealized as being a portion of a sphere, the geometry dictates that the embryo volume  $V_b$  is given by:

$$V_b = \frac{4}{3} \pi R^3 \left( \frac{2 + 3 \cos \theta - \cos^3 \theta}{4} \right) \quad (1-1)$$

wherein  $R$  is the embryo radius and  $\theta$  is the contact angle.

When the embryo radius is exactly the right size to be in thermodynamic equilibrium  $R_e$  with the surrounding liquid, its formation energy  $\Delta G_e$  is calculated as [1.1]:

$$\Delta G_e = \frac{4}{3} \pi R_e^2 \sigma_{lv} \left( \frac{2 + 3 \cos \theta - \cos^3 \theta}{4} \right) \quad (1-2)$$

wherein  $\sigma_{lv}$  is the liquid-vapour surface tension. Eq. (1-2) can be also written as:

$$\Delta G_e = \frac{4}{3} \pi R_e^2 \sigma_{lv} f(\theta) \quad (1-3)$$

where

$$f(\theta) = \frac{2 + 3 \cos \theta - \cos^3 \theta}{4} \quad (1-4)$$

Here,  $f(\theta)$  is called “energy factor” [1.2]. Indeed, it is the ratio of the energy needed to create a bubble having a contact angle  $\theta$  to that needed to create a full spherical bubble, which has the same diameter. As shown in Eq. (1-1), this factor is also the volume ratio of these two bubble shapes. If  $\theta$  is close to  $180^\circ$  (non-wetting surface),  $f(\theta)$  tends to 0, thus a minimum energy is required to form an equilibrium embryo. On wetting surfaces ( $\theta < 90^\circ$ ),  $f(\theta)$  varies from 0.5 to 1 and the maximum value of  $\Delta G_e$  can be obtained on the surface having a contact angle close to  $0^\circ$ .

### Critical radius

A bubble embryo of radius  $R_e$  is in an unstable equilibrium (cf. Figure 1-2). The loss of one molecule from the embryo decreases its radius into lower than  $R_e$ . The embryo is likely to collapse completely since the minimization of the Gibbs free energy results in decreasing bubble radius. Conversely, if the bubble embryo has a radius greater than  $R_e$ , it is expected to spontaneously grow. Hence,  $R_e$  is called “critical radius”. Heterogeneous nucleation occurs only if the heated surface contains cavities of radius greater than  $R_e$ . Should the surface be completely wetted by the liquid,  $R_e$  can be estimated as [1.1]:

$$R_e = \frac{2 \sigma_{lv} T_s}{H_{lv} \rho_v (T_w - T_s)} \quad (1-5)$$

wherein  $H_{lv}$  is the vaporisation latent heat, and  $T_w$  and  $T_s$  are the wall and saturation temperatures, respectively.

If the surface cavities contain entrapped gas,  $R_e$  becomes lower and its expression is given as:

$$R_e = \frac{2\sigma_{lv}}{\frac{H_{lv} \rho_v (T_w - T_s)}{T_s} + P_g} \quad (1-6)$$

wherein  $P_g$  is the pressure of the entrapped gas.

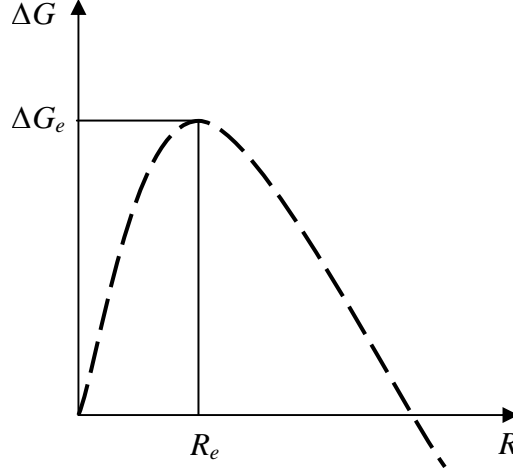


Figure 1-2. Variation of Gibbs free energy with bubble radius

### 1.1.2 Bubble growth and detachment

Once nucleation is initiated, bubble spontaneously grows and then detaches from the solid surface. The complete process of liquid heating, nucleation, bubble growth and release, collectively refers to as the boiling cycle. Three main features of this process that affect the rate of heat transfer are the bubble departure diameter  $D_d$ , the bubble emission frequency  $f$  and the number of active nucleation sites  $N_{as}$ . The bubble emission frequency  $f$  at a nucleation site is defined as:

$$f = \frac{1}{\tau_{gt} + \tau_{wt}} \quad (1-7)$$

where  $\tau_{gt}$ , called “growth time”, is the duration of the bubble growth and  $\tau_{wt}$ , called “waiting time”, is the duration between the departure of the former bubble and the appearance of the current bubble (cf. Figure 1-3).

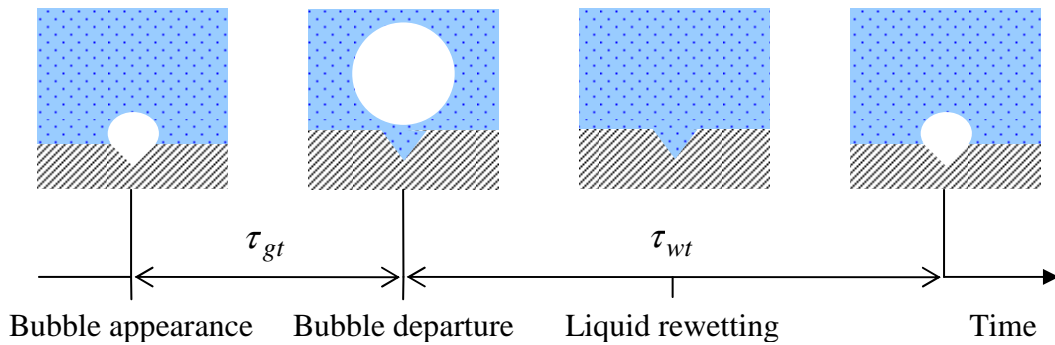


Figure 1-3. Time period associated with the growth of each bubble is the sum of the waiting time and the growth time.



Over the past eighty years, the bubble departure diameter during nucleate boiling has been the subject of numerous investigations. In experimental studies, it is typically determined from high-speed videos of boiling process. Based on experimental data, a number of correlations were suggested to estimate the bubble departure diameter. Many correlations reflect the role of the capillary length  $L_c$ , which is defined as:

$$L_c = \left( \frac{\sigma_{lv}}{g(\rho_l - \rho_v)} \right)^{1/2} \quad (1-8)$$

wherein  $g$  is the gravity, and  $\rho_l$  and  $\rho_v$  are the liquid and vapour densities, respectively.

Indeed, the capillary length accounts for a simple balance of surface tension force and buoyancy. In the context of this work, we are particularly interested in the correlation of Fritz [1.3] since it takes into account the effect of the surface wettability:

$$D_d = 0,0208 \times \theta \times L_c \quad (1-9)$$

wherein  $\theta$  is in degree. According to its definition (cf. Eq. (1-7)), the frequency of bubble emission depends on the waiting time, the bubble growth rate and the bubble departure diameter. Several studies [1.4]-[1.7] show that this frequency is inversely proportional to the departure diameter. Based on an analogy between the bubble release process and natural convection, Zuber [1.5] suggested the following relation:

$$f D_d = 0.59 \left[ \frac{\sigma_{lv} g(\rho_l - \rho_v)}{\rho_l^2} \right]^{1/4} \quad (1-10)$$

The density of active nucleation sites was first estimated by Wang and Dhir [1.8]. The authors performed experiments using copper heaters with different degrees of oxidation, which resulted in different contact angles. The correlation proposed is written as:

$$N_{as} = N_{ms} (1 - \cos \theta) (T_w - T_s)^6 \quad (1-11)$$

where  $N_{ms}$  is the number of micro-cavities on the heated surface of interest.

These classical correlations (Eqs. (1-9), (1-10) and (1-11)) have been widely used to as predictive tools. However, they are based on a limited quantity of experimental data and their accuracy has not been extensively verified. Thus, they should be treated as being approximate only.

### 1.1.3 Regimes of pool boiling

The regimes of pool boiling heat transfer are easily understood by referring to the pool boiling curve which is a plot of the imposed heat flux  $q$  versus the wall superheat ( $T_w - T_s$ ) for the circumstances of interest. Nukiyama [1.9] is well known as the first to publish a pool boiling curve based on results from experiment of boiling water at atmospheric pressure. The regimes

of pool boiling encountered for a horizontal flat surface are indicated schematically in Figure 1-4.

The discussion in this section is limited to pool boiling of wetting liquids. The boiling curve can be conveniently analysed in four different regimes, namely, the natural convection NC, the nucleate boiling NB, the transition boiling TB and the film boiling FB. In the present context, only the natural convection and nucleate boiling are needed to be described in detail.

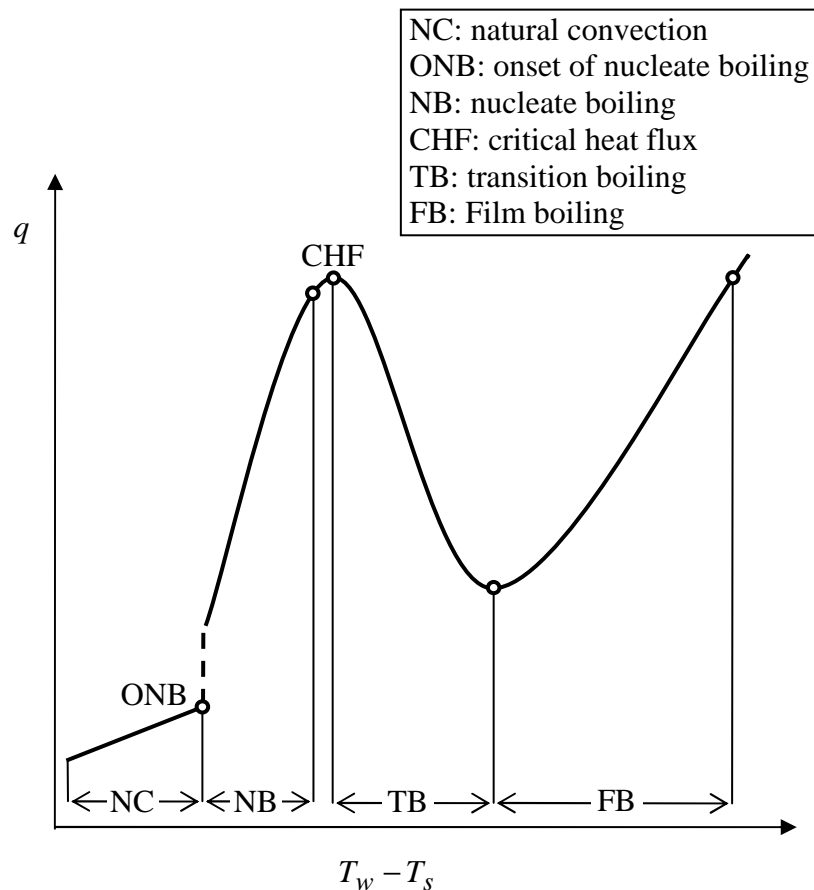


Figure 1-4. Schematic representation of the pool boiling curve.

#### Natural convection regime (NC)

Due to the temperature gradients, fluid motions are created, removing heat from the heated surface to the free liquid surface. The driving force of natural convection is the buoyancy force, a result of gradients of fluid density.

#### Nucleate boiling regime (NB)

If the superheat is large enough, nucleation is initiated at some cavities on the surface. This stage is called the “onset of nucleate boiling” (ONB). At low wall superheat levels, nucleate boiling is characterized by formation of isolated bubbles. With increasing surface superheat, more and more nucleation sites become active, and the bubble frequency at each site generally increases. Eventually the active sites are spaced so closely that bubbles from adjacent sites merge together. Bubble coalescence can occur in vertical or horizontal directions. If the superheat still increases, a vapour film is formed across the surface resulting from the replacement of liquid by vapour adjacent to the heated surface. Poor thermal conductivity of vapour phase suddenly decreases the efficiency of heat transfer. The heat flux at this condition

is called the “critical heat flux” (CHF), which describes the thermal limit of boiling phenomenon. Indeed, the CHF is the maximum heat flux that can be transferred by boiling process. A higher heat flux (compared to the CHF) can lead to the burnout of the heated surface.

In boiling condition, the local heat transfer coefficient is defined as:

$$h = \frac{q}{T_w - T_s} \quad (1-12)$$

For nucleate boiling, Cooper [1.10] developed the following correlation to determine the heat transfer coefficient:

$$h = 55 p^{*(0.12 - 0.2 \log_{10} R_p)} (-\log_{10} p^*)^{-0.55} q^{0.67} M^{-0.5} \quad (1-13)$$

where  $p^* = P / P_{cr}$  is the reduced pressure,  $R_p$  is the roughness as defined in German standard DIN 4762/1,  $q$  the heat flux and  $M$  the molecular weight of the fluid.

In general, the correlation of Cooper gives a good tendency of the heat transfer coefficient versus the heat flux. However, it should not be used to determine the surface roughness which is an adjustable parameter of this correlation.

### 1.1.4 Heat transfer models for nucleate boiling

Due to the complexity of boiling process, the mechanisms of heat transfer during nucleate boiling have been debated over many decades, resulting in the emergence of competing, mutually exclusive models. In many of the early models, the primary mechanism of heat transfer was bubble agitation and micro-convection. These models did not include phase change, but relied to an analogy with forced convection, in which, bubbles play the role of changing the characteristic scales of length and velocity.

#### Transient conduction model

This model by Mikic and Rosenhow [1.11] assumed no heat transfer from the wall during the bubble growth. However, the departure of a bubble scavenges away the superheated liquid layer surrounding it, allowing colder bulk liquid to contact the wall surface. Transient conduction into this bulk liquid after the bubble departure was assumed to be the dominant mode of heat transfer.

#### Microlayer heat transfer model

Cooper and Lloyd [1.12] performed experiments that showed the existence of a liquid microlayer beneath the bubble during the bubble growth. The authors argued that bubble gained most of its energy through evaporation of the microlayer. Hence, they suggested a model that assumed a high heat transfer by microlayer evaporation and negligible heat transfer outside the bubble footprint.

#### Contact line heat transfer model

Stephan and Hammer [1.13] argued that the dominant mode of heat transfer is due to the evaporation of a thin liquid meniscus at the three-phase contact line. The meniscus in the

vicinity of the contact line can become very thin due to stretching of the meniscus, resulting in high heat transfer in this region.

### Superheated liquid model

Demiray and Kim [1.14] conducted experiments that showed the dominant mechanism of heat transfer by isolated bubbles during boiling is through transient conduction and/or micro-convection. They argued that bubble gained the majority of its energy through the bubble cap and not from processes at the wall. Actually, heat transfer through microlayer evaporation and contact line heat transfer were shown to be not significant. A large heat transfer by transient conduction was observed during the wall rewetting process before the bubble departs, not only during rebuilding of the superheated liquid layer after the bubble departure.

## 1.2 Flow boiling

As its name implies, flow boiling is discussed in the case of circulation of a fluid by using external means, such as a pump. In flow boiling process, vapour and liquid are in simultaneous motion inside channels or pipes. Boiling occurs on the wall of the channel and the flow-patterns change due to vapour production.

### 1.2.1 Characteristic parameters

Before describing the processes of flow boiling, it is necessary to first introduce some important parameters that characterize a two-phase flow.

#### Vapour quality

Through the channel, the total mass flow rate  $\dot{m}$  is equal to the sum of the mass flow rates of vapour  $\dot{m}_v$  and liquid  $\dot{m}_l$ :

$$\dot{m} = \dot{m}_v + \dot{m}_l \quad (1-14)$$

The vapour quality  $x$  is defined as the ratio of vapour flow to total flow:

$$x = \frac{\dot{m}_v}{\dot{m}} \quad (1-15)$$

This parameter is often determined by establishing an energy balance:

$$x = \frac{q - G C_p (T_s - T_l)}{G H_{lv}} \quad (1-16)$$

wherein  $q$  is the heat flux,  $C_p$  is the liquid specific heat,  $H_{lv}$  is the vaporisation latent heat,  $T_l$  and  $T_s$  are the liquid and saturation temperatures, respectively, and  $G$  is the mass velocity defined as:

$$G = \frac{\dot{m}}{A_c} \quad (1-17)$$

wherein  $A_c$  cross-section area of the channel.

### Superficial velocities

The superficial velocities of vapour and liquid phases,  $j_v$  and  $j_l$ , are defined respectively:

$$j_v = \frac{Gx}{\rho_v} \quad (1-18)$$

$$j_l = \frac{G(1-x)}{\rho_l} \quad (1-19)$$

These velocities are equal to the velocity that each phase would have if it circulated at its specified mass flow rate through the channel alone.

### Void fraction

The void fraction  $\varepsilon$  is one of the key parameters used to characterize two-phase flows. It is of fundamental importance in models for predicting flow pattern transition, heat transfer and pressure drop. Various geometric definitions are used for specifying the void fraction: local, chordal, cross-sectional and volumetric. The most widely used definition is the cross-sectional void fraction, which is the ratio of the area occupied by the vapour phase  $A_{c,v}$  to the overall area at a cross section  $A_c$ :

$$\varepsilon = \frac{A_{c,v}}{A_c} \quad (1-20)$$

From this definition, the mean velocities of liquid and vapour phases at a cross section are given in terms of the vapour quality  $x$  as:

$$U_l = \frac{G}{\rho_l} \left( \frac{1-x}{1-\varepsilon} \right) \quad (1-21)$$

$$U_v = \frac{G}{\rho_v} \left( \frac{x}{\varepsilon} \right) \quad (1-22)$$

Hence, the void fraction can be calculated as:

$$\varepsilon = \frac{1}{1 + \frac{1-x}{x} \frac{\rho_v}{\rho_l} S} \quad (1-23)$$

where  $S$  is the velocity ratio (often referred to as the slip ratio), which is defined as:

$$S = \frac{U_v}{U_l} \quad (1-24)$$

For equal velocities (homogeneous model),  $S = 1$ . For upward and horizontal flows,  $U_v$  is frequently greater than  $U_l$ , and thus  $S \geq 1$ . For vertical down flows,  $U_v$  may be smaller than  $U_l$  due to gravity effects and so  $S \leq 1$ .

### 1.2.2 Regimes of flow boiling in conventional (macro) channels

In the context of this work, we are particularly interested in horizontal flow boiling, of which the flow regimes are schematically shown in Figure 1-5. At very low vapour quality, bubbly flow is often observed. Due to buoyancy, bubbles flow mainly in the upper portion of the channel. Coalescence of small bubbles occurs when the vapour quality increases, producing larger plug-type bubbles. This is referred to as the plug flow regime.

At low flow rates and somewhat higher vapour qualities, stratified flow may be observed when liquid and vapour are separated. In the regime of the stratified flow, if the flow rate is high enough to make unstable the liquid-vapour interface, the interface becomes wavy. This type of flow is categorized as wavy flow, which has strong vapour shear on the interface that ejects liquid droplets in the vapour core flow. For higher liquid flow rates, the amplitude of the waves may grow, forming large slug-type bubbles. This is referred to as the slug flow.

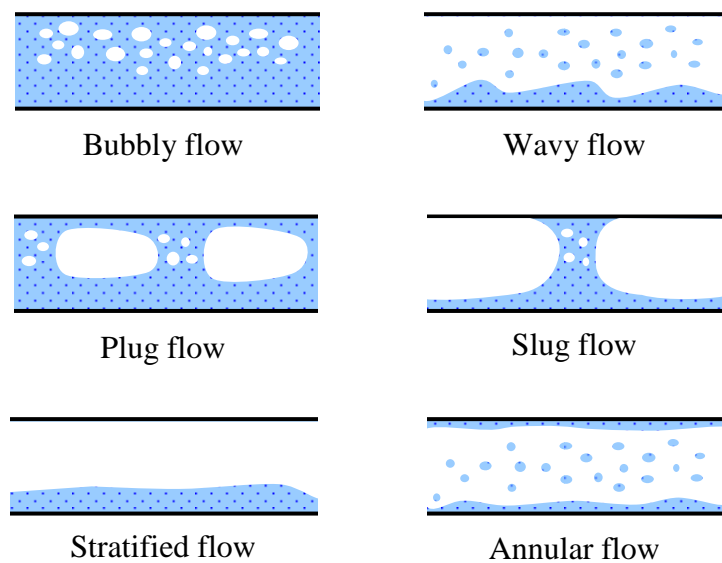


Figure 1-5. Schematic representation of regimes of flow boiling observed in a horizontal channel.

For high velocity of vapour and moderate velocity of liquid, annular flow may be observed. This regime is characterized by a thin liquid film on the top of the channel and a thicker liquid film at the bottom.

### 1.2.3 Flow boiling in microchannels

If the flow passage size is reduced from macroscale to microscale, the heat transfer phenomena of flow boiling will change. Only part of the available knowledge about macroscale phenomena can be transferred to the microscale.

#### Macro-to-microscale transition

In literature, the transition from macroscale to microscale heat transfer was classified by different methods based on the hydraulic diameter, the threshold to confined bubble flow, or the point at which boiling nucleation is altogether suppressed [1.15]. The transition criteria considering the size threshold of hydraulic diameter [1.16]-[1.17] have limitation since they do not reflect the influence of channel size on the physical mechanisms, e.g. bubble form and flow transition. The criterion of nucleation suppression [1.18] leads to a critical hydrodynamic diameter on the order of 1-2  $\mu\text{m}$  or less, thus it is probably better assigned to the micro-to-

nanoscale transition. The threshold to confined bubble flow [1.19]-[1.20] should be the most convenient criterion, since the confinement number  $Co$ , which is the ratio of the capillary length to the hydrodynamic diameter, is used as a criterion to differentiate between macro- and microscale flow boiling. This number is calculated as:

$$Co = \left[ \frac{\sigma_{lv}}{g(\rho_l - \rho_v)D_h^2} \right]^{1/2} \quad (1-25)$$

wherein  $D_h$  is the hydrodynamic diameter.

Beyond a critical value of the confinement number, heat transfer and flow characteristics will be significantly different from those observed in macroscale. Kew and Cornwell [1.19] suggested the criterion of  $Co \geq 0.50$ , but the criterion suggested by Ullmann and Brauner [1.20] is  $Co \geq 0.79$ .

### Flow patterns in microchannels

In microchannels, capillary effects become important, reducing stratification of the liquid and hence, the channel orientation is mostly of secondary importance. Over the past decade, flow patterns in microchannels were observed by various research groups [1.19], [1.21]-[1.24]. Similar to the macroscale situation, it is often not feasible to do a valid comparison between independent databases, since different names were used to describe the same pattern. In general, two-phase flows in microchannels can have four principal flow patterns as suggested by Revellin and Thome [1.24]. The schematic view of these patterns is presented in Figure 1-6.

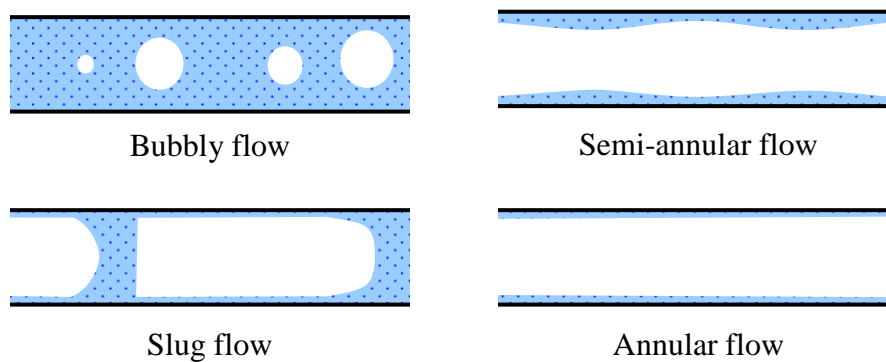


Figure 1-6. Schematic representation of principal flow patterns in microchannels.

In bubbly flow, discrete bubbles move inside the liquid phase. Generally, these bubbles are smaller in diameter than the hydrodynamic diameter of the channel. This flow pattern covers the range of very small vapour qualities. In slug flow, the bubbles have approximately the same diameter as the channel. The bubble nose is hemispherical and the vapour phase is separated from the wall by a thin liquid film. These bubbles are called “elongated bubbles” since they become greater in length due to the confinement effect. The liquid phase is contained mostly in the liquid slugs which separate successive vapour bubbles.

Increasing the vapour quality, semi-annular flow may be observed. This flow pattern refers to as a continuous vapour phase at the channel core together with some churning liquid zones at the wall. Indeed, the churning liquid zones are created by deformation and coalescence of the

previous elongated bubbles. When the churning liquid zones disappear, the flow regime is categorized as annular flow.

### Intermittent dryout in microchannels

In microchannel flow boiling, the local heat transfer coefficient increases with heat flux up to a critical value of the vapour quality beyond which, its deterioration occurs. Deterioration of the heat transfer coefficient is believed to be caused by the intermittent dryout, which refers to an unstable breakdown of the liquid film in contact with the wall. As an example of observation of intermittent dryout, Figure 1-7 was taken from the paper of Caney *et al.* [1.25] that investigated experimental study of flow boiling of HFE-7100 in 40 parallel rectangular channels having 0.84 mm hydraulic diameter. The critical vapour quality was shown to decrease with an increase of the mass velocity. Particularly, irrespective of variation of heat flux and mass velocity, the authors observed occurrence of intermittent dryout at a unique critical value of the total superficial velocity  $j$ , which is defined as:

$$j = j_v + j_l \quad (1-26)$$

$$j = \frac{Gx}{\rho_v} + \frac{G(1-x)}{\rho_l} \quad (1-27)$$

Madrid *et al.* [1.26] conducted experiments in the same conditions as Caney *et al.* [1.25] and had the same observations. Moreover, their experimental results showed no influence of the heat flux on the heat transfer coefficient at a given vapour quality.

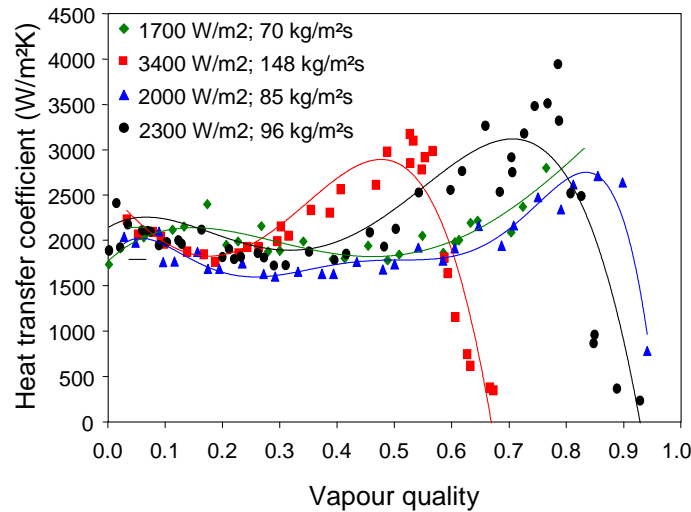


Figure 1-7. Local heat transfer coefficient versus local quality (from Caney *et al.* [1.25] for flow boiling of HFE-7100 in 40 parallel rectangular channels having 0.84 mm hydraulic diameter).

Callizo *et al.* [1.27] investigated flow boiling in a circular vertical microchannel with internal diameter of 640  $\mu\text{m}$  using refrigerants R-134a, R-22 and R-245fa as working fluids. They observed a decrease of the critical vapour quality with increasing vapour velocity. The force balance between gas shear and liquid surface tension was suggested to explain the phenomenon of intermittent dryout.

In summary, it seems that intermittent dryout is rather due to hydrodynamical instabilities than thermal fluctuations. High shear force can make the liquid-vapour interface wavy and



cause intermittent dryout if the wave amplitude becomes greater than the liquid film thickness. This approach was used by Revellin and Thome [1.28] to predict the critical heat flux under uniform or non-uniform heat fluxes in microchannels, giving a good prediction for a large set of experimental data.

## 1.3 Wetting phenomena

In heterogeneous boiling, the nature of the contact between the liquid, vapour and the heated surface can strongly impact the heat and mass transfer. At scales below the capillary length, this contact is mainly dominated by surface tension forces and is referred to as the wetting phenomena. Understanding of wetting laws is crucial in interpreting some boiling physics, such as bubble growth in nucleate boiling and intermittent dryout in microscale flow boiling.

### 1.3.1 Classical laws of wetting

If a liquid drop is small enough to neglect the flattening action of gravity, its sticking on a solid surface is referred to as the surface wettability. An important parameter used to characterize the surface wettability is the contact angle  $\theta$  made by the liquid on the solid. The solid surface is said wetted if  $\theta < 90^\circ$  (cf. Figure 1-8a) and is said unwetted if  $\theta \geq 90^\circ$  (cf. Figure 1-8b). In the case of water, the wetted surface is called “hydrophilic” and the unwetted surface is called “hydrophobic”.

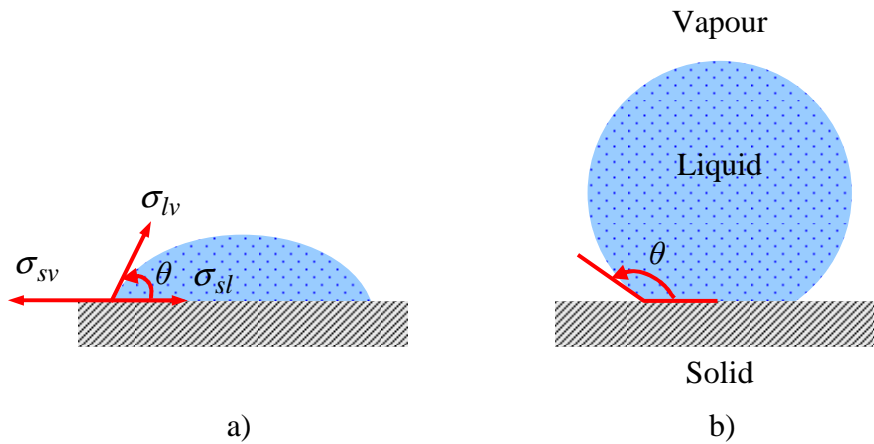


Figure 1-8. Liquid droplets on a) wetted surface and b) unwetted surface.

#### Young's relation

The value of the contact angle was first discussed by Young [1.29]. At the base of the liquid droplet, the three phases: solid, liquid and vapour coexist in the so-called “triple contact line” (TCL). Each interface draws the TCL so as to minimize the corresponding surface area. Thus, balancing the surface tensions on the direction of potential motion (i.e. the horizontal) enables determining the contact angle as:

$$\cos \theta = \frac{\sigma_{sv} - \sigma_{sl}}{\sigma_{lv}} \quad (1-28)$$

where  $\sigma_{sv}$ ,  $\sigma_{sl}$ ,  $\sigma_{lv}$  are the surface tensions (i.e. energy per unit surface) of the interface of solid-vapour, solid-liquid and liquid-vapour, respectively.

### Contact angle hysteresis

Solid surface is generally imperfect due to heterogeneity of surface roughness and chemistry. It can also be polluted by deposition of external contaminants floating in air. These defects allow the TCL to pin on the surface, generating multiple values for the observed contact angle. This is the so-called contact angle hysteresis (cf. Figure 1-9), which can be quantified by measurement of the contact angle when varying the droplet volume [1.30].

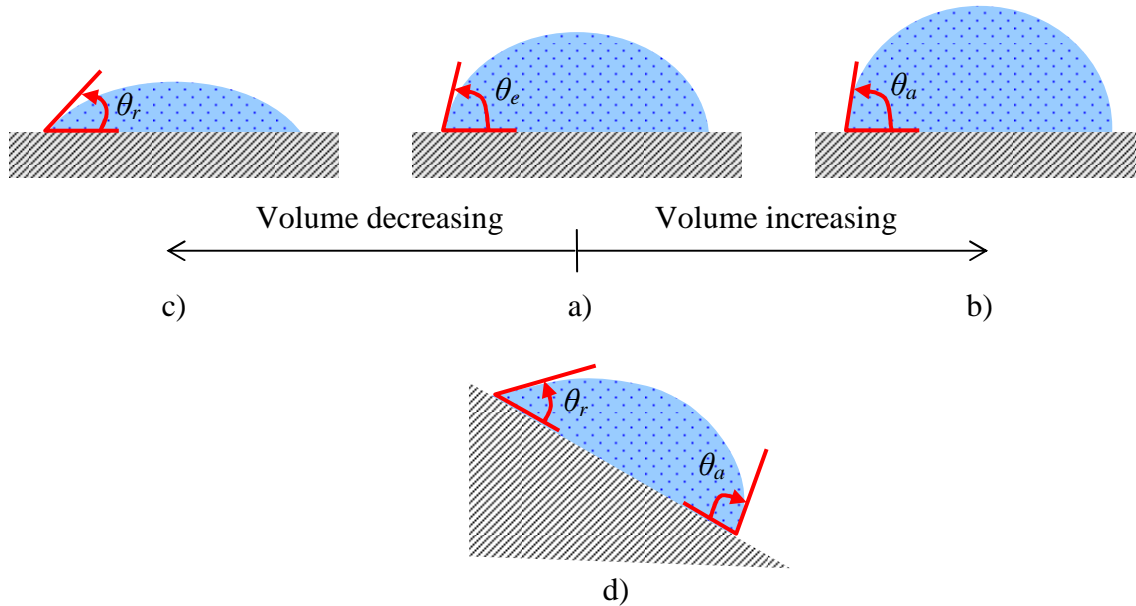


Figure 1-9. Contact angle hysteresis: a) static contact angle  $\theta_e$ , b) advancing contact angle  $\theta_a$ , c) receding contact angle  $\theta_r$  and d) contact angles of droplet on inclined surface.

Firstly, a droplet is deposited on the solid surface. The measured contact angle is equal to the static contact angle  $\theta_e$  (cf. Figure 1-9a). Afterwards, the droplet is slowly fed by using a syringe. If the contact angle is unique, the diameter of the TCL will gradually increase. However, the TCL frequently remains pinned, and the angle is observed to increase. If the droplet volume stops increasing, the contact angle remains stuck at its last value, which is one of the many possible observable angles. There is a critical value of the droplet volume, beyond which the TCL suddenly widens and the contact angle reaches the largest value, called the “advancing contact angle”  $\theta_a$  (cf. Figure 1-9b). Conversely, decreasing the droplet volume enables observing the smallest contact angle, below which the TCL reduces: this angle is called the “receding contact angle”  $\theta_r$  (cf. Figure 1-9c). The contact angle hysteresis is defined as the difference of the advancing and receding contact angles. This phenomenon can also be observed on an inclined solid surface where the angle is larger at the front than at the rear of the droplet (cf. Figure 1-9d).

### Adhesion energy

If the contact angle were unique, due to the gravity, a droplet would necessarily run down on an inclined surface. However, it still sticks on the surface for a threshold of inclined angle. Indeed, the contact angle hysteresis generates a capillary force that opposes the gravity. This force reaches its maximum value at the front and rear angles of  $\theta_a$  and  $\theta_r$  respectively. To characterize this adhesion of a liquid droplet on a solid surface, Dupré [1.31] defined the solid-liquid adhesion energy  $W_{sl}^a$  as:

$$W_{sl}^a = \sigma_{sv} + \sigma_{lv} - \sigma_{sl} \quad (1-29)$$

Combining Eqs. (1-28) and (1-29), we obtain the well-known Young-Dupré equation:

$$W_{sl}^a = \sigma_{lv} (1 + \cos \theta) \quad (1-30)$$

### 1.3.2 Theories of solid surface tension

As presented in the previous section, the contact angle is a result of minimization of the system energy and can be determined by a balance of the surface tensions. The surface tension of liquid-vapour, shortly called as liquid surface tension, is simple and can be measured by a variety of techniques. However, that of solid-vapour, shortly called as solid surface tension, is more complicated since it cannot be directly measured. In general, the values of the solid surface tension are calculated from a set of contact angle, developed by bringing various liquids in contact with the solid surface, but there is no universal agreement in the literature about its definition. The following paragraphs present two of the most well-known theories.

#### Zisman theory

The theory of Zisman [1.32] is probably the most widely used definition of solid surface tension. Zisman defines the solid surface tension as the highest liquid-vapour surface tension that a liquid should have to completely wet the solid surface, with a contact angle of  $0^\circ$ . This comes from the fact that generally, the contact angle decreases if the liquid surface tension decreases. Figure 1-10a presents an example of how Zisman theory is applied. The solid surface is a poly(ethylene) film on which, the contact angles of various liquids were measured [1.33]. According to Zisman definition, poly(ethylene) has a surface tension of 22.8 mN/m.

In surface science, the solid-liquid surface interactions are categorized into polar and dispersive types. The polar interactions account for dipole-dipole, dipole-induced dipole, hydrogen bonding, and other site-specific interactions. The dispersive interactions account for Van der Waals and other non-site specific interactions. A surface is called polar if it is capable of polar-type interactions with liquids. In general, the Zisman theory works best for non-polar surfaces, e.g. poly(ethylene) and poly(propylene), but it becomes inadequate for polar surfaces, e.g. glasses, ceramics and metals. This is because the Zisman theory is a one-parameter model since it only considers the overall values of the surface tensions.

#### Owens/Wendt Theory

Owens and Wendt [1.34] developed a theory that accounts for polar-type interactions between solids surfaces and liquids. This theory is based on the equation of Young (1-28) and the equation of Good and Girifalco [1.35] which defines the solid-liquid surface tension as:

$$\sigma_{sl} = \sigma_{sv} + \sigma_{lv} - 2 \left( \sigma_{lv}^D \sigma_{sv}^D \right)^{1/2} - 2 \left( \sigma_{lv}^P \sigma_{sv}^P \right)^{1/2} \quad (1-31)$$

wherein  $\sigma_{lv}^D$  and  $\sigma_{lv}^P$  are the dispersive and polar components of the liquid surface tension, respectively, and  $\sigma_{sv}^D$  and  $\sigma_{sv}^P$  are these components of the solid surface tension, respectively.

Owens and Wendt combined Eqs. (1-28) and (1-31) to produce the following equation:

$$\frac{\sigma_{lv}(\cos \theta + 1)}{2(\sigma_{lv}^D)^{1/2}} = (\sigma_{sv}^P)^{1/2} \left( \frac{\sigma_{lv}^P}{\sigma_{lv}^D} \right)^{1/2} + (\sigma_{sv}^D)^{1/2} \quad (1-32)$$

This equation has the linear form:

$$Y = (\sigma_{sv}^P)^{1/2} X + (\sigma_{sv}^D)^{1/2} \quad (1-33)$$

wherein:

$$Y = \frac{\sigma_{lv}(\cos \theta + 1)}{2(\sigma_{lv}^D)^{1/2}} \quad (1-34)$$

$$X = \left( \frac{\sigma_{lv}^P}{\sigma_{lv}^D} \right)^{1/2} \quad (1-35)$$

Firstly, the overall liquid surface tension should be separated into polar and dispersive components. This can be done by measuring the contact angle of the liquid on a standard reference surface, which is capable of no-polar type interactions. An example of such surface is poly(tetrafluoroethylene) (PTFE), for which,  $\sigma_{sv} = \sigma_{sv}^D = 18 \text{ mN/m}$  and  $\sigma_{sv}^P = 0 \text{ mN/m}$ . According to Eq. (1-32), the dispersive component of the liquid surface tension is given as:

$$\sigma_{sv}^D = \frac{[\sigma_{lv}(\cos \theta_{PTFE} + 1)]^2}{0.072} \quad (1-36)$$

where  $\theta_{PTFE}$  is the contact angle of the liquid on the PTFE surface.

Once all values of the liquid surface tensions (overall, polar and dispersive) and the equivalent contact angles are known, the solid surface tensions can be determined by plotting  $Y$  versus  $X$ , as shown in Figure 1-10b. Indeed, the polar and dispersive solid surface tensions can be calculated from the slope and the intercept of the fit line to the  $Y/X$  curve, respectively. The overall tension is the sum of these two components.

The Owens/Wendt theory is typically the most applicable to surfaces that have low surface charge and are moderately polar in nature. This theory has limitation since it leaves the choice of liquids used up to the experimenter. Based on the equation of Owens and Wendt (1-32), Fowkes [1.36] suggested a method to determine the solid surface tensions by using contact angle data from two reference liquids, e.g. diiodomethane and water. Diiodomethane has no polar component to its overall surface tension, thus enables calculating the dispersive solid surface tension. Water has both dispersive and polar to its surface tension. It is then used after diiodomethane and enables determining the polar solid surface tension.

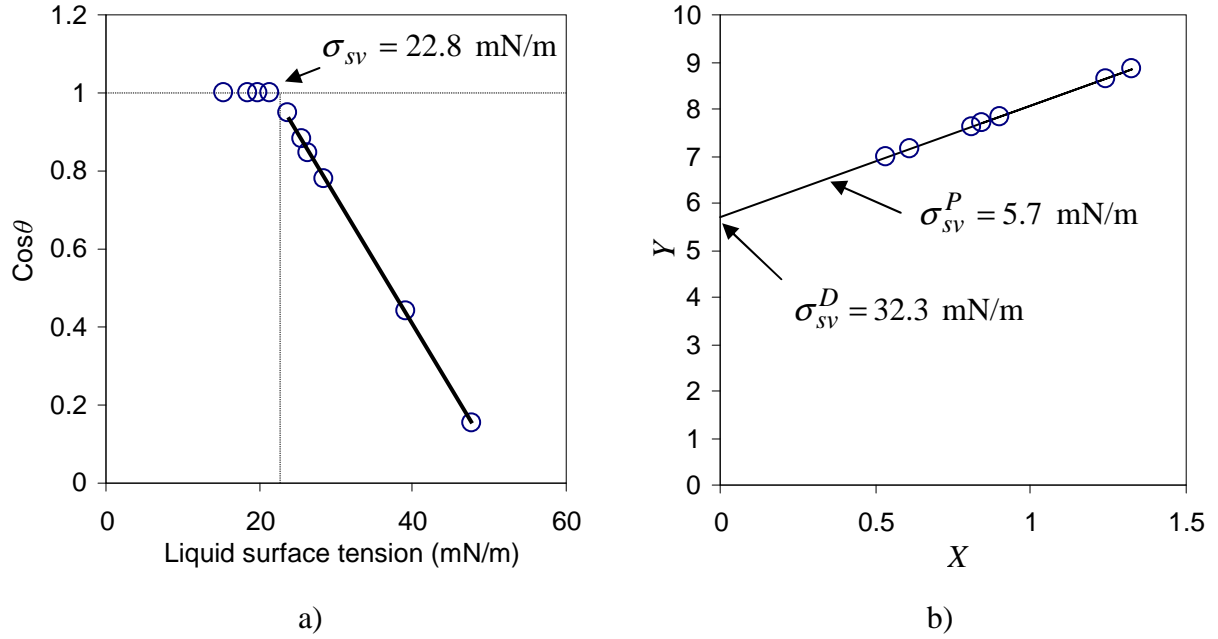


Figure 1-10. Determination of the solid surface tension: a) Zisman plot for a low density poly(ethylene) and b) Owens/Wendt plot for poly(methyl methacrylate) (data from KRÜSS technical note [1.33]).

### 1.3.3 Effect of surface roughness on wetting

Wetting of a liquid on a solid surface is impacted not only by the surface chemistry, but also by the surface topography. Two distinct models, developed independently by Wenzel [1.37] and Cassie and Baxter [1.38] (named as the Cassie model), are commonly used to explain the effect of surface roughness on the apparent contact angle of liquid drops.

#### Wenzel model

Wenzel [1.37] is known as the first person to analyze the effect of surface roughness on the static contact angle. He observed that surface roughness caused a wetted surface to behave as if it were more wetted and an unwetted surface to behave as if it were more unwetted. Hence, he suggested modifying Young's equation (1-28) by multiplying the numerator of the right side of Eq. (1-28) by a roughness factor,  $r$ , which is the ratio of the actual area to the apparent area of the contact surface:

$$\cos \theta = r \cos \theta_{smooth} \quad (1-37)$$

where  $\theta_{smooth}$  is the contact angle measured on a smooth surface of the same material, given by Young's equation (1-28) as  $\cos \theta_{smooth} = (\sigma_{sv} - \sigma_{sl}) / \sigma_{lv}$ .

#### Cassie model

The Cassie model [1.38], on the other hand, postulates that the hydrophobic nature of a rough surface is caused by microscopic pockets of air remaining trapped below the liquid droplet, leading to a composite interface (cf. Figure 1-11). If  $\Phi_s$  is the fraction of the solid in contact with the liquid, the Cassie equation yields:

$$\cos \theta = -1 + \Phi_s (1 + \cos \theta_{smooth}) \quad (1-38)$$

In contrast to the Wenzel relation, the Cassie model enables the possibility of  $\theta > 90^\circ$ , even with  $\theta_{smooth} < 90^\circ$ . The transition from the Wenzel to the Cassie state was observed [1.39]-[1.40] at a critical contact angle  $\theta_{cr}$ , which is obtained by equating Eqs. (1-37) and (1-38):

$$\cos \theta_{cr} = \frac{\Phi_s - 1}{r - \Phi_s} \quad (1-39)$$

The value of the critical contact angle is necessarily greater than  $90^\circ$  as  $r > 1 > \Phi_s$ . Thus, it may be anticipated that for  $\theta < 90^\circ$ , a surface cannot exist in the Cassie state or that the creation of highly nonwetting surfaces ( $\theta \gg 90^\circ$ ) requires  $\theta > \theta_{cr} > 90^\circ$ .

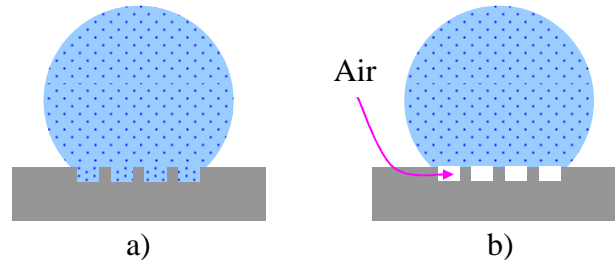


Figure 1-11. On a hydrophobic surface, schematic view of a water droplet in a) Wenzel state and b) Cassie state.

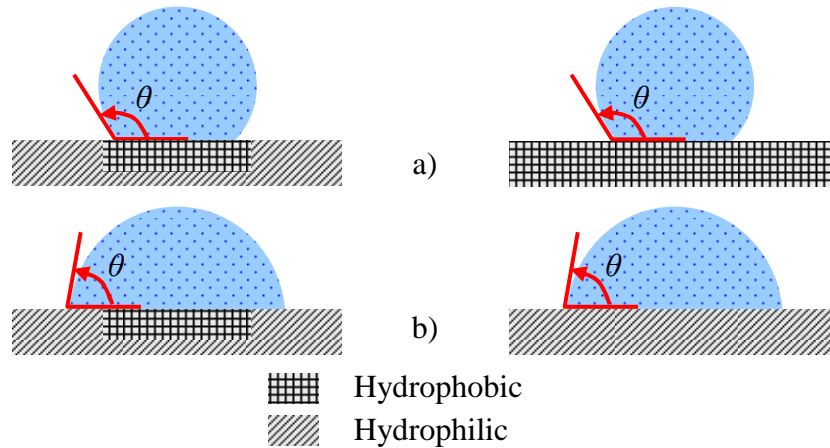


Figure 1-12. Contact angle behaviour is only determined by solid-liquid interactions at the TCL: a) inside the hydrophobic zone, the water contact angle is equal to that on the hydrophobic surface and b) if the TCL exceeds the hydrophobic zone, the contact angle is equal to that on the hydrophilic surface.

However, the validation of the Wenzel and Cassie models was questioned by Gao and McCarthy [1.41]. The authors used three types of two-component surfaces that contain “spots” in a surrounding field: a hydrophilic spot in a hydrophobic field, a rough spot in a smooth field, and a smooth spot in a rough field. They measured water contact angles within the spots and with the spot confined to within the TCL of the droplet. The results indicated that contact angle behaviour (advancing, receding, and hysteresis) is determined by interactions of the liquid and the solid at the TCL only, and that the interfacial area within the contact perimeter is irrelevant. Figure 1-12 shows an illustration to better understand the suggestion of Gao and McCarthy [1.41].

## 1.4 Boiling on enhanced surfaces

Over the years, the subject of heat transfer enhancement has been developed as a serious interest for heat exchanger applications. Investigations on this subject may have three objectives: reducing the heat exchanger size, operating at safety temperatures and increasing the rate of heat transfer. In boiling, a common technique for improving heat transfer is to structure the heated surface. The so-called “enhanced surface” is the surface having a special topography that provides higher heat transfer efficiency than the smooth surface. The enhanced surface is expected to initiate nucleate boiling at a minimal wall superheat, to sustain it at low heat fluxes or to improve the CHF. Ideal enhanced surface should address these three issues. In practice, some surfaces were proved to be good in one aspect but not in the others.

The effect of surface finish on nucleate boiling was early investigated by Jakob and Fritz in 1931, as reported by Jakob [1.42]. Water was boiled from a sandblasted surface and a surface having a square grid of machined grooves. The sandblasting provided no more than 15% improvement, which dissipated within a day. The grooved surface initially yielded boiling coefficients about three times higher than those of a smooth surface, but this performance also dissipated after several days.

Nearly eighty years after the work of Jakob and Fritz, much research have been made and brought about advances in understanding the principles for improving heat transfer by enhanced surfaces. Nowadays, the challenge is to create enhanced surfaces at lower scales (micro and nano) and to understand the physics of boiling at these scales.

### 1.4.1 Boiling on conventional enhanced surfaces

This section provides a general overview of boiling on enhanced surfaces. For more details, the reader may refer to the excellent book of Webb and Kim [1.43]. In general, enhanced surfaces account for coated, rough and extended surfaces. The coated surfaces are manufactured by depositing various materials on the working surfaces. Typical deposit materials are, for example, Teflon-like and metal powders. A fine-scale porous coating may lead to enhancement of nucleate boiling. Surface roughness is usually formed by machining or restructuring the surface. Rough surfaces contain artificial nucleation sites, which provide higher performances than a plain surface. Extended surfaces are enhanced surfaces which are the most widely employed in heat exchangers. They provide an area increase and thereby improve the heat transfer efficiency. In the present context, this work focuses on coated and rough surfaces only. Examples of enhanced surfaces are presented in Figure 1-13. Table 1-1 presents a summary of techniques of surface treatments that have been used to develop enhanced surfaces.

In the author’s opinion, the enhanced surfaces provide enhancement of nucleate boiling through three main concepts:

1. These surfaces have more nucleation sites than a plain surface.
2. The subsurface pores are substantially larger than those on natural surfaces, reducing the superheat needed to active the nucleation sites (cf. Eq. (1-5)).
3. Gas is trapped in cavities. This improves the nucleation activation and increases the bubble emission frequency (cf. Eq. (1-6)).



Figure 1-13. Illustration of cross section of: a) porous surface, b) rough surface.

However, the performance of boiling on enhanced surfaces may fluctuate and deteriorate with time due to the so-called “hysteresis effects”, which were observed by a number of researchers [1.44]-[1.46]. This phenomenon is detected when the boiling curve of increasing heat flux is different from that of decreasing heat flux. Apparently, it is thought to be caused by liquid penetration into nucleation sites. Highly wetting fluids are more susceptible to hysteresis effects than weakly wetting fluids since they are more likely to flood the cavities.

Table 1-1. Techniques to fabricate enhanced surfaces.

Technique	Description
Abrasive treatment	Abrasively roughening the surface
Chemical etching	Exposing the surface to an etching bath
Electroplating	Using electrical current to reduce the cations of a desired material from a solution and coat the surface with a thin layer of the material
Open grooves	Forming parallel grooves by sharp pointed scriber
Painting	Mixing the particles with a paint and applying on the surface
Sintering	High-temperature method to deposit a layer of metal particles or metal fibre on the surface
Spraying	Directing the molten metal on to the surface using a spray gun
Three-dimensional cavities	Pressing cylindrical or conical cavities into the surface

Griffith and Wallis [1.47] suggested that the geometry of a cavity containing trapped gas is directly related to nucleation process. To avoid the hysteresis effects, the cavities should have reentrant shape that ensures the stability of vapour generation. The reentrant cavity accounts for a cavity having a mouth smaller than its base, and hence it is expected to not become inactive during the boiling process. Examples of reentrant cavities are presented in Figure 1-14.

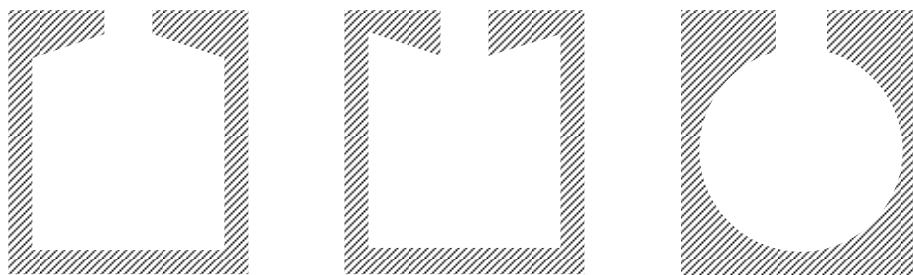


Figure 1-14. Schematic views of different interior shapes of reentrant cavities.

The gap between nucleation sites is also an important parameter of boiling on enhanced surfaces. Das *et al.* [1.48] investigated nucleate boiling of water from a plain surface and from surfaces with discrete nucleation sites. They found that boiling heat transfer increased with the increase of the number of nucleation sites, but the advantage of decreasing the gap between nucleation sites diminished rapidly. Hence, they assumed that there exists an



optimum spacing of nucleation sites beyond which extra effort of manufacturing is irrelevant. Furthermore, Alam *et al.* [1.49] questioned about the effects of coating thickness on nucleate boiling. They conducted experiments of water pool boiling from mild steel tubes which were either uncoated or coated with copper by spraying technique. The copper coating thicknesses were 19, 26, 33, 41 and 60  $\mu\text{m}$  respectively. They found that when the coating thickness increased, the heat transfer coefficient enhanced up to a maximal value and thereafter decreased.

In summary, many advances have been made to create enhanced surfaces that have better performance of boiling heat transfer than natural surfaces. The two basic techniques to fabricate enhanced surfaces are coating and structuring. The boiling process from enhanced surfaces is especially related to the geometry and the spacing of the nucleation sites. Today, researches on this subject focus on creating enhanced surfaces at small scales (micro- and nanoscale).

### 1.4.2 Boiling on surfaces structured at micro- and nanoscale

Recent interest of boiling with micro- and nano-structured surfaces has mainly derived from research on nanofluid boiling. Nanofluids are fluids containing suspended nanoparticles, which account for particles having sizes smaller than 100 nm. Compared to the milli- and microfluids, nanofluids are more stable since they undergo little erosion and gravitational deposition over long time periods. Boiling of nanofluids has become an attractive subject over the past decade. A number of researchers observed deposition of nanoparticles on the heated surface. This has the effect to increase the surface roughness and wettability. The critical heat flux was also found to be significantly improved. However, controversial results were obtained for the heat transfer coefficient. Most studies reported no change of heat transfer and even worse the presence of heat transfer deterioration. A few others reported heat transfer enhancements. Summary of some studies is presented in Table 1-2.

Underlining the role of the ratio of surface roughness  $R_a$  to particles size  $S_p$ , Narayan *et al.* [1.50] explained the mechanism of enhancement/deterioration of boiling heat transfer using nanofluids. The authors observed that the heat transfer coefficient increased by 70% in the case of a heater with an average roughness of 524 nm and suspensions with an average particle size of 47 nm. But when the ratio of the average surface roughness to the average particle size became close to unity, the pool boiling heat transfer deteriorated significantly due to the decrease of the number of nucleation sites.

In any case, the build-up of a thin porous layer of nanoparticles on the heated surface is within itself an interesting finding. Boiling nanofluids on the desired surface can turn out to be a new coating technique. For that, one should be able to control the deposition thickness. Kim *et al.* [1.51] assumed that the deposition of nanoparticles is primary due to evaporation of liquid microlayer underneath a bubble. Hence, they suggested the following equation to estimate the rate of growth of the nanoparticle layer  $\dot{\delta}$ :

$$\dot{\delta} = \frac{3}{2} \frac{\delta_m \varphi q}{D_d \rho_v H_{lv}} \quad (1-40)$$

wherein  $\delta_m$  is the microlayer thickness,  $\varphi$  is the nanoparticle volumetric concentration,  $q$  is the heat flux,  $D_d$  is the bubble departure diameter,  $\rho_v$  is the vapour density and  $H_{lv}$  is the vaporisation latent heat.

In addition, Kim *et al.* [1.62] performed flow boiling experiments with low concentrations (0.01% by volume) of  $\text{Al}_2\text{O}_3$  nanoparticles in water at atmospheric pressure, at moderate subcooling ( $<20^\circ\text{C}$ ) and relatively high mass flux ( $\geq 1000 \text{ kg/m}^2\text{s}$ ). They observed for the first time that nanofluids can enhance the flow CHF significantly (by as much as 30%). The enhancement of CHF in pool and flow boiling of nanofluids was clarified by Kim *et al.* [1.51], who established the nexus between CHF and surface wettability. According to these authors, the deposition of nanoparticle layer on the heated surface improves the surface wettability. When CHF occurs, high surface wettability mitigates the propagation of the hot spot, which could explain why burnout tends to be more localized in the nanofluid runs than in the water runs. Kim and Kim [1.63] conducted pool boiling experiments with Ag,  $\text{SiO}_2$ ,  $\text{Al}_2\text{O}_3$  and  $\text{TiO}_2$  nanofluids. They demonstrated that the CHF enhancement is a consequence of both the increase of surface wettability and the capillarity of the nanoparticle deposition layer.

Table 1-2. Summary of studies on nanofluid pool boiling.

Author	Year	Results
Narayan <i>et al.</i> [1.50]	2007	Heat transfer deterioration for $R_d/S_p \sim 1$ Heat transfer enhancement for $R_d$ of $0.524 \mu\text{m}$ and $S_p$ of $0.047 \mu\text{m}$
Kim <i>et al.</i> [1.51]	2007	Surface wettability improvement Critical heat flux enhancement ( $>50\%$ ) Heat transfer deterioration
Khandekar <i>et al.</i> [1.52]	2007	Surface wettability improvement Heat transfer deterioration
Kim <i>et al.</i> [1.53]	2007	Critical heat flux enhancement (up to 100%)
Wang <i>et al.</i> [1.54]	2006	Contact angle increase by nanocoating Heat transfer enhancement for coating of 20 and $80 \mu\text{m}$ thickness
Bang and Chang [1.55]	2005	Heat transfer deterioration increases with nanoparticle concentration, Critical heat flux enhancement of 32%
Wen and Ding [1.56]	2005	Heat transfer coefficient enhancement of 40%
Tu <i>et al.</i> [1.57]	2004	Heat transfer coefficient enhancement of 64%
You et Chang [1.58]	2004	Critical heat flux enhancement of 200% No change of heat transfer coefficient Bubble size increase of 30% Significant decrease of bubble departure frequency
Vassallo <i>et al.</i> [1.59]	2004	Critical heat flux enhancement (up to 200%) No change of heat transfer coefficient
Witharana [1.60]	2003	Heat transfer enhancement with gold-water nanofluids Heat transfer deterioration with silica-water nanofluids
Das <i>et al.</i> [1.61]	2003	Increase of heat transfer deterioration with nanoparticle concentration

The early works on boiling of nanofluids highlight the dominant effects of surface coating by nanoparticle deposition on boiling heat transfer. This subject has been discussed by only a few studies. For instance, Kunugi *et al.* [1.64] created a nanoparticle porous layer on sample surfaces by a chemical etching technique. They discovered an ultrahigh convective heat transfer performance compared to the well-known heat transfer correlations. The maximum increase of heat transfer coefficient was about 180%. Using Omegabond 200 high thermal conductivity epoxy, Vemuri and Kim [1.65] deposited a nanoporous layer  $70 \mu\text{m}$  thick on a plain surface, and observed a reduction of about 30% in the incipient superheat.

Kim *et al.* [1.66] used MEMS (micro-electro-mechanical systems) fabrication to mimic the structure and characteristics of a surface deposited by nanoparticles. They fabricated three surfaces with nanostructure, microstructure and nanostructure on microstructure, respectively. They observed that nanostructure intensified the surface wettability and liquid spreadability. The enhancement of CHF was also noticed and was related to the enhancement of surface wettability and liquid spreadability. The effect of microstructure on CHF enhancement was not explained. The greatest CHF enhancement was observed with the surface containing both the micro and nanostructures. Each surface also showed some enhancement in boiling heat transfer.

### 1.4.3 Effects of surface wettability on boiling heat transfer

The observations on nanofluid boiling lead to questioning the role of surface wettability on nucleate boiling mechanism. Up to now, this issue is frequently understood by classical models [1.8],[1.11]. Little experimental data about this are available because of the difficulty of varying the contact angle while keeping all other parameters constant.

One traditional method to modify the liquid contact angle is the use of surfactant solutions as Wen and Wang [1.67]. The authors found that the addition of surfactant could enhance the water boiling heat transfer by the change of surface wettability, which had been neglected for a long time and could be an important parameter influencing boiling heat transfer. The disadvantage of this method is that both the surface wettability and the surface tension vary. Hence, the enhancement of the boiling heat transfer might be due to the significant decrease of the surface tension rather than the increase of the surface wettability.

Oxidizing copper is another method widely applied. The surface wettability is modified by controlling the degree of oxidation of the surface. Using this method, Liaw and Dhir [1.68] found that for a given heat flux, the void fraction near the heated surface increases as the contact angle increases, whereas the maximum heat flux decreases with an increase in contact angle. However, oxidizing copper may change the surface topography at microscale which is the characteristic scale of nucleation sites.

Another method employed by Takata *et al.* [1.69] is  $\text{TiO}_2$  photocatalysis. The authors observed a significant decrease of water contact angle when the surface coated with  $\text{TiO}_2$  is irradiated by UV light. Due to this property of  $\text{TiO}_2$ , they made superhydrophilic surfaces of which the heat transfer characteristic in nucleate boiling is better than that of an uncoated one. Though, the study of Takata *et al.* [1.69] is limited in contact angle range and stability: the contact angle varied from  $0^\circ$  to  $20^\circ$  and was unstable during experiments.

Furthermore, most experiments on boiling heat transfer dealt with wetted surfaces. Few studies investigated nucleate boiling mechanism on nonwetting material as summarised in Chapter 11 of Webb and Kim [1.43]. Griffith and Wallis [1.70] performed experiments on single conical cavities 0.08 mm in diameter, formed by pressing a needle into the boiling surface. They found that unwetted (paraffin-coated) cavities are more stable in term of heat transfer than wetted ones.

Gaertner [1.71] carried out further work with artificial nucleation sites, covering the inside surface of the cavities with a nonwetting material. The coated cavity surface boiled at a lower superheat and remained active for a much longer time. However, the heat transfer coefficient was considerably reduced if the coating was deposited on the entire surface because of the bubble coalescence that caused the entire surface to become vapour blanketed.

Hummel [1.72] boiled water on a stainless steel surface which had been sprayed with Teflon, producing 30 to 60 spots/cm<sup>2</sup> with a spot diameter of 0.25 mm or less. The author observed a significant heat transfer enhancement. Gaertner [1.71] and Hummel [1.72] argue against the merits of a continuous surface coating because of the tendency of the surface to become vapour blanketed. Nevertheless, Vachon *et al.* [1.73] did not observe vapour blanketing when boiling water on stainless steel covered by an 8 µm thick layer of Teflon.

In summary, the surface wettability was early noticed as an important parameter of heterogeneous boiling. A number of investigations were carried out in order to determine its impact on the boiling process. However, in those studies, the techniques used to modify the surface wettability still exhibited some limitations because they led to unexpected modifications of some other parameters (micro-surface topography and surface tension force) and to the contact-angle instability. In addition, the lack of experiments with a large set of contact angles limits an overall understanding of the surface wettability role. Therefore, in the beginning of the present work, techniques of surface treatments for accurately modifying the surface wettability were developed, as described in the next chapter.

## 1.5 References

- [1.1] V.P. Carey, Liquid-vapour phase-change phenomena, Taylor and Francis (1992).
- [1.2] S.G. Bankoff, Ebullition from solid surfaces in the absence of a pre-existing gaseous phase, Trans. Am. Soc. Mech. Eng. 79 (1957), 735-740.
- [1.3] W. Fritz, Maximum volume of vapour bubbles, Physik Zeitschr 36 (1935), 379-384.
- [1.4] R. Cole, A photographic study of pool boiling in the region of the critical heat flux, AIChE J. 6 (1960) 533-542.
- [1.5] N. Zuber, Nucleate boiling: The region of isolated bubbles and the similarity with natural convection, Int. J. Heat and Mass Transfer 6 (1963), 53-78.
- [1.6] A.P. Hatton, I.S. Hall, Photographic study of boiling on prepared surfaces, Third International Heat Transfer Conference 4 (1966), 24-37, Chicago, USA.
- [1.7] H.J. Ivey, Relationships between bubble frequency, departure diameter and rise velocity in nucleate boiling, Int. J. Heat and Mass Transfer 10 (1967), 1023-1040.
- [1.8] C. H. Wang, V. K. Dhir, Effect of surface wettability on active nucleate site density during pool boiling of water on a vertical surface, Trans. ASME J. Heat Transfer 115 (1993), 670-679.
- [1.9] S. Nukiyama, The maximum and minimum values of heat transmitted from metal to boiling water under atmospheric pressure, J. Jap. Soc. Mech. Eng. 9 (1934), 367-374.
- [1.10] M.G. Cooper, Heat flows rates in saturated pool boiling – a wide ranging examination using reduced properties, Advanced in Heat Transfer, Academic Press (1984), 157-239, Florida, USA.
- [1.11] B.B. Mikic, W.M. Rohsenow, A new correlation of pool boiling data including the effect of heating surface characteristics, J. Heat Transfer 9 (1969), 245-250.
- [1.12] M.G. Cooper, A.J.P. Lloyd, The microlayer in nucleate boiling, Int. J. Heat and Mass Transfer 12 (1969), 895-913.

- [1.13] P. Stephan, J. Hammer, A new model for nucleate boiling heat transfer, *Warme Und Stoffubertragung* 30 (1994), 119-125.
- [1.14] F. Demiray, J. Kim, Microscale heat transfer measurements during pool boiling of FC-72: Effect of subcooling, *Int. J. Heat and Mass Transfer* 47 (2004), 3257-3268.
- [1.15] J.R. Thome, Boiling in microchannels: a review of experiment and theory, *Int. J. Heat and Fluid Flow* 25 (2004), 128-139.
- [1.16] S.S. Mehendale, A.M. Jacobi, R.K.Shah, Fluid flow and heat transfer at micro- and meso-scales with application to heat exchanger design, *Appl. Mech. Rev.* 53 (2000), 175-193.
- [1.17] S.G. Kandlikar, W.J. Grande, Evolution of microchannel flow passages: Thermohydraulic performance and fabrication technology, *Heat Transfer Eng.* 24 (2003), 3-17.
- [1.18] L. Lin, A.P. Pisano, Bubble forming on a micro line heater, micromechanical sensors, actuators, and systems, *ASME DSC* 32 (1991), 147-164.
- [1.19] P. Kew, K. Cornwell, Correlations for the prediction of boiling heat transfer in small-diameter channels, *Appl. Thermal Eng.* 17 (1997), 705-715.
- [1.20] A. Ullmann, N. Brauner, The prediction of flow pattern maps in minichannels, *Multiphase Science and Technology* 19 (2007), 49-73.
- [1.21] A. Serizawa, Z. Feng, Z. Kawara, Two-phase flow in microchannels, *Experimental Thermal and Fluid Science* 26 (2002), 703-714.
- [1.22] K. A. Triplett, S. M. Ghiaasiaan, S. I. Abdel-Khalik, D. L. Sadowski, Gas-liquid two-phase flow in microchannels, Part I: two-phase flow patterns, *Int. J. Multiphase Flow* 25 (1999), 377-394.
- [1.23] C.-Y. Yang, C.-C. Shieh, Flow pattern of air-water and two-phase R-134a in small circular tubes, *Int. J. Multiphase Flow* 27 (2001), 1163-1177.
- [1.24] R. Revellin, J. R. Thome, Experimental investigation of R-134a and R-245fa two-phase flow in microchannels for different flow conditions, *Int. J. Heat and Fluid Flow* 28 (2007), 63-71.
- [1.25] N. Caney, J. Bigot, P. Marty, Experimental flow boiling study in mini-channel, Thirteenth Int. Heat Transfer Conference (2006), Sydney, Australia.
- [1.26] F. Madrid, N. Caney, P. Marty, Study of a vertical boiling flow in rectangular minichannels, *Heat Transfer Engineering* 28 (2007), 753-760.
- [1.27] C.M. Callizo, R. Ali, P. Palm, Dryout incipience and critical heat flux in saturated flow boiling of refrigerants in a vertical uniformly heated microchannel, Sixth Inter. Conference on Nanochannels, Microchannels and Minichannels (2008), Darmstadt, Germany.
- [1.28] R. Revellin, J.R. Thome, A theoretical model for the prediction of the critical heat flux in heated microchannels. *Int. J. Heat Mass Transfer* 51 (2008), 1216-1225.
- [1.29] T. Young, An essay on the cohesion of fluids, *Phil. Trans. R. Soc. Lond.* 95 (1805) 65-87.
- [1.30] D. Quéré, Non-sticking drops, *Rep. Prog. Phys.* 68 (2005), 2495-2532.
- [1.31] A. Dupré, *Théorie mécanique de la Chaleur*, Paris: Gauthier-Villars (1869), 369.

- [1.32] W.A. Zisman, Relation of the equilibrium contact angle to liquid and solid constitution, *Advances in Chemistry Series* 43 (1964), 1-51.
- [1.33] C. Rulison, So you want to measure surface energy?, KRÜSS technical note TN306e.
- [1.34] D.K. Owens, R.C. Wendt, Estimation of the surface free energy of polymers, *J. Appl. Polymer Science* 13 (1969), 1741.
- [1.35] R.J. Good, L.A. Girifalco, A theory for estimation of surface and interfacial energies. III. Estimation of surface energies of solids from contact angle data, *J. Phys. Chem.* 64 (1960), 561–565.
- [1.36] F.M. Fowkes, Attractive forces at interfaces, *Industrial and Engineering Chemistry* 56 (1964), 40-52.
- [1.37] R.N. Wenzel, Resistance of solid surfaces to wetting by water, *Industrial and Engineering Chemistry* 28 (1936), 7426-7431.
- [1.38] A. B. D. Cassie, S. Baxter, Wettability of porous surfaces, *Trans. Faraday Soc.* 40 (1944), 546-551.
- [1.39] B. He, N.A. Patankar, J. Lee, Multiple equilibrium droplet shapes and design criterion for rough hydrophobic surfaces, *Langmuir* 19 (2003), 4999-5003.
- [1.40] A. Lafuma, D. Quéré, Superhydrophobic states, *Nature Materials* 2 (2003), 457-460.
- [1.41] L. Gao, T. J. McCarthy, How Wenzel and Cassie were wrong, *Langmuir* 23 (2007), 3762-3765.
- [1.42] M. Jakob, *Heat transfer*, John Wiley & Sons (1949), New York, 636-638.
- [1.43] R.L. Webb, N-H. Kim, *Principles of enhanced heat transfer*, 2<sup>nd</sup> ed., Taylor & Francis (2005), New York.
- [1.44] A.E. Bergles, M.C. Chyu, Characteristics of nucleate pool boiling from porous metallic coatings, *J. Heat Transfer* 104 (1982), 279-285.
- [1.45] C.J. Kim, A. E. Bergles, Incipient boiling behavior of porous boiling surfaces used for cooling of microelectronic chips, *Particulate Phenomena and Multiphase Transport* 2 (1988), 3-18.
- [1.46] J.T. Cieslinski, Nucleate pool boiling on porous metallic coatings, *Exp. Thermal and Fluid Science* 25 (2002), 557-564.
- [1.47] P. Griffith, J.D. Wallis, The role of surface conditions in nucleate boiling, *Chem. Eng. Prog. Symp. Ser.* 56 (1960), 49-63.
- [1.48] A.K. Das, P.K. Das, P. Saha, Nucleate boiling of water from plain and structured surfaces, *Experimental Thermal and Fluid Science* 31 2007, 967-977.
- [1.49] M. S. Alam, L. Prasad, S.C. Gupta, V.K. Agarwal, Enhanced boiling of saturated water on copper coated heating tubes, *Chemical Engineering and Processing: Process Intensification* 47 (2008), 159-167.
- [1.50] G.P. Narayan, K.B. Anoop, S.K. Das, Mechanism of enhancement/deterioration of boiling heat transfer using stable nanoparticle suspensions over vertical tubes, *J. Appl. Physics* 102 (2007), 074317.
- [1.51] S.J. Kim, I.C. Bang, J. Buongiorno, L.W. Hu, Surface wettability change during pool boiling of nanofluids and its effect on critical heat flux, *Int. J. Heat and Mass transfer* 50 (2007), 4105-4116.

- [1.52] S. Khandekar, Y.M. Joshi, B. Metha, Thermal performance of closed two-phase thermosyphon using nanofluids, *Int. J. Thermal Science* 47 (2007), 659-667.
- [1.53] H.D. Kim, J. Kim, M.H. Kim, Experimental studies on CHF characteristics of nanofluids at pool boiling, *Int. J. Multiphase Flow* 33 (2007), 691-706.
- [1.54] Y. Wang, L. Wang, M. Liu, Antifouling and Enhancing Pool boiling by TiO<sub>2</sub> Coating Surface in Nanometer Scale Thickness, *AIChE-Wiley InterScience* 53 (2006), 3062-3076.
- [1.55] I.C. Bang, S.H. Chang, Boiling heat transfer performance and phenomena of Al<sub>2</sub>O<sub>3</sub>-water nano-fluids from a plain surface in a pool, *Int. J. Heat and Mass Transfer* 48 (2005), 2407-2419.
- [1.56] D. Wen, Y. Ding, Experimental investigation into the pool boiling heat transfer of aqueous based  $\gamma$ -alumina nanofluids, *J. Nanoparticle Research* 7 (2005), 265-274.
- [1.57] J. Tu, N. Dinh, T. Theofanous, An experimental study of nanofluid boiling heat transfer, *Proc. 6<sup>th</sup> Int. Symp. Heat Transfer* (2004), 91-96, Beijing, China.
- [1.58] S.M. You, J.Y. Chang, Pool boiling Heat Transfer in Saturated Nanofluids, *ASME IMECE02004-61108* (2004).
- [1.59] Vassallo, R. Kumar, S. D'Amico, Pool boiling heat transfer experiments in silica-water nano-fluids, *Int. J. Heat and Mass Transfer* 47 (2004) 407-411.
- [1.60] S. Witharana, Boiling of refrigerants on enhanced surfaces and boiling of nanofluids, *Licenciate Thesis, Department of energy technology, The Royal Institute of Technology* (2003), Stockholm, Sweden.
- [1.61] S.K. Das, N. Putra, W. Roetzel, Pool boiling characteristics of nano-fluids, *Int. J. Heat and Mass Transfer* 46 (2003) 851-862.
- [1.62] S. J. Kim, T. McKrell, J. Buongiorno, L.-W. Hu, Enhancement of flow critical heat flux in water-based nanofluids with alumina nanoparticles, *Twelfth Int. Topical Meeting on Nuclear Reactor Thermal Hydraulics NURETH-12* (2007), Pennsylvania, U.S.A,
- [1.63] H. D. Kim, M. H. Kim, Effect of nanoparticle deposition on capillary wicking that influences the critical heat flux in nanofluids, *Applied Physics Letters* 91 (2007), 014104.
- [1.64] T. Kunugi, K. Muko, M. Shibahara, Ultrahigh heat transfer enhancement using nanoporous layer, *Superlattices and Microstructures* 35 (2004) 531-542.
- [1.65] S. Vemuri, K.J. Kim, Pool boiling of saturated FC-72 on nano-porous surface, *Int. Communications in Heat and Mass Transfer* 32 (2005) 27-31.
- [1.66] S. Kim, H. Kim, H. D. Kim, H. S. Ahn, M. H. Kim, J. Kim, G. C. Park, Experimental investigation of critical heat flux enhancement by micro/nanoscale surface modification in pool boiling, *The Sixth Int. ASME Conference on Nanochannels, Microchannels and Minichannels ICNMM2008* (2008), Darmstadt, Germany.
- [1.67] D.S. Wen, B.X. Wang, Effects of surface wettability on nucleate pool boiling heat transfer for surfactant solutions, *Int. J. Heat and Mass Transfer* 45 (2002), 1739-1747.
- [1.68] S.P. Liaw, V.P. Dhir, Void fraction measurements during saturated pool boiling of water on partially wetted vertical surfaces, *J. Heat Transfer* 111 (1989), 731-738.

- [1.69] Y. Takata , S. Hidaka, J.M. Cao, T. Nakamura, H. Yamamoto, M. Masuda, T. Ito, Effect of surface wettability on boiling and evaporation, *Energy* 30 (2005), 209-220.
- [1.70] P. Griffith, J.D. Wallis, The role of surface conditions in nucleate boiling, *Chem. Eng. Prog. Symp. Ser.* 56 (1960), 49-63.
- [1.71] R.F. Gaertner, Methods and means for increasing the heat transfer coefficient between a wall and boiling liquid, U.S. Patent 3,301,314 (1967).
- [1.72] R. L. Hummel, Means for increasing the heat transfer coefficient between a wall and boiling liquid, U.S. Patent 3,207,209 (1965).
- [1.73] R.I. Vachon, G.H. Nix, G.E. Tanger, Evaluation of constants for the Rohsenow pool-boiling correlation, *J. Heat Trans.* 90 (1968), 239-247.





## Chapter 2: Techniques for surface treatment and characterization

The previous chapter presents the benefits of enhanced surfaces in improving boiling heat transfer. Over the past eighty years, significant advances have been made in manufacturing enhanced surfaces on the macroscale. Today, progress in micro and nano technologies enables the fabrication of enhanced surfaces on the lower (micro and nano) scales, at which the mechanism of boiling enhancement should be different. Indeed, the wetting phenomenon can play an important role at these scales, and hence its effects need to be considered in the boiling processes. Some investigations have been carried out to explore the influence of surface wettability on boiling, but no accurate experiments have been conducted so far because of the lack of technology to modify the contact angle without a large change in other parameters.

This chapter is devoted to describing the techniques for surface treatment and the methods of surface characterization used in this study. The sample surfaces were micro- or nano-treated by chemical techniques (chemical vapour deposition) or physical techniques (physical vapour deposition and laser etching). In general, microscale surface treatments are used to create artificial surface patterns, while nanoscale surface treatments are used to modify the surface wettability. Characterization of the sample surfaces was made by measurements of different parameters, e.g. surface topography, surface roughness, contact angle and electrical resistance. The determination of these parameters is necessary for understanding the physical interactions at the solid-liquid interface. In this chapter, only experimental principles are referred to and technical details are not mentioned. The reader should consult the literature cited for a more complete understanding of the specific processes discussed.

### 2.1 Surface treatment

Thin film technologies and patterning techniques have been widely developed over the past decades, particularly for the microelectronics and IT<sup>1</sup>-related components and systems. Their direct implementation in the fields of heat and mass transfer is mostly recent and opens large expectations in making new surfaces which have not been assessed before in heat exchange systems. Table 2-1 summarizes the surface solutions realized in the present work. Those surfaces mainly address heating, structuring and wetting functions which were necessary to operate the experimental heat-exchanger systems. Related surface-treatment conditions will be presented in the following subsections.

Table 2-1. Summary of coating processes used in this study.

Material	Notation	Technique	Thickness	Function
Titanium	Ti	PVD	3-4 $\mu\text{m}$	Heating & structuring layer
Diamond-like carbon	DLC	PECVD	0.5-1 $\mu\text{m}$	Electrical-insulating & structuring layer
Low-carbon PDMS <sup>2</sup>	SiOx	PECVD	< 50 nm	Wetting layer
High-carbon PDMS	SiOC	PECVD	< 50 nm	Wetting layer
Teflon-like	Teflon	PECVD	< 50 nm	Wetting layer
Iron oxide	Fe <sub>2</sub> O <sub>3</sub>	MOCVD	< 50 nm	Wetting layer
Platinum	Pt	MOCVD	< 50 nm	Wetting layer

<sup>1</sup> Information Technologies

<sup>2</sup> Polydimethylsiloxane

### 2.1.1 Physical vapour deposition

#### Definition

Physical vapour deposition (PVD) is a vacuum deposition process used to deposit thin films by the condensation of a vaporized form of the material onto various surfaces [2.1]. The coating method involves purely physical processes such as high temperature vacuum evaporation or plasma sputter bombardment. Variants of PVD include:

- Evaporative deposition: in which the material to be deposited is heated to a high vapour pressure by electrically resistive heating in "low" vacuum,
- Electron beam physical vapour deposition: in which the material to be deposited is heated to a high vapour pressure by electron bombardment in "high" vacuum,
- Sputter deposition: in which a glow plasma discharge (usually localized around the "target" by a magnet) bombards the material sputtering some away as a vapour,
- Cathodic arc deposition: in which a high power arc directed at the target material blasts away some into a vapour,
- Pulsed laser deposition: in which a high power laser ablates material from the target into a vapour.

#### Titanium coatings by PVD

The CEA process used for titanium coatings is based on the sputter deposition variant [2.2]. Figure 2-1a illustrates the PVD reactor used in this study. The sputtering source is a magnetron that uses strong electric and magnetic fields to trap electrons close to the surface of the magnetron, which is known as the target (cf. Figure 2-1b).

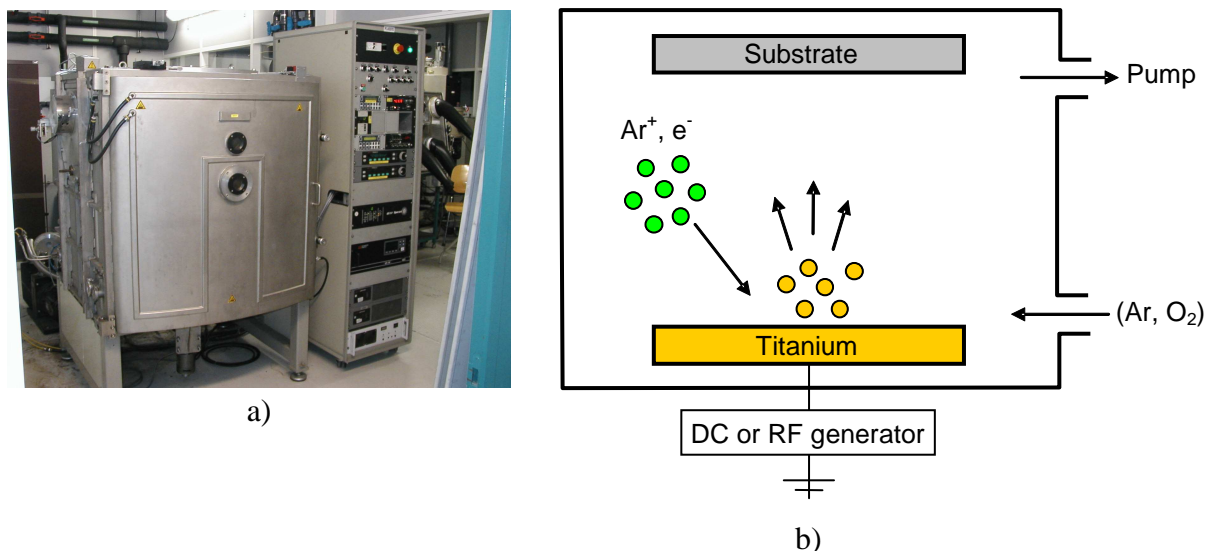


Figure 2-1. CEA magnetron sputtering reactor: a) experimental apparatus image and b) schematic diagram.

The electrons following helical paths around the magnetic field lines undergo more ionizing collisions with gaseous neutrals near the target surface than would otherwise occur. The sputter gas is inert, typically argon in this case. The extra argon ions created as a result of

these collisions lead to a higher deposition rate. It also means that the plasma can be sustained at a lower pressure. The sputtered atoms are neutrally charged and so are unaffected by the magnetic trap. Table 2-2 summarizes the operating conditions of the titanium coating process.

Table 2-2. PVD process conditions for depositing Ti coatings.

Target	Sputter gas	Working pressure (mbar)	Magnetron power (W)	Magnetron frequency (kHz) /Duty time ( $\mu$ s)	Process temperature ( $^{\circ}$ C)	Plates spacing (mm)	Deposition rate (nm/s)
Titanium 99.9%	Argon	0.005	600	30 /4	~100	80	~ 0.6

## 2.1.2 Chemical vapour deposition

### Definition

*Chemical vapour deposition (CVD)* accounts for the deposition of a solid coating on a heated surface from the chemical reaction of gaseous precursors [2.3]. In a typical CVD process, the substrate is exposed to one or more volatile precursors (chemical compounds), which react and/or decompose on the substrate surface, producing the desired deposit and volatile by-products (cf. Figure 2-2). An inert gas, such as argon or helium, is often used to improve transport of precursor vapour in the deposition chamber and also to remove the by-products.

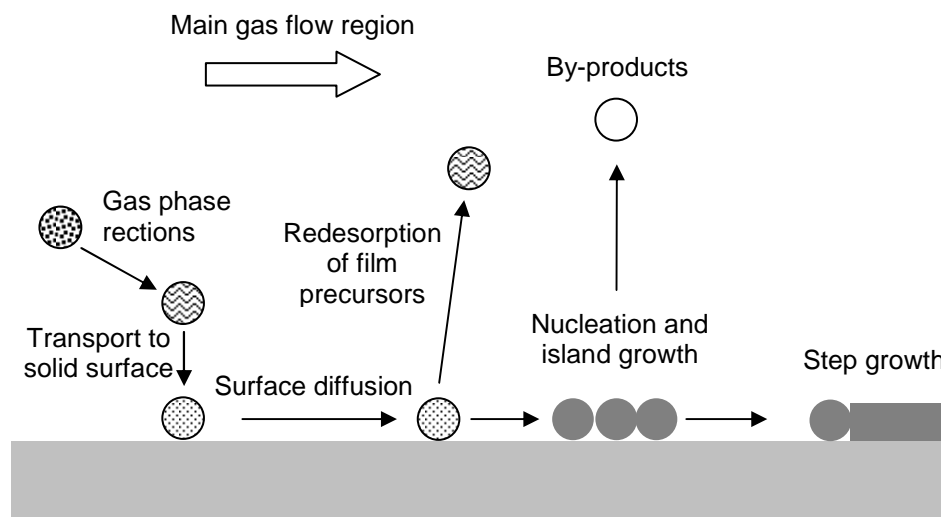


Figure 2-2. Diagram of CVD processes.

*Plasma enhanced chemical vapour deposition (PECVD)* is also known as glow discharge chemical vapour deposition. In PECVD process, plasma (ionic gases) is used to initiate chemical reactions. Generally, the plasma is created by radio frequency (RF) or direct current (DC) discharge between two electrodes, the space between which is filled with the reacting gases. The PECVD allows deposition process to occur at a lower temperature than the conventional CVD method.

*Metalorganic chemical vapour deposition (MOCVD)* is a chemical vapour deposition process that uses organometallic precursors, which refer to compounds containing metal atoms bonded to organic radicals. Generally, the metalorganic precursors undergo pyrolysis reactions. Compared to the conventional CVD process, MOCVD process requires a lower deposition temperature and gives higher deposition yield.

### Diamond-like-carbon coatings by PECVD

CEA processes developed for diamond-like-carbon (DLC) applications are based on the PECVD technique [2.4]. A 250-mm diameter samples holder is connected to the live plasma electrode which runs at low frequency (40 kHz). A 250-mm diameter showerhead is used to flow uniformly the gas precursors inside the reactor to the surface of the samples to be coated. Before operating the discharge, the reactor is pumped to  $2\text{--}4 \cdot 10^{-6}$  mbar by means of a rotary, a roots and a turbo-molecular pumping group. During plasma deposition, the chamber is evacuated by a rotary pump.

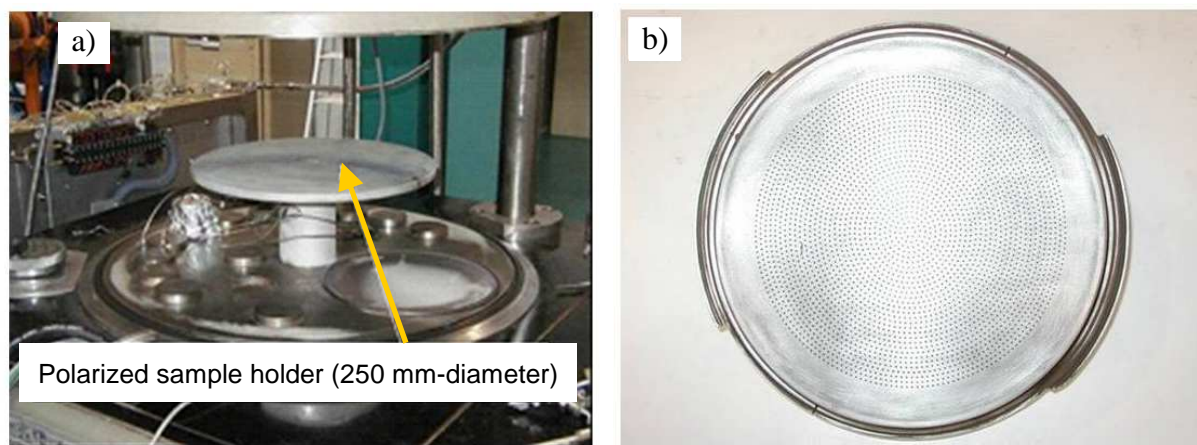


Figure 2-3. In-house built PECVD reactor: a) sample holder and b) showerhead.

Several carbon precursors can be used in PECVD to synthesize DLC coatings (e.g. benzene, acetylene, cyclohexane, pentane, propane, methane, etc.). In the present case, cyclohexane ( $\text{C}_6\text{H}_{12}$ ) is used together with a reducing mixture of hydrogen so to enable relatively faster growth rate at a given plasma power. As this coating was formerly developed on steel samples for mechanical applications it appeared necessary to co-develop an adhesion layer to improve the durability and toughness of the coated samples. So came the hydrogenated silicon carbide (SiCH) coating as an optimized candidate to reduce the overall stress within the coating assembly and to insure good chemical bonding at the interfaces. This coating is processed in-situ in the same reactor using tetramethylsilane TMS ( $\text{Si}(\text{CH}_3)_4$ ) and argon as precursor and carrier gas, respectively. Shown in Table 2-3 is a summary of the operating conditions for deposition of SiCH and DLC coating.

Table 2-3. PECVD process conditions for depositing SiCH and DLC coatings.

	Precursors Partial pressure (mbar)	Carrier	Working pressure (mbar)	Power (W)	Process temperature (°C)	Plate spacing (mm)	Deposition rate (nm/s)
SiCH	TMS ( $\text{Si}(\text{CH}_3)_4$ ) 0.05	Ar	0.10	100	120	200	~ 0.3
DLC	$\text{C}_6\text{H}_{12}$ 0.03	$\text{H}_2$	0.04	300	120	200	~ 1.5

### Polydimethylsiloxane coatings by PECVD

CEA processes developed for hydrophilic and hydrophobic applications are based on the PECVD technique [2.5]–[2.6]. Plasmas are produced inside a cylindrical stainless steel vacuum chamber (diameter 30 cm) with a parallel plate configuration. Substrates to be coated are positioned on the lower grounded electrode. The precursor vapour is uniformly distributed

in the reactor by the upper showerhead electrode (with pinholes diameter of 1 mm). The upper electrode is externally connected, through a semi-automated matching network, to a 13.56 MHz-RF power supplier which provides a RF voltage with respect to the grounded chamber. Before operating the discharge, the reactor is pumped below  $5.10^{-3}$  mbar by the mean of a rotary pump. During plasma deposition, the chamber is evacuated also by the mean of the rotary pump.



Figure 2-4. In-house built PECVD reactor for silicon oxide coatings.

Polydimethylsiloxane (PDMS)-based coating is an interesting solution towards tuneable surface energy. Precursors such as hexamethyldisiloxane (HMDSO), tetramethylsiloxane (OMCTSO) or tetraethoxysilane (TEOS) mixed with oxidants ( $O_2$ ) and/or noble gases (Ar, He) are commonly used. In particular, HMDSO is one of the most common monomer described in the literature concerning PECVD deposition of silicon oxide thin films. HMDSO is a monomer that cannot be polymerised following the conventional polymerisation methodologies in liquid phase because it does not have cyclic or double bonds in its structure. On the contrary, HMDSO can be polymerised during plasma treatments, by rearranging the radicals produced by its dissociation induced by electron impact. Soft coatings of  $SiO_xC_yH_z$  with high content of methylene and methyl groups are obtained by using pure HMDSO in plasma process yields [2.7]. As a replacement of HMDSO, OMCTSO can also be used for its respectively higher content of methyl groups and lower density which bring the surface energy further down.

Using either oxidizing or reducing mixtures together with PDMS precursors lead to low or high carbon containing PDMS coatings that present hydrophilic ( $SiO_x$ ) or hydrophobic ( $SiOC$ ) properties, respectively. Conditions of the PDMS coatings are summarized in Table 2-4 below.

Table 2-4. PVD process conditions for depositing PDMS coatings.

	Notation	Precursors, Partial pressure (mbar)	Carrier	Working pressure (mbar)	Power (W)	Process temperature ( $^{\circ}C$ )	Plate spacing (mm)	Deposition rate (nm/s)
High-carbon PDMS	SiOC	OMCTSO, 0.15	Reducing mixture	0.25	100	80	30	$\sim 1$
Low-carbon PDMS	SiOx	HMDSO, 0.15	Oxidizing mixture	0.50	800	80	15	$\sim 10$



### Iron oxide and Platinum coatings by MOCVD

CEA processes developed for Iron oxide ( $\text{Fe}_2\text{O}_3$ ) and Platinum (Pt) applications rely on the MOCVD technique using the same equipment as per PECVD applications (cf. section above). In the MOCVD configuration, the plasma source is not activated. A dedicated liquid injector is used to pulse the liquid precursor mixture (metallic acetylacetonate and toluene) through the showerhead inside the vacuum chamber. A stable gas phase of organometallic compounds is thereby generated with an accurate control of the gas flowrates inside the chamber. Conditions of these coatings are summarized in Table 2-5 below.

Table 2-5. MOCVD process conditions for depositing  $\text{Fe}_2\text{O}_3$  and Pt coatings.

Material	Precursors, [frequency [Hz]; impulsion No.; aperture [ms]]	Carrier	Working pressure (mbar)	Evaporator temperature ( $^{\circ}\text{C}$ )	Process temperature ( $^{\circ}\text{C}$ )	Plate spacing (mm)	Deposition type
$\text{Fe}_2\text{O}_3$	Iron acetylacetonate (1; 300; 1)	$\text{O}_2, \text{N}_2$	70-100	220	400	35	Nanoparticles – discontinuous coating
Pt	Platinum acetylacetonate (2; 1200; 10)	$\text{O}_2, \text{N}_2$	8	200	350	35	Nanoparticles – discontinuous coating

### 2.1.3 Laser ablation

#### Definition

Laser ablation is a direct-approach technique which plays an important role in machining and structuring materials. Applications cover high precision drilling, milling, fusion, scribing, etc., as well as surface preparation, texturation and 2D-3D patterns making with complex shapes at microscopic and submicroscopic scales [2.8]. Like UV lithography, ions beam or electron beam etching, laser ablation enables the fabrication of micro- and nanostructured functional surfaces with a top-down approach. Ablation can be achieved by UV, visible or IR sources in pulsed or continuous modes. Ablation principle is that light, at the considered wavelength, is quickly absorbed by the very superficial layers of the target material. This absorption leads to the breaking of chemical bonds and thus to the evaporation of the surface material (cf. Figure 2-5). This etching technique is based on light-matter interaction [2.10].

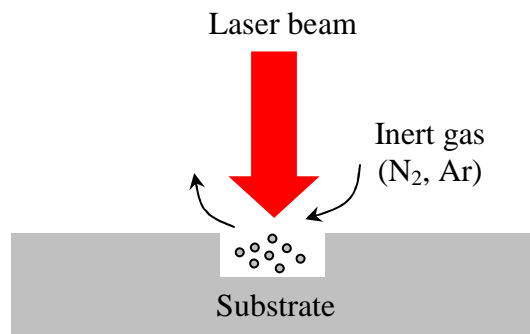


Figure 2-5. Schematic view of ablation process by laser beam.

### Micro-patterning by laser ablation

Shown in Figure 2-6 is the “Tamarack 412” equipment used in this study. This is a commercial laser ablation system based on mask projection. The working stage consists of a KrF excimer laser providing nanoseconds long pulses at 248 nm with 34-473 mJ/cm<sup>2</sup> fluence values. The laser source can further be pulsed between 1 Hz and 50 Hz. The sample-holder platform is x-y motorized and can receive 32x38 cm<sup>2</sup> flat but rigid or foldable substrates. In the present case, disk-shaped patterns of 40  $\mu$ m diameter and 60  $\mu$ m periods were ablated inside the samples surface in the conditions presented in Table 2-6.

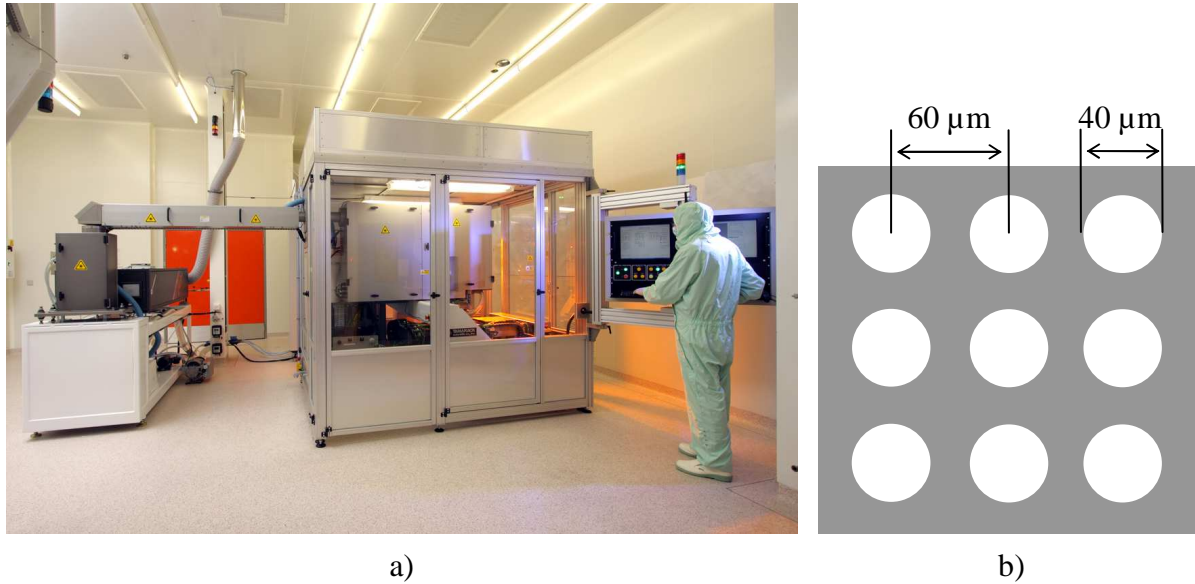


Figure 2-6. a) Laser ablation tool from Tamarack 412 ® and b) patterned mask used to ablate titanium and DLC coatings.

Table 2-6. Ablation process conditions.

Target material	Fluence (mJ/cm <sup>2</sup> )	Pulse frequency (Hz)	Number of pulses
Titanium	450	45	100
Diamond-like carbon	450	45	5

## 2.2 Surface characterization

This section describes the techniques of surface characterization used in the present study. Micro and nanoscale images of a sample surface are obtained by using a scanning electron microscope (SEM). Atomic force microscope (AFM) is used for accurate determination of the surface roughness. In order to quantify the surface wettability, the contact angle is measured by using the sessile drop technique with KRUSS EasyDrop systems. Furthermore, the 4-wire technique is used for the measurement of the electrical resistance, enabling the determination of the sample temperature.

### 2.2.1 Scanning electron microscope

The scanning electron microscope (SEM) is a microscope that uses a high-energy beam of electrons instead of light to form an image [2.7]. The electrons interact with the atoms of the sample surface, producing signals that contain information about the surface topography, composition and other properties such as electrical conductivity. Since their development in the early 1950's, scanning electron microscopes have developed new areas of study in the



medical and physical science communities. The SEM has allowed researchers to examine a much bigger variety of specimens since its magnifications can go to more than 300 000 X.

During SEM inspection, a beam of electrons is focused on a spot volume of the sample surface, resulting in the transfer of energy to the spot. Once the beam hits the sample, electrons and X-rays are ejected from the sample (cf. Figure 2-7). The incident electrons, also referred to as primary electrons, dislodge electrons from the sample itself. The dislodged electrons, named “secondary electron”, are attracted and collected by a detector, and then translated into a signal. To produce the SEM image, the electron beam is swept across the area being inspected, producing a lot of such signals. These signals are then amplified, analyzed, and translated into images of the topography being inspected. The principle components of a typical SEM are shown in Figure 2-8.

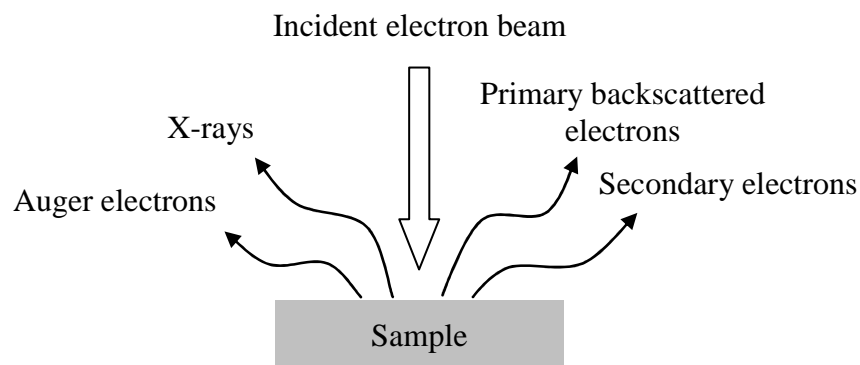


Figure 2-7. Interactions at the sample surface due to injection of electron beam.

Aside from secondary electrons, the primary electron beam also produces the emission of backscattered (or reflected) electrons from the sample surface. These electrons are often used in analytical SEM along with the spectra made from the characteristic X-rays. Indeed, the intensity of signal given by the backscattered electron is strongly related to the atomic number of the sample, and thus the backscattered-electron images can provide information about the distribution of different elements in the sample.

The SEM has many advantages over traditional microscopes. Indeed, it has a larger depth of field that allows focusing more specimens at one time. It also has much higher resolution, so closely spaced specimens can be magnified at much higher levels. Furthermore, the SEM enables more control in the degree of magnification since electromagnets rather than lenses are used. Thanks to these advantages, the scanning electron microscope becomes one of the most useful instruments in research today.

To improve the resolution and quality of images made by SEM, in the electron gun of the SEM, a field-emission cathode is used to provide an electron beam that is smaller in diameter and higher in electron energy than conventional thermionic emitters such as tungsten or lanthanum hexaboride ( $\text{LaB}_6$ )-tipped filaments. This microscope using a field-emission cathode is named “FEG-SEM”, which refers to as “Field-emission gun scanning electron microscope”. FEG-SEM produces clearer, less electro-statically distorted images with spatial resolution down to 1 nm, which is three to six times better than conventional SEM.

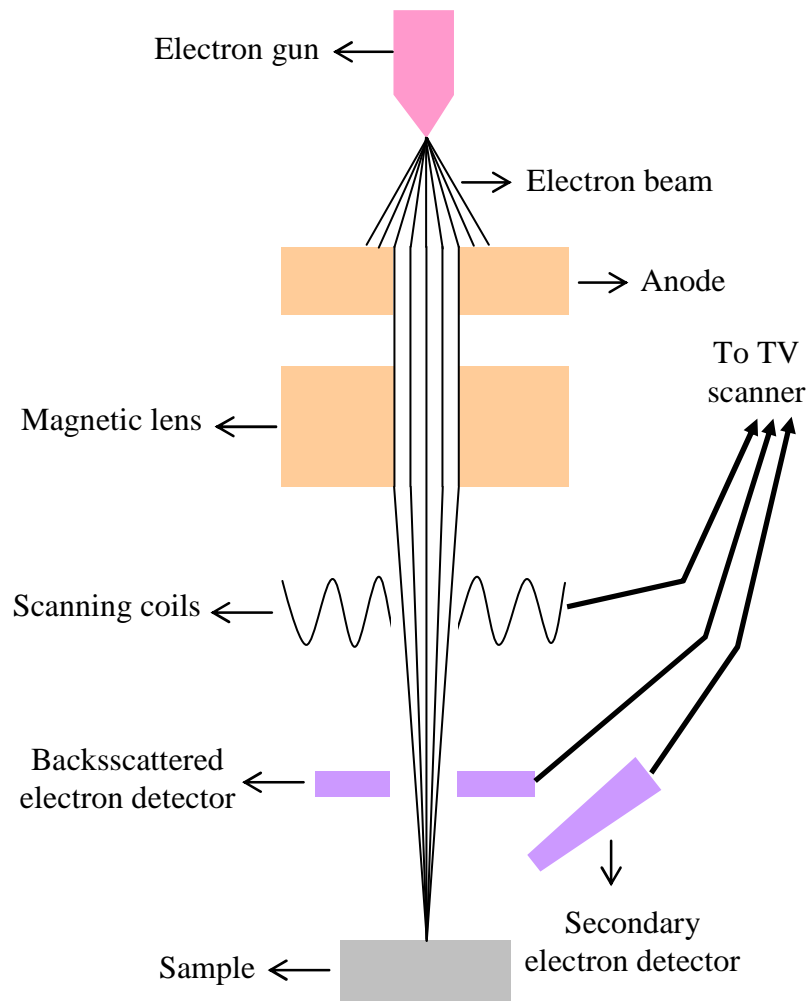


Figure 2-8. Schematic view of a typical SEM.

### 2.2.2 Atomic force microscopic

The atomic force microscope (AFM) is an instrument for analysing and characterizing samples surface, especially for imaging surface topography, at micro- and nanoscale. The first AFM was developed by Binnig, Quate and Gerber in 1986 [2.12], to overcome a limitation of the scanning tunneling microscope (STM) invented by Binnig and Rohrer in 1981 [2.13]. The STM only enables imaging materials that conducts a tunnelling current, while AFM opened the door to imaging other materials, such as polymers and biological samples.

As shown in Figure 2-9, the AFM consists of a sharp tip (probe) located at the free end of a cantilever 100 to 200  $\mu\text{m}$  long. This tip is usually a couple of microns long and less than 10 nm in diameter. When the tip is brought into proximity of a sample surface, different forces such as mechanical contact force, van der Waals forces, capillary forces, chemical bonding, electrostatic forces, etc. act to either attract or repel the tip. The deflection of the cantilever is measured using a laser spot reflected from the top surface of the cantilever into an array of photodiodes, giving the total contact force between the tip and the sample.

If the tip is scanned at a constant height, it may collide with the sample surface, causing damage. Therefore, in most cases, the tip-to-sample distance is adjusted to maintain a constant force between the tip and the sample using feedback mechanism. Typically, the sample is mounted on a piezoelectric tube that can move the sample in the  $z$  (vertical) direction for

maintaining a constant force, and the  $x$  and  $y$  (horizontal) directions for scanning the sample. The resulting map of  $z$  as a function of  $(x,y)$  represents the topography of the sample surface.

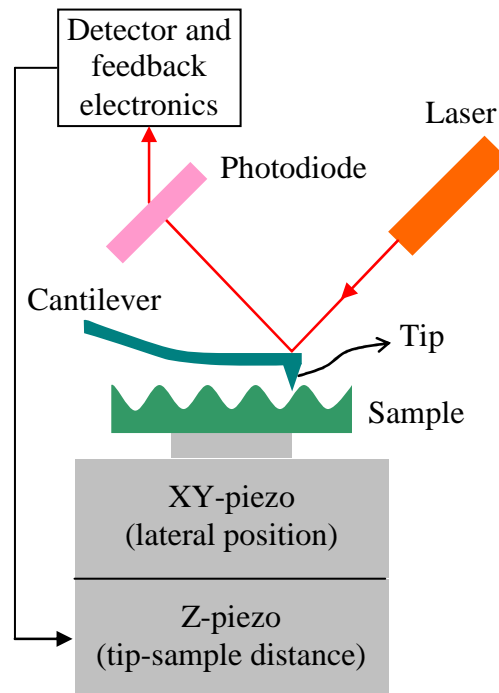


Figure 2-9. Block diagram of atomic force microscope.

The AFM can be operated in different modes [2.14], depending on the application, such as contact mode, non-contact mode and tapping mode. In the contact mode, the tip is constantly in contact with the surface. In the non-contact mode, the tip is oscillating above the surface. In the tapping mode, the tip is oscillating with given amplitude at a fixed frequency near the resonance of the cantilever, tapping gently the surface. The vibration amplitude is reduced as the tip enters in contact with the surface, and the tip sample distance is adjusted to keep it constant. The tapping mode will be used in this study to analyse the sample surface topography and roughness.

### 2.2.3 Contact angle measurement

The static contact angle is measured by the commercial system of KRÜSS EasyDrop DSA10 as shown in Figure 2-10. The used technique is called “sessile drop technique” that consists of the following steps [2.15]. First, a small (1-5  $\mu\text{l}$ ) sessile droplet is deposited by a syringe pointed vertically down onto the sample surface. Afterwards, image of the droplet is captured by a charge coupled device (CCD) camera (cf. Figure 2-11). Then, the captured image is analysed by KRÜSS software to determine the droplet contour and its baseline (the contact line between the droplet and the sample surface). Hence, the static contact angle is determined.

For a sample surface, the static contact angle is the mean value of the static contact angles measured at twenty distinct points uniformly distributed on the surface (five measurements are made at each point).

The higher image size, the higher number of pixels is available for evaluating the droplet contour. Therefore, the size of the droplet image should be adjusted to be as large as possible

on the screen. Example of a good droplet picture for contact angle determination is shown in Figure 2-12. The width of the droplet is equal to about 2/3 of the width of the whole image. The contour of the droplet is light, without any parasite by light reflection from the sample surface. Lighting was adjusted so that the area above the baseline has a uniform brightness and so that the droplet contour is not clipped. The reflected image of the droplet should be light to enable an easy determination of baseline by the image analysis software.

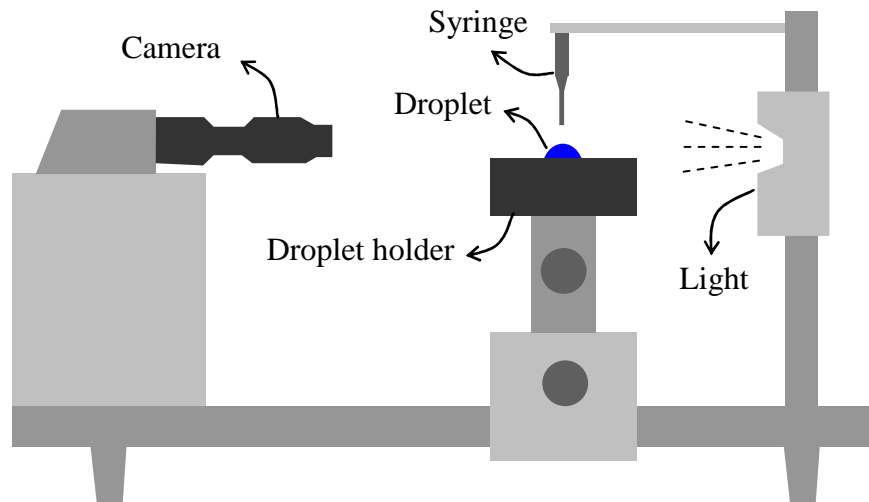


Figure 2-10. Block diagram of the KRÜSS EasyDrop DSA10 system.

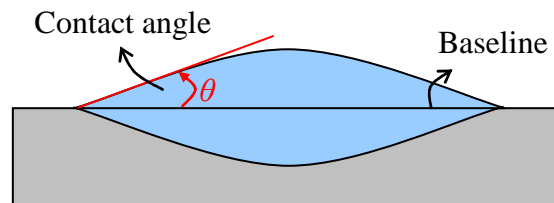


Figure 2-11. Diagram of a liquid droplet and its baseline.

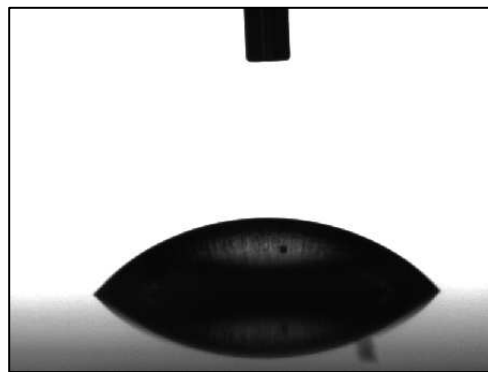


Figure 2-12. Example of a clear picture for determination of the contact angle [2.15].

### Contact angle hysteresis measurement

If the contact angle is measured when the volume of the droplet is increasing, practically this is done just before the contact line starts to advance; the so-called “advancing contact angle”  $\theta_a$  is obtained (cf. Figure 2-13). If the volume of the drop decreases and the contact angle is determined just before the contact line starts to recede, the so-called “receding contact angle”

$\theta_r$  is obtained. Usually  $\theta_a$  is significantly higher than  $\theta_r$  and the static contact angle  $\theta$  is included between  $\theta_r$  and  $\theta_a$ . The difference  $\theta_a - \theta_r$  is the so-called contact angle hysteresis.

The KRÜSS set-up enables the change of the droplet volume at a controlled flow rate through a system of pump and syringe. To measure the contact angle hysteresis, the droplet volume is set to increase from about 10 to 14  $\mu\text{l}$  and afterwards to decrease from 14 to 6  $\mu\text{l}$ . The evolution of the droplet volume with time is recorded by the CCD camera. Then, the images given by the recorded video are analysed by the KRÜSS software. The contact angle and the droplet diameter at each instant are thereby determined. A plot of these two parameters enables the determination of the dynamic angle ( $\theta_a$  and  $\theta_r$ ) and the contact angle hysteresis, as shown in Figure 2-14.

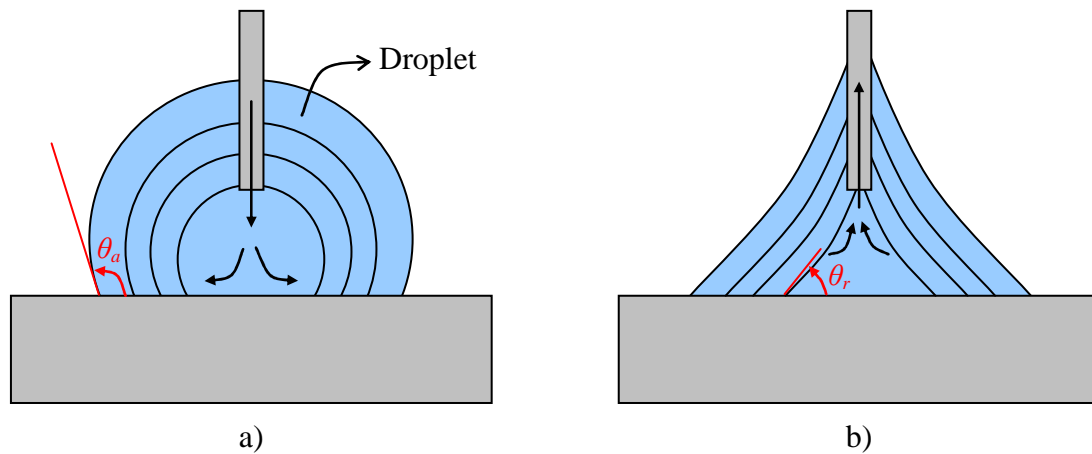


Figure 2-13. Determination of the contact angle hysteresis: a) increasing the droplet volume to obtain the advancing angle and b) decreasing the droplet volume to obtain the receding angle.

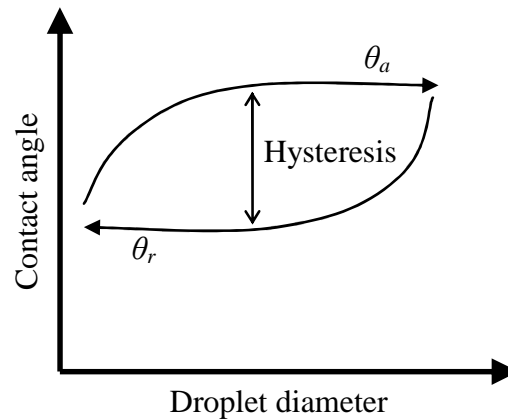


Figure 2-14. Theoretical curve of evolution of the contact angle with the droplet diameter.

Beside the sessile drop technique, some others techniques have been used to determined the contact angle such as: Wilhelmy plate method, captive air bubble method, capillary rise method and Washburn method (for porous materials) [2.16].

## 2.2.4 Surface temperature measurement

In this study, the surface temperature is determined from measurements of the electric resistance by using the electrical resistance/temperature (R/T) curve. The following

paragraphs describe the techniques for accurate measurement of the electrical resistance and R/T calibration.

### Resistance measurement by 4-wire technique

Assume that the electrical resistance  $R_{subject}$  of a component is desired to be measured (cf. Figure 2-15). If the used ohmmeter is located at a significant distance away from this component, the measurement could be problematic since the ohmmeter measures all resistances in the circuit loop, including the resistance of the wires  $R_{wire}$  connecting the ohmmeter to the component. Frequently, the wire resistance is very small, but if the connecting wires are very long, and/or the component to be measured has a very low resistance, the measurement error introduced by wire resistance will be substantial.

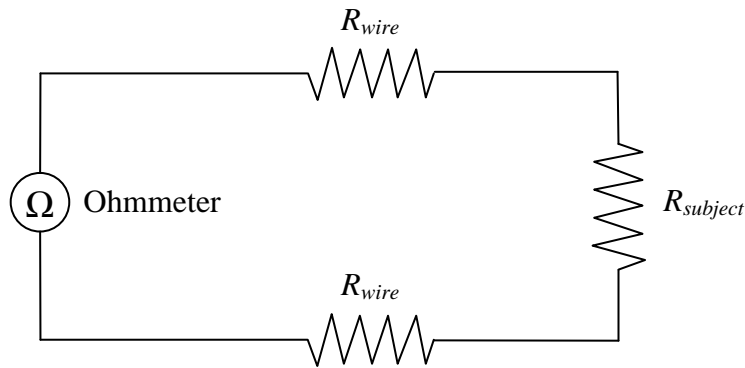


Figure 2-15. Diagram of circuit for resistance measurement by 2-wire technique.

To avoid error given by wire resistance, the so-called 4-wire technique is used. The desired resistance is determined from measurements of the current (by an ammeter) and the voltage of the component (by a voltmeter) according to the Ohm's law. Current is the same at all points in the circuit as it is a series loop and the current loss by the voltmeter is negligible. The calculated resistance is indicative of the desired resistance since only voltage dropped across the component is measured. Therefore, the desired resistance can be accurately measured by using the 4-wire technique; even though the ammeter and voltmeter are located far from the component.

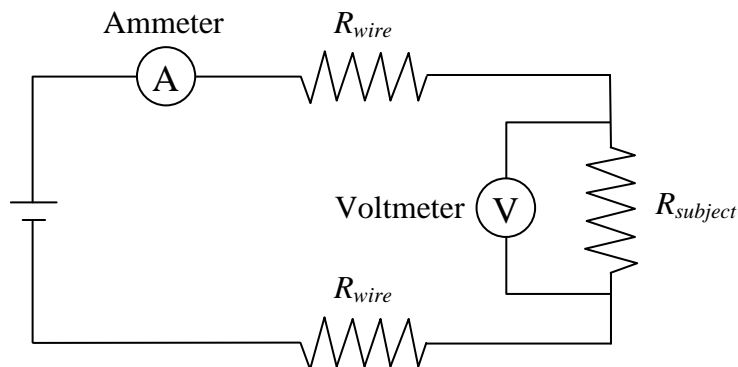


Figure 2-16. Diagram of circuit for resistance measurement by 4-wire technique.

In this study, instead of the ammeter, a shunt of  $0.01\ \Omega$  is used to measure the current (cf. Figure 2-17). The shunt is connected in series with the component and the voltage dropped across the shunt is measured by a voltmeter. From the resistance and voltage of the shunt, the current in the circuit is determined.

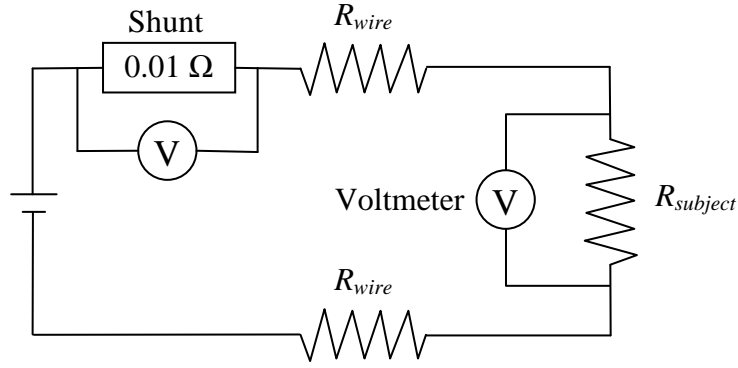


Figure 2-17. Shunt of 0.01 Ω is used to determine the current.

The temperature of the shunt is maintained constant at room temperature by air convection or by using a thermostat, and thereby the resistance of the shunt should not change by Joule effect even when high currents cross the circuit. Thus, the use of the shunt enables to measure accurately the current in a large threshold from 0 to 20 A.

### Resistance/temperature calibration

The resistivity of a metallic conductor increases with increasing temperature. Over a moderate temperature range, the resistivity of a metal can be represented by a linear relation as:

$$\rho_e(T) = \rho_{e,0} [1 + \alpha_e (T - T_0)] \quad (2-1)$$

wherein  $\rho_e(T)$  and  $\rho_{e,0}$  are the resistivity at the temperature  $T$  and the temperature of reference  $T_0$ , respectively and  $\alpha_e$  is the temperature coefficient of resistivity. The evolution of the electrical resistance as a function of the temperature is thereby given as:

$$R_e(T) = \frac{L}{A_e} \rho_{e,0} [1 + \alpha_e (T - T_0)] \quad (2-2)$$

wherein  $R_e(T)$  is the electrical resistance,  $L$  is the length of the conductor and  $A_e$  is the section of the conductor crossed by the current at the temperature  $T$ . The variations of  $L$  and  $A_e$  with the temperature are assumed to be negligible, giving the following expression of the variation of  $R_e$ :

$$\frac{dR_e(T)}{dT} = \frac{L}{A_e} \rho_{e,0} \alpha_e \quad (2-3)$$

Eq. (2-3) shows that the sensibility of the electrical resistance versus the temperature will increase with increasing  $L/A_e$  and/or  $\rho_{e,0}$  and/or  $\alpha_e$ . From equation (2-2), the temperature can be written as a function of the electrical resistance as:

$$T = K_1 R_e(T) + K_0 \quad (2-4)$$

wherein  $K_1$  and  $K_0$  are the constants depending on the geometry of the conductor and the temperature coefficient of resistivity as:

$$K_1 = \frac{1}{\rho_{e,0} \alpha_e} \frac{A_e}{L} \quad (2-5)$$

$$K_0 = T_0 - \frac{1}{\alpha_e} \quad (2-6)$$

The so-called resistance/temperature (R/T) calibration is the determination of  $K_1$  and  $K_0$  experimentally according to the following steps. The conductor is put inside a thermostat containing deionised water (cf. Figure 2-18). At steady state, the temperature of the conductor is equal to the temperature of water which is measured by a platinum probe of 0.1 °C accuracy. For temperature between 20 °C and 90 °C by step of 10 °C, the electrical resistance of the conductor is measured by using the 4-wire technique. The temperature is then plotted as a function of the electrical resistance. A linear regression of this curve will enable the determination of  $K_1$  and  $K_0$  (cf. Figure 2-19). Once these constants are known, the temperature of the conductor can be determined by measurements of the electrical resistance.

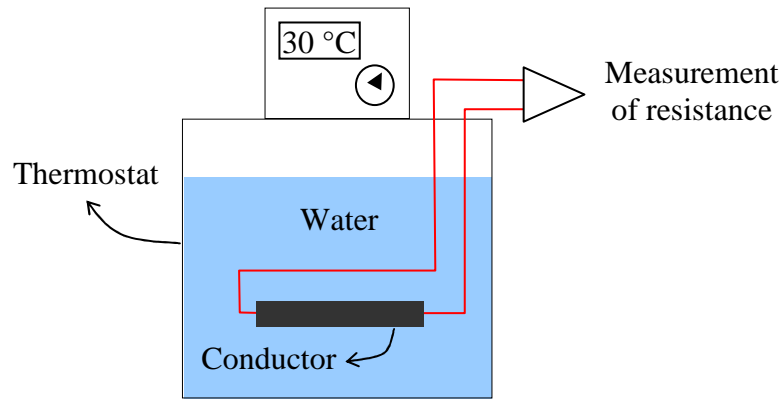


Figure 2-18. Schematic view of experimental setup for R/T calibration.

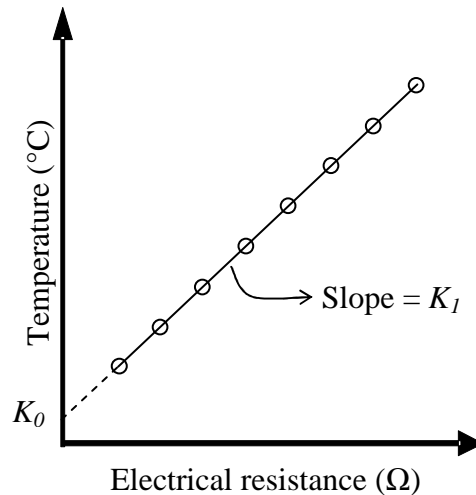


Figure 2-19. Example of T/R curve used for temperature determination from measurement of resistance.

The present technique enables an accurate determination of temperature with relatively low uncertainties ( $< 0.2$  °C). Therefore, it was used to determine the sample temperatures for both pool and flow boiling experiments as described in the following chapters.



## 2.3 References

- [2.1] D.M. Mattox, Handbook of physical vapor deposition (PVD) processing: film formation, adhesion, surface preparation and contamination control, 2nd ed., Noyes Publication (2010).
- [2.2] A. Billard, F. Perry, Pulvérisation cathodique magnétron, Techniques de l'Ingénieur M1654 (2005), 1-17.
- [2.3] D. M. Dobkin, M. K. Zuraw, Principles of Chemical Vapor Deposition: What's Going on Inside the Reactor, Kluwer Academic (2003).
- [2.4] C. Chouquet, Élaboration et caractérisation de revêtements type « Diamond-Like Carbon » déposés par un procédé chimique en phase vapeur assisté par un plasma basse fréquence, PhD thesis, Institut National Polytechnique de Lorraine (2008), Lorraine, France.
- [2.5] N. Blondiaux, E. Scolan, A.M. Popa, J. Gavillet, R. Pugin, Fabrication of superhydrophobic surfaces with controlled topography and chemistry, Applied Surface Science 256 (2009), S46-S53.
- [2.6] J. Nestler, A. Morschhauser, K. Hiller, T. Otto, S. Bigot, J. Auerswald, H. F. Knapp, J. Gavillet, T. Gessner, Polymer lab-on-chip systems with integrated electrochemical pumps suitable for large-scale fabrication, Int. J. Adv. Manuf. Technol. 47 (2010), 137-145.
- [2.7] S. Zanini, C. Riccardia, M. Orlandib, E. Grimoldia, Characterisation of SiO<sub>x</sub>CyHz thin films deposited by low-temperature PECVD, Vacuum 82 (2008), 290-293.
- [2.8] E. Billy, F. Maillard, A. Morin, L. Guetaz, F. Emieux, C. Thurier, P. Doppelt, S. Donet, S. Mailley, Impact of ultra-low Pt loadings on the performance of anode/cathode in a proton-exchange membrane fuel cell, Journal of Power Sources 195 (2010), 2737-2746.
- [2.9] J. Békési, J.-H. Klein-Wiele, P. Simon, Efficient submicron processing of metals with femtosecond UV pulses, Applied Physics A: Materials Science & Processing 76 (2003), 355-357.
- [2.10] H. Chen, X. Chen, Y. Zhang, Y. Xia, Ablation induced by single-and multiple-femtosecond laser pulses in lithium niobate, Laser Physics 17 (2007), 1378-1381.
- [2.11] H. Paqueton, J. Ruste, Microscopie électronique à balayage - Principe et équipement, Techniques de l'Ingénieur P865 (2006), 1-16.
- [2.12] G. Binnig, C.F. Quate, C. Gerber, Atomic force microscope, Physics Review Letters 56 (1986), 930-933.
- [2.13] G. Binnig, H. Rohrer, Scanning Tunneling Microscopy—from Birth to Adolescence (Nobel Lecture), Reviews of Modern Physics 59 (1987), 615.
- [2.14] F. Salvan, F. Thibaudau, Microscopie à sonde locale, Techniques de l'Ingénieur P895 (1999), 1-18.
- [2.15] DSA1/DSA10, KRÜSS short manual (2002), 4-40.
- [2.16] Y. Gu, Contact angle measurement techniques for determination of wettability, Encyclopedia of Surface and Colloid Science 2 (2006), 1525-1539.

## PART 2 - POOL BOILING EXPERIMENTS

The previous part describes an overview of the phenomenon occurring during heterogeneous boiling, as well as some basis fundamentals for a better understanding of the present study. This part also provides a review of surface treatment and characterization techniques. Currently, a number of surface treatment techniques enable close control of manufacture on the nano- and micro-scales. Although these techniques have been developed highly over the last twenty years, their applications in the field of boiling are still limited.

High interest in the use of micro- and nano-surface treatments in boiling heat transfer was inspired by the emergence of nanofluids, which are fluids containing particles of sizes less than 100 nm. Recent investigations show that during boiling of nanofluids, nanoparticles deposit along the heated surface, leading to modification of the surface properties and the boiling processes.

Therefore, pool-boiling experiments were performed in order to highlight the impact of nanoparticle deposition on nucleate boiling processes, especially on bubble growth mechanisms. This work is necessary for development of processes for sample fabrication and for the design of an experimental setup to study flow boiling in microchannels.

Two distinct experiments will be introduced in chapters 3 and 4, respectively. The first experiment aims at giving a better understanding of observations in literature concerning nanofluid boiling. Sample surfaces were coated by performing nucleate boiling of nanofluids. This is the first step to explore the effects of nanoparticle deposition on heterogeneous boiling. The second experiment was conducted to identify the impacts of nanocoating on boiling mechanism. In this experiment, coating of sample surfaces was made by various other techniques such as MOCVD and PECVD (cf. Section 2.1.2). The obtained experimental results enable the development of models that take into account the effects of surface wettability on pool boiling heat transfer.



## Chapter 3: Effects of surface coating by nanofluid boiling

This chapter is devoted to describing the first experiment which was conducted to obtain a better understanding of recent observations about nanofluid boiling. In the first step, pool boiling of nanofluids was performed to study the process of nanoparticle deposition on sample heated surfaces. Afterwards, experiments were carried out to measure the heat transfer coefficient of water boiling on an uncoated surface or on a surface coated by nanoparticle deposition. The obtained results give preliminary insights about the effect of nano-surface coating on the boiling heat transfer processes.

### 3.1 Sample-surface coating by nanofluid boiling

#### 3.1.1 Nanofluid preparation

Three nanoparticle materials were tested, i.e., gold (Au), alumina ( $\text{Al}_2\text{O}_3$ ) and titanium dioxide ( $\text{TiO}_2$ ) (cf. Figure 3-1). Water-based nanofluids of these three materials were supplied by the LITEN/L2T laboratory with low concentrations, i.e., 0.0003, 0.01 and 0.01% by volume. The nanoparticle sizes were measured with the dynamic light scattering technique and were found to range from 15 to 20 nm for Au nanofluid, 80 to 100 nm for  $\text{Al}_2\text{O}_3$  nanofluid and 20 to 30 nm for  $\text{TiO}_2$  nanofluid.

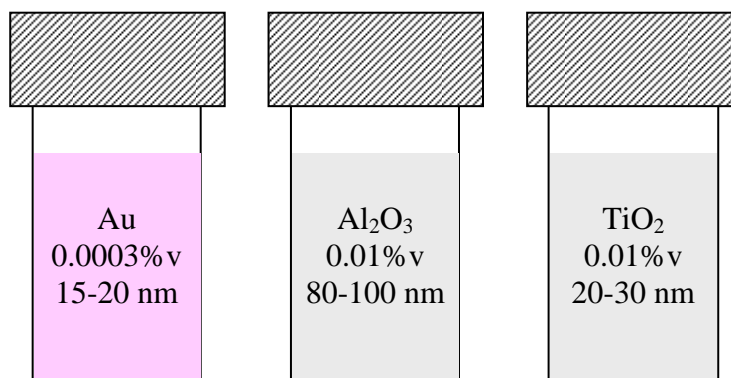


Figure 3-1. Nanofluids used for sample-surface coating.

#### Gold nanofluid

The Au nanofluid was prepared by reduction of aqueous hydrogen tetrachloroaurate hydrate ( $\text{HAuCl}_4 \cdot 3\text{H}_2\text{O}$ ) with sodium citrate ( $\text{C}_6\text{H}_5\text{O}_7\text{Na}_3$ ). This is a well-known process called “Turkevitch method” [3.1] which allows the nanofluid to obtain colloidal stability.

#### Alumina nanofluid

The  $\text{Al}_2\text{O}_3$  nanofluid was made by adding a powder of  $\alpha$   $\text{Al}_2\text{O}_3$  (Ventron; 80-100nm) to deionised water. The milky suspension was then vigorously stirred during 12 hours in order to obtain a stable colloidal solution.

#### Titanium dioxide nanofluid

The  $\text{TiO}_2$  nanofluid was prepared by hydrolysis of titanium alkoxides in absolute ethanol according to the following recipe.  $\text{Ti}(\text{OEt})_4$  (Aldrich) was added at room temperature to absolute ethanol under argon. Afterwards, an equimolar quantity of dry triethanolamine (Aldrich) versus titanium alkoxide was added to the latter solution. Then, the yellow solution

was stirred at room temperature during two hours. Finally, an equimolar quantity of deionised water versus titanium alkoxide was added. The solution was again stirred during 2 hours at room temperature. A large amount of water was added and the solution was dialysed against deionised water using a regenerated cellulose tubular membrane (Roth, MWCO: 4000-6000) during three days.

The obtained titanium dioxide was under rutile phase (XRD). The size of particles measured by dynamic light scattering (Malvern Nanosizer) was in the range of 4 to 10 nm. However this size increases with time and, after one month, the mean diameter was 20-30nm and then remained relatively constant.

### 3.1.2 Coating apparatus and procedure

The surface coating is achieved with the apparatus shown in Figure 3-2. The sample is a foil heater made of stainless steel (grade 301), 100 mm long, 5 mm wide and 20  $\mu\text{m}$  thick. The foil heater is submerged in the corresponding working nanofluid at atmospheric pressure. The faces 100 mm x 5 mm are maintained vertically by a screw system and heated by Joule effect with a DC power supply of 30-V and 20-A capacity. This position of the sample enables a homogeneous deposition of nanoparticles on the both sides.

Voltage and current are measured with Agilent 3458A multimeter and a shunt of 0.01  $\Omega$ . The sample temperature is estimated from measurement of the electric resistance and using the R/T calibration of stainless steel previously established (cf. Section 2.2.4). A K-type thermocouple of 1.1  $^{\circ}\text{C}$  accuracy is used to measure the fluid bulk temperature.

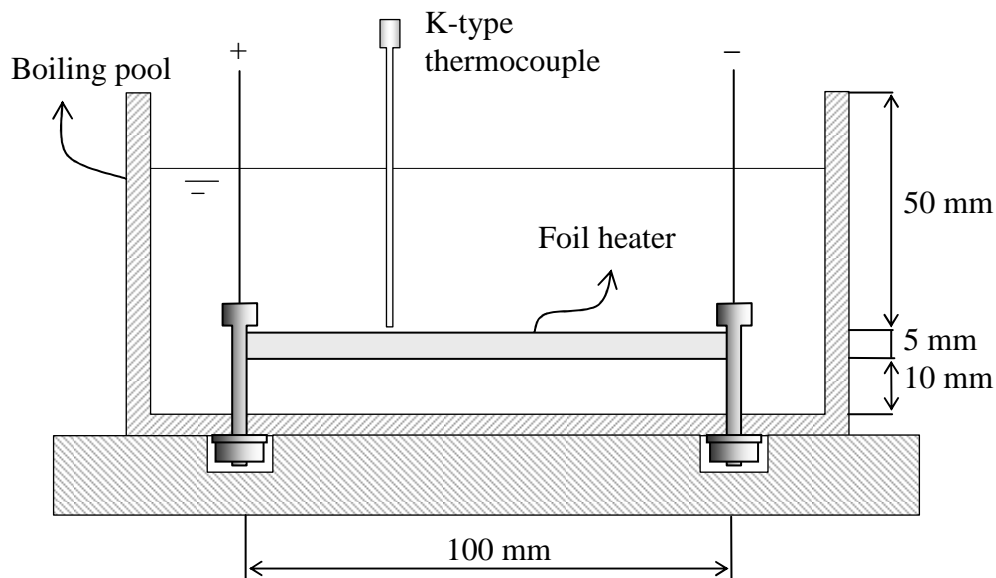


Figure 3-2. Diagram of nanofluid nucleate boiling apparatus.

Each nanofluid has a specific sample for latter topography study. A preliminary test with pure water showed that a 40  $\text{kW/m}^2$  heat flux is enough to reach nucleate boiling conditions. Thus, all nanofluids were heated at heat fluxes slightly greater than 40  $\text{kW/m}^2$ . Different boiling durations and different nanoparticle concentrations were established (cf. Table 3-1) in order to study their effects on the nanoparticle-deposition thickness.

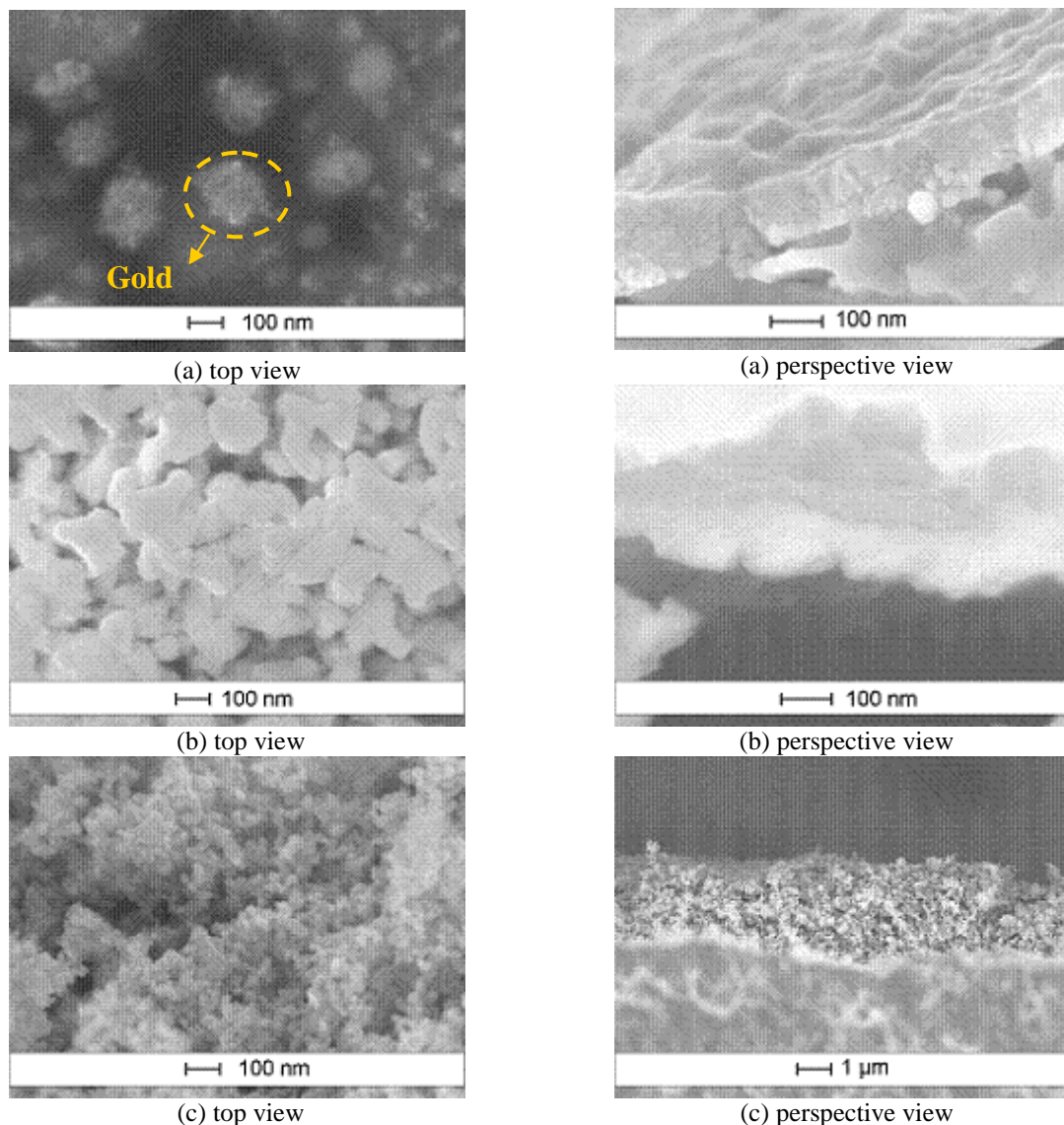
Table 3-1. Nanofluid boiling characteristics.

Particle material	Particle size (nm)	Concentration (% v)	Heat flux (kW/m <sup>2</sup> )	Boiling duration (s)
Au	15-20	0.0003	52	600
Al <sub>2</sub> O <sub>3</sub>	80-100	0.01	45	60
TiO <sub>2</sub>	20-30	0.01	54	250, 500

### 3.1.3 Coating results.

#### FEG-SEM images

After boiling, the sample surfaces were scanned by field-emission gun scanning electron microscope (FEG-SEM) (cf. Section 2.2.1). The obtained images are shown in Figure 3-3. Build-up of nanoparticle layer on the sample surfaces are observed, which is in agreement with observations in the literature (cf. Section 1.4.2).


 Figure 3-3. FEG-SEM images of nanoparticle deposition layer of a) Au; b) Al<sub>2</sub>O<sub>3</sub>; c) TiO<sub>2</sub>.

Compared to the other nanofluids, the TiO<sub>2</sub> nanofluid produces the best porous layer thickness uniformity, reasonably due to a long boiling duration (500s) and a high nanoparticle

concentration (0.01 %v). Because of a relatively low concentration (0.0003%v), the Au nanofluid give low deposition kinetics. In addition, XPS (X-ray Photoelectron Spectroscopy) analysis showed that sodium citrate, a dispersive material, originally used to maintain the Au particle size stable, is being deposited at the same time onto the corresponding sample surface.

### Nanoparticle deposition thickness

As described in Section 1.4.2, Kim *et al.* [3.2] assumed that the deposition of nanoparticles is primary due to evaporation of liquid microlayer underneath a bubble. Thus, they suggested the following equation to estimate the rate of growth of the nanoparticle layer:

$$\dot{\delta} = \frac{3}{2} \frac{\delta_m \varphi q}{D_d \rho_v H_{lv}} \quad (3-1)$$

wherein  $\delta_m$  is the microlayer thickness,  $\varphi$  is the nanoparticle volumetric concentration,  $q$  is the heat flux,  $D_d$  is the bubble departure diameter,  $\rho_v$  is the vapour density and  $H_{lv}$  is the vaporisation latent heat.

In the present experiments, similar conditions as Kim *et al.* [3.2] have been selected. Along the same lines, the same bubble departure diameter ( $D_b = 2.4$  mm) and the same liquid microlayer thickness ( $\delta_m = 1$   $\mu$ m) are chosen to estimate the nanoporous thickness. Actually,  $D_b$  is approximated by the correlation of Cole and Rosenhow [3.3] and  $\delta_m$  is correlated by the equation of Collier and Thome [3.4]. Unlike the experiments of Kim *et al.* [3.2] where the nanoparticle concentrations remain constant, the concentrations in this study increased gradually with time by evaporation. Assuming that the mass of nanoparticles lost by deposition and evaporation is negligible compared to that remaining in water, the concentration is given as:

$$\varphi(t) = \varphi_o \frac{V_{l,o}}{V_l(t)} \quad (3-2)$$

wherein  $t$  is the boiling duration,  $\varphi_o$  and  $\varphi(t)$  and  $V_{l,o}$  and  $V_l(t)$  are the concentrations and the liquid volumes at the initial instant and at the instant  $t$ , respectively. This implies:

$$\varphi(t) = \varphi_o (1 - k t)^{-1} \quad (3-3)$$

wherein  $k$  is a constant defined as:

$$k = \frac{q_{eva}}{V_{l,o} \rho_l H_{lv}} \quad (3-4)$$

wherein  $\rho_l$  is the liquid density and  $q_{eva}$  is the heat flux due to evaporation. The latter can be approximated as:

$$q_{eva} = \frac{V_{l,o} \rho_l H_{lv}}{t_\infty} \quad (3-5)$$

wherein  $t_\infty$  is the time required to evaporate all liquid in the pool. This parameter can be experimentally measured. Hence, the constant  $k$  can be determined as:

$$k = \frac{1}{t_\infty} \quad (3-6)$$

By replacing Eq. (3-3) into Eq. (3-1), the following expression of the deposition rate is obtained:

$$\dot{\delta}(t) = \dot{\delta}_o (1 - kt)^{-1} \quad (3-7)$$

wherein  $\dot{\delta}(t)$  is the deposition rate at the instant  $t$  and  $\dot{\delta}_o$  is the initial deposition rate given by:

$$\dot{\delta}_o = \frac{3}{2} \frac{\delta_m \phi_o q}{D_d \rho_v H_{lv}} \quad (3-8)$$

Therefore, the thickness of the deposition layer  $\delta$  can be estimated as:

$$\delta = -\dot{\delta}_o \ln(1 - kt) / k \quad (3-9)$$

The thicknesses of the deposition layers can also be determined by geometric measurement from FEG-SEM images. A comparison of the measured thicknesses to those calculated by Eq. (3-9) is shown in Figure 3-4.

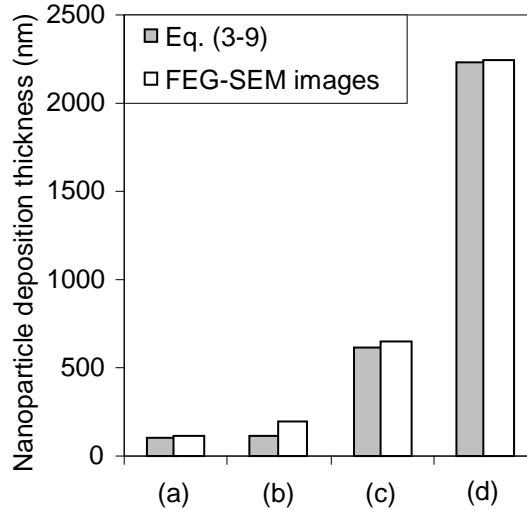


Figure 3-4. Deposition layer thickness in the conditions of: a) 0.0003%v of Au during 600 s, b) 0.01%v of  $\text{Al}_2\text{O}_3$  during 60 s, c) 0.01%v of  $\text{TiO}_2$  during 250 s and d) 0.01%v of  $\text{TiO}_2$  during 500 s.

It is shown that the deposition layers get indeed thicker with a longer boiling stage or with a higher initial nanoparticle concentration. The values of deposition thickness given by Eq. (3-9) are close to those given by geometric measurement for long boiling durations (more than 5 minutes) with a deviation of less than 5%, but are nearly twice smaller for a boiling duration less than 1 minute. This difference is attributed to uncertainties in the determination



of the beginning of nucleation by visualization. However, the validation of the model of Kim *et al.* [3.2] cannot be fully confirmed by the present experiment. To make a clear analysis, a parametric study should be done by varying only one parameter among the nanoparticle concentration, the boiling duration, the heat flux and the nanoparticle material. Moreover, the characteristic of the heater material should be also taken into account.

## 3.2 Pool boiling experimental setup

### Sample preparation

Among all test nanofluids, only  $\text{TiO}_2$  nanofluid gives a homogeneous deposition layer (cf. Figure 3-3). The surfaces tested in this experiment are thereby the surface coated by boiling of  $\text{TiO}_2$  nanofluid and the uncoated surface. They are made of stainless steel 301, 100 mm long, 5 mm wide and 20  $\mu\text{m}$  thick. The electrical resistance of each sample was previously calibrated, enabling the determination of the sample temperature (cf. Section 2.2.4).

### Experimental setup

The experimental apparatus is shown in Figure 3-5. The layout is designed to study the pool boiling heat transfer in a horizontal position. This position will enable to obtain high-speed images of bubbles from the perspective view in the second experiment described in the next chapter.

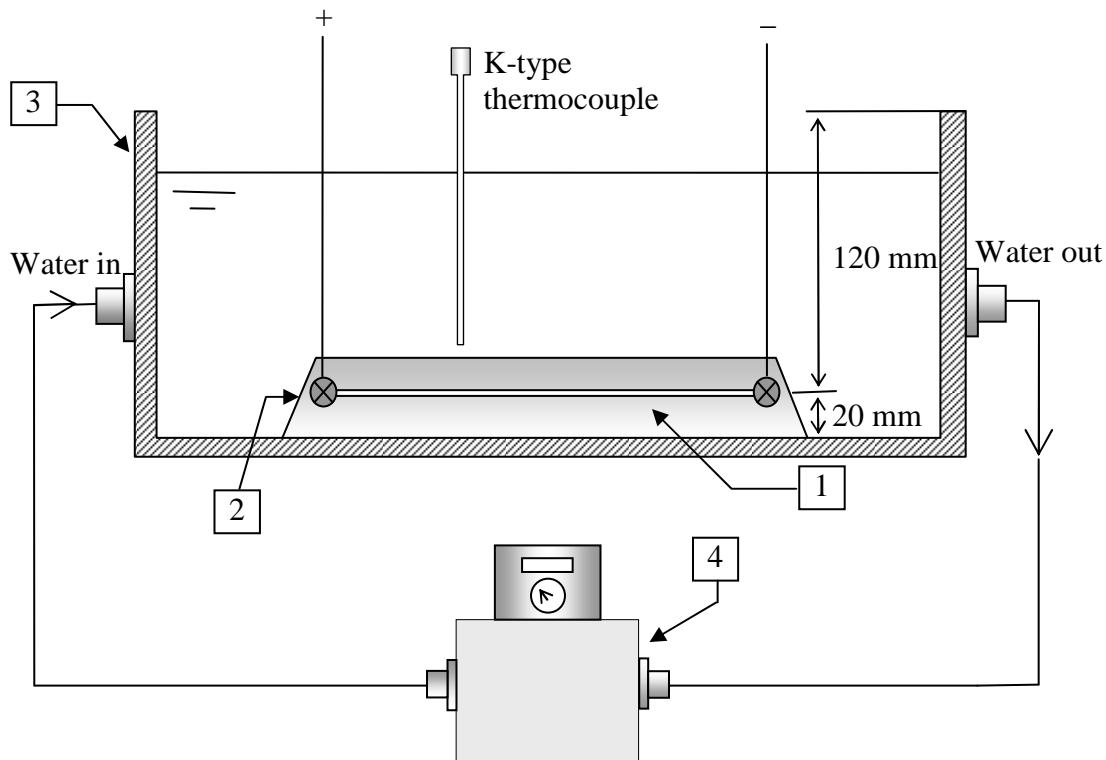


Figure 3-5. Experimental setup: (1) sample heater; (2) sample holder; (3) boiling vessel and (4) thermostat.

The layout consists of a sample heater (1) maintained horizontally by a sample holder (2) fixed inside a boiling vessel (3). A DC power supply of 30-V and 20-A capacity is connected to the sample for resistance heating. A thermostat (4) is provided for initial heating of water and for maintenance of the water bulk temperature at 85 °C. Water comes in and out of the boiling vessel at very low flow rate to avoid disturbing the boiling occurrence near the sample surfaces.

Voltage and current are measured by Agilent 3458A multimeter and a shunt of  $0.01 \, \Omega$  (cf. Section 2.2.4). The bulk temperature is measured by a K-type thermocouple of  $1.1 \, ^\circ\text{C}$  accuracy. The saturation temperature is determined from the measurement of the atmospheric pressure.

### 3.3 Experimental results

#### Data reduction

The boiling heat transfer coefficient is defined as:

$$h = \frac{q}{T_w - T_s} \quad (3-10)$$

wherein  $T_w$  is the wall temperature,  $T_s$  is the water saturation temperature and  $q$  is the heat flux calculated as:

$$q = \frac{VI}{A_h} \quad (3-11)$$

wherein  $V$  is the voltage dropped across the sample heater,  $I$  is the current and  $A_h$  is the total heat exchange area.

From the uncertainties in the measurements of the test foil length, the test foil width, voltage, current and pressure, the uncertainties in the derived parameters ( $q$ ,  $T_s$ ,  $T_w$  and  $h$ ) are estimated using the law of propagation of absolute error (cf. Appendix), as shown in Table 3-2.

Table 3-2. Operating conditions and uncertainties.

Parameter	Operational range	Systematic uncertainty
$A_h$ (cm <sup>2</sup> )	10	3%
$V$ (V)	5-20	0.008-0.011%
$I$ (A)	5-20	0.010-0.015%
$P$ (bar)	1	$\pm 0.01$ bar
$T_s$ (°C)	100	$\pm 0.2 \, ^\circ\text{C}$
$T_w$ (°C)	100 – 150	$\pm 1 \, ^\circ\text{C}$
$q$ (kW/m <sup>2</sup> )	50-400	3%
$h$ (W/m <sup>2</sup> K)	3000-16000	10-20%

Voltage and current are accurately measured. Indeed, the maximum uncertainties in the voltage and the current are 0.011% and 0.015% respectively. The saturate temperature is determined from measurement of atmospheric pressure. The maximum uncertainty is about  $0.2 \, ^\circ\text{C}$ . The wall temperature is determined from electrical resistance/temperature calibration. The uncertainty in the wall temperature is calculated to be less than  $1 \, ^\circ\text{C}$ . Uncertainty in the heat transfer coefficient is mainly attributed to uncertainties in the wall temperature and the heat exchange area.

### Heat transfer measurements

The heat transfer coefficients of the uncoated heater and the heater coated by deposition of  $\text{TiO}_2$  nanoparticles were measured. After the boiling tests, the  $\text{TiO}_2$ -coated heater underwent a cleaning in acetone ultrasonic bath for 30 minutes in order to reduce the deposition layer thickness. Afterwards, the heat transfer coefficient of this heater was measured for the second time.

The boiling curve of the uncoated surface is shown in Figure 3-6a. Low heat transfer hysteresis is observed when the heat flux increases and decreases. Figure 3-6b compares the heat transfer performance of the three distinct surfaces: uncoated surface, surface with  $\text{TiO}_2$  deposition and the same surface with  $\text{TiO}_2$  deposition cleaned in ultrasonic bath. The obtained results show that nanoparticle deposition leads to deterioration of the heat transfer coefficient. Compared to the clean surface, the  $\text{TiO}_2$ -coated surface shows an average heat transfer coefficient of 27% lower. Cleaning this surface in ultrasonic bath to remove unstable deposit particles leads to 50% deterioration of the heat transfer coefficient.

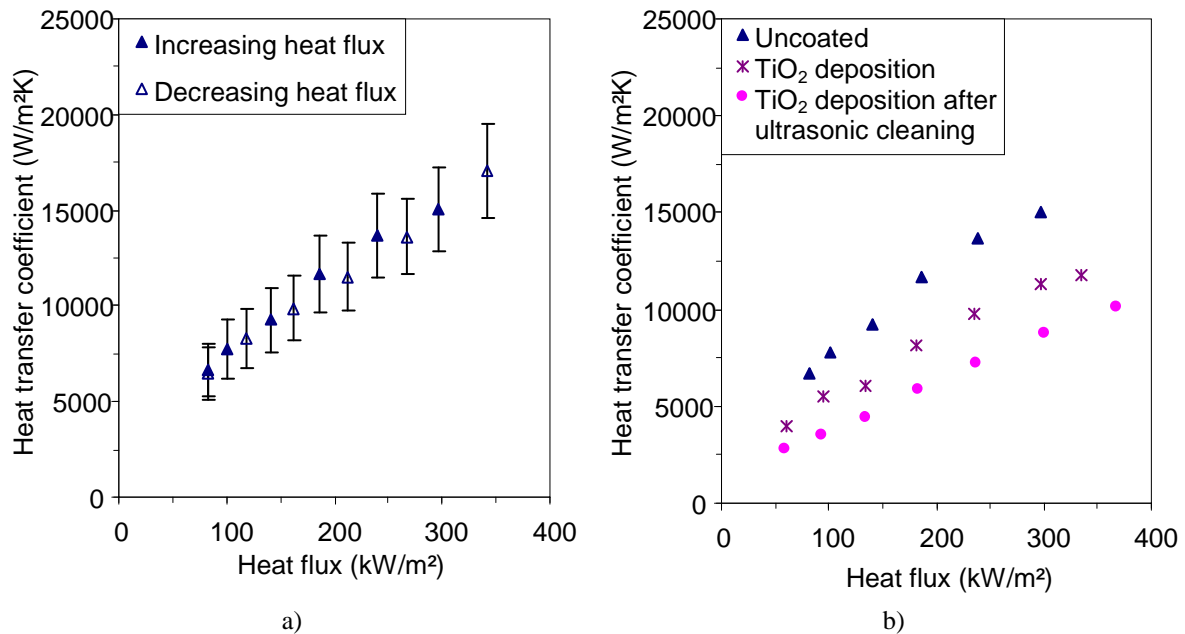


Figure 3-6. Boiling curves of: a) uncoated surface with uncertainty bars and b) uncoated and coated surfaces.

## 3.4 Discussion

In the previous sections, it was shown that during nucleate boiling of nanofluids, the heated surface is coated by nanoparticle deposition. When the coated surface is used in water pool boiling, deterioration of the heat transfer coefficient was observed. This section is devoted to discussing the heat transfer coefficient deterioration.

### Effect of thermal conduction through the deposition layer

The deterioration of the boiling heat transfer coefficient may be the consequence of the poor thermal conductivity of titanium dioxide ( $\text{TiO}_2$ ). If this hypothesis is correct, a gradual decrease of the heat transfer coefficient would be observed during the boiling of  $\text{TiO}_2$  nanofluid, since the deposition layer is increasingly thicker. However, Figure 3-7 shows no

significant change in the boiling heat transfer coefficient of  $\text{TiO}_2$  nanofluid in the course of time. For analytical explanations, the Biot number of the deposition layer was determined as:

$$\text{Bi} = \frac{h\delta}{\lambda} \quad (3-12)$$

wherein  $h$  is the boiling heat transfer coefficient ( $\approx 10^4 \text{ W/m}^2\text{K}$ ),  $\delta$  is the deposition layer thickness ( $\approx 2 \mu\text{m}$ ) and  $\lambda$  is the  $\text{TiO}_2$  thermal conductivity ( $\approx 1 \text{ W/mK}$ ). The obtained value of the Biot number is indeed negligible compared to unity ( $\text{Bi} \approx 10^{-2}$ ). Therefore, the conduction through the  $\text{TiO}_2$  layer has a neglected influence on the boiling heat transfer.

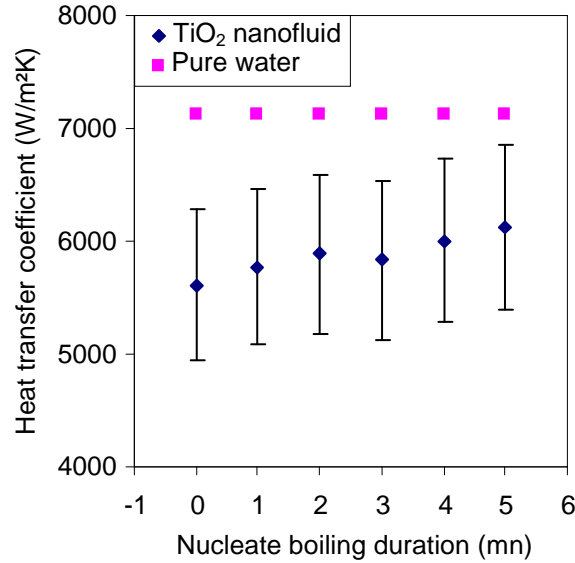


Figure 3-7. Evolution of the heat transfer coefficient with time at  $100 \text{ kW/m}^2$ .

The heat transfer deterioration may be then related to a change in interactions at the solid-fluid interface, which is characterized by the surface wettability.

#### Effect of nanoparticle deposition on surface wettability

The water contact angles of the sample surfaces were measured by the sessile-drop technique (cf. Section 2.2.3). As shown in Figure 3-8, the nanoparticle deposition layer significantly enhances the surface wettability, which is in agreement with observations in literature (cf. Section 1.4.2).

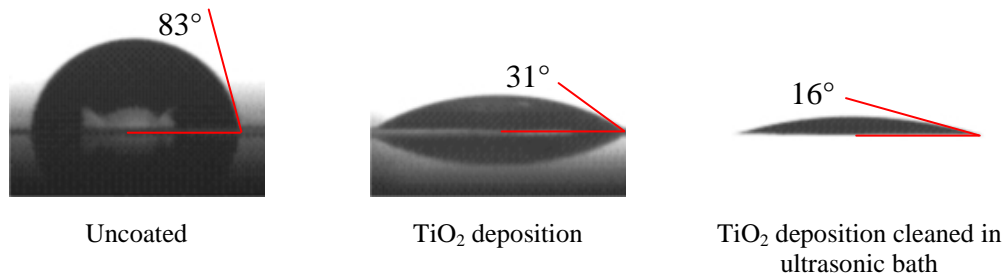


Figure 3-8. Static contact angles of  $3\text{-}\mu\text{L}$  sessile water-droplets on the sample surfaces.

The Wenzel model [3.5] can be used to explain this phenomenon (cf. Section 1.3.3). Indeed, deposition of  $\text{TiO}_2$  nanoparticles should lead to an increase of the roughness factor, which is the ratio of the actual area to the apparent area of the solid-liquid surface. Hence, the contact angle decreases as stainless steel and titanium dioxide are both hydrophilic.

This increase of the roughness factor can be explained by a qualitative analysis about the modification of the surface topography due to nanoparticle deposition. The roughness of the uncoated (clean) surface was measured by atomic force microscope (cf. Section 2.2.2) and has a maximum value of  $0.2\ \mu\text{m}$ . Hence, a  $2\text{-}\mu\text{m}$ -thick deposition layer of  $\text{TiO}_2$  nanoparticles should level out most of the cavities of the clean surface and create a new roughness with a higher roughness factor (cf. Figure 3-9). When the  $\text{TiO}_2$ -coated surface is treated in ultrasonic bath, unstable deposited particles are removed from the surface as shown in Figure 3-10. As the remaining nanoparticles do not fully fill the stainless steel cavities, a highest surface area could be generated.

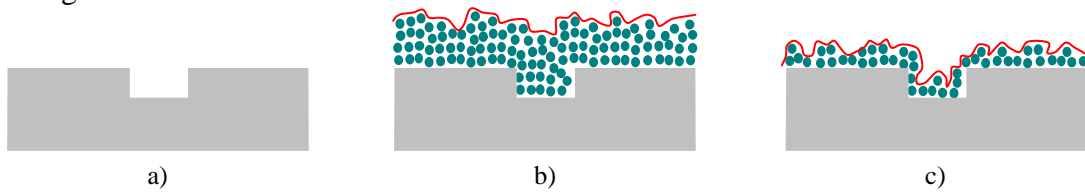


Figure 3-9. Schematic view of the cross section of a) uncoated surface, b) surface with  $\text{TiO}_2$ -particle deposition and c) surface with  $\text{TiO}_2$ -deposition cleaned in ultrasonic bath.

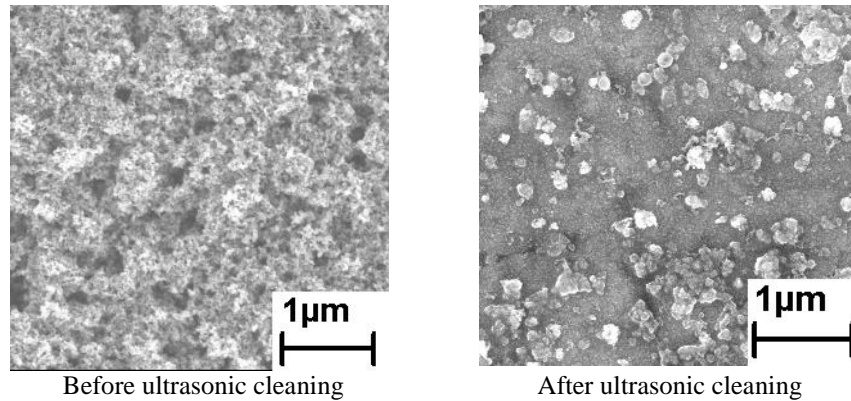


Figure 3-10. FEG-SEM images of surface coated by  $\text{TiO}_2$ -nanoparticle deposition.

To obtain a full validation of the Wenzel model, the roughness factors of all the sample surfaces should be measured. However, it was not possible to make accurate measurements of the roughness factor on the coated surfaces, because the deposition layer is porous and the variation threshold of the surface roughness is relatively large (from a dozen to a few thousand nanometers).

#### Effect of solid-liquid adhesion energy

A change of the surface wettability leads to a change of the solid-liquid adhesion energy, which is determined as (cf. Section 1.3.1):

$$W_{sl}^a = \sigma_{lv} (1 + \cos \theta) \quad (3-13)$$

wherein  $\sigma_{lv}$  is the liquid-vapour surface tension and  $\theta$  is the contact angle.

For water, the adhesion energy is highly sensitive to the variation of the contact angle, because the liquid-vapour surface tension of water is relatively high (72 mN/m at 25 °C). As shown in Figure 3-11, significant enhancement of the adhesion energy is obtained with surfaces coated by nanoparticle deposition. The deterioration of the boiling heat transfer coefficient is then related to the increase of the adhesion energy (cf. Table 3-3).

Indeed, when the adhesion energy increases, more energy is needed to generate bubbles because liquid penetrates more efficiently in the surface cavities. The force acting against the expansion of the bubble foot will also become higher because of higher surface tension force in the horizontal direction. Thus, the residence time of bubbles on the heated surface would become longer, decreasing the bubble emission frequency. Furthermore, on the coated surfaces, the number of active nucleation sites might decrease, because water wets almost completely the coating layer becoming highly porous. Besides, the size of cavities created by nanoparticle deposition are relatively small (a few dozen nanometers) compared to the critical radius of the water at atmospheric pressure (a few thousand nanometers).

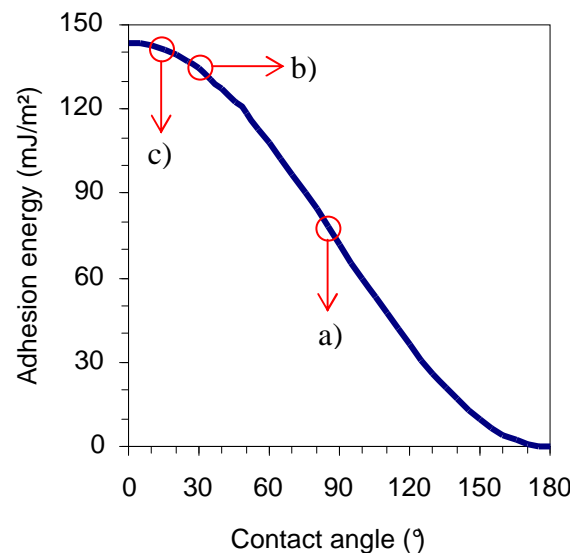


Figure 3-11. Adhesion energy of water versus the contact angle at 25°C for: a) uncoated surface, b) surface with  $\text{TiO}_2$ -particle deposition and c) surface with  $\text{TiO}_2$ -deposition cleaned in ultrasonic bath.

Table 3-3. The modified surfaces versus the clean surface.

Surface	Adhesion energy increasing (%)	Heat transfer coefficient deterioration (%)
$\text{TiO}_2$ deposition	66	30
$\text{TiO}_2$ deposition after ultrasonic	75	50

### Hypothesis for enhancement of heat transfer coefficient

As shown in Section 1.4.2, a few studies on nanofluid boiling reported a heat transfer enhancement. This section aims at explaining this observation based on the effect of adhesion energy.

Recent researches [3.6]-[3.7] show that when the nanoparticle concentration increases, the surface tension of nanofluids decreases. Thereby, the adhesion energy will also decrease if the surface wettability lightly changes, leading to an enhancement of the heat transfer coefficient.

As an example, Wen and Ding [3.8] used  $\text{Al}_2\text{O}_3$  water-based nanofluids with concentration of 0.32, 0.71, 0.95, and 1.25 w%, respectively. The concentrations are high enough to significantly reduce the liquid surface tension according to Sohel Murshed and Nguyen [3.6] and Shi *et al.* [3.7]. Moreover, neither nanoparticle deposition nor noticeable changes onto the sample surface topography were observed after the boiling tests. Therefore, the adhesion energy of the nanofluids would be smaller than pure water; leading to lower energy required for bubble formation, higher bubble emission frequency and higher number of active sites on the heated surfaces. Hence, the heat transfer coefficient improves.

The results of Narayan *et al.* [3.9] might be explained by the same reasoning. The authors also used  $\text{Al}_2\text{O}_3$  water-based nanofluids with concentration of 0.5, 1, and 2 v% respectively. The surface tension of these nanofluids should be lower than that of pure water. When the heated surface has low roughness (48 nm), the initial contact angle is relatively high (near  $80^\circ$  for stainless steel). Thus, the deposition of the alumina particles would lead to a significant decrease of the contact angle by increasing the roughness factor. In this case, the decrease of the contact angle should have a more significant effect than that of the surface tension. Therefore, the adhesion energy would increase and would result in deterioration of the heat transfer coefficient. However, when the surface roughness is high (524 nm), according to Wenzel model, the initial contact angle is relatively low. Hence, the deposition of the particles would slightly change the contact angle. Contrary to the previous case, the decrease of the surface tension should have a more significant effect. The adhesion energy would decrease, leading to the heat transfer coefficient enhancement.

As a general tendency, most of nanofluid researches report heat transfer deterioration. The main reason for this observation should be the deposition of nanoparticles during nucleate boiling that increases the adhesion energy and reduces the number of active nucleation sites. However, beyond a range of nanoparticle concentration, both the adhesion energy and the number of active nucleation sites can be unchanged as the liquid surface tension highly decreases. This accounts for the fact that some studies report no change of heat transfer coefficient. If the contact angle slightly changes and the liquid surface tension significantly changes, enhancement of heat transfer can be obtained due to the decrease of the adhesion energy. In summary, the decrease of the liquid surface tension enhances the heat transfer whereas the nanoparticle deposition tends to deteriorate it. The interaction of these opposite effects could explain the controversial results published in the literature.

### 3.5 Conclusion

In order to understand the controversial results about nanofluid-boiling heat transfer, the present work performs experiments exploring the mechanisms and impacts of surface coating during nucleate boiling in nanofluids. The thickness of the nanoparticle layer was observed to depend on the nanoparticle concentration and the experiment duration.

Compared to a clean surface, the wettability of the surfaces with  $\text{TiO}_2$  nanoparticle layer has been significantly improved. However, up to 50% of heat transfer coefficient deterioration was observed with  $\text{TiO}_2$  coated surfaces in water pool boiling. An explanation is proposed which involves the role of adhesion energy on heat transfer. Indeed, an enhancement or a deterioration of the heat transfer coefficient would be due to a decrease or an increase of the adhesion energy, respectively.



Therefore, the important role of surface wettability is highlighted by the present experimental work. However, the present experiment still has limitations because of a limited number of samples. For a more complete understanding of the impact of surface wettability on the boiling processes, another pool-boiling experiment was conducted, in which various samples having various contact angles were used. The details of this experiment will be given in the next chapter.

### 3.6 References

- [3.1] J. Turkevitch, P.C. Stevenson, J. Hillier, *Disc. Farad. Soc.*, 11, 55 (1951).
- [3.2] S.J. Kim, I.C. Bang, J. Buongiorno, L.W. Hu, Surface wettability change during pool boiling of nanofluids and its effect on critical heat flux, *Int. J. Heat and Mass transfer* 50 (2007), 4105-4116.
- [3.3] R. Cole, W. Rosenhow, Correlation of bubble departure diameters for boiling of saturated liquids, *Chem. Eng. Prog. Symp. Ser.* 65 (1969), 211–213.
- [3.4] J.G. Collier, J.R. Thome, *Convective Boiling and Condensation*, 3d ed., Oxford Science Publications (1996).
- [3.5] R.N. Wenzel, Resistance of solid surfaces to wetting by water, *Industrial and Engineering Chemistry* 28 (1936), 7426-7431.
- [3.6] S.M. Sohel Murshed, N.T. Nguyen, Characterisation of temperature dependence of interfacial tension and viscosity of nanofluid, *Micro/Nanoscale Heat Transfer Int. Conference* (2008), Tainan, Taiwan.
- [3.7] M. Shi, M. Shai, Z. Chen, Q. Li et Y. Xuan, Study on Pool Boiling Heat Transfer of Nano-Particle Suspensions on Plate Surface, *J. of Enhanced Heat Transfer* 14 (2008), 223-231.
- [3.8] D. Wen, Y. Ding, Experimental investigation into the pool boiling heat transfer of aqueous based  $\gamma$ -alumina nanofluids, *J. Nanoparticle Research* 7 (2005), 265-274.
- [3.9] G.P. Narayan, K.B. Anoop, S.K. Das, Mechanism of enhancement/deterioration of boiling heat transfer using stable nanoparticle suspensions over vertical tubes, *J. Appl. Physics* 102 (2007), 074317.





## Chapter 4: Effects of surface wettability modified by nanocoatings

In the previous experiment, it was shown that surface coating by nanoparticle deposition has a significant impact on the boiling heat transfer. Modification of surface wettability was highlighted as the major factor contributing to this observation. However, this experiment has limitations because of a limited number of sample surfaces. Furthermore, the effect of surface wettability could not be accurately determined, since the deposition process leads to a change of not only the contact angle but also the number of nucleation sites.

Therefore, a second experiment was conducted to obtain a more complete understanding of the impact of surface wettability on nucleate boiling. More sample surfaces were made by well-controlled techniques of surface coating such as “Metal-Organic Chemical Vapour Deposition” (MOCVD) and “Plasma Enhanced Chemical Vapour Deposition” (PECVD) (cf. Section 2.1.2), which enable modification of the contact angle without a large change in other parameters. For the first time, a complete set of experimental data have been provided to explore the role of surface wettability in heterogeneous boiling.

In order to understand the experimental observations, a new approach of nucleation mechanisms will be established. In this approach, the concept of macro- and micro-contact angles will be introduced to describe the bubble growth processes. Based on this concept, an analytical model will be developed, giving an explicit relation between the bubble departure diameter and the contact angle. This model then enables development of a new correlation of nucleate boiling heat transfer and the critical heat flux, which will be described in the last sections of this chapter.

### 4.1 Sample preparation

Seven sample surfaces 100 mm long, 5 mm wide and 20  $\mu\text{m}$  thick were made from a stainless steel (grade 301) ribbon, which has a contact angle with water of about  $85^\circ$ . One of them, called “S-ref”, is used as reference of the uncoated surface. The others were coated by nanoparticle deposition of different materials to obtain different water contact angles from  $22^\circ$  to  $112^\circ$  (cf. Figure 4-1). Prior to coating, the sample surfaces were cleaned by acetone washing in ultrasonic bath for 15 minutes and dried by compressed air.

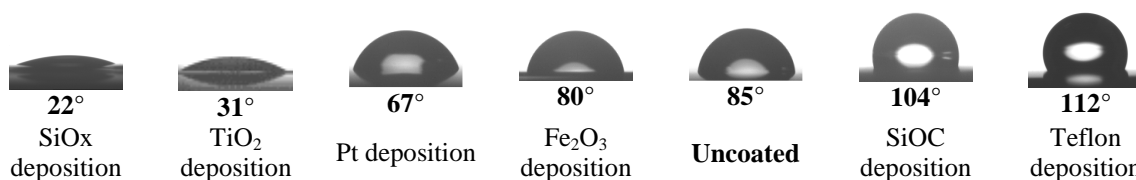


Figure 4-1. Static contact angles of 2- $\mu\text{L}$  sessile water-droplets on stainless steel surfaces with and without nanoparticle deposition.

#### 4.1.1 Coating process

The techniques used for nano-surface coatings are chemical vapour deposition (cf. Section 2.1.2) and boiling of nanofluids as described in Section 3.1. The latter technique is referred to as “Nanofluid Nucleate Boiling Deposition” (NNBD). Indeed, MOCVD is used for platinum

and iron-oxide coating to produce the so-called surfaces “S-Pt” and “S-Fe<sub>2</sub>O<sub>3</sub>” which have relatively low wetting with water. Highly-hydrophilic or hydrophobic samples were made by PECVD of SiO<sub>x</sub>, SiOC and Teflon-like, giving the three sample surfaces called “S-SiO<sub>x</sub>”, “S-SiOC” and “S-Teflon”, respectively. The last surface called “S-TiO<sub>2</sub>” is fabricated by boiling water-based TiO<sub>2</sub> nanofluid which contains particles with diameters of 10-50 nm. Characteristics of the sample surfaces are shown in Table 4-1 below.

Table 4-1. Sample- surface characteristics.

Surface name	Deposited-particle material	Deposition technique	Deposition type
S-SiO <sub>x</sub>	SiO <sub>x</sub>	PECVD	Continuous monolayer of 20 nm thickness
S-TiO <sub>2</sub>	TiO <sub>2</sub>	NNBD	Non-continuous multilayer of 100 nm thickness
S-Pt	Pt	MOCVD	Non-continuous monolayer of 20 nm thickness
S-Fe <sub>2</sub> O <sub>3</sub>	Fe <sub>2</sub> O <sub>3</sub>	MOCVD	Non-continuous monolayer of 20 nm thickness
S-ref	-	-	-
S-SiOC	SiOC	PECVD	Continuous layer of 20 nm thickness
S-Teflon	Teflon-like	PECVD	Continuous layer of 20 nm thickness

#### 4.1.2 Surface characterization

##### AFM analysis

In order to benchmark surface topography changes induced by nanoparticle deposition, AFM (Atomic Force Microscope) scanning of the uncoated surface was carried out in a 10 μm × 10 μm representative area of the surface (cf. Figure 4-2). The scan shows surface machining patterns in the shape of parallel micro-grooves with an average period of about 5 μm and an apparent depth of about 140 nm.

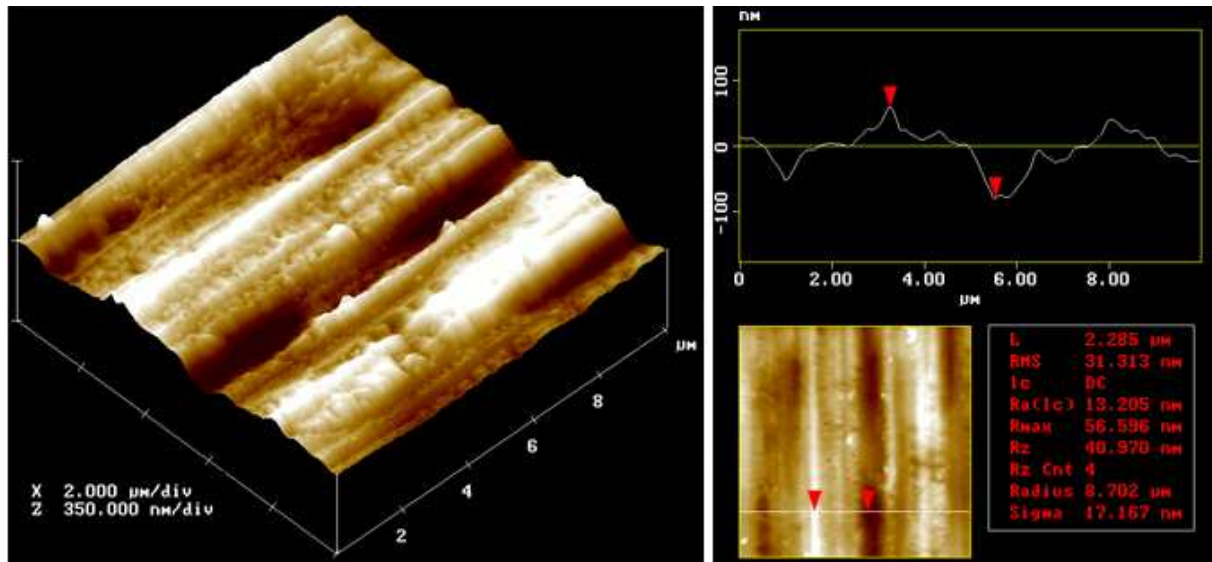


Figure 4-2. AFM topography of the uncoated surface S-ref.

The rough-mean-squared roughness of the uncoated surface is about 31 nm. It is then expected that nanoparticle deposition with a thickness lower in scale than 100 nm will not affect the number of cavities available for nucleation. Table 4-1 shows that surface coatings satisfy this condition in the cases of PECVD and MOCVD processes.

### FEG-SEM analysis

Qualitative analysis was performed by Field-Emission Gun Scanning Electron Microscopy (FEG-SEM) as shown in Figure 4-3. It is observed that the surfaces with non-continuous layer of nanoparticle deposition (S-TiO<sub>2</sub>, S-Pt and S-Fe<sub>2</sub>O<sub>3</sub>) seem to be quite homogenous and their topographies are changed in nanometric scale only. Thereby, the deposition of TiO<sub>2</sub> particles by NNBD is expected to do not affect the micro-cavities initially existed on the clean surface. Beyond, as a result of very thin nanoparticle layer deposition, the topographies of the surfaces coated by PECVD technique (S-SiOx, S-SiOC and S-Teflon) remain similar to that of the uncoated surface.

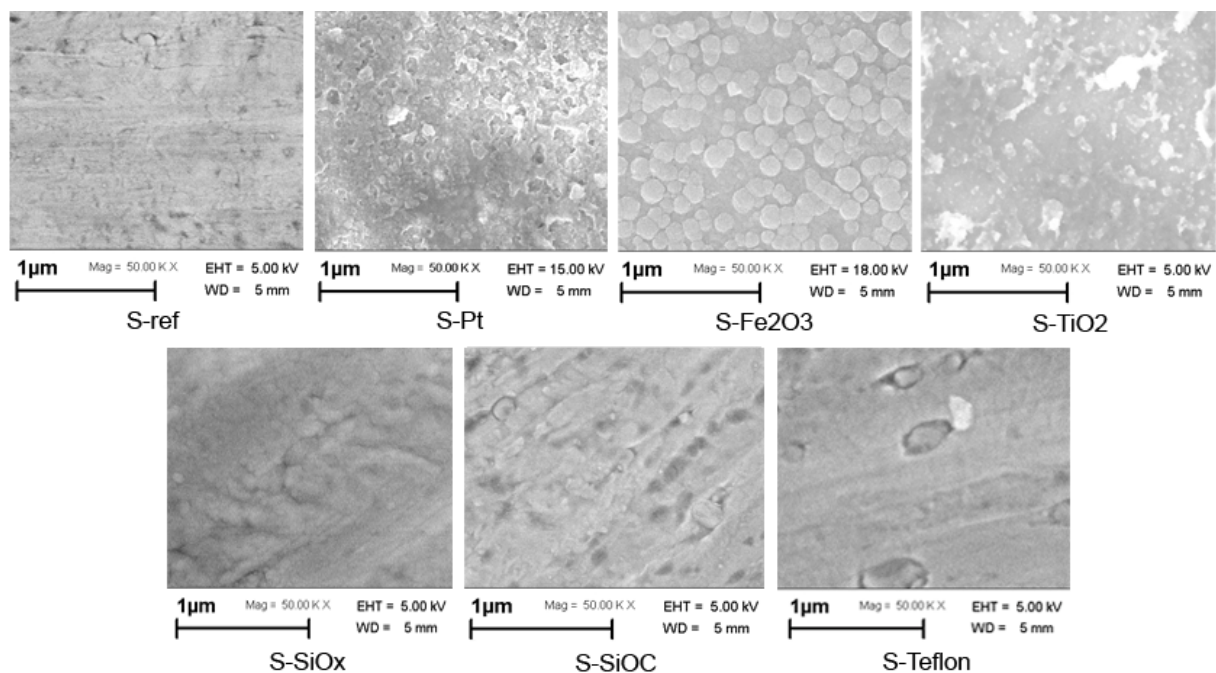


Figure 4-3. FEG-SEM images of the tested surfaces (by MOCVD: S-Pt and S-Fe<sub>2</sub>O<sub>3</sub>; by NNBD: S-TiO<sub>2</sub> and by PECVD: S-SiOx, S-SiOC and S-Teflon).

### Contact angle measurements

The wettability of the sample surfaces is quantified by measurements of static contact angle  $\theta$  at 25 °C, for which the sessile drop technique is used (cf. Section 2.2.3). Figure 4-1 presents the contact angle data window and corresponding water droplet images. It is noticed that the surfaces with SiOC or Teflon deposition are hydrophobic ( $\theta > 90^\circ$ ) and the surface with SiOx deposition is highly hydrophilic ( $\theta < 30^\circ$ ).

## 4.2 Experimental setup and results

### 4.2.1 Experimental setup

The experimental apparatus used for boiling tests has been described in Section 3.2. The layout is designed to study boiling of sample surfaces in horizontal position. This position

enables to obtain images of bubbles from the perspective view made by a high-speed camera set at 6000 fps.

Before each measurement, the sample surface is heated to a temperature higher than that of the saturate temperature to remove gasses trapped inside its cavities. The electrical resistance of each sample was previously calibrated, enabling the determination of the sample temperature (cf. Section 2.2.4).

## 4.2.2 Experimental results

### Hydrophobic surfaces

Figure 4-4 presents some captured images of boiling process on the hydrophobic surfaces (S-SiOC and S-Teflon) of which the static contact angles at 25 °C are respectively 104° and 112°. Compared to standard surfaces which are usually wetted, the bubbles appeared on hydrophobic surfaces at very low heat flux and then remained on the surfaces. Increasing the heat flux, the bubble size increased but the bubbles still did not detach from the wall. At higher heat flux, the bubbles spread over the surface, causing bubble coalescence that led to film boiling. No bubble emission was observed on hydrophobic surfaces. This phenomenon could be due to the effect of the surface tension force which will be discussed in detail in Section 4.3. It could also be due to condensation occurring at the bubble head by highly subcooled liquid. Indeed, condensation reduces the bubble volume and thereby reduces the buoyancy force acting on the bubble to move it upward. However, the bubble volume decrease caused by vapour condensation should be neglected compared to the bubble volume increase caused by evaporation of liquid underneath the bubbles. This is mainly due to the high water liquid to vapour density ratio, which is about 1600 at 100°C.

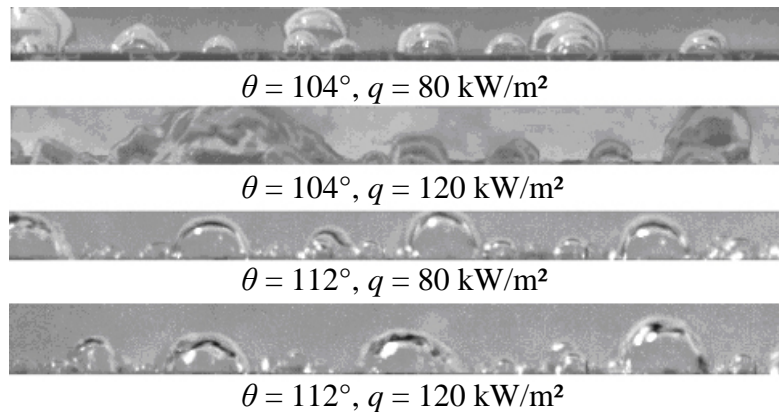


Figure 4-4. For hydrophobic surfaces, bubbles are created at low superheats but cannot detach from the wall. There is no bubble emission and film boiling occurs because of bubble coalescence.

At the same heat flux, the surface S-Teflon with higher static contact angle had a greater bubble base radius. It was also observed that film boiling appeared at lower heat flux on higher contact angle surfaces: 120 kW/m² for S-Teflon versus 200 kW/m² for S-SiOC. These observations are in agreement with that of Gaertner [4.1] and Hummel [4.2] which showed that a continuous hydrophobic surface tends to become vapour blanketed during nucleate boiling. However, no bubble departure was noticed, causing instability of the heat transfer. The wall temperature increased during boiling time and after about fifteen minutes, local wall destruction occurred. Thus, it was impossible to measure the heat transfer coefficient in steady state regime.

### Hydrophilic surfaces

For hydrophilic surfaces, bubble emission occurs and the steady state of boiling heat transfer can be reached after a few minutes.

#### ▪ Bubble size

The bubble departure diameter is determined by analysing pictures taken from video recorded by the high-speed camera. Kolev [4.3] showed that the bubble departure diameter significantly depends on the heat flux. Hence, to strictly determine its dependence on the contact angle, the bubble departure diameter was measured at a constant heat flux of 200 kW/m<sup>2</sup>. Figure 4-5 shows that the bubble departure size increases with the increase of the surface wettability. For highly wetted surfaces ( $\theta \leq 31^\circ$ ), the bubble grew and spread over the wall. Contrary to the well-known correlation of Fritz [4.4] where the bubble diameter is proportional to the static contact angle, the experimental results (cf. Figure 4-6) show that a greater surface wettability yields bigger bubbles detached from the surface.

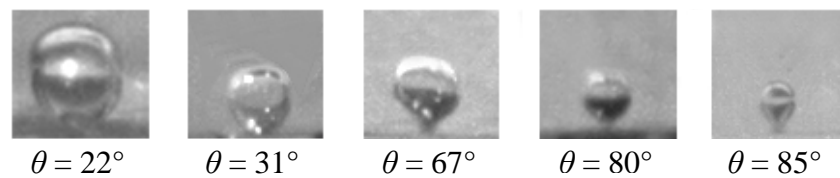


Figure 4-5. Bubble departure on hydrophilic surfaces.

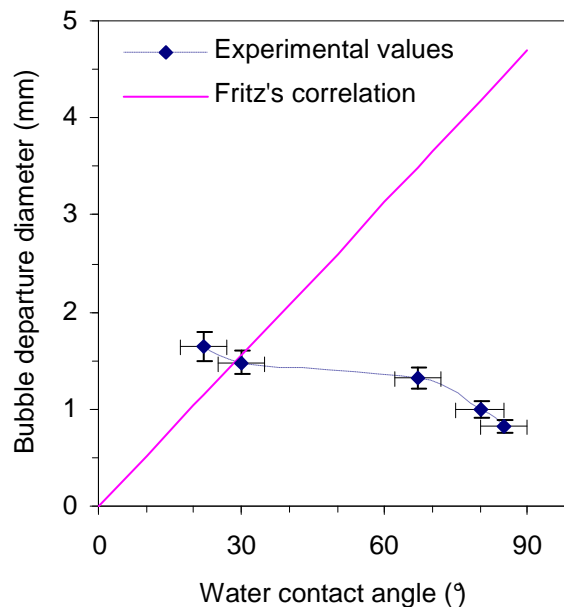


Figure 4-6. Bubble departure diameter (measured at 200 kW/m<sup>2</sup>) versus the static contact angle at 25 °C. The correlation of Fritz has the opposite tendency compared to the experimental values.

#### ▪ Bubble emission frequency

From the videos captured by the high-speed camera, the waiting time and the growth time were also measured, so that the bubble emission frequency was determined. Figure 4-7 shows that the waiting time is much greater than the growth time. This might be due to high liquid subcooling as the bulk temperature is 15 °C below the saturated temperature [4.5]. Also, the waiting time reduces more rapidly with the increase of the heat flux compared to the growth time. Indeed, the change of the heat flux from 220 to 300 kW/m<sup>2</sup> results in 70% mean

decrease of the waiting time but only 23% mean decrease of the growth time. Moreover, the waiting time and the growth time both increase with the increase of the surface wettability. When the static contact angle is below  $30^\circ$ , this effect becomes especially significant. As a result, the bubble emission frequency deteriorates for a greater surface wettability (cf. Figure 4-8). Many studies [4.6]-[4.8] show that the higher the bubble emission frequency, the lower the bubble departure diameter. For instance, Zuber [4.6] estimated that the product  $D_b f$  is about constant and his correlation is relatively in agreement with the experimental data as shown in Figure 4-8.

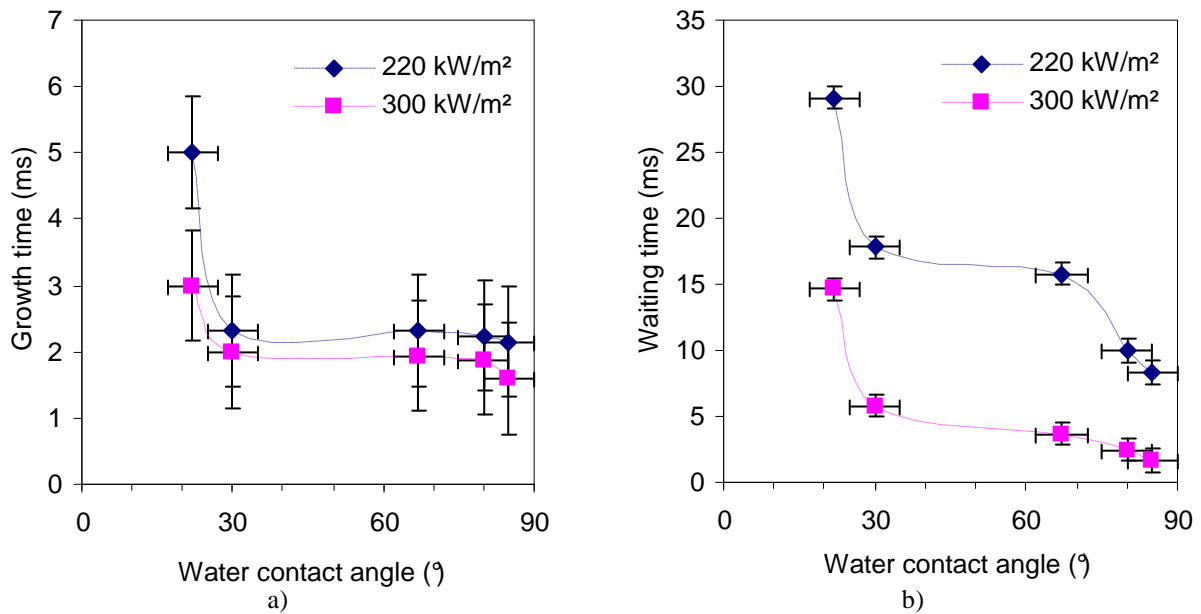


Figure 4-7. Evolution of growth time (a) and waiting time (b) as a function of contact angle.

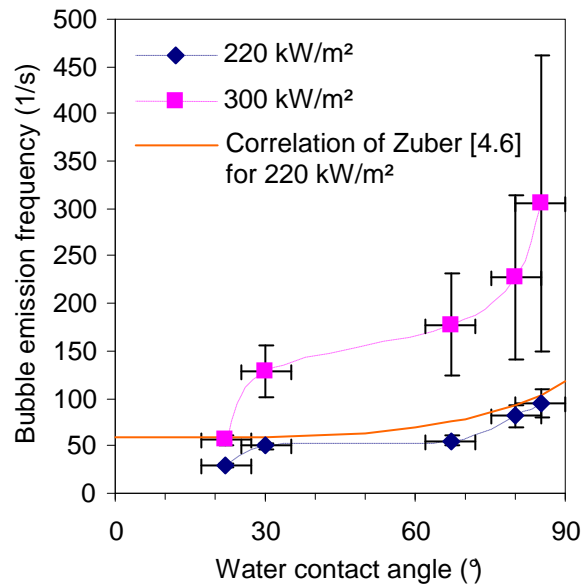


Figure 4-8. Bubble emission frequency versus the contact angle.

#### ▪ Heat transfer coefficient

The data reduction and uncertainty analysis of the boiling heat transfer has been described in Section 3.3. Figure 4-9 depicts the comparison of experimental values and predictions given



by Cooper [4.23] correlation for the uncoated surface S-ref. The roughness is chosen to be 0.4, 0.65, and 1  $\mu\text{m}$  respectively to fit the experimental values. The changing tendencies of the measured and correlated heat transfer coefficients as a function of the heat flux show a very good coherence, therefore guarantying the reliability of our measurements. Nevertheless, the correlation of Cooper should not be used to predict the surface roughness. Indeed, the roughness measured by AFM (cf. Section 4.1.2) is significantly lower than the best fitting roughness to this correlation.

Figure 4-10a compares the heat transfer performance of subcooled pool boiling on the hydrophilic surfaces. The tendency of the presented curves is relatively good and shows a significant change of the heat transfer coefficient with the surface wettability change.

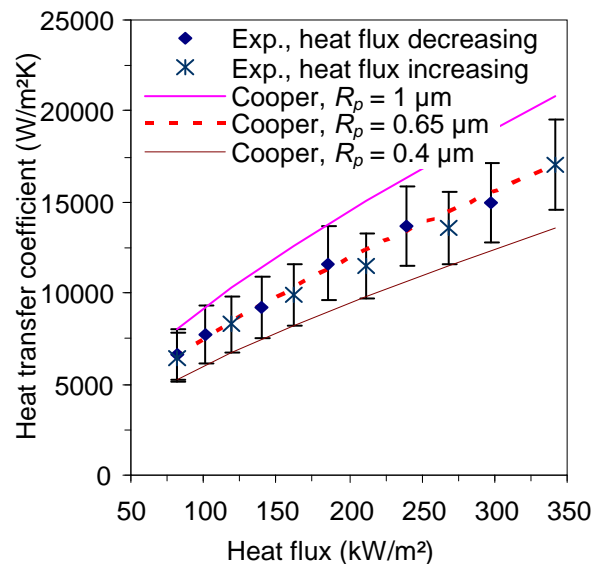


Figure 4-9. Heat transfer coefficient of an untreated stainless steel surface.

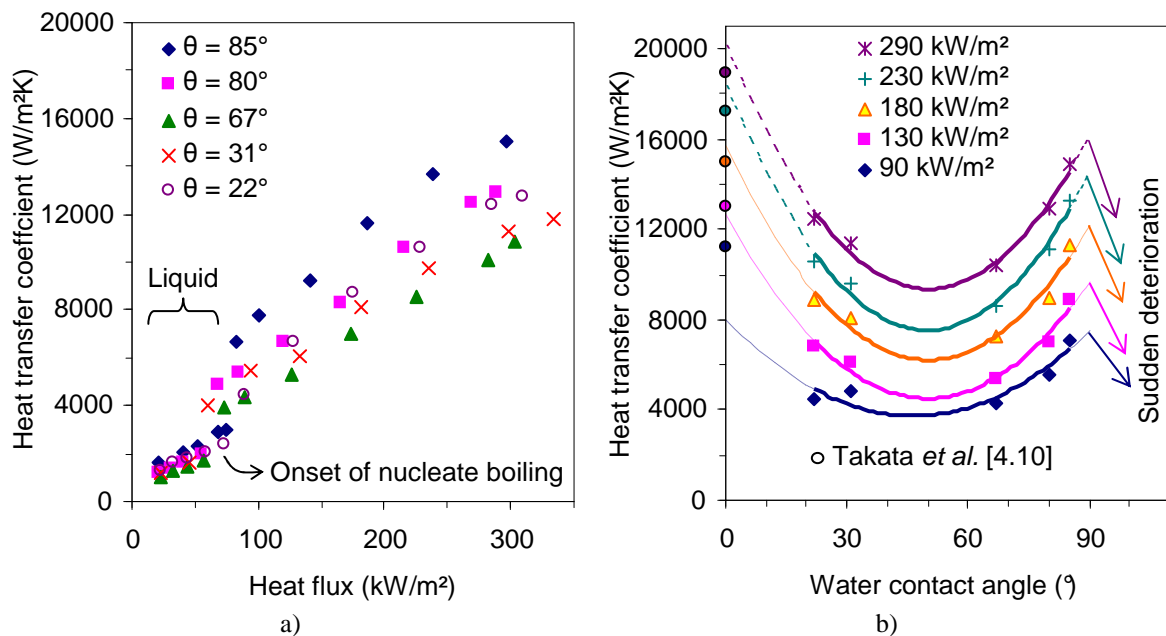


Figure 4-10. Effects of the surface wettability on the heat transfer coefficient. In b), the same colour indicates the same heat flux.



Figure 4-10b highlights this observation and shows that the best heat transfer coefficient can be obtained with the surface which has a static contact angle close to either  $0^\circ$  or  $90^\circ$ . Indeed, the experimental data are fitted by 2<sup>nd</sup>-order-polynomial curves. Extensions of these curves at  $0^\circ$  reach relatively well the experimental data of Takata *et al.* [4.10] which show enhancement of boiling heat transfer by using superhydrophilic surfaces.

## 4.3 Model of bubble growth

### 4.3.1 Dynamic contact angle approach for nucleation

The videos recorded by the high speed camera showed a progressive change of the contact angle during the bubble growth (cf. Figure 4-11). As the test surfaces have small deep cavities (cf. Figure 4-2), the sample surfaces are thereby assumed to be completely wetted during experiment. Hence, a new mechanism of bubble formation during nucleate boiling has been developed (cf. Figure 4-12) and is described in the following paragraphs.

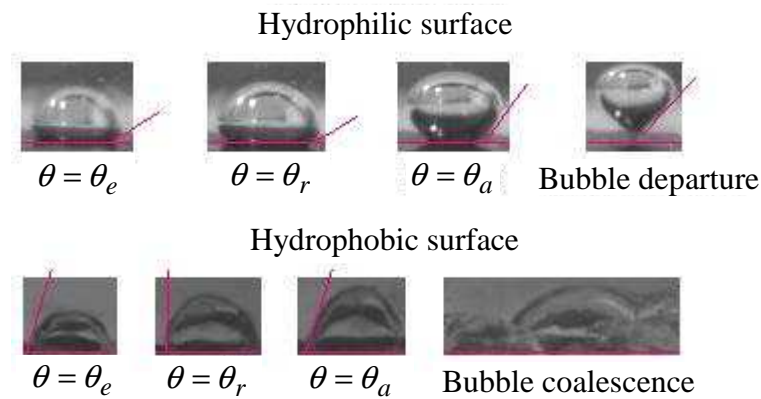


Figure 4-11. Contact angle change during growth time ( $\theta_r \leq \theta_e \leq \theta_a$ ).

#### Hydrophilic surface

- Step 1: a convex vapour shape appears at the cavity base. The contact angle is the equilibrium angle at saturated temperature  $\theta_e$ .
- Step 2: the liquid continues evaporating to form a bubble at the cavity mouth. The contact angle is still equal to  $\theta_e$ .
- Step 3: the liquid microlayer underneath the bubble evaporates, expanding the triple contact line (TCL) and the bubble diameter. Thus, the liquid recedes from the cavity and the contact angle decreases to the receding angle at saturated temperature  $\theta_r$ .
- Step 4: the gravity force stretches the bubble vertically when the liquid moves towards the cavity. The TCL reduces and the contact angle increases to the advancing angle at saturated temperature  $\theta_a$ .
- Step 5: the bubble detaches from the wall.

#### Hydrophobic surface

- Step 1: a concave vapour shape is formed at the cavity base. Its contact angle is equal to the equilibrium angle  $\theta_e$ .
- Step 2: the bubble appears at the cavity mouth by the liquid evaporation. The contact angle remains constant but this time the vapour shape becomes convex.

- Step 3: the gravity force increases the bubble height, moving the liquid backward. The contact angle decreases to the receding angle  $\theta_r$ . As the latter is greater than  $90^\circ$ . Hence, the bubble cannot detach from the wall.
- Step 4: the liquid moves toward the cavity, increasing the contact angle to the advancing angle  $\theta_a$ .
- Step 5: the liquid continues evaporating, expanding the TCL. Hence, the bubble coalesces with bubbles formed at neighbouring sites. Critical heat flux is reached by low vapour conductivity.

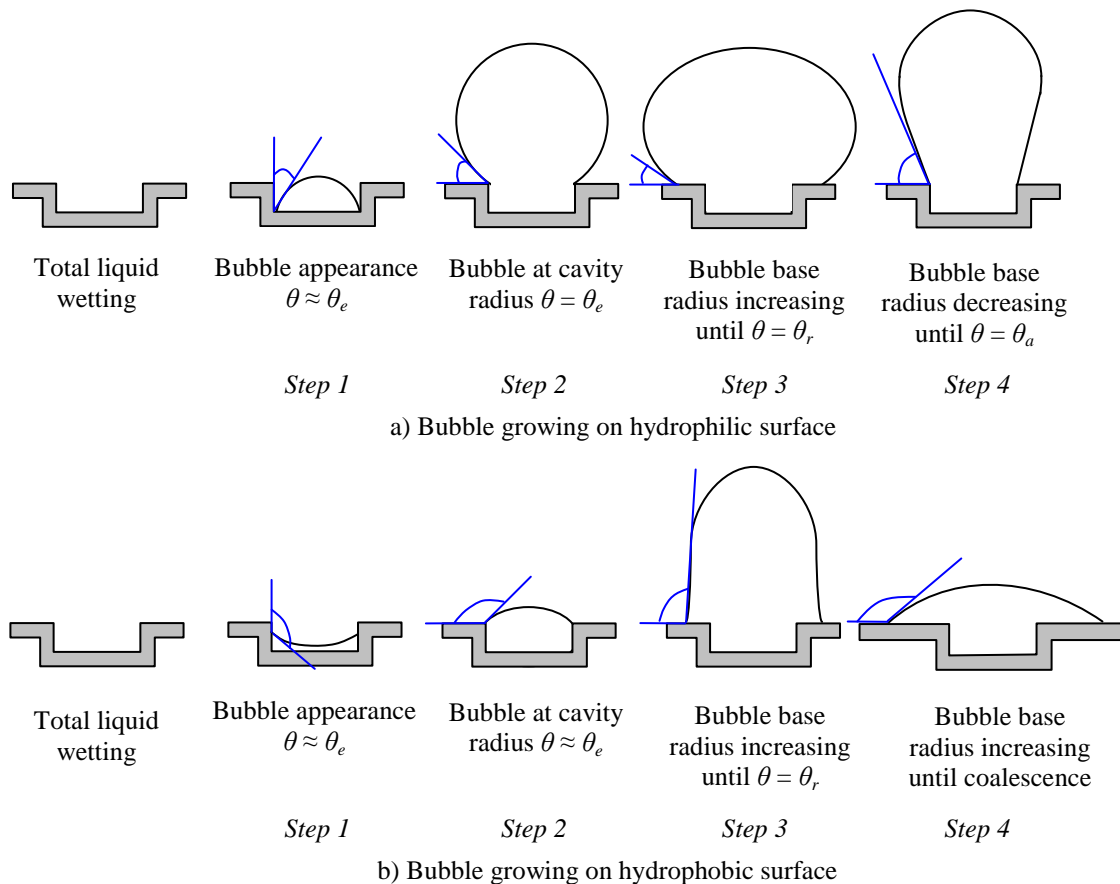


Figure 4-12. Dynamic contact angle approach for nucleate boiling.

The effect of contact angle on bubble detachment process is mainly related to modification of the surface tension force. For hydrophobic surfaces, the fact that bubbles cannot detach from the wall and rapidly coalesce is mainly due to the horizontal component of the surface tension force, which acts to moving the contact line away from the bubble axis. For hydrophilic surfaces, the variation of the contact angle during the bubble growth can be explained by the concept of macro- and micro-contact angles which will be described in the following section.

### 4.3.2 Concept of macro- and micro-contact angles

The contact angle is usually measured at the room temperature ( $25^\circ\text{C}$ ) by depositing a liquid droplet on the sample surface. The surface and the droplet are at the same temperature, thus there is no heat exchange between them. This contact angle is denoted as  $\theta^\circ$ . However, during the nucleate boiling, the bubble is formed by the liquid evaporation caused by the heat transfer from the wall to the liquid. The contact angle that follows  $\theta$  is different from  $\theta^\circ$ , because the liquid is now at saturated temperature (cf. Figure 4-13). In general, the liquid

surface tension decreases when the temperature increases. Hence,  $\theta$  is lower than  $\theta^\circ$  when the saturated temperature is higher than the room temperature. In addition, in boiling conditions, the balance of the three surface energies: solid-liquid, liquid-vapour and solid-vapour, becomes unstable due to the non-zero heat flux imposed at the solid-liquid interface. For the hydrophilic surfaces, this heat flux causes evaporation of the liquid micro-layer underneath the bubble. The thinner this layer is, the higher the heat flux passes through. Close to the TCL, the heat transfer would be extremely high and would create a liquid evaporation with a rate that is much higher than in the surrounding areas. Therefore, the curvature of the liquid-vapour interface would change, leading to the emergence of another contact angle named «micro-contact angle»  $\theta_\mu$ . The contact angle  $\theta$  is relatively at a larger scale. It is named «macro-contact angle».

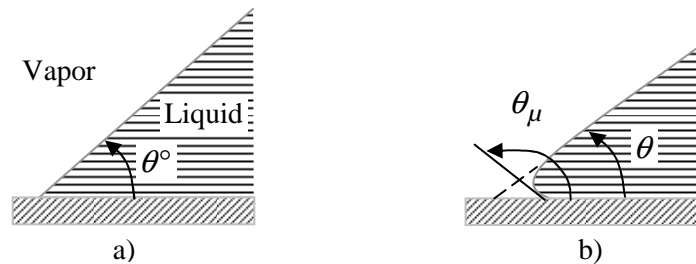


Figure 4-13. Contact angle of a liquid droplet: a) at 25° without any heat transfer and b) at saturation temperature on a heated surface: macro-contact angle  $\theta$  and micro-contact angle  $\theta_\mu$ .

### Influence of the micro-contact angle

The surface tension force  $F_\sigma$  is determined by the micro-contact angle and not by the macro-contact angle. When the nucleation is initiated, close to the TCL, the liquid evaporation may cause a micro-contact angle greater than 90°, as described by Mitrovic [4.11]. Due to the horizontal component of the surface tension force  $F_{\sigma,h}$ , the liquid in the micro-layer moves backward from the bubble axis and the TCL expands from A to B (cf. Figure 4-14). Along with the liquid movement, the micro-contact angle decreases as a result of the restoration of the surface energies balance. At position B, the micro-contact angle is equal to 90° and the surface tension force stops displacing the TCL. However, the liquid inertia and the energy minimization of the system will result in a decline of the micro-contact angle to a value close to that of the macro-contact angle. The horizontal component of the surface tension force reappears, but this time it moves the liquid forward by reducing the TCL radius. At position C, the TCL disappears and the bubble detaches from the wall.

The micro-contact angle is an important parameter in nucleate boiling. First, it directly affects the vertical component of the surface tension force  $F_{\sigma,v}$ , which contributes to maintain the bubble on the wall. Then, it creates the TCL movement and thus affects the dynamic forces caused by the liquid inertia and viscosity. Indeed, when the TCL is expanding from A to B, the bubble becomes bigger and the inertia of the liquid surrounding the bubble exerts a reaction force to maintain it on the wall. But when the TCL retracts from B to C, the liquid goes forward to the bubble axis, enabling the bubble departure. During the bubble growth, the macro-contact angle changes according to the hysteresis phenomenon: it decreases when the liquid recedes and increases when the liquid advances.

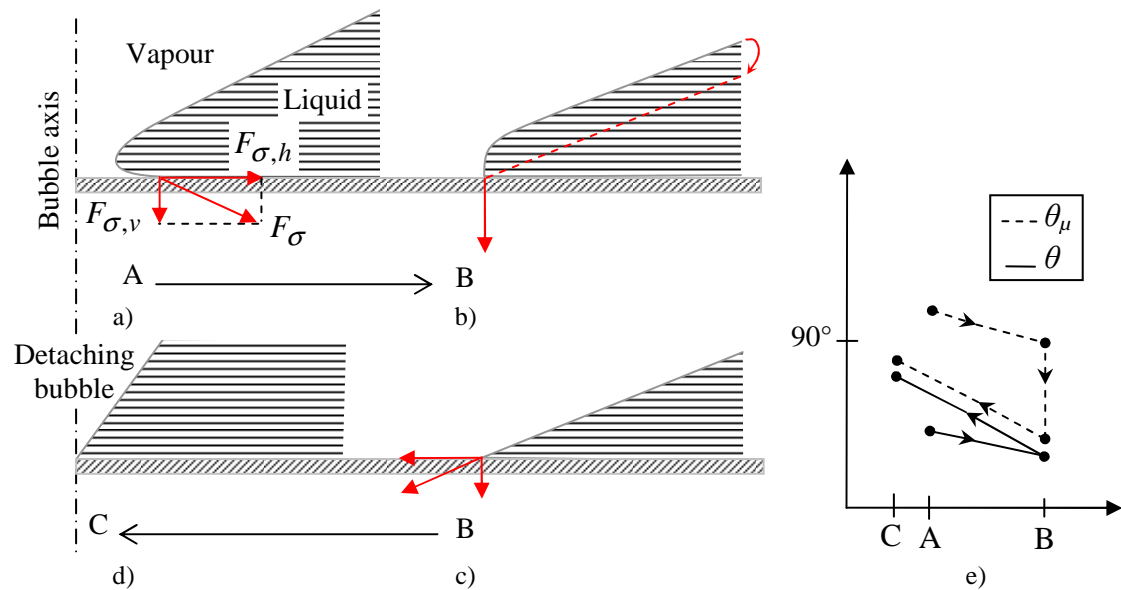


Figure 4-14. Movement of the contact line during bubble growth: a) the bubble growth initiates, b) the contact line stops displacing at  $\theta_{\mu} = 90^{\circ}$ , c) the contact line starts moving toward the bubble axis, d) the bubble detaches from the wall and e) hysteresis of  $\theta$  and  $\theta_{\mu}$ .

### Influence of the macro-contact angle

Although the surface tension force depends on the micro-contact angle, the macro-contact angle always plays a key role. A simple way of understanding the effects of the macro-contact angle is to analyze its influence on the bubble form. The initial radius of the TCL is assumed to be equal to that of the nucleation sites. At the same TCL, for a simple geometric reason, the bubble which has a lower contact angle is bigger (cf. Figure 4-15).

This might explain why the increase of the surface wettability leads to the increase of the energy required to activate the nucleation sites. Therefore, between the departure of a bubble and the appearance of the next one, the waiting time would be longer when the macro-contact angle is lower. The decrease of the macro-contact angle would then intensify the phase difference caused by the time delay between the active nucleation sites (two nucleation sites are said to be «in phase» if they emit the bubbles at the same time). That might explain why, at a given time, while increasing the contact angle, we observed fewer active nucleation sites, whereas if the observation is made over a long period, the number of active sites remained almost independent of the macro-contact angle.

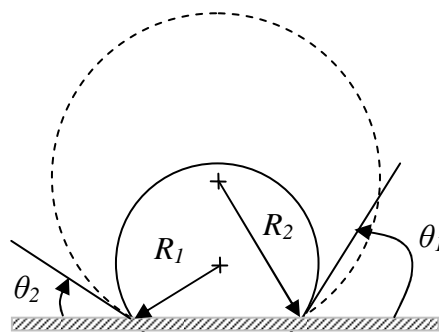


Figure 4-15. Two spherical bubbles are assumed to have the same TCL. If  $\theta_2$  is lower than  $\theta_1$ , the bubble having the contact angle  $\theta_2$  is then bigger than that having the contact angle  $\theta_1$ .

## 4.4 Model of bubble departure diameter

A number of correlations were suggested to estimate the bubble departure diameter over the past eighty year [4.12]. Most of them indicate the effects of wall superheat, operating pressure, gravity and fluid characteristics, but the role of contact angle has seldom been reported. Before 2008, to our knowledge, the correlation developed by Fritz [4.4] was the only known correlation taking the wetting effect into account. Its expression is given as:

$$\frac{D_d}{L_c} = 0,0208 \times \theta \quad (4-1)$$

wherein  $\theta$  is the contact angle in degrees and  $L_c$  is the capillary length defined as:

$$L_c = \sqrt{\frac{\sigma}{g(\rho_l - \rho_v)}} \quad (4-2)$$

It is important to note that in his paper [4.4], Fritz only showed the existence of a maximum volume of a vapour bubble, which can be written as a function of contact angle and capillary length. Eq. (4-1) does not even explicitly appear in this publication. The effect of the contact angle is empirically taken into account. The correlation was established based on measurements with air bubbles and not with vapour bubbles in boiling conditions. A complete review on bubble departure diameter measured in boiling systems was given by Zeng *et al.* [4.13]. It was shown that Eq. (4-1) gives questionable results for well-wetting fluids, large range of operating pressures and in microgravity conditions. Recent study of McHale and Garimella [4.14] with FC-77, a well-wetting fluid, gave the same conclusion. The present data obtained with a large set of contact angle also show that the evolution trend of departure diameter with contact angle disagrees with that suggested by Fritz (cf. Figure 4-6).

It is thereby necessary to develop new models which enable reliable prediction of the impact of contact angle on the bubble departure diameter. This section is divided into two parts. The first part concerns a new correlation of bubble departure diameter which will be developed based on the experimental data. The second part is devoted to describing a theoretical model that takes into account the role of contact angle in bubble growth process. This model will be based on the concept of macro- and micro-contact angles and will be developed for isolated bubbles detaching from upward-facing horizontal surface.

### 4.4.1 New correlation of bubble departure diameter

As mentioned in Section 4.3.2, the measured contact angle (macro-contact angle) affects boiling process mainly through its influence on the bubble form, for which the energy factor is an important parameter. This factor is not only an energy ratio, but also a volume ratio of the bubble having a contact angle  $\theta$  to the full spherical bubble having the same diameter. Its expression was given by Bankoff [4.15] as:

$$f(\theta) = \frac{2 + 3 \cos \theta - \cos^3 \theta}{4} \quad (4-3)$$

The energy factor reaches its maximum value at  $0^\circ$  contact angle, and then decreases with increasing contact angle. It reaches the minimum value at  $180^\circ$  contact angle. Thus, the higher

contact angle, the lower energy required to form initial vapour shape at a cavity. This can explain why the bubble is formed at very low heat flux for hydrophobic surfaces and why the waiting time increases with decreasing contact angle. For hydrophilic surfaces, a new correlation is therefore established to estimate the bubble departure. The energy factor is taken into account as the contribution of the wetting effects:

$$\frac{D_b}{L_c} = 0.626977 \times \frac{(2 + 3 \cos \theta - \cos^3 \theta)}{4}, (\theta < 90^\circ) \quad (4-4)$$

Comparison with experimental data of this study and some studies in literature is shown in Figure 4-16 and Figure 4-17.

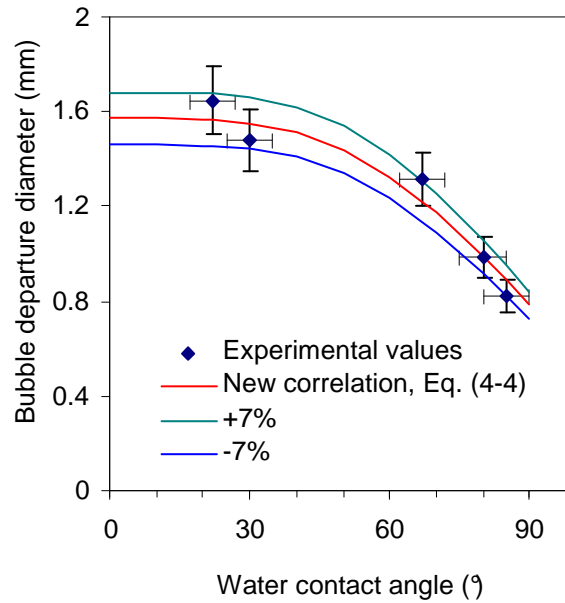
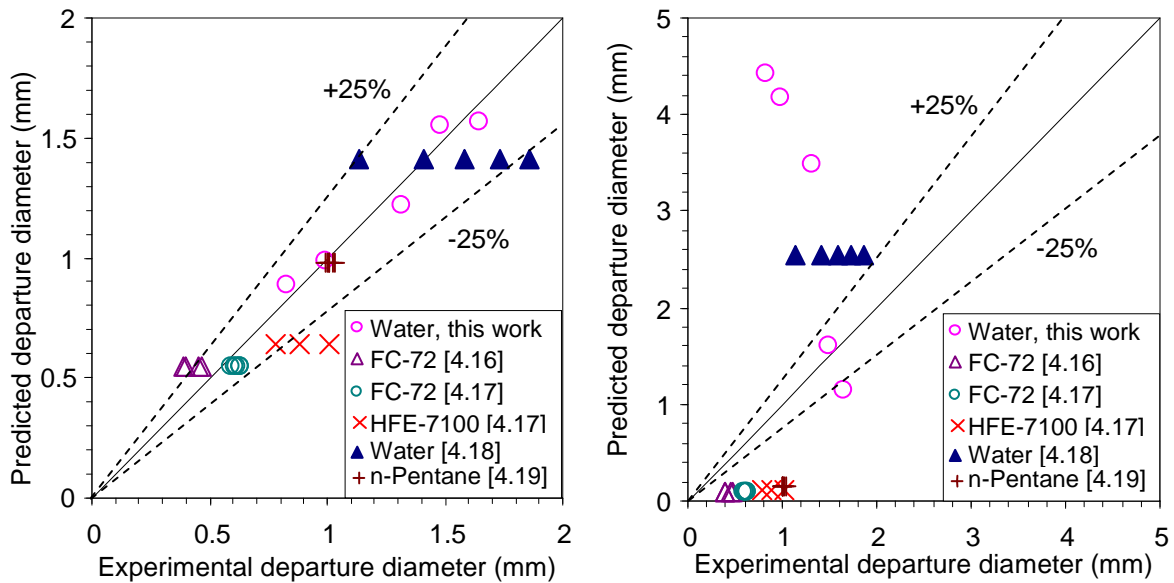


Figure 4-16. New correlation to estimate the bubble departure diameter.



a) Correlation of this work

b) Correlation of Fritz [4.4]

Figure 4-17. Comparison of predicted and measured vapour bubble departure diameters.

Figure 4-16 shows that the new correlation fits the experimental data of this study relatively well with a maximum deviation of only 7%. In Figure 4-17a, most of the experimental points (90%) are included within the lines of 25% deviation of the theoretical line given by this correlation. The correlation of Fritz gives a worse agreement as shown in Figure 4-17b.

#### 4.4.2 New theoretical model of bubble departure diameter

##### Introduction to the model

In the previous section, a new correlation has been developed for estimating the bubble departure diameter by taking into account the energy factor as the contribution of the wetting effect. It has been shown that this correlation is in good agreement with the experimental data. However, the physics hidden behind Eq. (4-4) are not understood yet. For instance, ones might ask why the constant in this equation is equal to 0.626977. Therefore, a theoretical model of bubble departure will be developed in this section. This model aims at giving a better understanding of the effect of contact angle on bubble growth process.

According to the concept of macro- and micro-contact angles, the bubble reaches its maximum size at point B, when the micro-contact angle is equal to  $90^\circ$  (cf. Figure 4-14). Furthermore, the liquid-vapour interface stops displacing at this moment, cancelling the dynamic forces acting on the bubble. Hence, when the size of the bubble is maximal, the force balance in the direction of the bubble axis gives:

$$F_g - F_{\sigma,v} + F_{cp} = 0 \quad (4-5)$$

where  $F_g$  is the buoyancy,  $F_{\sigma,v}$  is vertical component of the surface tension force, and  $F_{cp}$  is the contact pressure force, which is also called as the “corrected buoyancy force” (cf. Figure 4-18). This force is due to the existence of the contact line [4.20]-[4.21]:

$$F_{cp} = \pi R_{cl}^2 [P_v - P_l]_{cl} \quad (4-6)$$

where  $R_{cl}$  is the radius of the contact line and  $(P_v - P_l)_{cl}$  is the pressure difference between the vapour and liquid phases at the contact line. This difference of pressure can be determined by using Young-Laplace relation [4.22] as:

$$[P_v - P_l]_{cl} = \sigma \left( \frac{1}{R_1} + \frac{1}{R_2} \right) \quad (4-7)$$

where  $R_1$  and  $R_2$  are the principal radii of the bubble curvature at the contact line.

When the micro-contact angle is equal to  $90^\circ$ , the bubble curvature at the contact line is similar to that of a cylinder, which has the same axis as the bubble and has the same radius as the contact line. Therefore, the radii of the bubble curvature at the contact line can be obtained as  $R_1 = R_{cl}$  and  $R_2 \rightarrow \infty$ . Hence, the expression of the contact pressure force becomes:

$$F_{cp} = \pi R_{cl} \sigma \quad (4-8)$$

Furthermore, for a micro-contact angle of  $90^\circ$ ,  $\sin \theta_\mu = 1$  and hence, the vertical component of the surface tension force can be calculated as:

$$F_{\sigma,v} = -2\pi R_{cl} \sigma \quad (4-9)$$

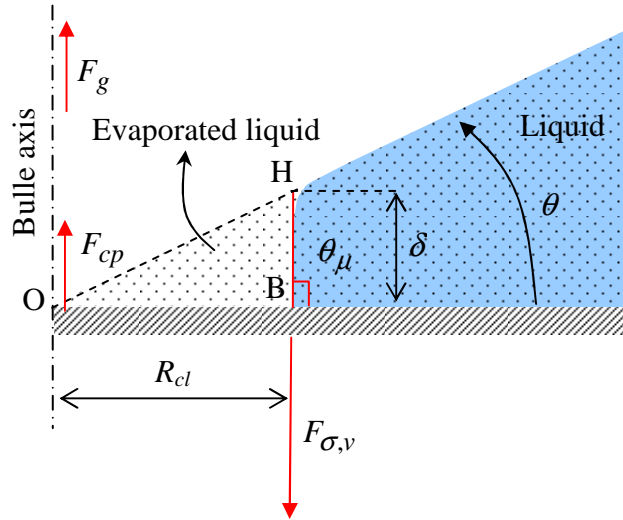


Figure 4-18. Schematic view of the base of the bubble when the micro-contact angle is equal to  $90^\circ$ .

Eqs. (4-5), (4-8) and (4-9) give:

$$F_g = \pi R_{cl} \sigma \quad (4-10)$$

$$g V_b^* (\rho_l - \rho_v) = \pi R_{cl} \sigma \quad (4-11)$$

wherein  $V_b^*$  is the bubble volume at a micro-contact angle of  $90^\circ$ , which is also the maximum bubble volume. Eq. (4-11) implies:

$$V_b^* = \pi R_{cl} L_c^2 \quad (4-12)$$

If the volume of air trapped inside the nucleation site is neglected compared to that of the bubble, the bubble volume can also be determined by mass conservation as:

$$V_b^* = \frac{\rho_l}{\rho_v} V_l^* \quad (4-13)$$

wherein  $V_l^*$  is the volume of the evaporated liquid.

The bubble volume is mainly generated by evaporation of the liquid microlayer beneath the bubble, as suggested by Cooper and Lloyd [4.23]. In reality, the bubble also gains a part of its volume by evaporation of liquid around the bubble cap [4.24]. However, for a simple preliminary model, this part of volume is assumed to be negligible in this study. The volume



of the evaporated liquid is assumed to be equal to that created by rotating the triangle OBH around the bubble axis (cf. Figure 4-18):

$$V_l^* = \frac{2}{3} \pi R_{cl}^2 \delta \quad (4-14)$$

where  $\delta$  is the thickness of the evaporated liquid microlayer, which has the following relation with the contact line radius:

$$\frac{\delta}{R_{cl}} = \tan \theta \quad (4-15)$$

Eqs. (4-13), (4-14) and (4-15) implies :

$$V_b^* = \frac{2}{3} \pi \frac{\rho_l}{\rho_v} R_{cl}^3 \tan \theta \quad (4-16)$$

Combining Eqs. (4-12) and (4-16), the radius of the contact line is given as:

$$R_{cl} = \sqrt{\frac{3}{2}} \left( \frac{\rho_l}{\rho_v} \right)^{-1/2} \tan \theta^{-1/2} L_c \quad (4-17)$$

Replacing Eq. (4-17) into Eq. (4-12), the expression of the bubble volume becomes:

$$V_b^* = \sqrt{\frac{3}{2}} \pi \left( \frac{\rho_l}{\rho_v} \right)^{-1/2} \tan \theta^{-1/2} L_c^3 \quad (4-18)$$

This is an explicit relation that enables the maximum bubble volume during nucleate boiling from an upward-facing horizontal surface to be estimated. To determine the bubble diameter, the bubble shape is simplified as shown in Figure 4-19. At its maximum size, the bubble is assumed to have a spherical shape with a foot that has the same volume as the evaporated liquid (cf. Figure 4-19a). The maximum bubble volume is thereby given as:

$$V_b^* = \frac{1}{6} \pi D_b^{*3} + V_l^* \quad (4-19)$$

wherein  $D_b^*$  is the diameter of the bubble at its maximum size.

Combining Eqs. (4-13) and (4-19), the volume of the evaporated liquid is obtained as:

$$V_l^* = \left( \frac{\rho_l}{\rho_v} - 1 \right)^{-1} \frac{1}{6} \pi D_b^{*3} \quad (4-20)$$

Eqs. (4-18), (4-19) and (4-20) imply:

$$D_b^* = \left( 6\sqrt{\frac{3}{2}} \right)^{1/3} \left( \frac{\rho_l}{\rho_v} \right)^{-1/2} \left( \frac{\rho_l}{\rho_v} - 1 \right)^{1/3} \tan \theta^{-1/6} L_c \quad (4-21)$$

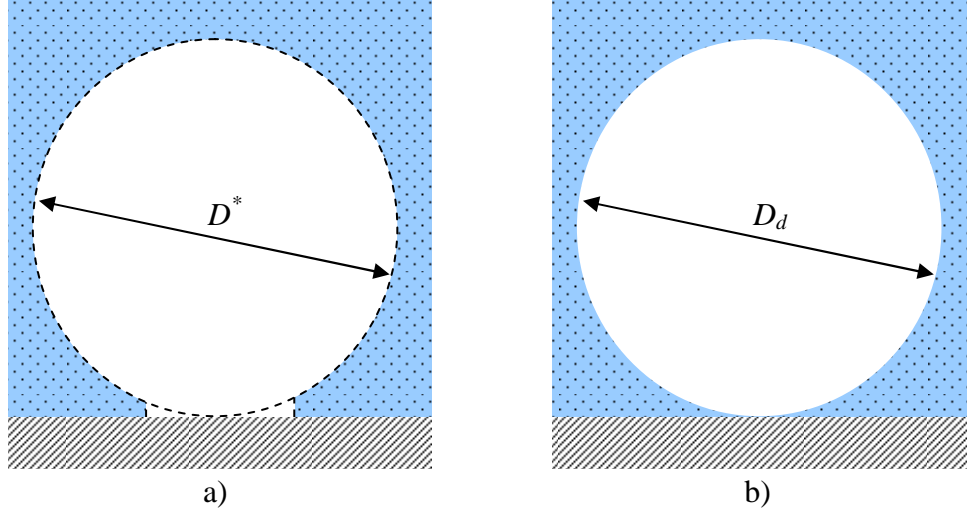


Figure 4-19. Schematic view of a) the bubble at its maximum size and b) the bubble at departure.

After reaching its maximum size, the bubble detaches from the wall due to liquid rewetting which removes the contact line. During this stage, the mass transfer occurs weakly because the wall temperature is close to the saturation temperature, and thus, the bubble size is assumed to remain constant:

$$D_d \approx D_b^* \quad (4-22)$$

Therefore, the bubble departure diameter can be explicitly determined as:

$$D_d = \left( 6\sqrt{\frac{3}{2}} \right)^{1/3} \left( \frac{\rho_l}{\rho_v} \right)^{-1/2} \left( \frac{\rho_l}{\rho_v} - 1 \right)^{1/3} \tan \theta^{-1/6} L_c, \quad (0^\circ < \theta < 90^\circ) \quad (4-23)$$

In summary, an explicit relation to determine the bubble departure diameter has been developed by using the following assumptions:

- Determination of the maximum bubble volume by force balance (Eq. (4-12)) is based on the concept of macro- and micro-contact angles,
- The bubble gains its volume by evaporation of the liquid microlayer which has a simplified geometry as shown in Figure 4-18. The maximum volume of the bubble can thereby be determined by using the conservation of mass (Eq. (4-16)). Thus, the explicit relation to estimate the maximum bubble volume (Eq. (4-18)) is given by combining Eqs. (4-12) and (4-16),
- A simplified geometry of the bubble at its maximum size is suggested in Figure 4-19, leading to an explicit relation of the maximum bubble diameter (Eq. (4-21)),
- During the stage of liquid rewetting, the mass transfer is assumed to be negligible and then the bubble departure diameter can be determined explicitly by Eq. (4-23).

### Comparison to experimental data

Although a number of experimental studies were made to determine the bubble departure diameter, only a few of them reported data about the operating contact angle. Table 4-2 represents some representative data in literature that contains information concerning both the contact angle and the bubble departure diameter.

Table 4-2. Experimental data of the bubble departure diameter.

Fluid	Operating pressure (bar)	Contact angle (°)	Bubble departure diameter (mm)
Water, this study	1	22	1.65
		31	1.48
		67	1.32
		80	0.99
		85	0.82
Water [4.18]	1	43	0.75
	1.93	45	0.78
	2.76	47	0.82
Water [4.25]	1	35	1.9
HFE-7100 [4.17]	1	25 <sup>‡</sup>	1.1
R11 [4.26]	1	31	0.7
R113 [4.26]	1	11	0.8

It is important to note that the model of this study does not take into account the effects of superheat and subcooling, which may lead to different processes of bubble growth. Indeed, high superheat frequently lead to coalescence of bubbles formed at neighboring sites, while high subcooling causes condensation at the bubble head. Therefore, the comparison is made by choosing experimental data at low superheat and low subcooling only. To compare the evolution trend of the bubble departure diameter with the contact angle, a new dimensionless number is defined as

$$Mi = \frac{D_d}{L_c} \left( 6\sqrt{\frac{3}{2}} \right)^{-1/3} \left( \frac{\rho_l}{\rho_v} \right)^{1/2} \left( \frac{\rho_l}{\rho_v} - 1 \right)^{-1/3} \quad (4-24)$$

Eq. (4-23) becomes

$$Mi = \tan\theta^{-1/6} \quad (4-25)$$

Figure 4-20a shows the evolution of the new dimensionless number given by predicted and experimental data as a function of the contact angle. Most of the experimental points (75 %) follow the theoretical curve  $\tan\theta^{-1/6}$  with a maximum deviation of 10 %, confirming the evolution trend of the bubble departure diameter with the contact angle given by the present model. Compared to the correlation of Fritz [4.4], the present model gives a lower sensibility of the bubble departure diameter with the contact angle. Indeed, if the contact angle changes from 25° to 80°, this model predicts a change in the bubble departure diameter of 35 % whereas that of Fritz predicts a change of 320 %. The low sensibility given by this model may explain why there is a moderate scattering in measurement of the bubble departure diameter, even though the effect of the contact angle was ignored in many previous studies.

<sup>‡</sup> The contact angle of HFE-7100 was measured in our laboratory under the same conditions as [4.17].

Comparison to a larger set of experimental data measured at different superheats is shown in Figure 4-20b. It is noticeable that the experimental departure diameter increases with increasing heat flux. This effect is not taken into account in the present model and thus underestimation is obtained at high superheat. However, most of the experimental data (85 % of 32 points) is included within the lines of 30 % error, confirming the predictive ability of the present model.

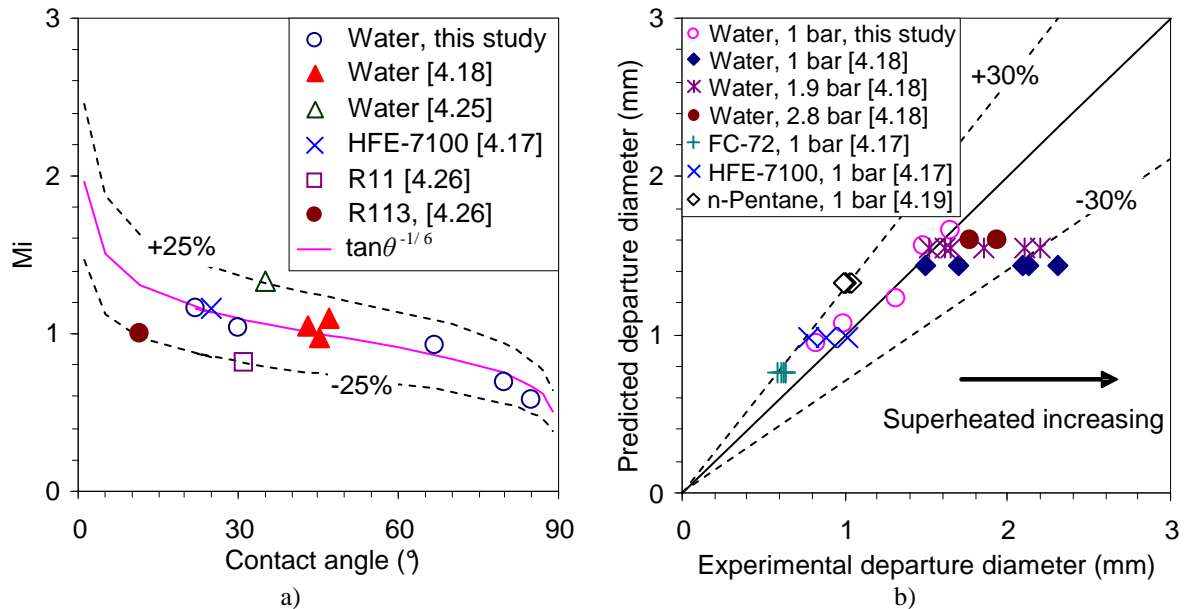


Figure 4-20. Comparison of the predicted and experimental values of a) dimensionless number defined by (4-24) and b) bubble departure diameter.

If the bubble departure diameter is known, both the present model and the correlation of Fritz can be used to predict the wetting of a fluid. Recently, McHale and Garimella [4.14] measured the diameter at departure of FC-77 bubbles formed at aluminium surfaces. Based on their data, prediction of the wetting of FC-77 is made as shown in Figure 4-21.

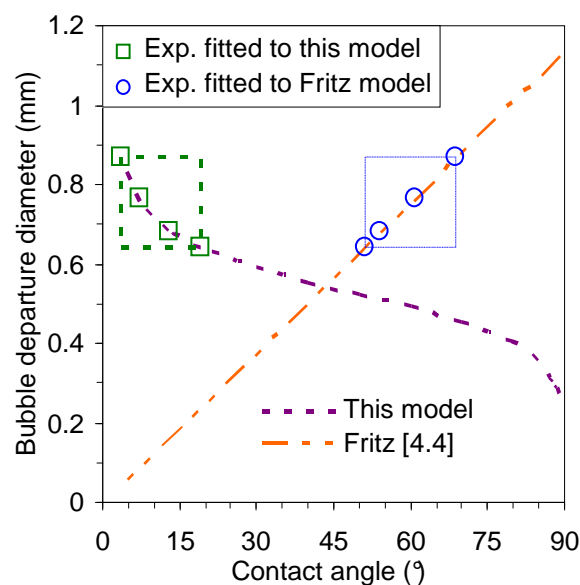


Figure 4-21. Prediction of the wetting of FC-77 on aluminium surfaces.

The present model predicts the wetting of FC-77 is high ( $\theta < 20^\circ$ ), which is relatively correct because FC-77 has low liquid surface tension (5.7 mN/m given by [4.14]). However, the correlation of Fritz gives a worse prediction since it predicts that FC-77 has a low wetting ( $\theta > 50^\circ$ ).

## 4.5 Model of heat transfer coefficient

### 4.5.1 Discussion about heat transfer on hydrophobic surfaces

In section 4.2.2, it was observed that the boiling heat transfer on hydrophobic surfaces differs from that on hydrophilic surfaces. Indeed, on hydrophobic surfaces, the heat transfer coefficient could not reach the steady-state regime and deteriorates after several minutes of boiling. The three-zone model [4.27] can be used to explain this observation. According to this model, a hydrophilic surface has three different modes of heat transfer in zone I, II and III (cf. Figure 4-22a). Zone I is the dry patch regime where no evaporation occurs. The heat transfer in this zone is relatively poor because of the poor conductivity of the vapour. Zone II is the conventional microlayer regime where very thin liquid layer evaporates to evacuate most of the heat coming from the wall. Zone III is an extended microlayer to bulk regime where the heat transfer is similar to that of single phase flow.

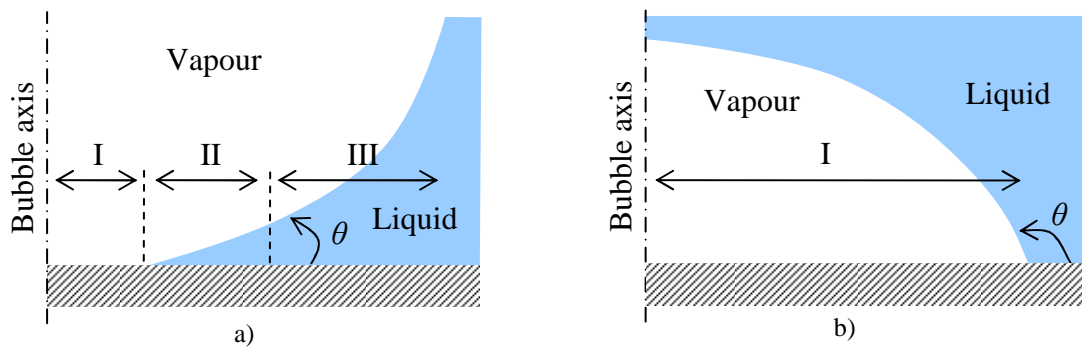


Figure 4-22. Heat transfer zones on: a) hydrophilic and b) hydrophobic surfaces.

For a hydrophobic surface, there is no liquid microlayer underneath the bubbles. The heat transfer occurs from superheat liquid layer [4.28] and through the dry patch zone (cf. Figure 4-22b) only. The heat transfer in the dry patch zone is poor, causing local deterioration of the sample surface. Furthermore, as bubbles do not detach from the wall, the steady-state regime of the heat transfer coefficient cannot be reached.

### 4.5.2 Correlation of nucleate boiling heat transfer

For hydrophilic surfaces, the experimental data showed that the heat transfer coefficient (HTC) can reach its maximum value if the contact angle is close to either  $0^\circ$  or  $90^\circ$ . This observation can be explained by analysing the opposite effects of contact angle on the bubble emission frequency and the liquid-microlayer thickness. Indeed, near  $90^\circ$  contact angle, enhancement of the HTC can be reached as a result of enhancement of the bubble emission frequency. However, near  $0^\circ$  contact angle, the bubble emission frequency is poor, but significant enhancement of the HTC can also be obtained, as a result of high heat transfer by conduction through the liquid microlayer.

Based on this reasoning, an analytical approach to estimate the HTC will be developed in the following paragraphs.

### Dependence of heat transfer coefficient on contact angle

According to the theoretical model presented in Section 4.4.2, the bubble departure diameter depends on the contact angle as:

$$D_d \propto \tan \theta^{-1/6} \quad (4-26)$$

In Section 4.2.2, Zuber [4.6] and the present experimental data shows that the product  $D_d f$  is about constant. This implies:

$$f \propto \tan \theta^{1/6} \quad (4-27)$$

The bubble emission frequency of water is in the order of 100 Hz. Since the HTC increases when the bubble emission frequency increases, from Eq. (4-27), the variation of HTC with  $f$  can be estimated as a function of the contact angle as:

$$h_f \propto \left( \tan \theta^{1/6} \right)^m \quad (4-28)$$

wherein  $m$  is a constant.

Combining Eqs. (4-15) and (4-17) in the model of bubble departure diameter, the liquid microlayer thickness at the departure of bubble can be determined as:

$$\delta = \sqrt{\frac{3}{2} \left( \frac{\rho_l}{\rho_v} \right)^{-1/2}} L_c \tan \theta^{1/2} \quad (4-29)$$

For water at 100°,  $\delta$  is in the order of 10-100  $\mu\text{m}$ . From Eq. (4-29), the heat transfer coefficient by conduction through the liquid microlayer is assumed to be dependent on the contact angle as:

$$h_\delta \propto \tan \theta^{-1/2} \quad (4-30)$$

Assuming that the contact angle impacts the heat transfer coefficient through its effects on  $f$  and  $\delta$ , from Eqs. (4-27) and (4-30), the dependence of the average heat transfer coefficient on the contact angle can be approximated as:

$$h \propto \Psi(\theta) = a \left[ \left( \tan \theta^{1/6} \right)^{m \times n} + b \left( \tan \theta^{-1/2} \right)^n \right]^{1/n} \quad (4-31)$$

wherein  $a$ ,  $b$ ,  $m$  and  $n$  are constants determined from experimental data.

### Correlation of heat transfer coefficient

The boiling heat transfer coefficient depends on fluid characteristics, boiling conditions, surface roughness and wettability. To take all of these factors into account, the following correlation is suggested:

$$h = h_o \times \Psi(\theta), (\theta < 90^\circ) \quad (4-32)$$

wherein  $h_o$  is independent of the contact angle. To determine  $h_o$ , some well-known correlations in literature can be used such as the Mostinski correlation [4.29], the Cooper correlation [4.9], the Gorenflo correlation [4.30] and the Ribatski-Siaz Jabardo correlation [4.31]. Comparisons between these correlations and the experimental data are shown in Figure 4-23. Information about the experimental database is given in Table 4-3. Indeed, data were selected from studies in which the contact angle and surface roughness are precisely reported.

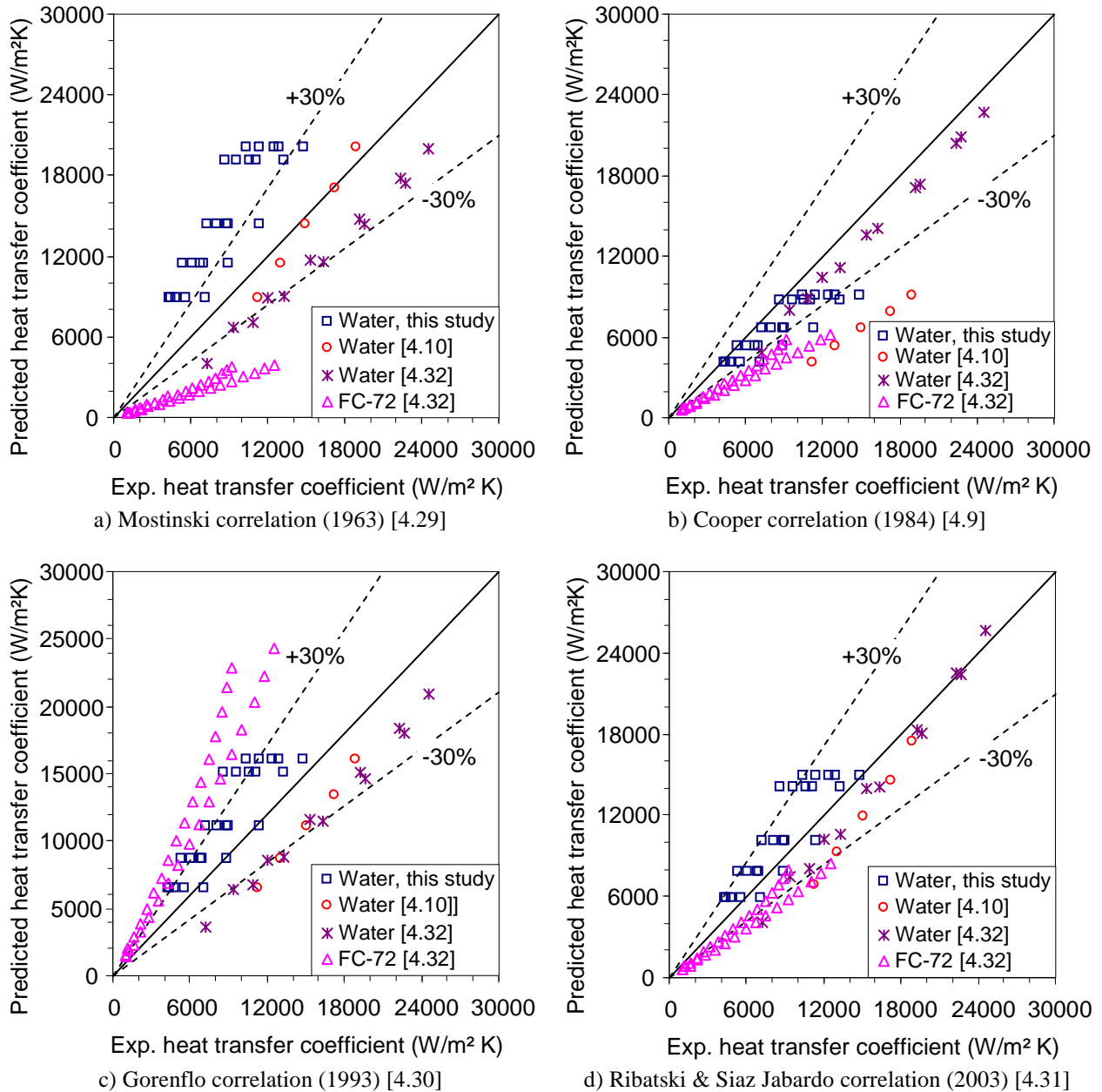


Figure 4-23. Comparison between the experimental data and some correlations in literature.

To evaluate the predictive ability of these correlations, the mean average error (MAE) and the mean relative error (MRE) are determined as:

$$\text{MAE} = \frac{1}{N} \sum_1^N \left| \frac{\text{Predicted value} - \text{exp. value}}{\text{exp. value}} \right| \times 100\% \quad (4-33)$$

$$\text{MRE} = \frac{1}{N} \sum_1^N \left( \frac{\text{Predicted value} - \text{exp. value}}{\text{exp. value}} \right) \times 100\% \quad (4-34)$$

Table 4-4 shows the results of the comparison between the experimental data and the different prediction methods.

Table 4-3. Experimental database of heat transfer coefficient.

Fluid	Number of data points	Contact angle (°)	Roughness (μm)
Water, this study	25	22, 31, 67, 80, 85	0.2
Water, Takata <i>et al.</i> [4.10]	5	1	0.2 <sup>§</sup>
Water, Wu <i>et al.</i> [4.32]	12	9, 57	1.55, 1.41
FC-72, Wu <i>et al.</i> [4.32]	34	2	1.55, 1.41

Table 4-4. Experimental database compared to the prediction methods.

Mostinski [4.29]		Cooper [4.9]		Gorenflo [4.30]		Ribatski & Siaz Jabardo [4.31]	
MAE	MRE	MAE	MRE	MAE	MRE	MAE	MRE
58	-11	33	-33	56	43	26	-11

The Cooper correlation [4.9] and the Ribatski-Siaz Jabardo correlation [4.31] show the best prediction abilities. Although the correlation of Cooper is less accurate, it is more general than the correlation of Ribatski and Siaz Jabardo which was developed based on pool boiling data of refrigerants only and contains empirical constants for wall material effects. Therefore,  $h_o$  would better to be determined by the correlation of Cooper, giving the following expression of the average heat transfer coefficient:

$$h = 55 p^{*(0.12-0.2 \log_{10} R_p)} (-\log_{10} p^*)^{-0.55} q^{0.67} M^{-0.5} \Psi(\theta) \quad (4-35)$$

wherein  $p^* = P/P_{cr}$  is the reduced pressure,  $R_p$  is the surface roughness,  $q$  the heat flux density and  $M$  the molecular weight of the fluid.

Fitting Eq. (4-35) to the present data gives the following expression of  $\Psi(\theta)$ :

$$\Psi(\theta) = \tan \theta^{1/6} + \frac{1}{4} \tan \theta^{-1/2} \quad (4-36)$$

The new correlation is compared to the experimental data as shown in Figure 4-24. The prediction lines fit relatively well the trend of the data obtained in this study and in the study of Takata *et al.* [4.10] (cf. Figure 4-24a). The predictive ability of the present correlation is also confirmed by comparison with the recent data for water and FC-72 of Wu *et al.* [4.32], in which the roughness and contact angle were measured (cf. Figure 4-24b). The present correlation predicts 95% of the entire database within  $\pm 15\%$ . The maximum deviation is

<sup>§</sup> The roughness of samples used by Takata *et al.* [4.10] is taken as the same as the present sample roughness since both studies have similar processes for sample fabrication.



about  $\pm 20\%$  and the MEA is about 9%. This correlation is thereby the best prediction method compared to the above presented correlations.

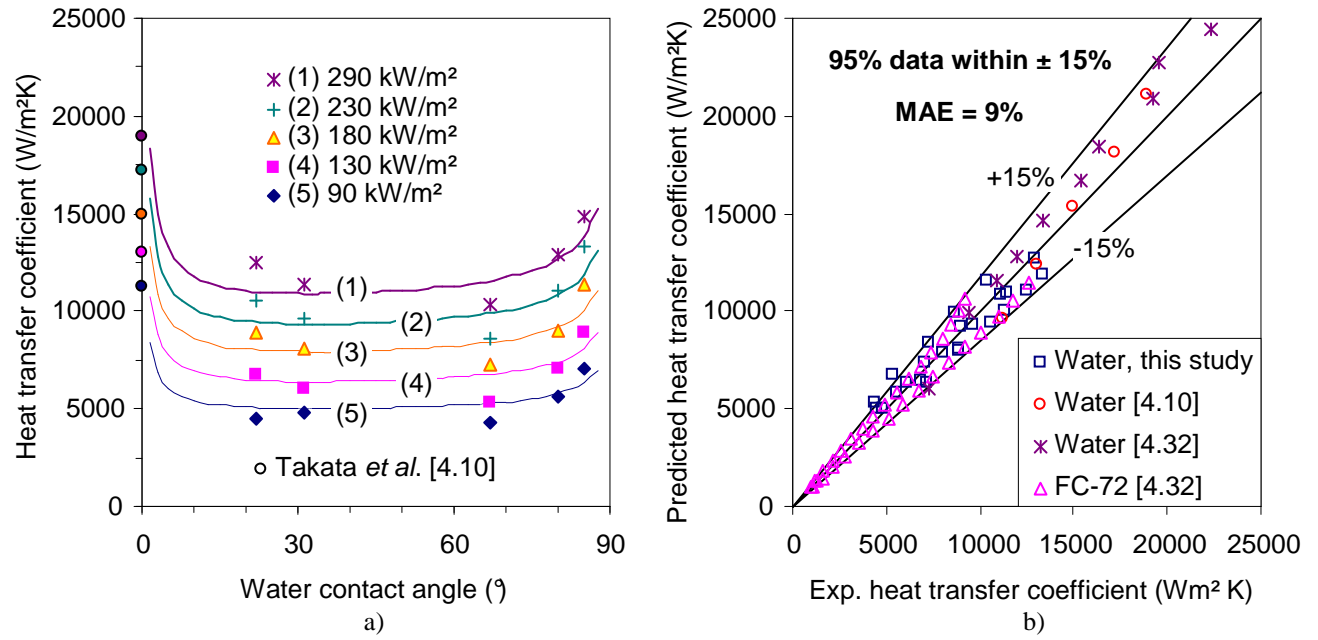


Figure 4-24. Comparison with experimental data: a) lines are prediction curves and points are experimental points and b) predicted HTC vs. experimental HTC.

## 4.6 Model of critical heat flux

### 4.6.1 Introduction

Two models of critical heat flux (CHF) that account for the effect of wettability on CHF are those of Theofanous and Dinh [4.33] and Kandlikar [4.34], both based on the assumption that CHF occurs as an irreversible expansion of a hot/dry spot. Theofanous and Dinh derived the following expression to predict CHF:

$$q_{CHF} = \kappa^{-1/2} \rho_v^{1/2} H_{lv} [\sigma(\rho_l - \rho_g)]^{1/4} \quad (4-37)$$

wherein  $\kappa$  is the surface dependent parameter, which is large for a poor wetting surface but small for highly wetted surface. However, Theofanous and Dinh did not provide an analytical expression for  $\kappa$ . Kim *et al.* [4.35] provided an expression for  $\kappa$  using elementary geometry and Lord Rayleigh's formula for the volume of static liquid meniscus:

$$\kappa = \left( 1 - \frac{\sin \theta}{2} - \frac{\pi/2 - \theta}{2 \cos \theta} \right)^{-1/2} \quad (4-38)$$

The above expression only applies for hydrophilic surfaces ( $\theta < 90^\circ$ ). Based on force balance, Kandlikar provides the following correlation:

$$q_{CHF} = \rho_v^{1/2} H_{lv} [\sigma(\rho_l - \rho_g)]^{1/4} \frac{1 + \cos \theta}{16} \left[ \frac{2}{\pi} + \frac{\pi}{4} (1 + \cos \theta) \cos \phi \right]^{1/2} \quad (4-39)$$

wherein  $\theta$  is the contact angle and  $\phi$  is the heater orientation angle relative to horizontal.

In this section, a theoretical model of critical heat flux will be developed based on the concept of macro- and micro-contact angles. This model aims at giving a new point of view to interpret the pool-boiling critical heat flux.

#### 4.6.2 Development of the model

As shown in Section 4.3.2, during a period of bubble growth, liquid movement occurs in the microlayer zone beneath the bubble. Assuming that this layer is similar to a cylinder made by the contact line of radius  $R_{cl}$  and the thickness  $\delta$  when bubble reaches its maximum size (cf. Figure 4-25), the time-average of liquid mass flux (cf. Figure 4-26) toward the bubble axis can be estimated as:

$$\dot{m}_l = f \rho_l \pi R_{cl}^2 \delta \quad (4-40)$$

wherein  $f$  is the bubble emission frequency,  $\rho_l$  is the liquid density;  $R_{cl}$  and  $\delta$  are respectively the radius of the contact line and the thickness of the microlayer at maximum bubble size.

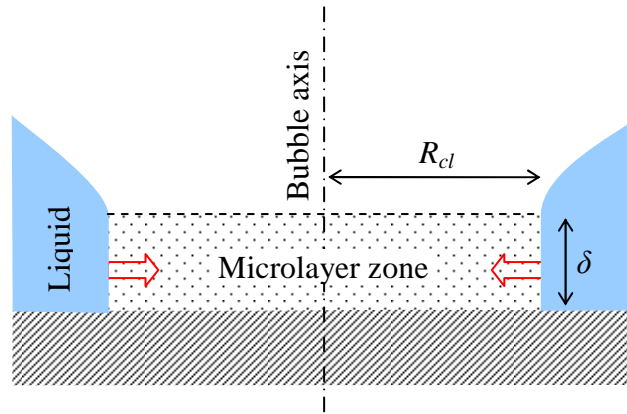


Figure 4-25. Schematic view of the microlayer zone at maximum bubble size.

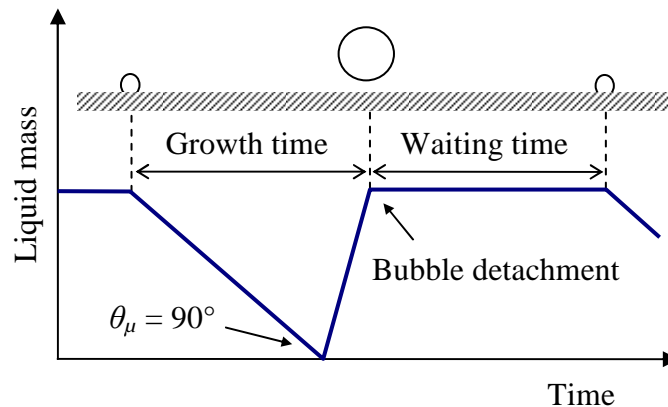


Figure 4-26. Schematic view of evolution of liquid mass in the microlayer zone.

The bubble emission frequency can be determined from the bubble departure diameter using the correlation of Zuber [4.6] as (cf. Section 4.2.2):

$$f = 0.59 \left[ \frac{\sigma g (\rho_l - \rho_v)}{\rho_l^2} \right]^{1/4} \times \frac{1}{D_b} \quad (4-41)$$

Using the model of bubble departure diameter,  $R_{cl}$ ,  $D_b$  and  $\delta$  can be determined by Eq.(4-17), (4-21) and (4-29), respectively. Thereby, Eq. (4-40) becomes:

$$\dot{m}_l = \frac{K_f \times K_a}{K_d} \tan \theta^{-1/3} \quad (4-42)$$

wherein  $K_f$ ,  $K_d$  and  $K_a$  are the constants depending on the fluid properties as:

$$K_f = 0.59 \left[ \frac{\sigma g (\rho_l - \rho_v)}{\rho_l^2} \right]^{1/4} \quad (4-43)$$

$$K_d = \left( 6 \sqrt{\frac{3}{2}} \right)^{1/3} \left( \frac{\rho_l}{\rho_v} \right)^{-1/2} \left( \frac{\rho_l}{\rho_v} - 1 \right)^{1/3} L_c \quad (4-44)$$

$$K_a = \pi \rho_l \left[ \sqrt{\frac{3}{2}} \left( \frac{\rho_l}{\rho_v} \right)^{-1/2} L_c \right]^3 \quad (4-45)$$

The inlet temperature of the liquid flow is assumed to equal to the bulk temperature. Hence, the energy balance implies the following expression of the heat flux:

$$q = \frac{1}{A_h} \dot{m}_l [C_{p,l}(T_s - T_\infty) + H_{lv} x] \quad (4-46)$$

wherein,  $A_h$  is the mean heat exchange area,  $C_{p,l}$  is the liquid specific-heat capacity,  $T_s$  and  $T_\infty$  are respectively the saturation temperature and the temperature of the bulk liquid,  $H_{lv}$  is the latent heat of vaporisation and  $x$  is the vapour quality.

The critical heat flux occurs when all liquid is vaporized, i.e.  $x = 1$ . This implies:

$$q_{CHF} = \frac{1}{A_h} \dot{m}_l [C_{p,l}(T_s - T_\infty) + H_{lv}] \quad (4-47)$$

Eqs. (4-42) and (4-47) imply:

$$q_{CHF} = q_{CHF,45^\circ} \times \tan \theta^{-1/3} \quad (4-48)$$

wherein  $q_{CHF,45^\circ}$  is the critical heat flux at  $\theta = 45^\circ$ , which is determined as:

$$q_{CHF,45^\circ} = \frac{1}{A_h} \frac{K_f \times K_a}{K_d} [C_{p,l}(T_s - T_\infty) + H_{lv}] \quad (4-49)$$

The mean heat exchange area has the following form:

$$A_h = \frac{\pi}{4} D_x^2 \quad (4-50)$$

wherein  $D_x$  corresponds to the mean diameter of heat exchange surface between the heated surface and the fluid. At a first approximation, it is taken as  $D_x = D_d / 2\sqrt{2}$ . For a contact angle of  $45^\circ$ , the model of bubble departure diameter gives:

$$D_x = \frac{K_d}{2\sqrt{2}} \quad (4-51)$$

Eqs. (4-49), (4-50) and (4-51) imply:

$$q_{CHF,45^\circ} = \frac{32}{\pi} \frac{K_f \times K_a}{K_d^3} [C_{p,l}(T_s - T_\infty) + H_{lv}] \quad (4-52)$$

This is an analytical equation to determine the CHF based on the concept of macro- and micro-contact angles, the present model of bubble departure diameter and the energy balance. The CHF predicted by the correlation of Kandlikar [4.34], the correlation of Kim *et al.* [4.35] and the present model are compared to the experimental CHF given by recent literature studies on water and nanofluids [4.35]-[4.38]. The present model shows the best agreement with the trend of CHF evolution as a function of contact angle with 80% of data included within  $\pm 30\%$  (cf. Figure 4-27).

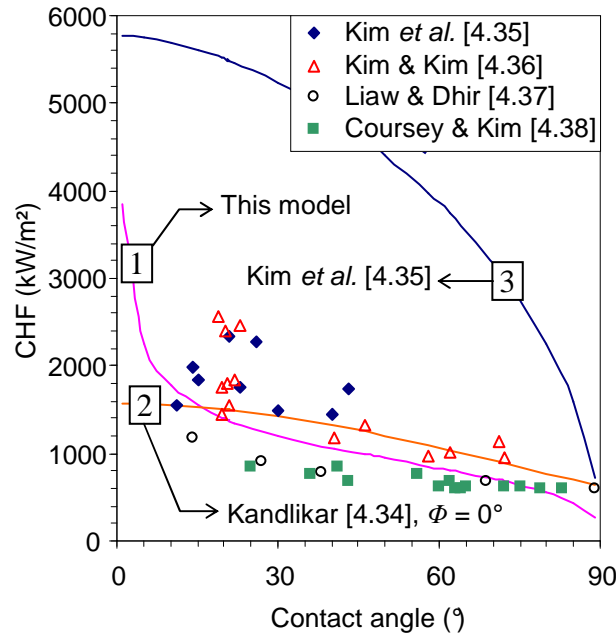


Figure 4-27. Evolution of the CHF with the contact angle for water and water-based nanofluids.

## 4.7 Conclusion

Subcooled pool boiling experiments were performed to investigate the effects of the surface wettability on nucleation mechanism and boiling heat transfer. Nano-surface coating was used to vary the static contact angle from 22 to 112°. The main results of this study are summarized as follows:

1. Hydrophobic surfaces
  - Bubbles appear on the heated surface at lower heat fluxes compared to the hydrophilic surfaces
  - Bubbles cannot detach from the wall and rapidly coalesce with bubbles formed at neighbouring sites
  - Local deterioration of the heated surface occurs at lower heat fluxes (100-200 kW/m<sup>2</sup>) compared to the hydrophilic surfaces
2. Hydrophilic surfaces
  - Decreasing the contact angle, the bubble departure diameter increases whereas the bubble emission frequency decreases
  - For low wetted surfaces ( $45^\circ < \theta < 90^\circ$ ), the heat transfer coefficient (HTC) deteriorates with decreasing contact angle.
  - However, for highly wetted surfaces ( $\theta \leq 45^\circ$ ), the inverse effect was observed: the HTC improves if the contact angle decreases. Thus, we believe that the best HTC can be obtained at a contact angle close to 0° or 90°
3. Dynamic contact angle approach to the nucleation mechanism was developed for a better understanding of the observed phenomenon. The contact angle hysteresis was shown to play an important role in the bubble growth. Afterwards, the concept of macro- and micro-contact angle was introduced to describe the bubble growth process.
4. Based on this concept, a theoretical model of bubble departure diameter was established using force and mass balances. This model next enabled development of new models of pool boiling heat transfer and critical heat flux.

Along the same line as the present work, experiments were performed to determine the effects of surface wettability on flow-boiling heat transfer in a microchannel. For this, an experimental setup and some processes for sample fabrication were developed as described in the next chapter.

## 4.8 References

- [4.1] R.F. Gaertner, Methods and means for increasing the heat transfer coefficient between a wall and boiling liquid, U.S. Patent 3,301,314 (1967).
- [4.2] R. L. Hummel, Means for increasing the heat transfer coefficient between a wall and boiling liquid, U.S. Patent 3,207,209 (1965).
- [4.3] N. Kolev, How accurately can we predict nucleate boiling, *Multiphase Flow Dynamics 2*, Springer, 2002.
- [4.4] W. Fritz, Maximum volume of vapour bubbles, *Physik Zeitschr* 36 (1935), 379-384.

- [4.5] R. Situ, M. Ishii, T. Hibiki, J.Y. Tu, G.H. Yeoh, M. Mori, Bubble departure frequency in forced convective subcooled boiling flow, *Int. J. Heat Mass Transfer* 51 (2008), 6268–6282.
- [4.6] N. Zuber, Nucleate boiling: The region of isolated bubbles and the similarity with natural convection, *Int. J. Heat and Mass Transfer* 6 (1963), 53-78.
- [4.7] A.P. Hatton, I.S. Hall, Photographic study of boiling on prepared surfaces, *Third Int. Heat Transfer Conference* 4 (1966), 24-37, Chicago, USA.
- [4.8] H.J. Ivey, Relationships between bubble frequency, departure diameter and rise velocity in nucleate boiling, *Int. J. Heat and Mass Transfer* 10 (1967), 1023-1040.
- [4.9] M.G. Cooper, Heat flows rates in saturated pool boiling – a wide ranging examination using reduced properties, *Advanced in Heat Transfer*, Academic Press (1984), 157-239, Florida, USA.
- [4.10] Y. Takata, S. Hidaka, J.M. Cao, T. Nakamura, H. Yamamoto, M. Masuda, T. Ito, Effect of surface wettability on boiling and evaporation, *Energy* 30 (2005), 209-220.
- [4.11] J. Mitrovic, Formation of a liquid jet after detachment of a vapour bubble, *Int. J. of Heat and Mass Transfer* 40 (1997), 4309-4317.
- [4.12] V.P. Carey, *Liquid-vapour phase-change phenomena*, Taylor and Francis (1992).
- [4.13] L.Z. Zeng, J.F. Klausner, R. Mei, A unified model for the prediction of bubble detachment diameters in boiling systems– I. Pool boiling, *Int. J. Heat and Mass Transfer* 36 (1993), 2261-2270.
- [4.14] J. P. McHale, S. V. Garimella, Bubble nucleation characteristics in pool boiling of a wetting liquid on smooth and rough surfaces, *Int. J. Multiphase Flow* 36 (2010), 249-260.
- [4.15] S.G. Bankoff, Ebullition from solid surfaces in the absence of a pre-existing gaseous phase, *Trans. Am. Soc. Mech. Eng.* 79 (1957), 735-740.
- [4.16] F. Demiray, J. Kim, Microscale heat transfer measurements during pool boiling of FC-72: effect of subcooling, *Int. J. Heat and Mass Transfer* 47 (2004), 3257-3268.
- [4.17] A. Cattide, G.P. Celata, P. Di Marco, W. Grassi, Experimental study on bubble detachment under variable heat load and the action of electric field, *Fluid Dynamics Research* 40 (2008), 485-496.
- [4.18] B. E. Staniszewski, Bubble growth and departure in nucleate boiling, *Tech. Rept. No. 16* (1959), MIT, Cambridge, Mass.
- [4.19] S. Siedel, S. Cioulachtjian, J. Bonjour, Experimental analysis of bubble growth, departure and interactions during pool boiling on artificial nucleation sites, *Exp. Thermal and Fluid Science* 32 (2008), 1504-1511.
- [4.20] C.W.M. Van Der Geld, Bubble detachment criteria: some criticism of ‘Das Abreissen von Dampfblasen an festen Heizflächen’, *Int. J. Heat Mass Transfer* 39 (1996), 653-657.
- [4.21] Y. Chen, M. Groll, Dynamics and shape of bubbles on heating surfaces: A simulation study, *Int. J. Heat and Mass Transfer* 49 (2006), 1115-1128.
- [4.22] P. S. Laplace, *Theory of capillary attraction*, Supplements to the 10th book of *Celestial Mechanics* (1806, 1807), translated and annotated by N. Bowditch (1839). Reprinted by Chelsea Pub. Co., New York, (1966).

- [4.23] M.G. Cooper, A.J.P. Lloyd, The microlayer in nucleate boiling, *Int. J. Heat and Mass Transfer* 12 (1969), 895-913.
- [4.24] F. Demiray, J. Kim, Microscale heat transfer measurements during pool boiling of FC-72: Effect of subcooling, *Int. J. Heat and Mass Transfer* 47 (2004), 3257-3268.
- [4.25] G. Hetsroni, A. Mosyak, E. Pogrebnyak, I. Sher, Z. Segal, Bubble growth in saturated pool boiling in water and surfactant solution, *Int. J. Multiphase Flow* 32 (2006), 159-182.
- [4.26] H.L. Lee, B.D. Oh, S.W. Bae, M.H. Kim, Single bubble growth in saturated pool boiling on a constant wall temperature surface, *Int. J. Multiphase Flow* 29 (2003), 1857-1874.
- [4.27] P.C. Wayner, Intermolecular forces in change of phase heat transfer: 1998 Donald Q. Kern award review, *AIChE J.* 45 (1999), 2055-2068.
- [4.28] F. Demiray, J. Kim, Microscale heat transfer measurements during pool boiling of FC-72: Effect of subcooling, *Int. J. Heat and Mass Transfer* 47 (2004), 3257-3268.
- [4.29] I.L. Mostinski, Application of the rule of corresponding states for the calculation of heat transfer and critical heat flux, *Teploenergetika* 4 (1963), 66-71.
- [4.30] D. Gorenflo, Pool boiling, *VDI Heat Atlas*, VDI Verlag, Düsseldorf (1993).
- [4.31] G. Ribatski, J.M. Saiz Jabardo, Experimental study of nucleate boiling of halocarbon refrigerants on cylindrical surfaces, *Int. J. Heat Mass Transfer* 46 (2003), 4439-4451.
- [4.32] W. Wu, H. Bostanci, L.C. Chow, Y. Hong, M. Sua, J.P. Kizito, Nucleate boiling heat transfer enhancement for water and FC-72 on titanium oxide and silicon oxide surfaces, *Int. Journal of Heat and Mass Transfer* 53 (2010), 1773-1777.
- [4.33] T. G. Theofanous, T. N. Dinh, High Heat Flux Boiling and Burnout as Microphysical Phenomena: Mounting Evidence and Opportunities, *Multiphase Science and Technology* 18 (2006), 1-26.
- [4.34] S. G. Kandlikar, A Theoretical Model to Predict Pool Boiling CHF Incorporating Effects of Contact Angle and Orientation, *J. Heat Transfer* 123 (2001), 1071-1079.
- [4.35] S.J. Kim, I.C. Bang, J. Buongiorno, L.W. Hu, Surface wettability change during pool boiling of nanofluids and its effect on critical heat flux, *Int. J. Heat and Mass transfer* 50 (2007), 4105-4116.
- [4.36] H. D. Kim, M. H. Kim, Effect of nanoparticle deposition on capillary wicking that influences the critical heat flux in nanofluids, *Applied Physics Letters* 91 (2007), 014104.
- [4.37] S.P. Liaw, V.P. Dhir, Void fraction measurements during saturated pool boiling of water on partially wetted vertical surfaces, *J. Heat Transfer* 111 (1989), 731-738.
- [4.38] J. S. Coursey, J.H. Kim, Nanofluid boiling: The effect of surface wettability, *Int. J. Heat and Fluid Flow* 29 (2008), 1577-1585.

## PART 3 - FLOW BOILING EXPERIMENTS

In the foregoing part, nanofluid boiling has been introduced as a technique of surface coating beside the well-known chemical vapour deposition techniques. Sample-surfaces coated by such techniques show different wetting properties, for instance, their static contact angles with water vary from  $22^\circ$  to  $112^\circ$ . These surfaces were used as heater elements in pool boiling experiments of water at atmospheric pressure. In the regime of nucleate boiling, it was shown that the surface wettability impacts the bubble growth and the heat transfer significantly. A change in the contact angle causes modification of some other parameters such as bubble departure diameter, bubble emission frequency and heat transfer coefficient.

Along the same line as the foregoing work, experiments were performed to determine the effects of micro- and nano-surface coating on flow boiling of water at atmospheric pressure. The test channel was a rectangular channel 0.5 mm high, 5 mm wide and 180 mm long. Its dimensions were precisely determined in order to reduce measurement uncertainties. Therefore, the test hydraulic diameter is equal to 0.96 mm and the confinement number is equal to 2.6. The test channel is considered as microchannel according to Kew and Cornwell theory [1.19], but as minichannel according to Kandlikar and Grande [1.17] classification. The mass flux was set at 100 and 120 kg/m<sup>2</sup> s and the base heat flux was varied from 30 to 80 kW/m<sup>2</sup>. Water entered the test channel under subcooled conditions (90 °C). More details of experimental setup and procedures will be introduced in Chapter 5. The obtained results will be presented and discussed in Chapter 6.





## Chapter 5: Experimental setup, procedure and validation

The working fluid is water, as it enables significant change in contact angle by surface treatments. This is also a stable fluid with accurately known properties. However, the range of experimental vapour quality will be limited when water is used since its latent heat is relatively high. Another issue could be the heat loss due to a significant difference between the saturation temperature of water (at atmospheric pressure) and the ambient temperature.

In order to accurately control the surface parameters, a reliable and repeatable method of sample surface fabrication was developed based on physical and chemical techniques of surface treatments through a mask assembly. Using this technique, smooth surfaces having different wettability were produced. Some of them were used to determine the impact of contact angle on water flow boiling. The others were structured by laser etching for tests on the surface treatment impact at the microscale level.

The test section was designed for the purpose of simplifying sample implementation and visualizing flow patterns. Hence, the test channel is fabricated by putting a glass lid including a groove in the desired size over a Pyrex wafer containing the sample surface. Afterwards, these two elements are bonded by vacuum aspiration. To prevent fluid leakage, their contact area should be smooth and plane. More details about the experimental setup will be described in the following sections.

### 5.1 Sample surface fabrication

#### 5.1.1 Fabrication processes

##### Smooth surfaces

Smooth sample surface were fabricated for determination of the surface wettability effects. It is necessary that all the sample surfaces have the same geometry with only change in contact angle. In other words, they should have the same dimensions (length, width and thickness) and the same topography at microscale. The sample surfaces are thereby produced by deposition of nanoparticles through patterning masks using techniques of physical and chemical vapour depositions (cf. Section 2.1) according to the following steps (cf. Figure 4-23).

- *Step 1: deposition of titanium (Ti) layer.*

The base substrate is a Pyrex wafer of 200 mm diameter and 1.1 mm thickness. This layer is used as a heating element. It consists of a rectangular track corresponding to the testing area and pads for electrical connections.

- *Step 2: deposition of diamond-like carbon (DLC) layer.*

This layer is used for electrical insulation.

- *Step 3: deposition of nanoparticle layer.*

This layer enables modification of the surface wettability in a larger threshold. The deposition layers are hydrophilic PDMS (SiOx) and hydrophobic PDMS (SiOC), respectively.

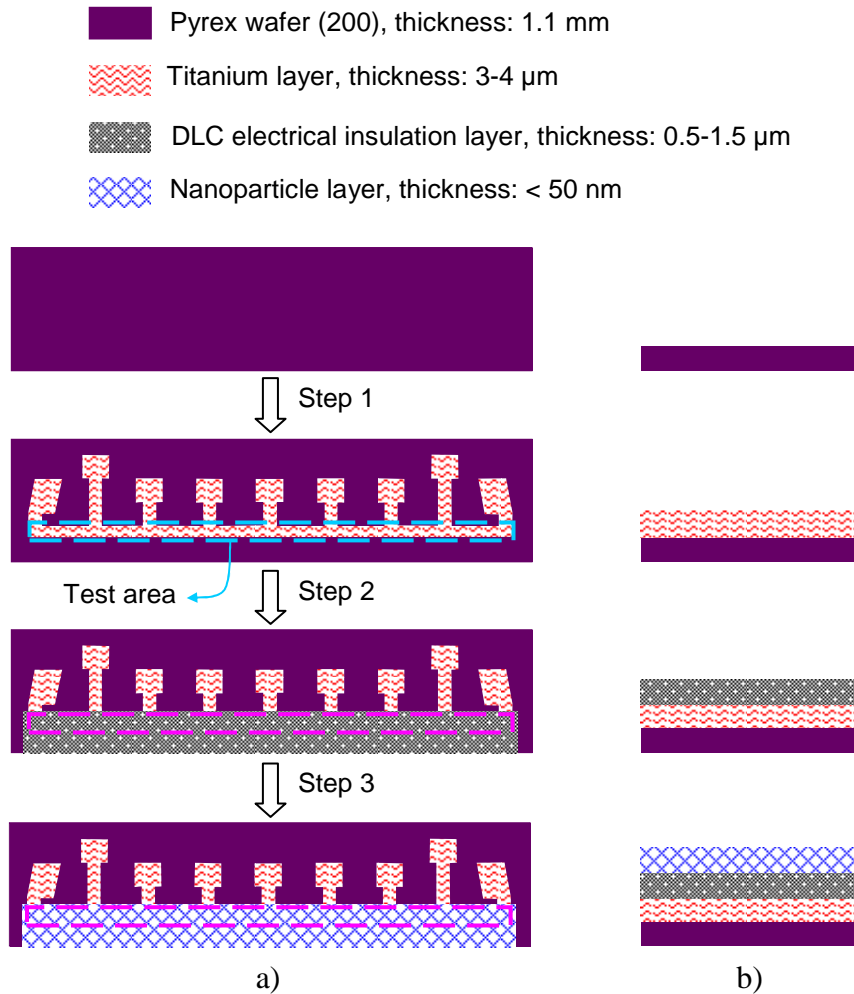


Figure 5-1. Fabrication procedure of smooth surfaces: a) top view and b) perspective view.

Applying the above method, four smooth sample surfaces were fabricated and characterized such as:

- Titanium (Ti) surface made by step 1,
- Diamond-like carbon (DLC) surface made by step 1 and 2,
- Hydrophilic PDMS (SiOx) surface and hydrophobic PDMS (SiOC) surface made by step 1, 2 and 3.

### Structured surfaces

In order to determine the effects of micro-surface treatment, two sample surfaces were fabricated following the steps shown in Figure 5-2. The first sample is called “ $\mu$ -Ti”. To produce this surface, a titanium layer was firstly deposited by step 1, described previously. Afterwards, micro-holes were made by laser etching through a patterning mask which contains holes with radius of 20  $\mu\text{m}$ . As shown in Figure 5-3, according to the theory of critical radius (cf. Section 1.1.1), the holes having this size are able to generate water bubbles at a wall superheat lower than 2°C.

The second sample is called “ $\mu$ -SiOx”, which is a structured surface of hydrophilic PDMS (SiOx). At first, depositions of titanium and diamond-like carbon (DLC) were made according to steps 1 and 2 in the above section. Then, the micro-holes were created by laser etching of

the DLC layer through the same patterning mask used for the “ $\mu$ -Ti” surface. Finally, a deposition of SiOx layer is made on the surface of interest according to step 3.

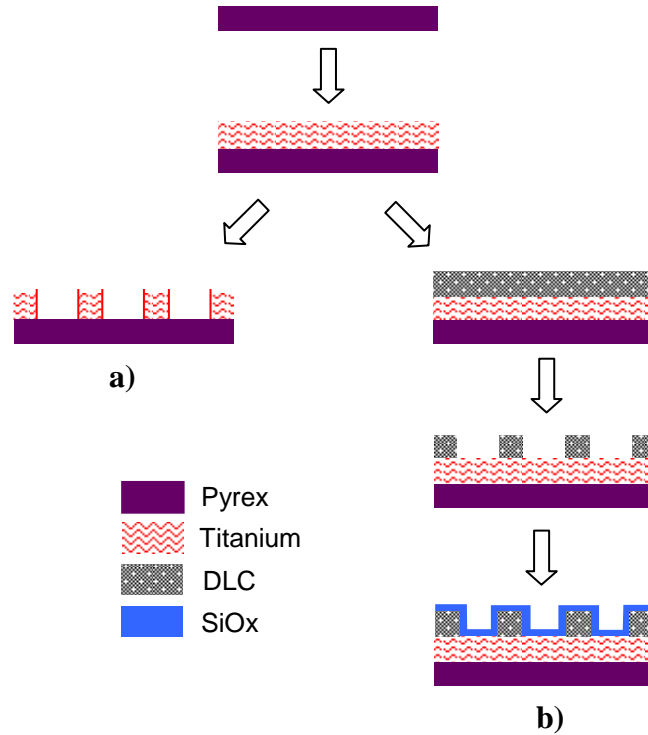


Figure 5-2. Side view of fabrication procedure of structured surfaces: a)  $\mu$ -Ti surface and b)  $\mu$ -SiOx surface.

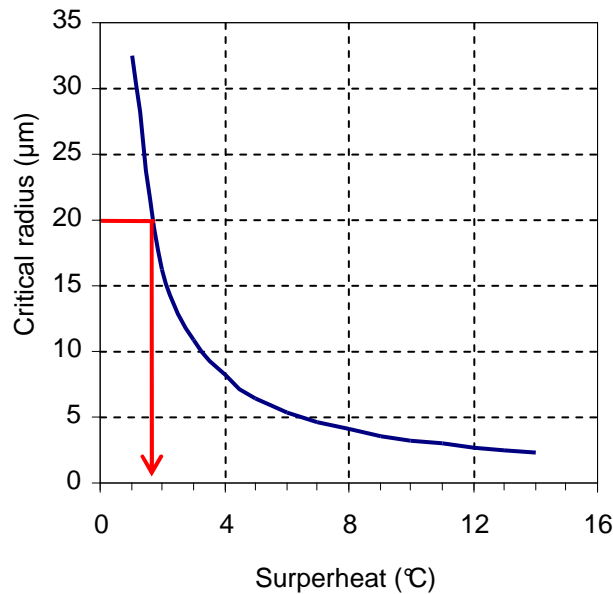


Figure 5-3. Active cavity size range for saturated boiling of water at atmospheric pressure.

### 5.1.2 Electrical connexions

The testing area is 5 mm wide and 180 mm long. It is divided into eight sections called “ $S_1$ ”, “ $S_2$ ”... and “ $S_8$ ”, respectively, as shown in Figure 5-4. Dimensions of these sections are shown in Table 5-1. The testing area is heated by Joule effect from the metallic layer. Electrical wires are fixed on the electrical pads by mechanical support. Current and voltages

of different sections are measured by Agilent 34970A and a 0.01- $\Omega$  shunt, which has an accurately known resistance for determination of current by measurement of voltage.

Figure 5-5 shows image of a typical wafer, on which two sample surfaces are produced. These surfaces are identical but only one of them will be used for boiling test (surface *a*) and the other one is saved as a backup copy (surface *b*). Furthermore, close to the wafer edge, samples for surface characterisations are also deposited (surfaces *c* and *d*). They will be used to determine the surface topography by field-emission gun scanning electron microscopic (FEG-SEM) as well as to measure the surface wettability.

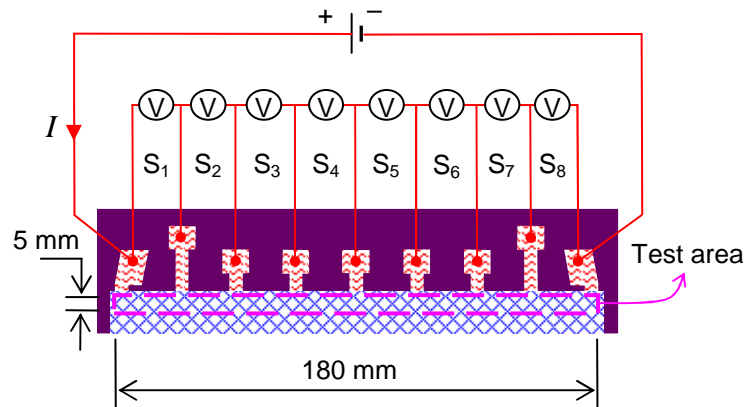


Figure 5-4. Schematic view of electrical connexions.

Table 5-1. Dimensions of the testing area sections.

Name	S <sub>1</sub>	S <sub>2</sub>	S <sub>3</sub>	S <sub>4</sub>	S <sub>5</sub>	S <sub>6</sub>	S <sub>7</sub>	S <sub>8</sub>
Width (mm)	5	5	5	5	5	5	5	5
Length (mm)	25	20	22.5	22.5	22.5	22.5	20	25

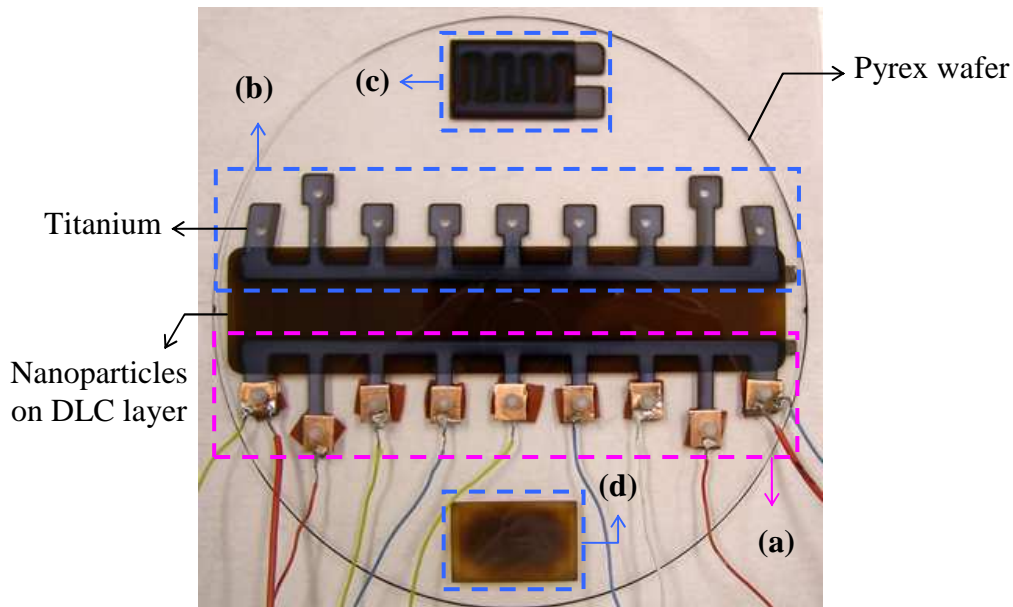


Figure 5-5. Image of a typical wafer: a) test surface with electrical connexions, b) backup surface and c) and d) samples for surface characterisations.

### 5.1.3 FEG-SEM images

#### Smooth surfaces

In order to estimate the thicknesses of the deposition layers, images of the sample surfaces are taken using a field-emission gun scanning electron microscopic (FEG-SEM). For instance, FEG-SEM images of SiOC surface are shown in Figure 5-6. Pixel analyses give the thicknesses of titanium (Ti) and diamond-like carbon (DLC) layers of about  $3.5\ \mu\text{m}$  and  $1\ \mu\text{m}$ , respectively. These values are close to those determined by DEKTAK<sup>3</sup>- surface profile measuring system, which gives  $3.2\text{-}\mu\text{m}$  thickness for Ti layer and  $0.8\text{-}\mu\text{m}$  thickness for DLC layer.

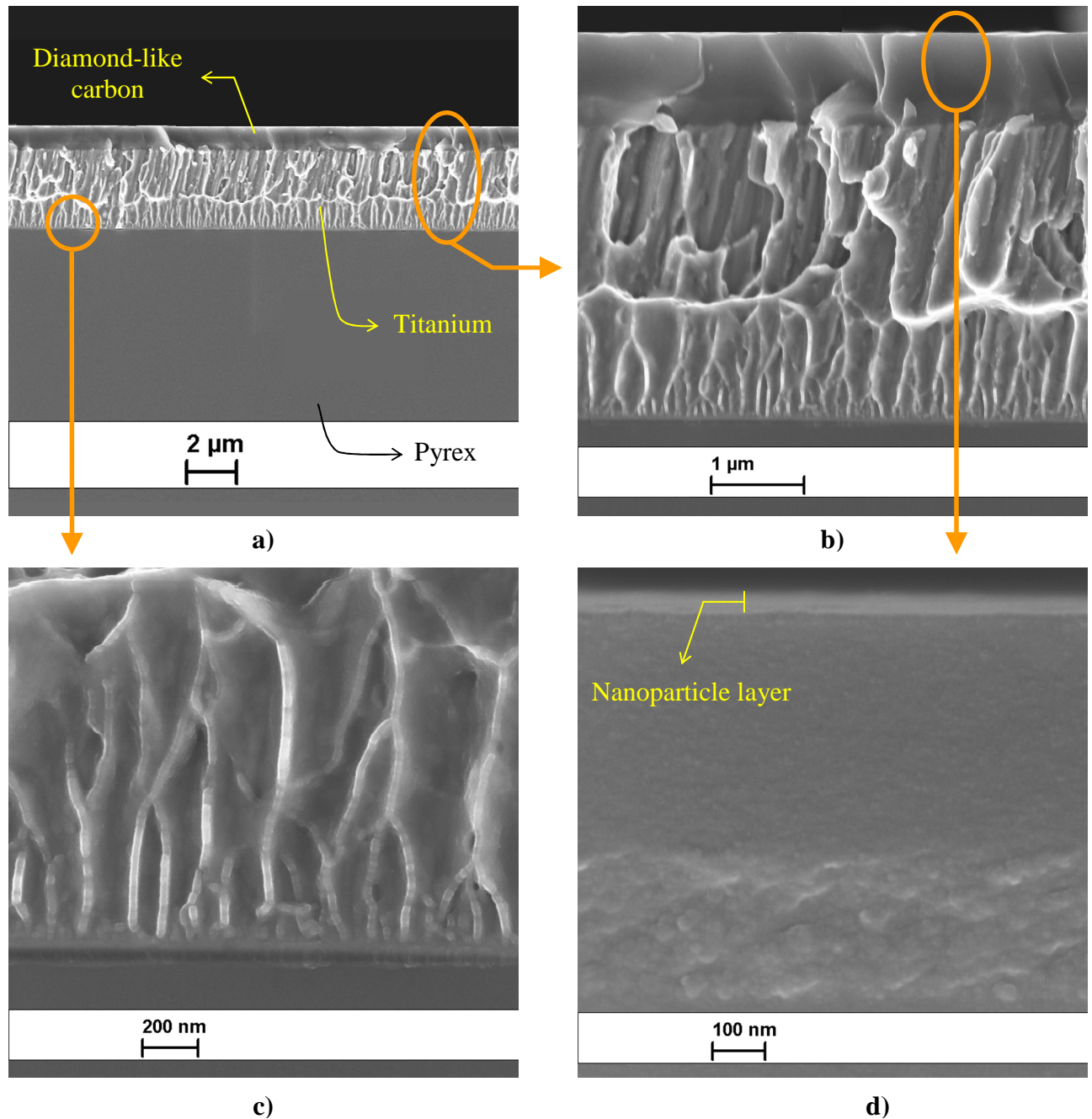


Figure 5-6. FEG-SEM images of SiOC surface in the perspective view: a) and b) deposition layers on Pyrex wafer, c) nanoparticle layer and d) interface between titanium layer and Pyrex wafer.



### Structured surfaces

For structured surfaces, FEG-SEM images were also taken in order to characterize the micro-holes. As shown in Figure 5-7a, the “ $\mu$ -Ti” surface contains holes of about  $35\ \mu\text{m}$  diameter, in a distance of about  $60\ \mu\text{m}$  between each other. Sloping view of a typical micro-hole is shown in Figure 5-7b and Figure 5-7c. These holes have a depth of about  $3.5\ \mu\text{m}$ , which corresponds to the thickness of the titanium layer.

Shown in Figure 5-8 are FEG-SEM images of the “ $\mu$ -SiOx” surface. The holes on this surface have diameters of about  $40\ \mu\text{m}$ . The distance between two consecutive holes centres is also near by  $60\ \mu\text{m}$ . The side view in Figure 5-8b exhibits that the etching depth of this surface is close to the thickness of the DLC layer ( $0.8\ \mu\text{m}$ ).

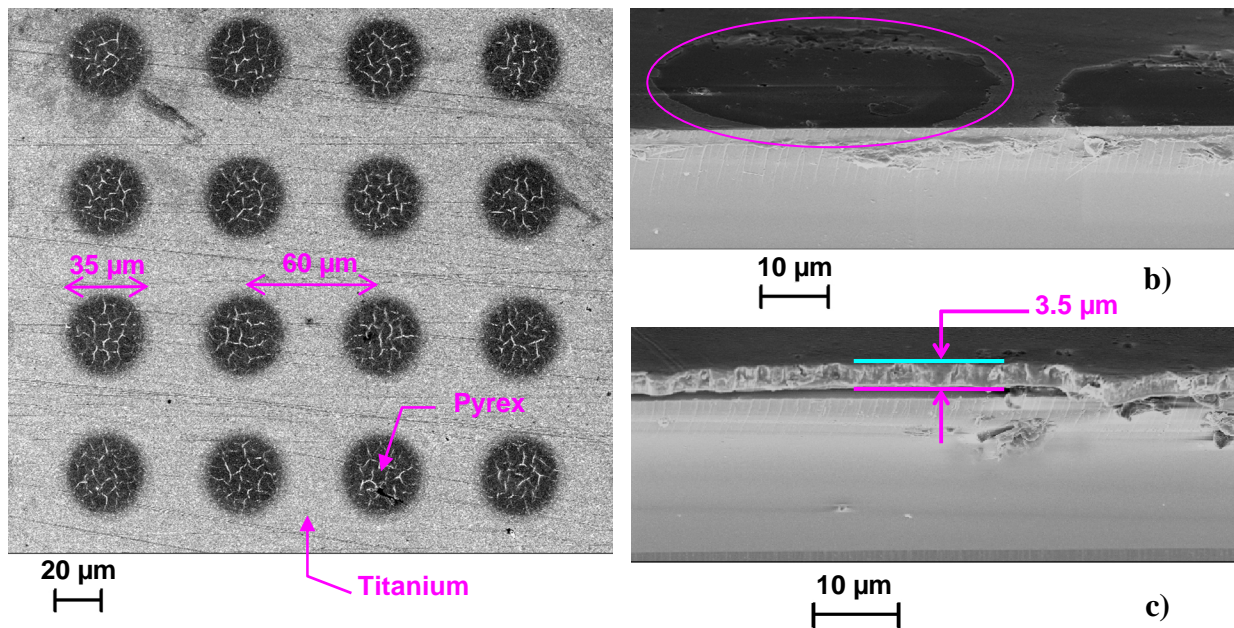


Figure 5-7. FEG-SEM images of the  $\mu$ -Ti surface: a) top view, b) sloping view and c) side view.

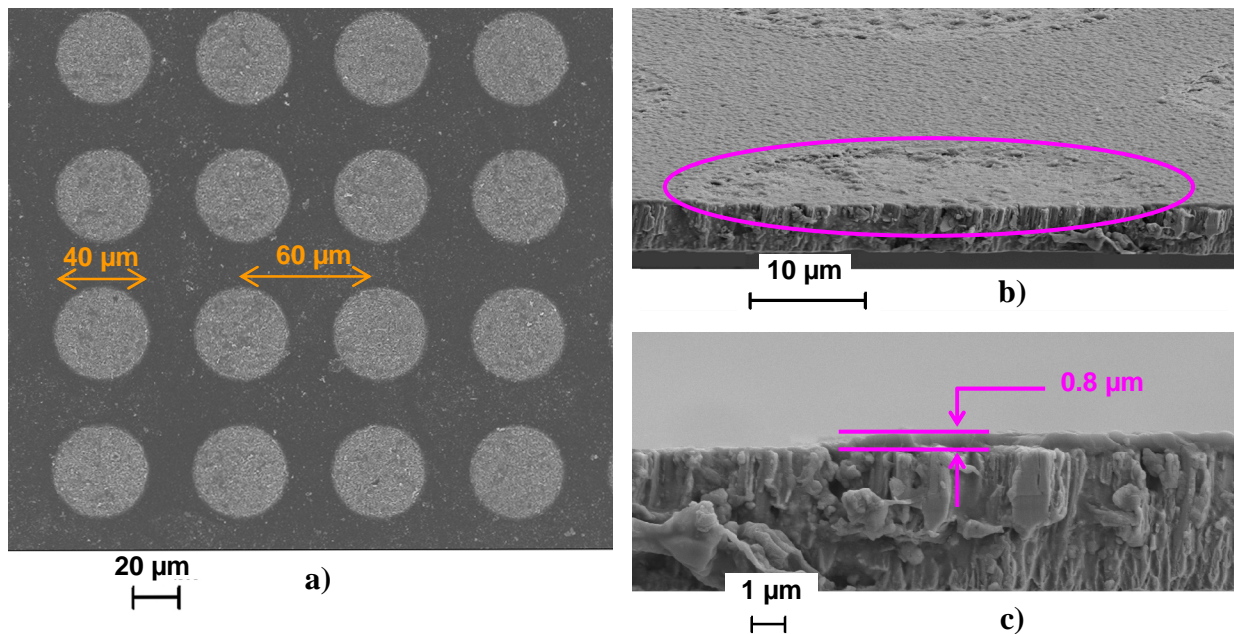


Figure 5-8. FEG-SEM images of the  $\mu$ -SiOx surface: a) top view, b) sloping view and c) side view.

In summary, the structured sample surfaces contain numbers of spherical micro-holes having the dimensions which are schematically presented in Figure 5-9.

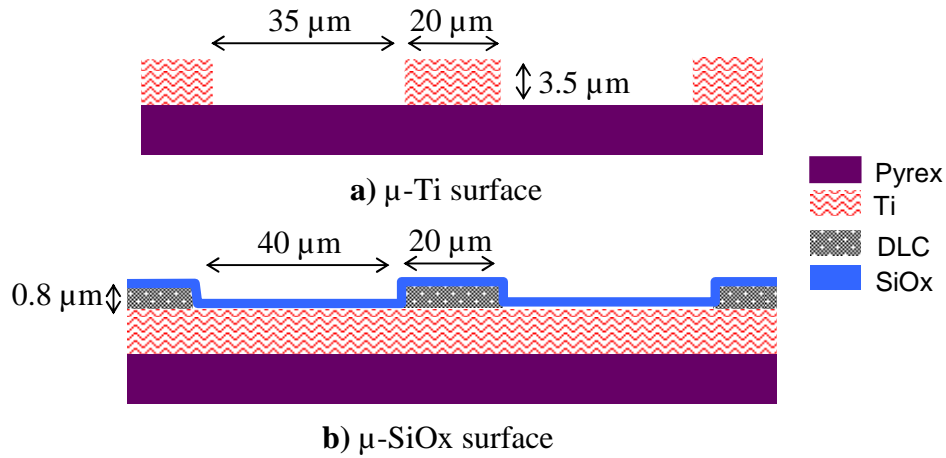


Figure 5-9. Schematic view of topographies of the structured sample surfaces.

#### 5.1.4 R/T curves of titanium surface

Once a sample surface is produced, stabilization of its deposition layers is made by annealing in a vacuum chamber at 300 °C for 3 hours. Afterwards, it is put inside a thermostat where the temperature is measured by a platinum probe of 0.1 °C accuracy. At steady state, the temperature of the sample surface could be determined from the temperature of the thermostat. For temperature between 20 °C and 90 °C, the electrical resistances of different sections of the sample surface are determined. In this way, the local wall temperature at each section of the sample surface can be deduced from measurements of the electric resistance by using the Resistance/Temperature (R/T) curve. For instance, Figure 5-10 shows the R/T curves at different sections of the titanium surface defined in Figure 5-4. These curves can be accurately correlated by linear regressions with coefficients of determination greater than 0.999.

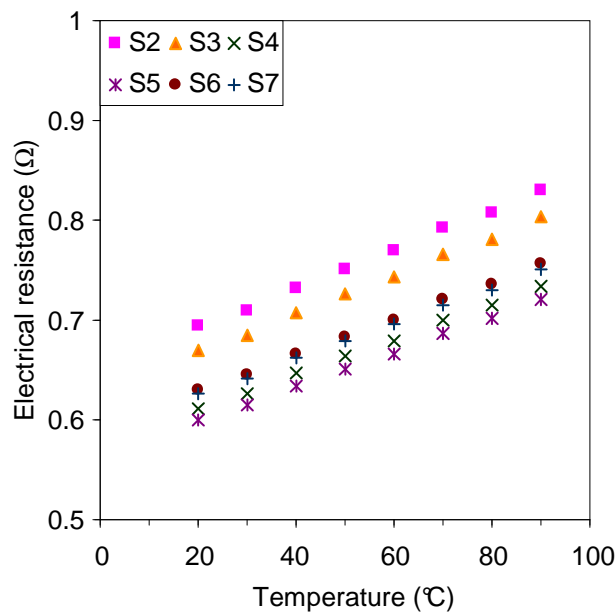


Figure 5-10. Electrical resistance evolution with temperature at different sections of the titanium layer.



## 5.2 Test section

### 5.2.1 Test section setup

The channel is defined by putting a glass lid over the sample surface. This lid has two rectangular grooves 180 mm long, 5 mm wide and about 0.5 mm deep. The depth of each groove is the average depth measured by ZEISS SPECTRUM scanning at twenty different points along the groove. Relative uncertainty in groove depth is less than 2% (cf. Table 5-2).

The glass lid is bonded to the Pyrex wafer by vacuum aspiration as shown in Figure 5-11a, giving two sample channels. However, only one channel will be used for boiling test and the other one is saved as a backup copy (cf. Figure 5-11b). To prevent fluid leakage, silicone compound is placed around the external contact between the glass cap and the Pyrex wafer. The channel is thermally insulated with foam. Visualisation of the fluid flow can be made from the top of the glass lid.

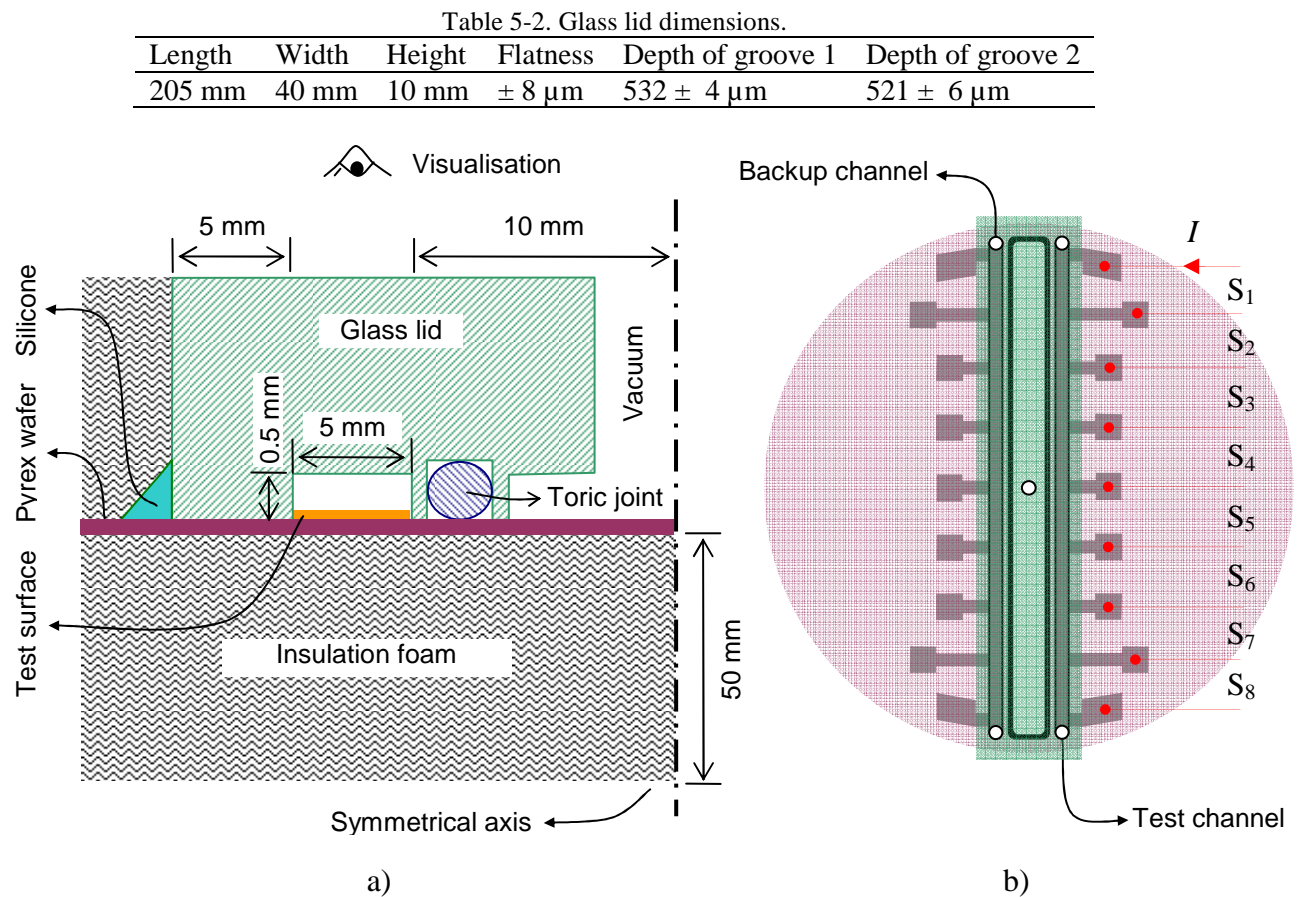


Figure 5-11. Assembly of the test section: a) cross-section view and b) top view without silicone compound and insulation foam.

### 5.2.2 End effects

As discussed before, the testing surface is divided into eight distinct sections called “S<sub>1</sub>”, “S<sub>2</sub>”...and “S<sub>8</sub>” where S<sub>1</sub> and S<sub>8</sub> refer to sections at the inlet and outlet of current, respectively. According to the electrical diagram shown in Figure 5-4, because of the end effects, the measured electrical resistances for these two sections are greater than the corresponding resistances in the testing area. Hence, the local temperatures giving by the R/T

curves for sections  $S_1$  and  $S_8$  will not be used to determine the corresponding temperatures of the wall in contact with the working fluid.

As a consequence, for sections  $S_1$  and  $S_8$ , the local heat transfer coefficients are not determined. Only the local vapour qualities are calculated from measurements of the local heat fluxes, since the electrical heat loss is negligible as shown in section 5.4.

## 5.3 Experimental apparatus and procedure

### 5.3.1 Experimental apparatus

The experimental setup is shown in Figure 5-12. It consists of a test section, a condenser with a cooling bath, a liquid pump (ISMATEC MCP\_Z), a mass flowmeter (Micro Motion Elite MVD) and a pre-heater. A reservoir is used to store the fluid and to control the working pressure at atmospheric pressure.

The experimental facility is instrumented with an absolute pressure transducer (1 bar) to measure the pressure at the inlet of the test section, and a differential pressure transducer (100 mbar) to measure the pressure drop across the test section. The absolute pressures at the outlet of the condenser and at the inlet of the pre-heater are also measured. K-type thermocouples are inserted at different locations to measure the bulk fluid temperature.

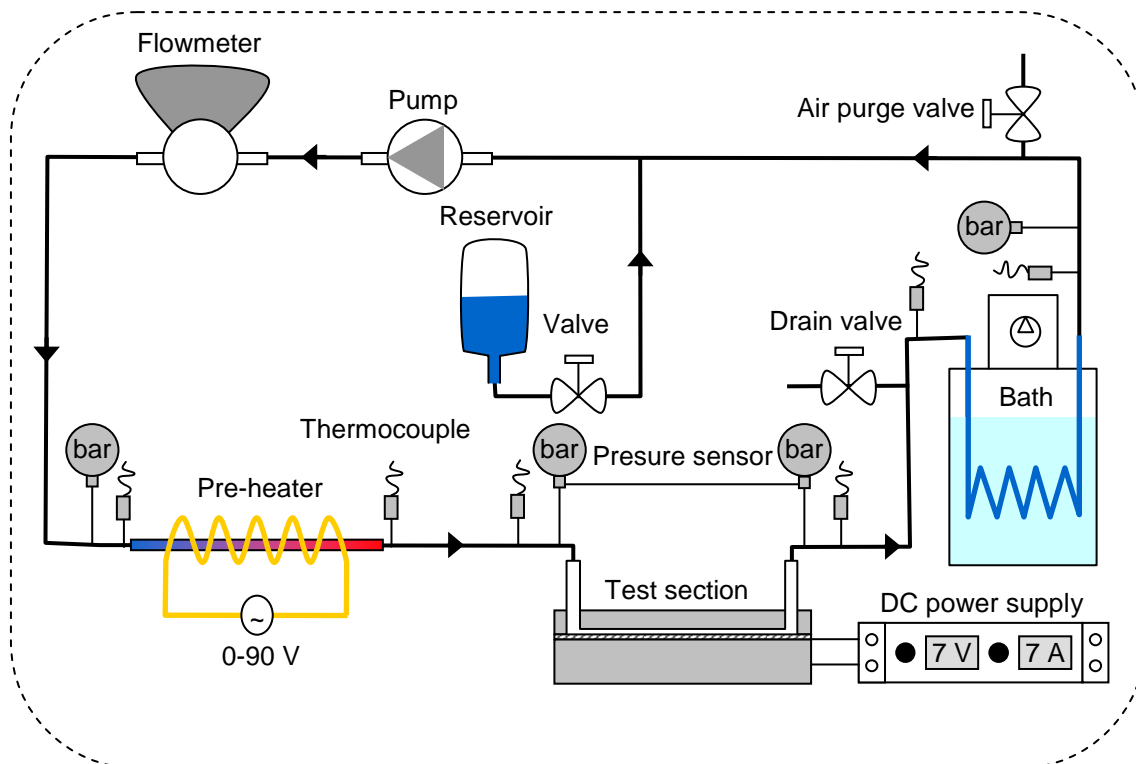


Figure 5-12. Schematic view of the experimental apparatus.

### 5.3.2 Experimental procedure

Before each test point, degassing of water is made by boiling at saturated temperature (100 °C) for two hours. Then, the desired flow rate is established and the electrical power is raised in steps lasting a few minutes each until a new steady state is achieved. The flow rate, current,

voltages, pressures, and bulk temperatures are monitored and recorded at each power step with a data logger (Agilent 34970A) connected to a computer. The mass flux was set at 100 kg/m<sup>2</sup> s and 120 kg/m<sup>2</sup> s, respectively and the base heat flux was varied from 30 to 80 kW/m<sup>2</sup>. Flow visualisation was made by a high speed camera set at 500 or 1000 fps.

## 5.4 Single-phase flow validation tests

Validation tests are made using titanium surface. To validate the test facility and the test section instrumentation, the first step was to perform energy balance tests with highly-subcooled water flow. Afterwards, measurements of pressure loss and heat transfer in single-phase liquid flow were performed to validate the measurement techniques and the data reduction procedure.

### 5.4.1 Heat loss

Due to air convection and radiation around the test section, the working fluid loses a part of its energy  $Q_{loss}^o$  when flowing along the test channel even though no electrical power is generated:

$$Q_{loss}^o = \dot{m} C_p \left[ T_{f,in} - T_{f,out}^o \right] \quad (5-1)$$

wherein  $\dot{m}$  is the mass flow,  $C_p$  is the liquid specific heat,  $T_{f,in}$  is the fluid inlet temperature and  $T_{f,out}^o$  is the fluid outlet temperature when the fluid is not heated by electrical power from the sample surface ( $T_{f,out}^o \leq T_{f,in}$ ).

Now, if an electrical power  $Q_e$  is generated from the sample surface, a part of it  $Q_{e,f}$  goes toward the working fluid and the other part  $Q_{d,loss}$  is dissipated by conduction through the Pyrex wafer as shown in Figure 5-13:

$$Q_e = Q_{e,f} + Q_{d,loss} \quad (5-2)$$

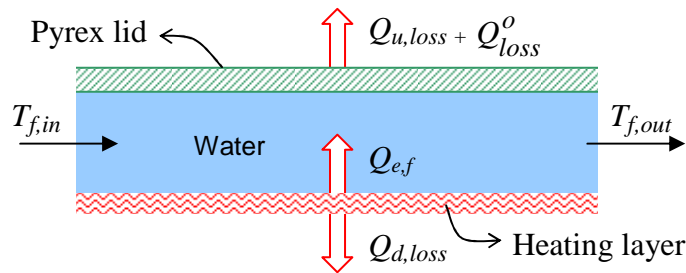


Figure 5-13. Schematic view of distribution of heat flux generated by Joule effect from the titanium layer.

For the heat flux received by the fluid  $Q_{e,f}$ , a part contributes to recoup the initial heat loss  $Q_{loss}^o$ , another part contributes to heat the fluid up and the other  $Q_{u,loss}$  is dissipated to the ambient:

$$Q_{e,f} = Q_{loss}^o + \dot{m} C_p (T_{f,out} - T_{f,in}) + Q_{u,loss} \quad (5-3)$$

Eqs. (5-1), (5-2) and (5-3) give the following relation of energy balance in single-phase flow:

$$Q_e = \dot{m} C_p \left[ T_{f,out} - T_{f,out}^o \right] + \dot{m} C_p (T_{f,out} - T_{f,in}) + (Q_{d,loss} + Q_{u,loss}) \quad (5-4)$$

The overall heat loss due to generation of electrical power is defined as:

$$Q_{loss} = Q_{d,loss} + Q_{u,loss} \quad (5-5)$$

Eqs. (5-4) and (5-5) imply:

$$Q_{loss} = Q_e - \dot{m} C_p \left[ T_{f,out} - T_{f,out}^o \right] + \dot{m} C_p (T_{f,out} - T_{f,in}) \quad (5-6)$$

Shown in Table 5-3 is a summary of the heat fluxes participated to the energy balance.

Table 5-3. Heat fluxes balance.

Symbol	Description
$Q_{loss}^o$	Heat loss before generation of electrical power due to air convection and radiation
$Q_e$	Electrical power
$Q_{d,loss}$	Electrical power loss by conduction through the Pyrex wafer
$Q_{e,f}$	Electrical power towards the working fluid
$Q_{u,loss}$	Part of $Q_{e,f}$ dissipated to the ambient
$Q_{loss}$	Overall heat loss due to electrical power generation, $Q_{loss} = Q_{d,loss} + Q_{u,loss}$

Experiments were performed to determine this heat loss according to Eq. (5-6). The inlet temperature of water was fixed at 75°C. The mass flux was set at 120 kg/m<sup>2</sup> s since the operating mass fluxes for boiling tests are 100 and 120 kg/m<sup>2</sup> s, respectively. As shown in Figure 5-14, the heat loss from the sample surface to the fluid flow are less than 5% for base heat fluxes greater than 10 kW/m<sup>2</sup> and less than 3% for base heat fluxes greater than 20 kW/m<sup>2</sup>. The heat loss generated by electrical power can be thereby neglected.

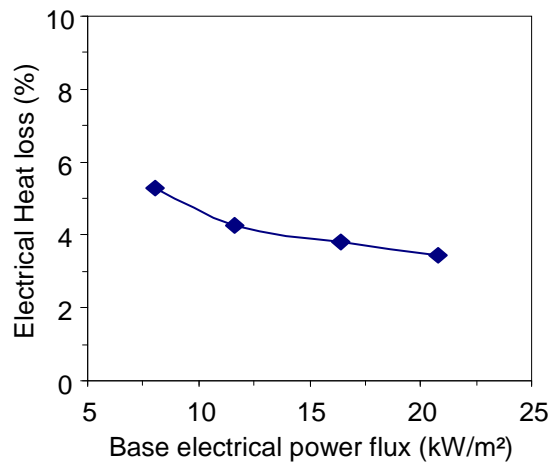


Figure 5-14. Electrical heat loss vs. electrical power generated by Joule effect at 120 kg/m<sup>2</sup> s.

### 5.4.2 Single-phase pressure drops

In the present study, the static pressure drop is negligible because the test channel is placed in the horizontal position (cf. Figure 5-15). Numerical calculations and experimental measurements show that the frictional pressure drop in the intermediate tubes between the pressure transducer and the test channel is less than 0.1 mbar, which is in the order of the measurement uncertainty. This pressure drop is thereby neglected. Indeed, in the intermediate tubes, the fluid velocity is relatively low ( $\leq 0.06$  m/s on the operating conditions). Therefore, the measured pressure drop is approximated to the sum of the frictional and singular pressure drops in the test channel as:

$$\Delta P_{\text{exp}} = \Delta P_{\text{frict}} + \Delta P_{\text{sing}} \quad (5-7)$$

wherein  $\Delta p_{\text{frict}}$  is the frictional pressure drop along the test channel and  $\Delta p_{\text{sing}}$  is the singular pressure drop at the inlet and outlet of the test channel.

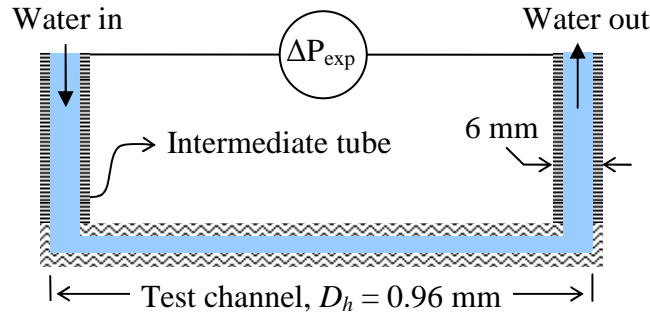


Figure 5-15. Schematic view of the fluid flow in the test section.

#### Frictional pressure loss

The frictional pressure loss is expressed as:

$$\Delta P_{\text{frict}} = 4f_p \frac{G^2}{2\rho_l} \frac{L}{D_h} \quad (5-8)$$

wherein  $G$  is the mass flux,  $\rho_l$  is the liquid density,  $L$  is the test-channel length,  $D_h$  is the test-channel hydrodynamic diameter and  $f_p$  is the single-phase frictional factor, which can be determined by the ratio of the Poiseuille number to the Reynolds number:

$$f_p = \frac{\text{Po}}{\text{Re}} \quad (5-9)$$

On the operating conditions, the Reynolds number is lower than 1000, and hence, the fluid flow is in laminar regime. For rectangular channels, Shah and London [5.1] gives an approximation of the Poiseuille number in terms of the geometry ratio as:

$$\text{Po} = 24[-0,2537 \zeta^5 + 0,9564 \zeta^4 - 1,7012 \zeta^3 + 1,9467 \zeta^2 - 1,3553 \zeta + 1] \quad (5-10)$$

where  $\zeta$  is the ratio of the channel height to the channel width. In the present study,  $\zeta$  is equal to 0.1, and therefore Eq. (5-9) gives  $\text{Po} = 21$ .

### Singular pressure loss

The singular pressure loss is expressed as:

$$\Delta P_{\text{sing}} = \xi \frac{G^2}{2\rho_l} \quad (5-11)$$

wherein  $\xi$  is the singular pressure loss coefficient. This coefficient can be estimated using the case of two 90° sharp corner elbows with sudden contraction at the inlet and sudden enlargement at the outlet. According to the theory presented in [5.2],  $\xi$  is close to 4.5.

### Experimental measurements

From (5-7), (5-8) (5-9) and (5-11), the experimental pressure drop is expressed as:

$$\Delta P_{\text{exp}} = 4 \frac{\text{Po}}{\text{Re}} \frac{G^2}{2\rho_l} \frac{L}{D_h} + \xi \frac{G^2}{2\rho_l} \quad (5-12)$$

Hence, it is expressed as a function of the liquid velocity  $U_l$  as:

$$\Delta P_{\text{exp}} = K_{\text{frict}} U_l + K_{\text{sing}} U_l^2 \quad (5-13)$$

wherein  $K_{\text{frict}}$  and  $K_{\text{sing}}$  are the constants defined as :

$$K_{\text{frict}} = 2\mu_l \text{Po} \frac{L}{D_h^2} \quad (5-14)$$

$$K_{\text{sing}} = \frac{1}{2} \xi \rho_l \quad (5-15)$$

These constants can be determined experimentally, giving the experimental Poiseuille number and the singular pressure loss coefficient:

$$\text{Po} = \frac{K_{\text{frict}}}{2} \frac{D_h^2}{\mu_l L} \quad (5-16)$$

$$\xi = \frac{2K_{\text{sing}}}{\rho_l} \quad (5-17)$$

Water entered the test section at the ambient temperature (20 °C) and at different mass fluxes varying from 95 to 580 kg/m<sup>2</sup> s. The measured pressure drop is plotted as a function of the liquid velocity as shown in Figure 5-16a. A second-order polynomial is fitted with the experimental data, giving  $K_{\text{frict}} = 8546.5$  and  $K_{\text{sing}} = 2431.7$ . This regression has a determination coefficient greater than 0.9999. Therefore, using Eqs. (5-16) and (5-17),  $\text{Po} = 22.3$  and  $\xi = 4.87$ . The frictional and singular pressure drops are then determined as shown in Figure 5-16b according to Eq. (5-8) and (5-11).

For the frictional pressure drop, the experimental points show a good agreement with the theoretical solutions of Shah and London [5.1], with a maximum deviation of 6%. For the singular pressure drop, low deviation is also obtained between the experimental and theoretical values of the singular-pressure-drop coefficient as shown in Table 5-4. Furthermore, the singular pressure drop is significantly lower than the frictional pressure drop in the test channel. The ratio between them is less than 6% for Reynolds numbers lower than 200.

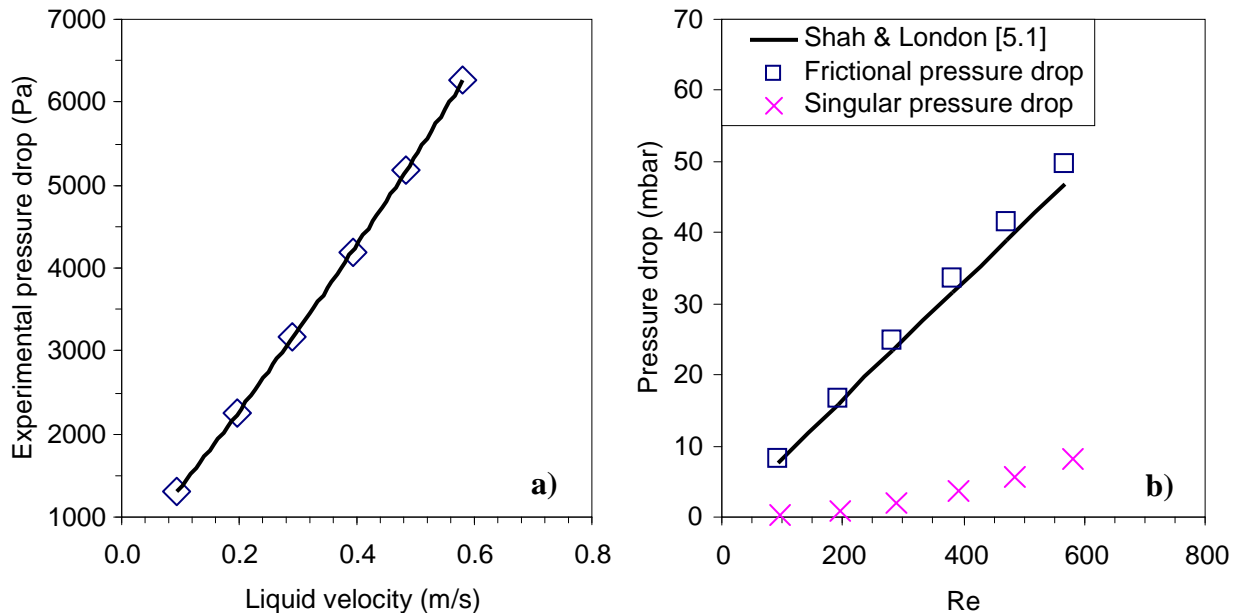


Figure 5-16. Pressure drops: a) experimental pressure drop and b) frictional and singular pressure drops.

Shown in Figure 5-17 are the overall single-phase pressure drops measured for all the sample surfaces. The same evolution of the experimental single-phase pressure drops with the Reynolds number is observed, validating the reproducibility of the sample implementation procedure.

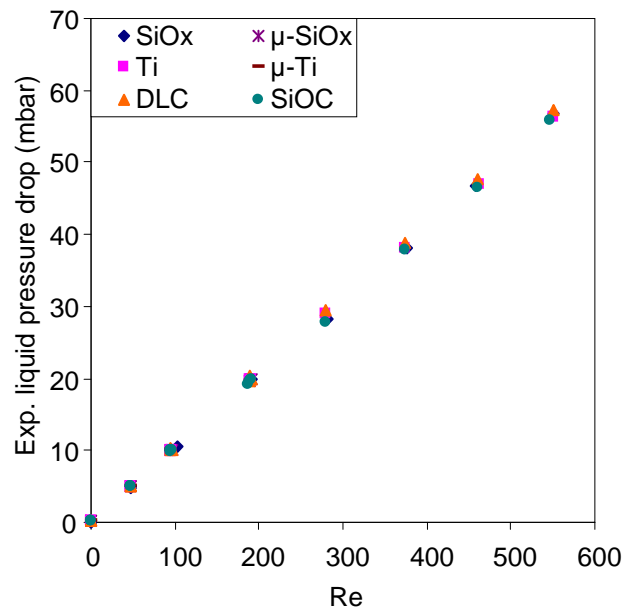


Figure 5-17. Total liquid pressure drop vs. Reynolds number.

Indeed, the average deviation of the experimental data shown in Figure 5-17 is about 0.8 mbar, which is in the order of the uncertainty in measurement of the pressure drop. Therefore, the experimental values of  $P_o$  and  $\zeta$  given in Table 5-4 can be used for the all sample surfaces to estimate the single-phase pressure drops.

Table 5-4. Single-phase pressure drop constants.

Constant	Theoretical value, ref.	Experimental value	Deviation (%)
$P_o$	21, [5.1]	22.3	6
$\zeta$	4.5, [5.2]	4.9	8

### 5.4.3 Single-phase heat transfer

#### Data reduction

As shown in section 5.4.1, the heat loss generated by electrical power is negligible. Therefore, the heat flux from the sample surface to the fluid at section  $i$  of the sample surface can be determined as:

$$q_i = \frac{IV_i}{A_{h,i}} \quad (5-18)$$

wherein  $I$  is the current,  $V_i$  is the voltage and  $A_{h,i}$  is the area of section  $i$ . The local heat transfer coefficient is determined from the local wall to bulk temperature difference and the heat flux as:

$$h_i = \frac{q_i}{T_{w,i} - T_{f,i}} \quad (5-19)$$

Along section  $i$  of the sample surface, the fluid temperature is assumed to vary linearly. Thus, the average temperature of the fluid at this section is determined as:

$$T_{f,i} = \frac{T_{f,i,in} + T_{f,i,out}}{2} \quad (5-20)$$

wherein  $T_{f,i,in}$  and  $T_{f,i,out}$  are the fluid temperatures at the inlet and outlet of section  $i$ , respectively.

The fluid temperature at the inlet of a section is also the temperature of the fluid at the outlet of the previous section, and hence Eq. (5-20) can also be expressed as:

$$T_{f,i} = \frac{T_{f,i-1,out} + T_{f,i,out}}{2} \quad (5-21)$$

The fluid outlet temperature of each section is calculated from the inlet temperature and the heat added to the fluid as:



$$T_{f,i,out} = T_{f,in} + \sum_{j=1}^i \frac{A_{h,j} (q_j - \bar{q}_{loss}^o)}{\dot{m} C_{p,j}} \quad (5-22)$$

wherein  $\bar{q}_{loss}^o$  is the average heat loss flux before generation of electrical power, which is approximated as:

$$\bar{q}_{loss}^o = \frac{Q_{loss}^o}{A_h} \quad (5-23)$$

wherein  $A_h$  is the overall heat exchange area between the sample surface and the fluid and  $Q_{loss}^o$  is the overall heat loss before generation of electrical power calculated by Eq. (5-1). When the fluid enters the test section at the ambient temperature, this heat loss is negligible.

In single-phase flow, the local Nusselt number at section  $i$  is defined as:

$$Nu_i = \frac{h_i D_h}{\lambda_i} \quad (5-24)$$

wherein  $\lambda_i$  is the fluid thermal conductivity at section  $i$ .

The local reduced length is defined as:

$$z^+ = \frac{z_i}{D_h Re Pr} \quad (5-25)$$

wherein  $z_i$  is the length of section  $i$  and  $Pr$  is the Prandtl number.

### Thermal entrance length

The thermal entrance length  $L_{th}$  is the length until the flow temperature profile is fully developed. Its dimensionless number is defined as:

$$L_{th}^+ = \frac{L_{th}}{D_h Re Pr} \quad (5-26)$$

From the numerical solution by Shah and London [5.1], the following correlation of the reduced thermal entrance is obtained:

$$L_{th}^+ = -0,1320 \zeta^4 + 0,299 \zeta^3 - 0,2905 \zeta^2 + 0,1780 \zeta + 0,0115 \quad (5-27)$$

where  $\zeta$  is the ratio of the channel height to the channel width. In the present study,  $\zeta$  is equal to 0.1, and therefore Eq. (5-26) gives  $L_{th}^+ = 0.027$ . Thus, the thermal entrance is calculated at different fluid temperatures as shown in Figure 5-18. The thermal entrance length decreases when the fluid temperature increases. In boiling tests, the fluid temperature is near by 100 °C and the operating Reynolds number is less than 500. Thereby, the single-phase liquid flow

will be thermally fully developed after a travel of about 22 mm, which is close to the length of the first section  $S_1$ .

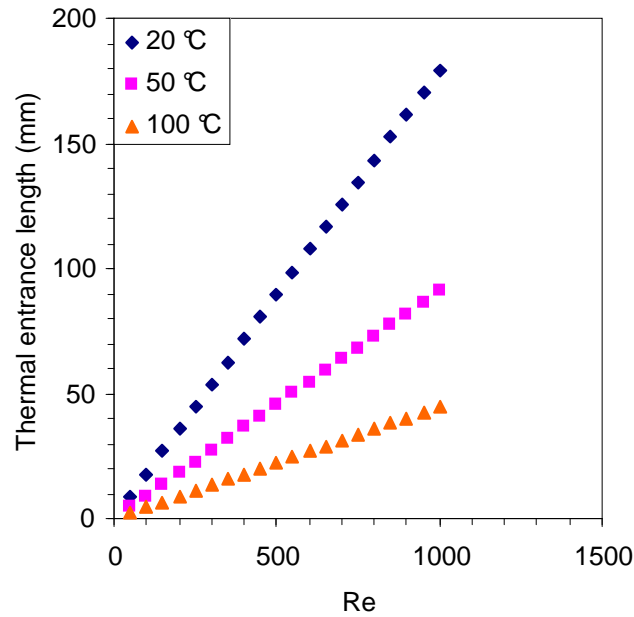


Figure 5-18. Thermal entrance length vs. Reynolds number at different fluid temperatures.

#### Comparison between theoretical and experimental data

The numerical solution of Shah and London [5.1] is used to estimate the local Nusselt number as:

$$Nu_i = \frac{1}{\frac{1}{Nu_\infty} - 0.092 \exp(-88.6 z^+)} \quad (5-28)$$

wherein  $Nu_\infty$  is the Nusselt number for thermally fully-developed flow. In the case of a rectangular channel with heat flux imposed at one side and fluid temperature imposed at the other sides,  $Nu_\infty = 4$  according to Shah and London [5.1].

For experimental measurements, water entered the test section at the ambient temperature (20 °C). The mass flux was varied from 45 to 480 kg/m<sup>2</sup> s and the heat flux was varied from 8 to 60 kW/m<sup>2</sup>. Evolution of the Nusselt number with the reduced flow length is shown in Figure 5-19. A good agreement between the experimental and the theoretical data is obtained, with only a maximum deviation of 5%, even at low Reynolds numbers. This deviation is lower than the uncertainty in measurement of the Nusselt number which is about 14%.

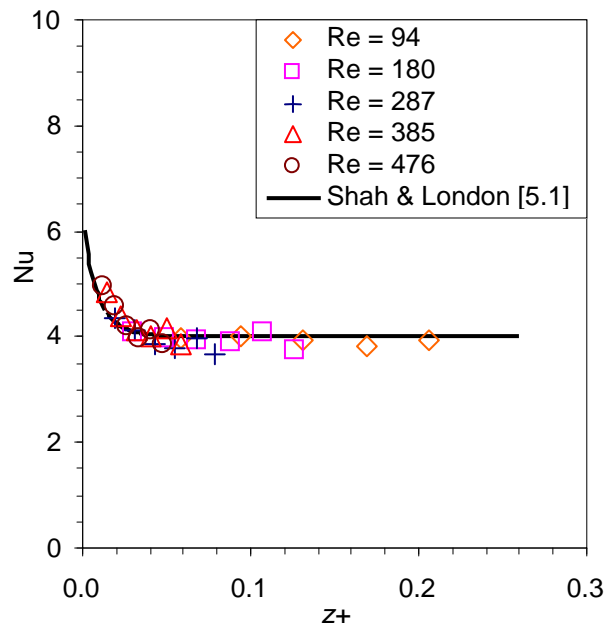


Figure 5-19. Local Nusselt number vs. local reduced length.

## 5.5 Conclusion

The main remarks of this chapter are as follows:

- In order to accurately control the surface parameters, a reliable and repeatable method of sample surface fabrication was developed. It consists of three steps of surface coating and structuring which enable the samples to be used as the heating elements as well as the sensors of local temperature and heat flux. This method also enables modification of surface topography and chemistry at nano- and microscales
- The test section was setup so that visualisation of flow patterns can be made and replacement of samples is easy to implement
- Single-phase validation tests were performed to validate the test facility, measurement techniques and data reduction procedure. The experimental data of single-phase pressure drop and heat transfer coefficient show good agreements with the data predicted by Shah and London [5.1].

In the next chapter, the experimental results for boiling tests will be introduced and discussed.

## 5.6 Reference

- [5.1] R. Shah, A. London, Laminar Flow Forced Convection in Ducts, Academic Press, 1978.
- [5.2] A. Lallemand, Écoulements des fluides- Écoulements en conduites. Réseaux, Techniques de l'Ingénieurs BE8161 (2001), 1-19.

## Chapter 6: Data reduction and experimental results

### 6.1 Data reduction

#### 6.1.1 Heat flux

As shown in the previous chapter, heat losses by electrical generation are negligible. Therefore, the local heat flux exchanged between the fluid and the wall at section  $i$  of the sample surface is calculated as:

$$q_i = \frac{IV_i}{A_{h,i}} \quad (6-1)$$

wherein  $I$  is the current and  $V_i$  and  $A_{h,i}$  are the voltage and the area of section  $i$ , respectively.

The average heat flux along the test channel is calculated as:

$$\bar{q} = \frac{IV}{A_h} \quad (6-2)$$

wherein  $V$  is the overall voltage and  $A_h$  is the overall heat exchange area between the working fluid and the sample surface.

However, as mentioned in Section 5.4, due to air convection and radiation around the test section, the working fluid loses a part of its energy  $Q_{loss}^o$  when flowing along the test channel even though no electrical power is generated:

$$Q_{loss}^o = \dot{m} C_p \left[ T_{f,in} - T_{f,out}^o \right] \quad (6-3)$$

wherein  $\dot{m}$  is the mass flow,  $C_p$  is the liquid specific heat,  $T_{f,in}$  is the fluid inlet temperature and  $T_{f,out}^o$  is the fluid outlet temperature when the fluid is not heated by electrical power from the sample surface.

The average heat loss flux before generation of electrical power is approximated as:

$$\bar{q}_{loss}^o = \frac{Q_{loss}^o}{A_h} \quad (6-4)$$

#### 6.1.2 Subcooled conditions

Along section  $i$  of the sample surface, the fluid temperature is assumed to vary linearly. Thus, the average temperature of the fluid at this section is determined as:

$$T_{f,i} = \frac{T_{f,i,in} + T_{f,i,out}}{2} \quad (6-5)$$

wherein  $T_{f,i,in}$  and  $T_{f,i,out}$  are the fluid temperatures at the inlet and outlet of section  $i$ , respectively.

The fluid temperature at the inlet of a section is also the temperature of the fluid at the outlet of the previous section, and hence Eq. (6-5) can also be expressed as:

$$T_{f,i} = \frac{T_{f,i-1,out} + T_{f,i,out}}{2} \quad (6-6)$$

The fluid outlet temperature of each section is calculated from the inlet temperature and the heat added to the fluid as:

$$T_{f,i,out} = T_{f,i,in} + \frac{\sum_{j=1}^i A_{h,j} (q_j - \bar{q}_{loss}^o)}{\dot{m} C_{p,j}} \quad (6-7)$$

The local heat transfer coefficient is determined from the local wall to bulk temperature difference and the heat flux as:

$$h_i = \frac{q_i}{T_{w,i} - T_{f,i}} \quad (6-8)$$

### 6.1.3 Two-phase length

An iterative method is used to calculate the single-phase length  $z_{onb}$  where bulk boiling starts, i.e. where the fluid bulk temperature is equal to the saturation temperature at the local pressure.

Initial condition for the iteration is:

$$z_{onb} = L \quad (6-9)$$

wherein  $L$  is the test-channel length.

At each iteration step, the absolute pressure  $P_{onb}$  and saturation temperature  $T_{s,onb}$  are calculated, updating the value of the single-phase length.

$$P_{onb} = P_{in} - 4 \frac{Po}{Re} \frac{G^2}{2\rho_l} \frac{z_{onb}}{D_h} \quad (6-10)$$

wherein  $P_{in}$  is the absolute pressure at the inlet of the test section and  $Po$  is the Poiseuille number determined by single-phase tests (cf. Section 5.4.2). The singular pressure drop at the inlet of the test channel is not taken into account in Eq. (6-10) since it is less than 2% of the overall single-phase pressure drop as shown in Section 5.4.2.

The saturation temperature is determined using a second-order polynomial regression given by REFPROP 7.0, developed by NIST (2002):

$$T_{s,onb} = -1.17405 \times 10^{-5} P_{onb}^2 + 5.14761 \times 10^{-2} P_{onb} + 59.8705 \quad (6-11)$$

wherein  $P_{onb}$  is in mbar and  $T_{s,onb}$  is in °C.

The energy balance from the inlet of the test channel to the position where bulk boiling starts implies:

$$\dot{m} C_p (T_{s,onb} - T_{f,in}) = (\bar{q} - \bar{q}_{loss}^o) W z_{onb} \quad (6-12)$$

wherein  $W$  is the test channel width.

Therefore, the following expression of the single-phase length is obtained:

$$z_{onb} = \frac{\dot{m} C_p (T_{s,boil} - T_{f,in})}{(\bar{q} - \bar{q}_{loss}^o) W} \quad (6-13)$$

The iteration stops when the convergence criterion is obtained:

$$\left| z_{onb}^{n+1} - z_{onb}^n \right| \leq 10^{-6} \quad (6-14)$$

wherein  $n$  is the number of iteration.

Hence, the two-phase length  $L_{tp}$  is determined as:

$$L_{tp} = L - z_{onb} \quad (6-15)$$

#### 6.1.4 Boiling conditions

The overall two-phase pressure drop  $\Delta P_{tp}$  along the test channel is calculated as:

$$\Delta P_{tp} = \Delta P_{exp} - (P_{in} - P_{onb}) \quad (6-16)$$

wherein  $\Delta P_{exp}$  is the pressure drop measured experimentally and  $(P_{in} - P_{onb})$  is the single-phase pressure drop. The singular pressure drop at the outlet of the test channel is not taken into account in Eq. (6-16) since it is less than 3% of the overall single-phase pressure drop as shown in Section 5.4.2.

Thus, the average gradient per unit length of the two-phase pressure drop is calculated as:

$$\left( \frac{dP}{dz} \right)_{tp} = \frac{\Delta P_{tp}}{L_{tp}} \quad (6-17)$$

The local saturation temperature  $T_{s,i}$  is determined by taking into account the drop in saturation temperature due to pressure drop, where the pressure drop is assumed to vary

linearly along the test section. In other words, for sections  $i$  on boiling conditions, the local absolute pressure drop is determined as:

$$P_i = P_{onb} - \left( \frac{dP}{dz} \right)_{tp} (z_i - z_{onb}) \quad (6-18)$$

This assumption is acceptable since it gives an uncertainty of less than 0.03 °C in the determination of the saturation temperature. Indeed, Eq. (6-18) gives an uncertainty of less than 1 mbar in the determination of the local pressure at each section of the sample surface.

The two-phase heat transfer coefficient is determined as:

$$h_i = \frac{q_i}{T_{w,i} - T_{s,i}} \quad (6-19)$$

### 6.1.5 Vapour quality

The variation of the vapour quality is calculated using energy balance as:

$$\Delta x_i = \frac{A_{h,i} (q_i - q_{loss,i}^o) - \dot{m} C_{p,i} (T_{s,i} - T_{f,i})}{\dot{m} h_{lv,i}} \quad (6-20)$$

wherein  $h_{lv,i}$  is the latent heat of vaporisation at section  $i$ .

The vapour quality is equal to zero when bulk boiling starts. It is negative on subcooled conditions and positive on boiling conditions.

### 6.1.6 Average parameters

For average analysis, the average wall and saturation temperatures are determined by the following relation:

$$\bar{T}_w = \sum_{i=1}^N A_{h,i} \times T_{w,i} / \sum_{i=1}^N A_{h,i} \quad (6-21)$$

$$\bar{T}_s = \sum_{i=1}^N A_{h,i} \times T_{s,i} / \sum_{i=1}^N A_{h,i} \quad (6-22)$$

wherein  $N$  is the number of sections of interest on the sample surface.

### 6.1.7 Operating conditions

A Matlab program was written in order to determine the parameters of interest according to the above equations. Thermodynamic properties of water are calculated with the computer code REFPROP 7.0, developed by NIST (2002). Experimental parameters and operating conditions are summarized in Table 6-1. The measurement uncertainties are estimated using the error propagation law suggested by Kline and McClintock [6.1] (cf. Appendix).

Table 6-1. Operating parameters and uncertainties.

Parameter	Range	Uncertainty
$D_h$ (mm)	0.96	$\pm 0.02$ mm
$G$ (kg/m <sup>2</sup> s)	80-120	$\pm 2\%$
$P_{in}$ (mbar)	1000	$\pm 0.2\%$
$P_{in} - P_{out}$ (mbar)	0-100	$\pm 0.3\%$
$T_s$ (°C)	100	$\pm 0.2$ °C
$T_w$ (°C)	100-120	$\pm 0.2$ °C
$q$ (kW/m <sup>2</sup> )	30-100	$\pm 2\%$
$h$ (kW/m <sup>2</sup> K)	3-100	$\pm 4$ -10%
$x$	-0.1-0.1	$\pm 2\%$

## 6.2 Smooth surfaces

### 6.2.1 Contact angle

The contact angles of water on the sample surfaces were measured using the sessile drop technique with KRÜSS EasyDrop systems in a cleanroom at the ambient temperature (cf. 2.2.3). Pictures of water drops on different sample surfaces are shown in Figure 6-1.

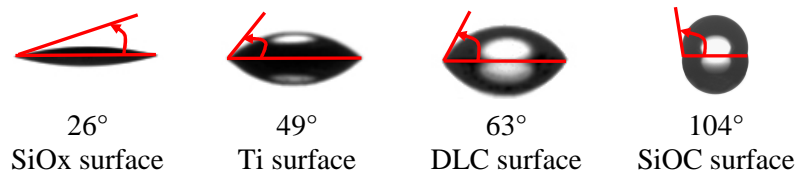


Figure 6-1. Static contact angles of a water-droplet on the sample surfaces at room temperature.

The SiOx surface shows a relatively high wettability; whereas the SiOC surface is an unwetted (hydrophobic) surface. The Ti and DLC surfaces are both wetted (hydrophilic) and have static contact angles ( $\theta$ ) of  $49^\circ$  and  $63^\circ$ , respectively. The contact angle hysteresis  $\Delta\theta$  of each sample surface is also determined by measurements of receding and advancing contact angles ( $\theta_a$  and  $\theta_r$ , respectively). The results of contact angle measurements are summarized in Table 6-2.

Table 6-2. Contact angle measurements.

Surface	$\theta$ (°)	$\theta_a$ (°)	$\theta_r$ (°)	$\Delta\theta$ (°)
SiOx	26	38	15	23
Ti	49	82	36	46
DLC	63	94	51	43
SiOC	104	108	96	12

### 6.2.2 Pressure drop

In the previous chapter (Section 5.4.2), it was shown that the surface wettability has a negligible impact on the single-phase pressure drop. However, in boiling conditions, the surface wettability can play a significant role because of surface tension force generated at the fluid-wall interface. This remark is highlighted by experimental measurements as shown in Figure 2. For various samples with various contact angles, different evolution curves of two-phase pressure drop as functions of vapour quality are obtained.

Indeed, at the operating mass fluxes, it is noticed that the two-phase pressure drop decreases with the contact angle. Especially, between SiOC hydrophobic surface and SiOx highly-hydrophilic surface, the average deviation is about 270%. The impact of contact angle on two-



phase pressure drop can be related to its impact on the surface tension force generated at the triple contact line. For wetted surfaces, this force acts to reduce the dry zone perimeter, and a decrease of the contact angle leads to an increase of this effect. However, for unwetted surface, as shown in Chapter 4, the surface tension force tends to maintain the bubbles at the solid wall, increasing the frictional pressure drop of the moving fluid.

For all samples, the two-phase pressure drop increases when the mass flux or the vapour quality increases. The dependence of the two-phase pressure drop on the vapour quality can be fitted by linear or second-order regression with a regression coefficient greater than 0.999.

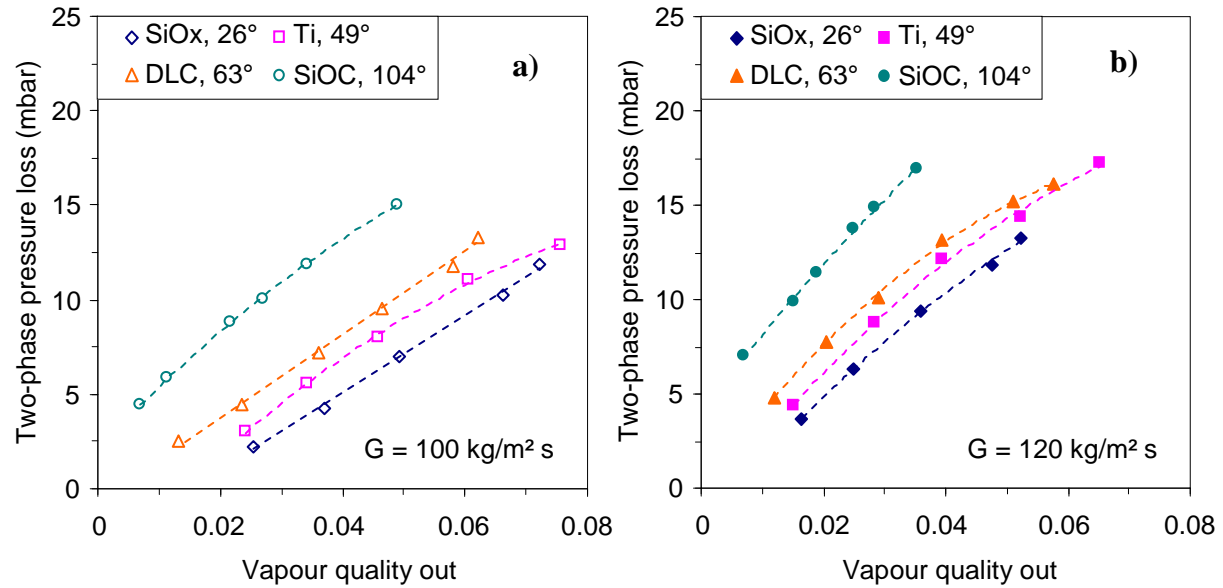


Figure 6-2. Two-phase pressure drops: a) at  $100 \text{ kg/m}^2 \text{ s}$  and b) at  $120 \text{ kg/m}^2 \text{ s}$ .

### 6.2.3 Flow patterns visualisation

#### Flow patterns

In order to clarify the boiling processes, images taken from the high speed camera were analysed. As shown in Figure 6-3, four flow patterns were identified as:

- *Confined-bubbly flow (CBF)*: where discrete bubbles move inside the liquid phase. These bubbles are confined because they rapidly reach the channel height and then homogeneously grow in the directions of the channel width and length.
- *Slug flow (SF)*: when confined bubbles have the same width as the channel, they mainly grow in the direction of the channel length. Thus, they are called “elongated bubble” or “slug”. Slugs can be also created by coalescence of confined bubbles.
- *Slug-annular flow (SAF)*: where churning liquid zones are created at the wall by coalescence and deformation of slugs. This type of flow pattern is also referred to as “semi-annular flow” by Revellin and Thome [6.2].
- *Churn flow (CF)*: where the flow is highly agitated, resulting in a highly irregular liquid-vapour interface.

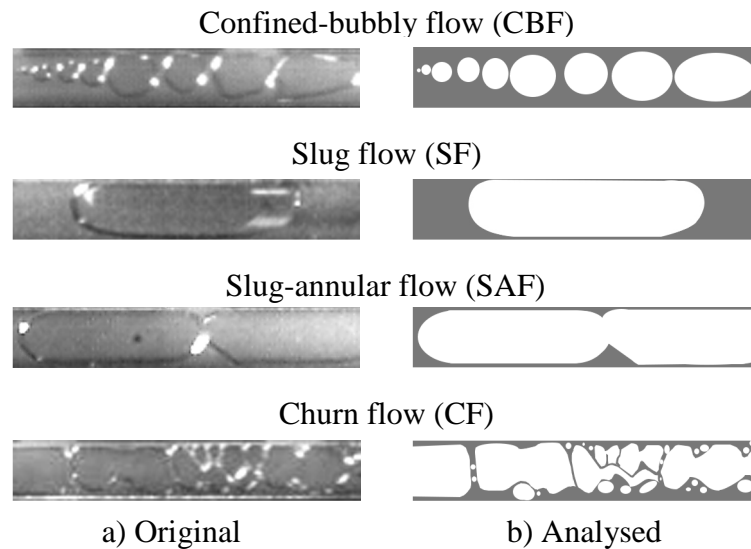


Figure 6-3. Representative top-view images of flow patterns in the test channel for all the sample surfaces.

In the following paragraphs, the impact of surface wettability on two-phase flow patterns will be discussed. For illustration, only representative images at  $120 \text{ kg/m}^2 \text{ s}$  will be presented, since no significant change in the flow patterns was observed when the mass flux changes from  $100 \text{ kg/m}^2 \text{ s}$  to  $120 \text{ kg/m}^2 \text{ s}$ .

#### Low-wetted surfaces

For Ti and DLC surfaces which are low wetted, three types of flow patterns were identified as: confined-bubbly flow, slug flow and slug-annular flow. For instance, Figure 6-4 shows the original and analysed images of flow patterns on Ti surface at different heat fluxes. It is observed that along the test channel, different flows patterns coexist, e.g. confined-bubbly and slug flows for heat flux of 42 and 44  $\text{kW/m}^2$ , confined-bubbly, slug and slug-annular flows for heat flux of 49  $\text{kW/m}^2$ , and confined-bubbly and slug-annular flows for heat flux of 53, 57, and 61  $\text{kW/m}^2$ .

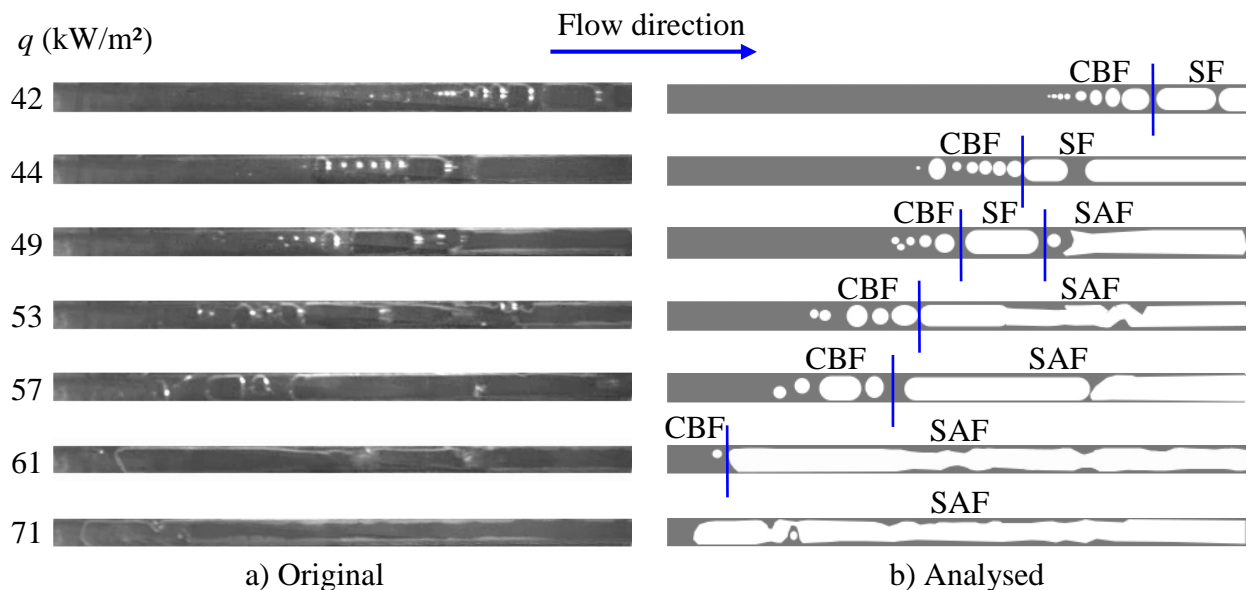


Figure 6-4. Representative top-view images of flow patterns on Ti surface at different heat fluxes.

Furthermore, the flow patterns along the test channel periodically change. As an example, the evolution of flow patterns on Ti surface at a heat flux of  $61 \text{ kW/m}^2$  is illustrated in Figure 6-5. It is noticed that at a relatively high heat flux ( $\geq 50 \text{ kW/m}^2$ ), the nucleation of a bubble followed by its rapid growth into a vapour slug resulted in reverse flow, as illustrated in Figure 6-5 from 100 to 200 ms. This is the so-called “backflow” phenomenon which was early observed by Kandlikar *et al.* [6.3] and Brutin *et al.* [6.4], who reported this phenomenon as a main cause for the two-phase flow instability. At the end of a flow-pattern period, the liquid rewets the test-channel walls as shown in Figure 6-5 from 300 to 600 ms. The period of two-phase flow-pattern in a microchannel is relatively similar to the one of bubble growth in pool boiling. Indeed, both periods contain three main stages such as: nucleation, bubble growth and liquid rewetting.

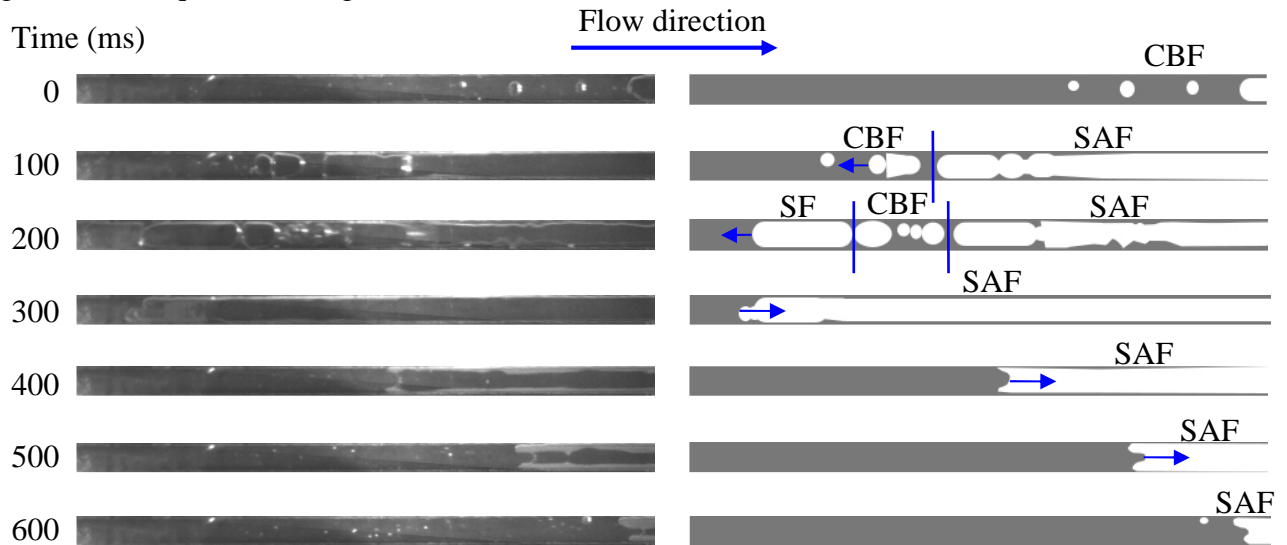


Figure 6-5. Evolution of flow patterns on Ti surface at  $61 \text{ kW/m}^2$ .

Similar observations are obtained with DLC surface as shown in Figure 6-6. Compared to Ti surface, bubbles grow more rapidly on DLC surface, leading to a shorter period of flow-pattern (about 500 ms) and to a regime of slug-annular flow at a lower heat flux. This observation can be related to the bubble emission frequency, which is higher on DLC surface due to a higher contact angle.

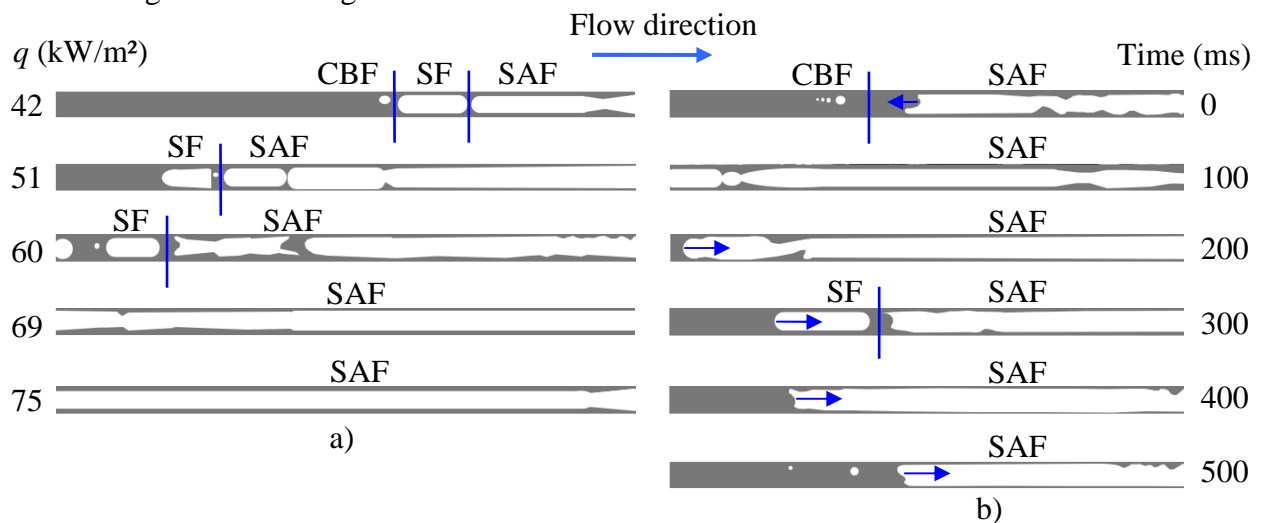


Figure 6-6. Analysed images of flow patterns on DLC surface: a) vs. heat flux and b) vs. time at  $60 \text{ kW/m}^2$ .

### Highly-wetted surface

For highly-wetted SiOx surface, three types of flow patterns were identified, which are confined-bubbly flow, slug flow and churn flow. Compared to Ti and DLC surfaces, instead of the slug-annular flow, the churn flow was observed with SiOx surface (cf. Figure 6-7). The appearance of this new pattern can be related to the high superheat needed for onset of nucleate boiling (cf. Section 6.2.4) which causes rapid evaporation rate and thus instabilities at the liquid-vapour interface. Especially, in the bottom corners along the test channel, due to the presence of a large liquid amount, nucleation occurred inside the liquid film around the pre-existent slugs and hence agitated the two-phase flow. On SiOx surface, backflow phenomenon was also observed.

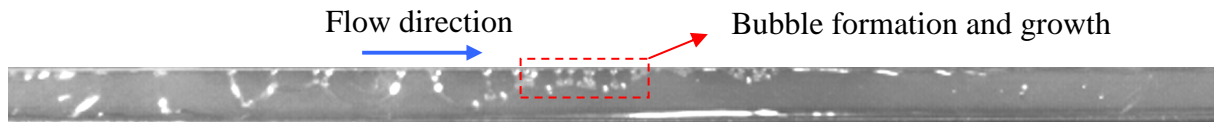


Figure 6-7. Representative image of churn flow regime (CF) observed on SiOx surface.

### Unwetted surface

On SiOC surface, a large amount of bubbles was rapidly generated, even though the fluid was not in saturation conditions ( $T_f - T_s \approx -1^\circ\text{C}$ ) as shown in Figure 6-8a. These bubbles resided long time on SiOC surface, and their motions were discontinuous and unstable. Some of them coalesced to form confined bubbles and slugs. These behaviours are probably related to the formation energy and the surface tension force as described in Chapter 4. During the movement of slugs, bubbles emission still occurred in the liquid film around them, generating the churn flow (cf. Figure 6-11). The flow patterns of SiOC surface are thereby identified as: confined-bubbly flow, slug flow and churn flow. Unlike the other surface, on SiOC surface, backflow phenomenon was not observed. The present observations are in good agreement with those reported by Choi *et al.* [6.5].

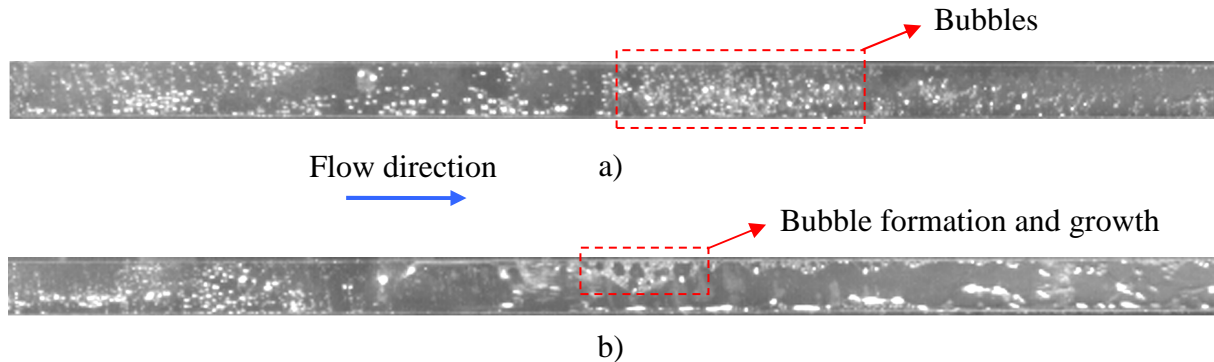


Figure 6-8. Representative images of flow pattern on SiOC surface: a) bubbles are created in  $1^\circ\text{C}$ -subcooled fluid and b) churn flow regime (CF).

### Intermittent dryout

For all sample surfaces, in the regime of slug-annular flow or churn flow, dryout was observed by detection of condensation of vapour on the top wall of the test channel, as illustrated in Figure 6-9 for DLC surface. Similar images were obtained with the other surfaces. This dryout is intermittent because of later liquid rewetting. The intermittent dryout is mainly caused by coalescence and deformation of slugs, or by nucleation inside the liquid film.

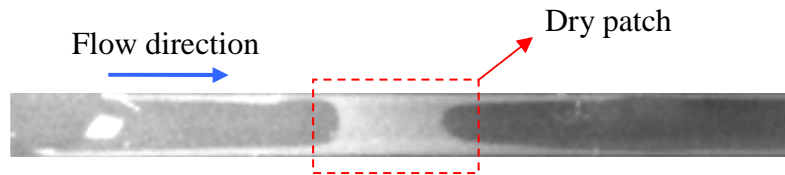


Figure 6-9. Representative image intermittent dryout on DLC surface detected by condensation of vapour.

### Flow-pattern map

Various two-phase flow pattern maps have been proposed for microchannels over the years. A complete review of study on microchannel two-phase pattern maps can be found in the book of Thome [6.6]. In the present study, the map suggested by Triplett *et al.* [6.7] is used for comparison with the present experimental visualisation, since the operating conditions of Triplett *et al.* [6.7] are relatively similar to the present operating conditions. The major differences are: in Triplett *et al.* [6.7], the tests were conducted with a circular channel in adiabatic conditions; whereas the present tests were carried out in boiling condition with a rectangular channel.

Indeed, Triplett *et al.* [6.7] proposed a graphical map in terms of the superficial liquid velocity versus the superficial vapour velocity, based on their flow pattern observations for air-water in a 1.1 mm horizontal Pyrex channel. The flows were made using a mixer for air and water upstream of the observation point. They identified five types of flow patterns which are bubbly flow (BF), slug flow (SF), slug-annular flow (SAF), churn flow (CF) and annular flow (AF) (cf. Figure 6-10a). According to their definition, the confined-bubbly flow observed in the present study can also be classified as “slug” since the bubbles are confined in height.

As shown in Figure 6-10a, for all the sample surfaces, the main flow patterns are slug and slug-annular flows. This prediction shows good agreement with the present visualization on Ti and DLC surfaces. However, for SiO<sub>x</sub> and SiOC surfaces, the map of Triplett *et al.* [6.7] does not predict the churn flow which was observed in current experiments. This should relate to the wetting property of the Pyrex surface tested by Triplett *et al.* [6.7], which is relatively similar to those of Ti and DLC surfaces but significantly different from those of SiO<sub>x</sub> and SiOC surfaces.

In order to take into account the effect of contact angle on two-phase flow patterns, a new pattern map is suggested in terms of the contact angle versus the outlet vapour quality as shown in Figure 6-10b. It is important to notice that the transition boundaries were qualitatively determined by experimental visualisation and the present map is valid for only water with mass flux of 100 and 120 kg/m<sup>2</sup> s. The given flow patterns are the dominant ones observed in boiling period. In general, for all sample surfaces, at low outlet vapour qualities ( $\leq 0.3$ ), the confined-bubbly flow and the slug flow are the two major flow patterns. At higher outlet vapour qualities, slug-annular flow appears on the low-wetted surfaces, but churn flow dominates on the highly-wetted and unwetted surfaces. Future work is needed to validate the present map by comparison with a larger set of experimental data. The major observations of flow pattern on smooth samples surface are summarized in Table 6-3.

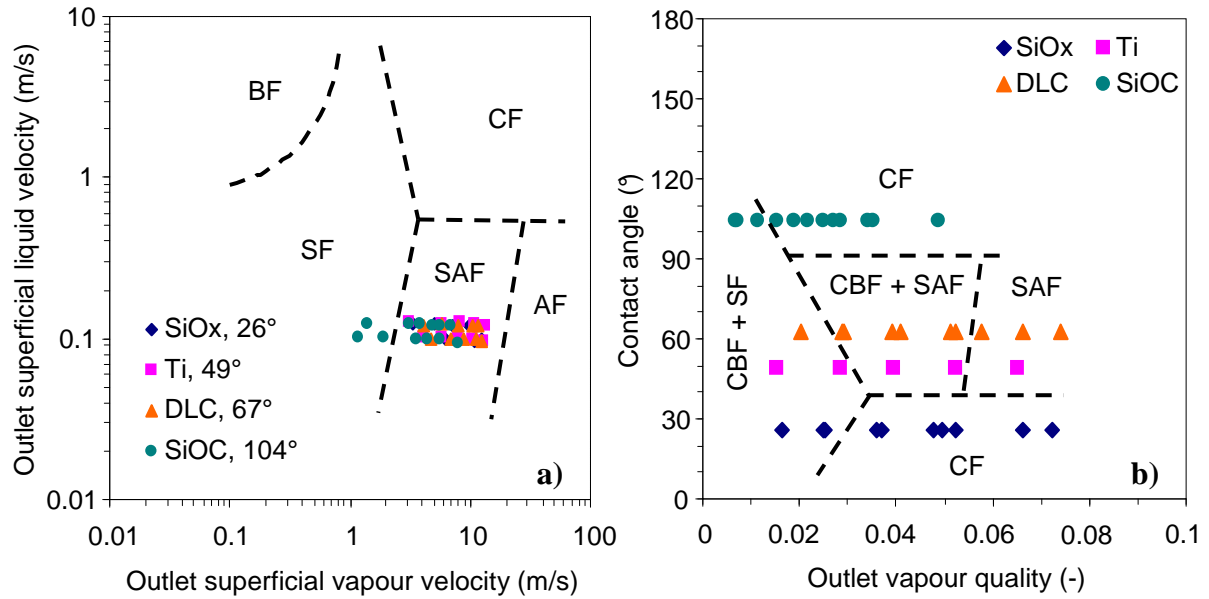


Figure 6-10. Flow pattern map: a) of Triplett *et al.* [6.7] for air-water in a 1.1 mm horizontal channel and b) given by the present visualization for 100 and 120 kg/m<sup>2</sup> s where the transition boundaries are qualitatively determined.

Table 6-3. Summary of flow-pattern visualization.

Surface	Contact angle (°)	Wetting property	Flow patterns	Backflow occurring
SiOx	26°	High	CBF, SF, CF	Yes
Ti	49°	Low	CBF, SF, SAF	Yes
DLC	67°	Low	CBF, SF, SAF	Yes
SiOC	104	Unwetted	CBF, SF, CF	No

## 6.2.4 Heat transfer

### Experimental measurements

The evolution of the local heat transfer coefficient with the vapour quality on various sample surfaces at 100 and 120 kg/m<sup>2</sup> s are presented in Figure 6-11 and Figure 6-12, respectively. In boiling conditions, the experimental heat transfer coefficient varies from 5000 W/m<sup>2</sup> K to 30000 W/m<sup>2</sup> K. At a given heat flux, when boiling occurs, it is noticed that the heat transfer coefficient increases when the vapour quality increases. For a vapour quality between 0.005 and 0.015, the heat transfer coefficient reaches its maximum value, and then decreases to a constant value. An increase in the heat flux leads to an increase in this value. These observations are in agreement with those of Sobierska *et al.* [6.8] who investigated flow boiling of water in a vertical narrow rectangular microchannel with the hydraulic diameter  $D_h = 0.48$  mm.

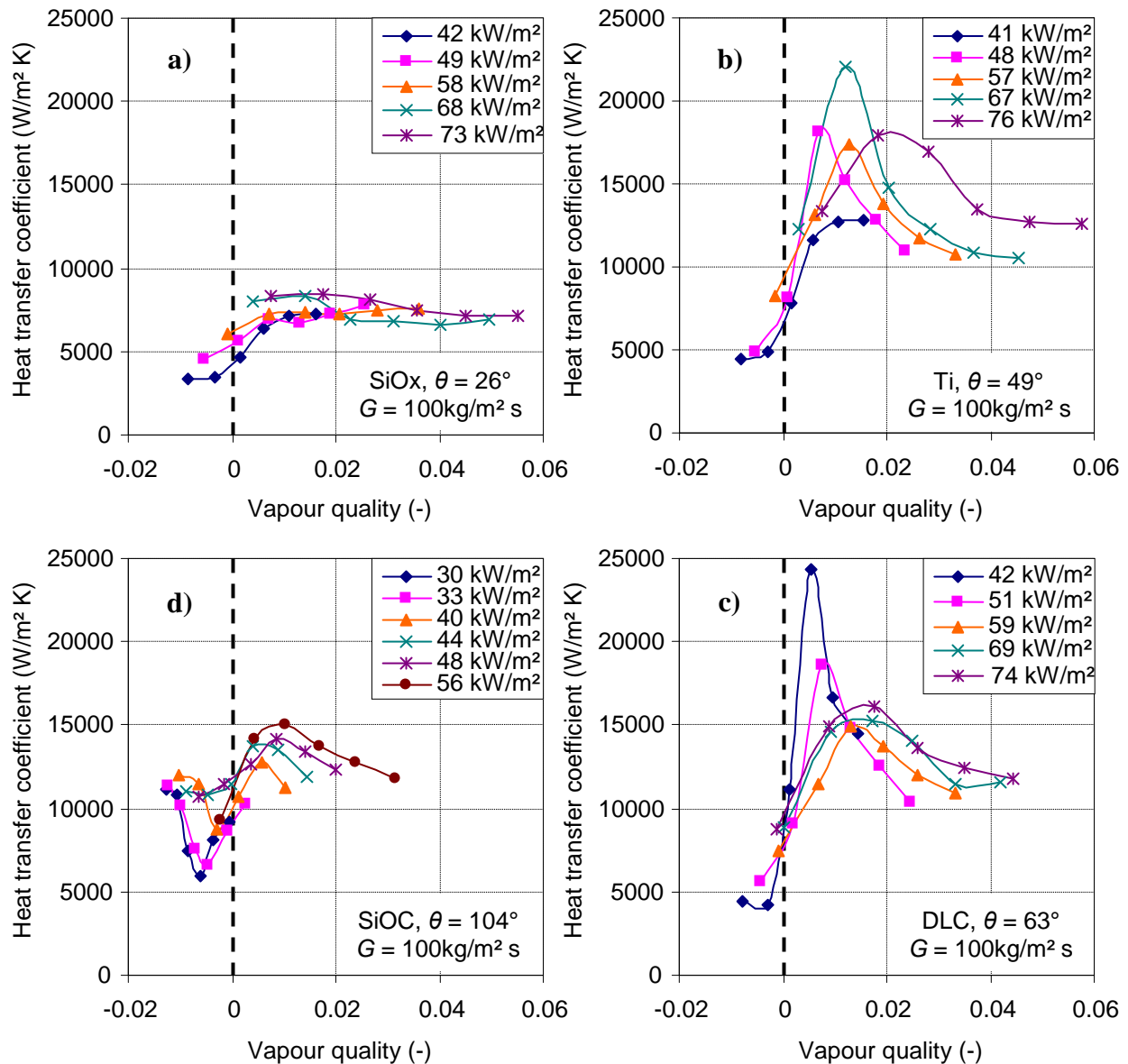


Figure 6-11. For  $100 \text{ kg/m}^2 \text{ s}$ , heat transfer coefficient vs. vapour quality on a) SiOx surface; b) Ti surface; c) DLC surface and d) SiOC surface.

However, for SiOx surface which has a relatively high wettability, the heat transfer coefficient slightly changes when the vapour quality or the heat flux increase. This surface also shows the lowest heat transfer performance. For SiOC surface which is hydrophobic, bubble generation occurred even at negative vapour quality, i.e. at a fluid temperature lower than the saturation temperature. The two low-wetted surfaces have relatively the same evolution tendency of the heat transfer coefficient with the vapour quality or heat flux. Compared to Ti surface, the heat transfer coefficient on DLC surface is lower with an average deterioration of about 10%.



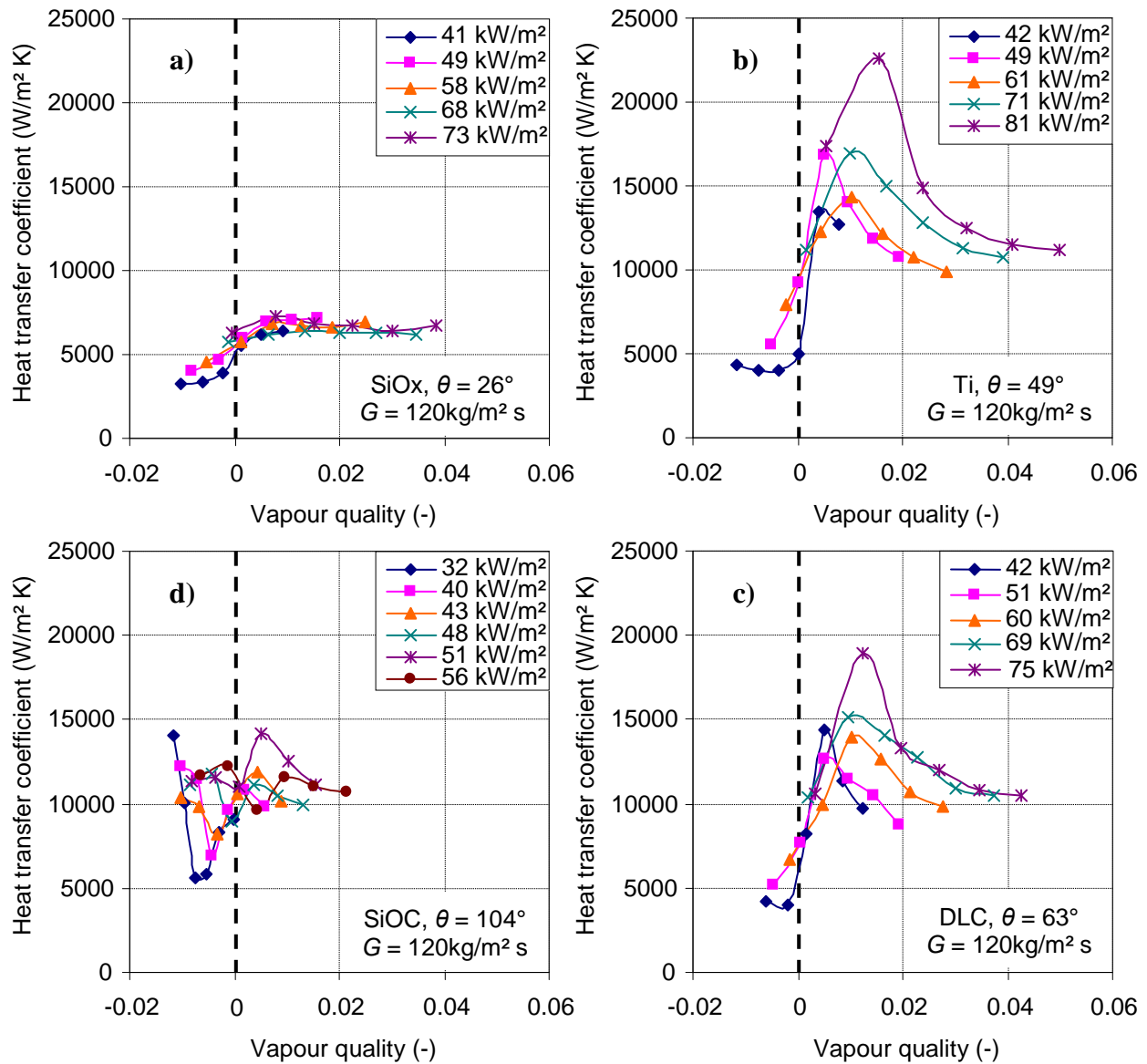


Figure 6-12. For  $120 \text{ kg/m}^2 \text{ s}$ , heat transfer coefficient vs. vapour quality on a) SiOx surface; b) Ti surface; c) DLC surface and d) SiOC surface.

It is noticed that the mass flux has a slight effect on the heat transfer coefficient. For all the sample surfaces, at  $120 \text{ kg/m}^2 \text{ s}$ , the best heat transfer coefficients are obtained with the maximum operating heat fluxes, which are 73, 81, 75 and  $56 \text{ kW/m}^2$  for SiOx, Ti, DLC and SiOC surfaces, respectively. However, at  $100 \text{ kg/m}^2 \text{ s}$ , lower heat fluxes can give higher values of the maximum heat transfer coefficient. Especially, for DLC surface, the heat transfer coefficient reaches the maximum value of  $25000 \text{ W/m}^2 \text{ K}$  when the heat flux is equal to  $42 \text{ kW/m}^2$ . This effect of mass flux may be due to the impact of nucleate boiling at low vapour qualities, which is frequently higher for a lower mass flux.

### Discussion

Dependence of the heat transfer coefficient on the vapour quality can be explained by local flow patterns as illustrated in Figure 6-13. It is observed that the heat transfer coefficient significantly increases in the confined bubbly and slug configurations. Its maximum value would be obtained in slug flow when the liquid layer thickness reaches its minimum value. The heat transfer deterioration occurs when the slug flow is disrupted to become slug-annular



or churn flow. This can be explained by the presence of the intermittent dryout observed in the semi-annular and churn flows, as well as the increase of liquid film thickness in wavy conditions.

The experimental observations are also revealed by interpreting the boiling curves shown in Figure 6-14, where the wall and saturation temperatures are taken as the average temperatures defined by Eqs. (6-21) and Eq. (6-22), respectively. It is shown that the superheat needed for onset of nucleate boiling (ONB) decreases when the contact angle increases. This observation can be related to the formation energy which increases with increasing contact angle as discussed in Chapter 4.

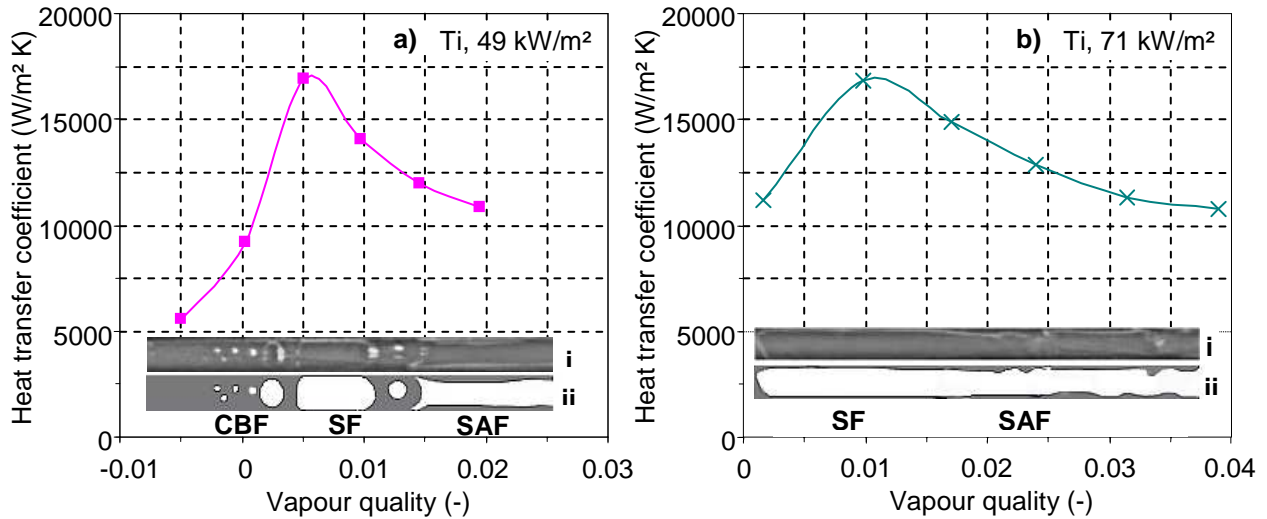


Figure 6-13. Flow patterns on titanium surface at 120 kg/m<sup>2</sup> s with i) original image and ii) analysed image.

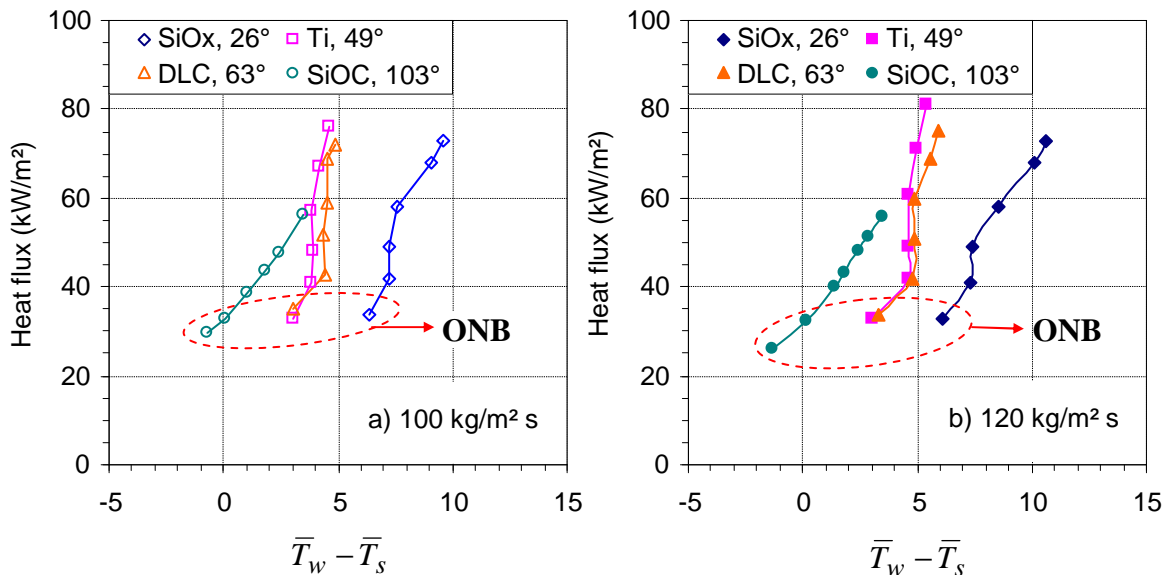


Figure 6-14. Boiling curves for various sample surfaces at 100 and 120 kg/m<sup>2</sup> s.

For SiOC hydrophobic surface, bubble generation occurs even at a fluid temperature lower than the saturation one. The main reason for this would be a large amount of pre-existing gas on the sample surface, even though the surface is relatively smooth. Indeed, when a hydrophobic surface is in contact with water, it will be covered by nanobubbles as shown by

Tyrell and Attard [6.10]. However, high rate of gas production leads to rapid bubble coalescence, causing deterioration of the heat transfer coefficient.

For SiOx highly-wetted surface, because of high superheat needed for the ONB, the heat transfer coefficient is relatively poor. Heat transfer would be mainly generated by conduction through the liquid layer, which is in contact with the heated surface. This layer is a result of balance of different factors such as the shear force at the liquid-vapour interface, the evaporation rate and the capillary effect. Since the surface is highly wetted, the capillary effect is thought to be the dominant factor. Thus, the thickness of the liquid layer is partially unchanged when the vapour quality or the heat flux increase. Therefore, the heat transfer coefficient remains almost constant as shown in Figure 6-11 and Figure 6-12. Another explanation for this would be the dominance of heat transfer by nucleate boiling, since the slight impact of heat flux on the heat transfer coefficient can be related to measurement uncertainties.

For Ti and DLC surfaces, the heat transfer performances in terms of local or average values are relatively similar, mainly because these surfaces have the same flow-pattern configuration. However, on DLC surface, the slug-annular flow occurred at a lower vapour quality and in a shorter time compared to Ti surface. This behaviour would be a consequence of the higher bubble emission frequency of DLC surface, since this surface has a higher contact angle (cf. Chapter 4). As a consequence, in average analysis, at a given heat flux, DLC surface shows a lower heat transfer coefficient than Ti surface.

The delay of onset of nucleate boiling was identified by Kandlikar [6.9] as a major cause for the back flow phenomenon. The author reported that the onset of nucleate boiling introduces a pressure spike, which may overcome the inertia of the incoming liquid and the pressure in the inlet manifold, and hence cause a reverse flow of varying intensity depending on the local conditions. To avoid this phenomenon, the author suggested reducing the superheat needed for onset of nucleate boiling. His suggestion is in good agreement with the present observations. Indeed, in this study, back flow occurred on the wetted sample surfaces which required more than 2°C of superheat for nucleate-boiling onset, but it is completely suppressed on unwetted surface for which bubble is generated at a superheat near by zero.

### 6.2.5 Analytical approaches

In this section, some analytical models will be presented with the purpose of highlighting the impact of the surface wettability on flow boiling in microchannels. Those models give the first insights into the role of contact angle on two-phase pressure drop, backflow velocity and boiling heat transfer coefficient. However, since they were developed based on several simple hypotheses, those models need to be improved in the future works for prediction of a larger set of experimental data.

#### Two-phase pressure drop

The two-phase pressure drop is classically calculated as a sum of the static pressure drop  $\Delta P_{static}$ , the momentum pressure drop  $\Delta P_{ac}$  and the frictional pressure drop  $\Delta P_{frict}$  as:

$$\Delta P_{tp} = \Delta P_{static} + \Delta P_{ac} + \Delta P_{frict} \quad (6-23)$$

Eq. (6-23) implies the following equation of pressure gradient per unit length:

$$\frac{dP_{tp}}{dz} = \frac{dP_{static}}{dz} + \frac{dP_{ac}}{dz} + \frac{dP_{frict}}{dz} \quad (6-24)$$

In the present study, because the test channel is in horizontal position, the static pressure drop can be neglected, leading to:

$$\frac{dP_{tp}}{dz} = \frac{dP_{ac}}{dz} + \frac{dP_{frict}}{dz} \quad (6-25)$$

wherein, the gradients per unit length of the momentum and frictional pressure drops can be estimated using the homogeneous or separated flow models for flow inside plain tubes such as: Lockhart and Martinelli [6.11], Mishima and Hibiki [6.12], Friedel [6.13], Chisholm [6.14], Bankoff [6.15], and Muller-Steinhagen and Heck [6.16]. A complete review of these models can be found in the book of Thome [6.6].

*In the homogeneous model*, the two-phase flow is approached by a homogeneous fluid which has a homogeneous viscosity  $\mu_{tp}$  and a homogeneous density  $\rho_{tp}$  defined as:

$$\mu_{tp} = x\mu_g + (1-x)\mu_l \quad (6-26)$$

$$\rho_{tp} = \rho_l(1-\varepsilon_h) + \rho_g\varepsilon_h \quad (6-27)$$

wherein,  $x$  is the vapour quality;  $\mu_l$  and  $\mu_g$  are the liquid and gas viscosities, respectively;  $\rho_l$  and  $\rho_g$  are the liquid and gas velocities, respectively; and  $\varepsilon_h$  is the homogenous void fraction determined as:

$$\varepsilon_h = \frac{1}{1 + \frac{1-x}{x} \frac{\rho_g}{\rho_l}} \quad (6-28)$$

*The separated flow model* considers the two phases to be artificially separated into two streams, each flowing in its own pipe. The areas of the two pipes are proportional to the void fraction  $\varepsilon_{sf}$ . Numerous methods are available for predicting the void fraction. In the present study, the correlation of Steiner [6.17] is used as recommended by Thome [6.6]:

$$\varepsilon_{sf} = \frac{x}{\rho_g} \left( \left[ 1 + 0.12(1-x) \right] \left( \frac{x}{\rho_g} + \frac{1-x}{\rho_l} \right) + \frac{1.18(1-x) \left[ g\sigma(\rho_l - \rho_g) \right]^{0.25}}{G^2 \rho_l^{0.5}} \right)^{-1} \quad (6-29)$$

wherein,  $g$  is the gravity,  $\sigma$  is the liquid-vapour surface tension and  $G$  is the mass flux.

The present experimental data are then compared to the data given by the above correlations, as shown in Figure 6-15 and Figure 6-16. It is important to notice that for the correlation of Lockhart and Martinelli [6.11], the case of laminar liquid flow and turbulent gas flow is applied for the present study, since the liquid Reynolds number is about 400 and the vapour Reynolds number is about 8000.

It is shown that the method of Lockhart and Martinelli [6.11] gives the best estimation for the experimental-data evolution trend and values. The second best method is the correlation of Bankoff [6.15] and the third best is the correlation of Muller-Steinhagen and Heck [6.16]. However, none of these correlations predicts the dependence of the two-phase pressure drop with the contact angle. For a better prediction, it is necessary to take into account the pressure drop caused by the surface tension force generated at the triple contact line. This pressure drop is called “wetting pressure drop”  $P_\theta$ . Therefore, Eq. (6-25) is modified as:

$$\frac{dP_{tp}}{dz} = \frac{dP_{ac}}{dz} + \frac{dP_{frict}}{dz} + \frac{dP_\theta}{dz} \quad (6-30)$$

Thus, the gradient of the wetting pressure drop can be determined as:

$$\frac{dP_\theta}{dz} = \frac{dP_{tp}}{dz} - \left( \frac{dP_{ac}}{dz} + \frac{dP_{frict}}{dz} \right) \quad (6-31)$$

wherein, the two-phase pressure drop gradient is determined by experimental measurements, and the gradients of the momentum and frictional pressure drops can be estimated by the correlation of Lockhart and Martinelli [6.11] which give the best estimation:

$$\frac{dP_\theta}{dz} = \left( \frac{dP_{tp}}{dz} \right)_{\text{exp}} - \left( \frac{dP_{ac}}{dz} + \frac{dP_{frict}}{dz} \right)_{\text{Lockhart and Martinelli}} \quad (6-32)$$

At a first approximation, the wetting pressure drop is assumed to be independent of the vapour quality and mass flux. Hence, for a given contact angle, the wetting pressure drop is taken as the statistical average value as:

$$\frac{dP_\theta}{dz} = \frac{1}{N} \sum_{i=1}^N \left[ \left( \frac{dP_{tp}}{dz} \right)_{\text{exp}}^i - \left( \frac{dP_{ac}}{dz} + \frac{dP_{frict}}{dz} \right)_{\text{Lockhart and Martinelli}}^i \right] \quad (6-33)$$

wherein,  $N$  is the number of experimental points for each contact angle.

Besides, the wetting pressure drop gradient can be analytically determined by a simple model in which, a confined bubbly (or slug) with a length  $L_b$  circulates inside a circular tube of hydraulic diameter  $D_h$  as shown in Figure 6-17. At bubble head and tail, the contact angles are the advancing contact angle  $\theta_a$  and the receding contact angle  $\theta_r$ , respectively. For wetted surfaces, the surface tension force at the bubble tail acts to push the bubble in the flow direction, but this force at the bubble head acts to pull the bubble backward. The wetting pressure drop is thereby defined as the pressure difference generated by the difference of the surface tension forces at the bubble head and tail. Thus, it can be determined as:

$$\Delta P_\theta = \frac{4\sigma(\cos \theta_r - \cos \theta_a)}{D_h} \quad (6-34)$$

The gradient per unit length of the wetting pressure drop can be thereby expressed as:

$$\frac{dP_\theta}{dz} = \frac{4\sigma(\cos\theta_r - \cos\theta_a)}{D_h} \frac{1}{L_b} \quad (6-35)$$

In boiling conditions, the advancing and receding contact angles of a bubble are difficult to be measured. At a first approximation, the advancing contact angle  $\theta_a$  is assumed to be equal to the static contact angle  $\theta$  and the receding contact angle  $\theta_r$  is assumed to be equal to 0. This hypothesis implies:

$$\frac{dP_\theta}{dz} = K_\theta (1 - \cos\theta) \quad (6-36)$$

wherein  $K_\theta$  is a constant defined as:

$$K_\theta = \frac{4\sigma}{D_h} \frac{1}{L_b} \quad (6-37)$$

Eq. (6-37) shows that the gradient of the wetting pressure drop has a linear relation with  $(1 - \cos\theta)$ . In order to validate this observation, the gradient of the wetting pressure drop determined by Eq. (6-33) is plotted as a function of  $(1 - \cos\theta)$ , as shown in Figure 6-18. Indeed, it is observed that the data evolution can be fitted by a linear regression with a regression coefficient greater than 0.999. The following correlation is thereby suggested to estimate the wetting pressure drop:

$$\frac{dP_\theta}{dz} = 10^3 \times [6.81(1 - \cos\theta) - 1.51] \quad (6-38)$$

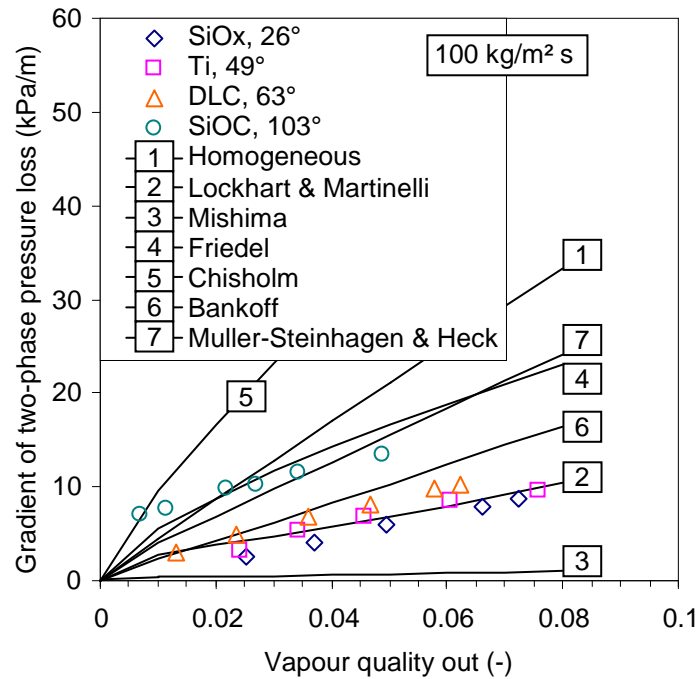


Figure 6-15. Comparison between exp. and theoretical data of two-phase pressure drop gradient at 100 kg/m² s.

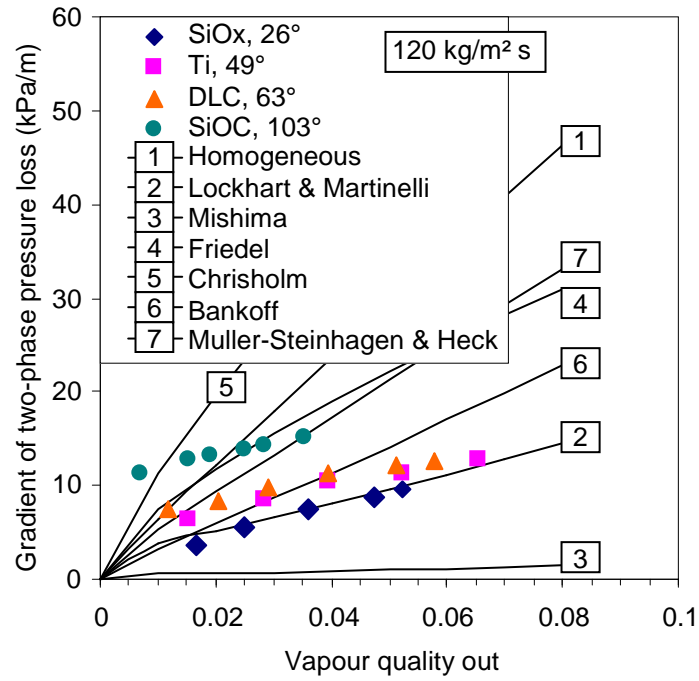


Figure 6-16. Comparison between exp. and theoretical data of two-phase pressure drop gradient at 120 kg/m<sup>2</sup> s.

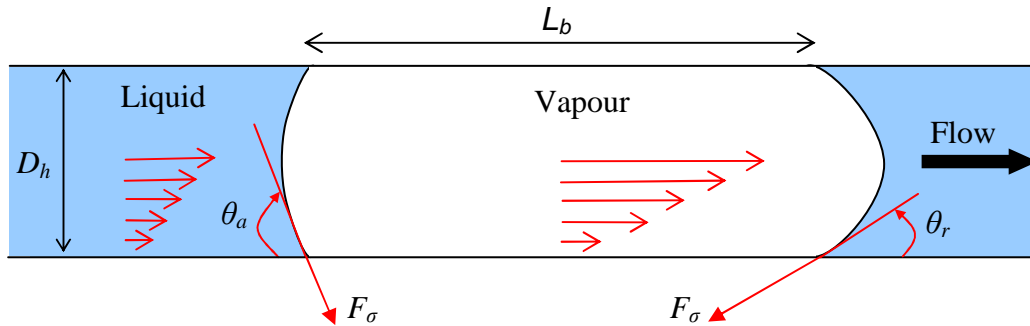


Figure 6-17. Schematically view of a confined bubble or slug inside a circular tube.

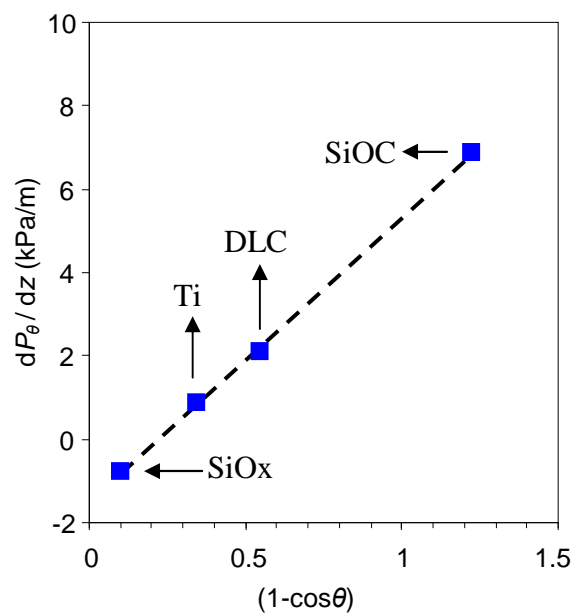


Figure 6-18. Gradient of the wetting pressure drop vs.  $(1-\cos\theta)$ .

Therefore, using Eq. (6-30) where the gradients of the momentum and friction pressure drops are estimated by the correlation of Lockhart and Martinelli [6.11], and the gradient of the wetting pressure is determined by Eq. (6-38), the two-phase pressure can be approximated. Figure 6-19 shows a good agreement of the predicted and measured two-phase pressure drop. Indeed, about 86% of the data are included within the lines of 20% error.

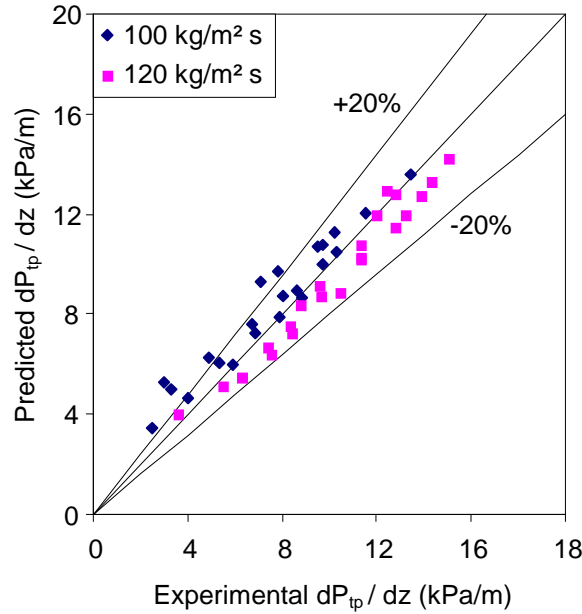


Figure 6-19. Comparison of the predicted and experimental values of the wetting pressure-drop gradient.

### Backflow phenomenon

As discussed in the previous sections, backflow phenomenon was observed on the wetted sample surfaces. This observation would be related to the delay of onset of nucleate boiling which generates a reverse flow by high evaporation rate at the liquid-vapour interface. In the following paragraphs, a simple model will be developed, giving a first insight of the backflow phenomenon.

Assuming that a slug of volume  $V_b$  is created in the test channel, the energy needed for this process can be expressed as:

$$E = \rho_v V_b H_{lv} \quad (6-39)$$

wherein  $\rho_v$  is the vapour density and  $H_{lv}$  is the liquid-vapour latent heat.

Due to the delay of onset of nucleate boiling, before the formation of this slug, liquid in the test channel is superheated. Assuming that the temperature of the superheat liquid is equal to the wall temperature, the power released by the superheat-liquid flow when its temperature decreases to the saturation temperature can be estimated as:

$$\dot{E} = \pi \frac{D_h^2}{4} G C_p \Delta T_{wf, ONB} \quad (6-40)$$

wherein,  $D_h$  is the hydraulic diameter,  $G$  is the mass flux,  $C_p$  is the liquid specific heat and  $\Delta T_{wf, ONB}$  is the wall superheat for onset of nucleate boiling.

Therefore, the time needed to obtain the slug of volume  $V_g$  can be approximated as:

$$\tau = \frac{E}{\dot{E}} = \frac{1}{G} \frac{\rho_v H_{lv}}{C_p \Delta T_{wf, ONB}} L_b \quad (6-41)$$

wherein  $L_b$  is the slug length which can be estimated as:

$$L_b = \frac{V_b}{\pi \frac{D_h^2}{4}} \quad (6-42)$$

Assuming that the slug homogeneously grows in both sides of its tail and head, the average growth velocity of this slug by evaporation in one side can be determined as:

$$U_{eva} = \frac{L_b}{2\tau} = \frac{G}{2} \frac{C_p \Delta T_{wf, ONB}}{\rho_v H_{lv}} \quad (6-43)$$

At its tail, the slug is pushed by the liquid flow with an average velocity calculated as:

$$U_l = \frac{G}{\rho_l} \quad (6-44)$$

wherein  $\rho_l$  is the liquid density.

Therefore, the average velocity of the reverse flow can be estimated as:

$$U_{backflow} = \frac{G}{\rho_l} \left( \frac{Ja}{2} - 1 \right) \quad (6-45)$$

wherein  $Ja$  is the Jakob number defined as:

$$Ja = \frac{\rho_l C_p \Delta T_{wf, ONB}}{\rho_v H_{lv}} \quad (6-46)$$

Eq. (6-45) shows that the backflow occurs when  $\mathbf{Ja} \geq 2$ . This criterion is in good agreement with the present experimental observation. Indeed, among all the sample surfaces, only SiOC surface has a Jakob number lower than 2, as shown in Figure 6-20, and only on this surface, the backflow was not experimentally observed.



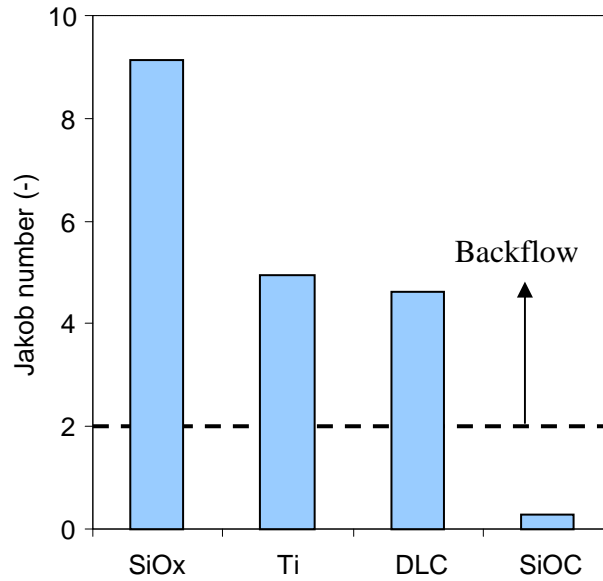


Figure 6-20. Jakob numbers for all smooth sample surfaces.

### Heat transfer coefficient

The purpose of this section is to develop an analytical model which enables a better understanding of the impact of flow patterns on the heat transfer coefficient. Three modes of heat transfer are suggested as:

- $H_1$ : conduction through the liquid layer in contact with the heated surface,
- $H_2$ : evaporation of the superheated liquid,
- $H_3$ : nucleate boiling.

For the mode  $H_1$ , the heat transfer coefficient  $h_l$  is determined as the ratio of the liquid thermal conductivity  $\lambda_l$  to the thickness  $\delta_l$  of the liquid layer at the heated surface:

$$h_l = \frac{\lambda_l}{\delta_l} \quad (6-47)$$

At a first approximation, because the Pyrex lid is low wetted, liquid is assumed to be homogeneously distributed at the top and bottom of the test channel when low-wetted sample surfaces are used (cf. Figure 6-21a). Hence, the liquid layer thickness can be determined as:

$$\delta_l = \frac{H}{2}(1 - \varepsilon) \quad (6-48)$$

wherein  $\varepsilon$  is the void fraction, which is calculated by Eq. (6-29) given by Steiner [6.17].

However, when the sample surface is highly-wetted, due to high capillary effect at this surface, the whole amount of liquid is assumed to be concentrated at the bottom of the test channel as shown in Figure 6-21b. This implies:

$$\delta_l = H \times (1 - \varepsilon) \quad (6-49)$$

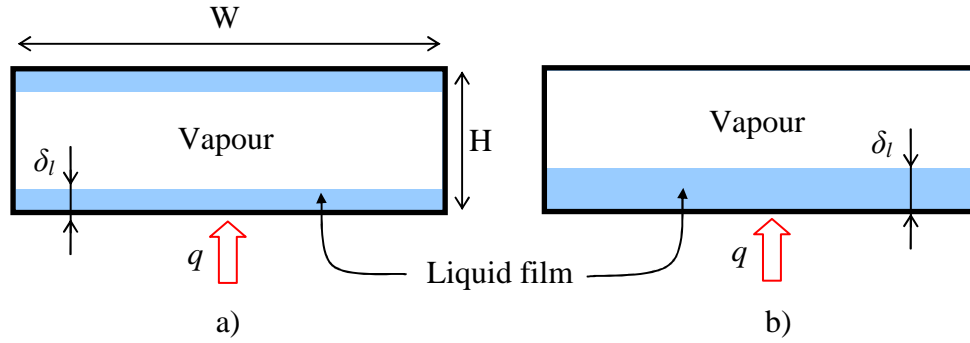


Figure 6-21. Schematically view of the cross section of the test channel for a) low-wetted surfaces and b) highly-wetted surfaces.

For the mode  $H_2$ , vapour is mainly formed by evaporation of the superheated liquid at the liquid-vapour interface. If a mass flux  $\dot{m}_g$  is generated, the energy balance gives:

$$\dot{m}_g = \frac{C_p \Delta T_{ls}}{H_{lv}} \dot{m}_l \quad (6-50)$$

wherein  $\dot{m}_l$  is the mass flux of the superheated liquid,  $C_p$  is the liquid specific heat,  $H_{lv}$  is the liquid-vapour latent heat and  $\Delta T_{ls}$  is the liquid superheat.

Eq. (6-50) can be also expressed as:

$$\frac{x}{1-x} = \frac{C_p \Delta T_{ls}}{H_{lv}} \quad (6-51)$$

wherein  $x$  is the vapour quality.

Moreover, the heat transfer coefficient of mode  $H_2$  is calculated as:

$$h_2 = \frac{q}{\Delta T_{ls}} \quad (6-52)$$

wherein  $q$  is the heat flux.

Eqs. (6-51) and (6-52) lead to:

$$h_2 = \frac{1-x}{x} \frac{C_p}{H_{lv}} q \quad (6-53)$$

For the mode  $H_3$ , the correlation of Cooper [6.18] is used to estimate the nucleate boiling heat transfer coefficient:

$$h_3 = 55 p^{*0.12} (-\log_{10} p^*)^{-0.55} q^{0.67} M^{-0.5} \quad (6-54)$$

It is important to notice that at a first approximation, the effects of surface roughness and wettability are not considered in Eq. (6-54).

The evolution trends of the heat transfer coefficient with the vapour quality for the three modes are illustrated in Figure 6-22.

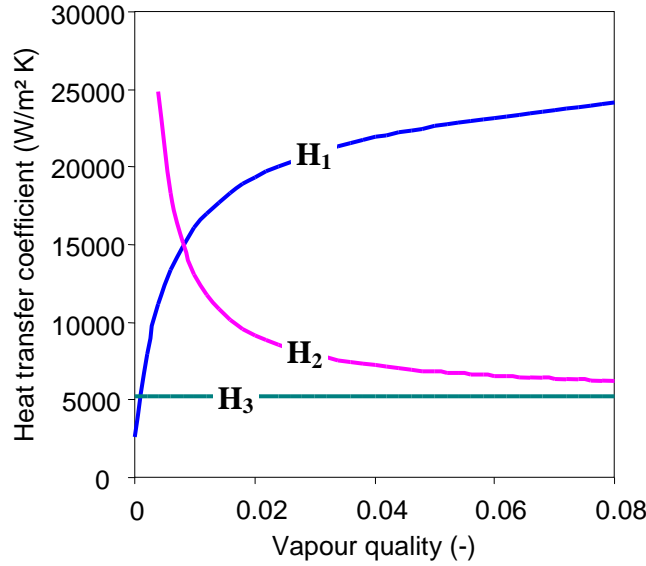


Figure 6-22. Heat transfer coefficient vs. vapour quality for the three modes  $H_1$ ,  $H_2$ ,  $H_3$  at  $40 \text{ kW/m}^2$ .

It is observed that the curves for  $H_1$  and  $H_2$  have the opposite tendency, and for  $H_3$  the curve is a horizontal line. When the flow patterns change, the heat transfer modes should also change. The following hypotheses are used in the present model:

- In confined-bubbly and slug flow:  $H_1$  is the dominant heat transfer mode. The average heat transfer coefficient is thereby determined as:

$$h = h_1 \quad (6-55)$$

- In slug-annular flow: heat is transferred by modes  $H_2$  and  $H_3$  together, which implies:

$$h = h_2 + h_3 \quad (6-56)$$

- In churn flow (on highly-wetted surface): heat is transferred only by nucleate boiling inside the liquid film at the wall, leading to:

$$h = h_3 \quad (6-57)$$

Based on the above hypotheses and on the variation trends of the heat transfer coefficient for the three heat transfer modes, the average heat transfer coefficients are calculated as:

- For low-wetted surfaces:

$$h = \min(h_1, h_2 + h_3) \quad (6-58)$$

- For highly-wetted surfaces:

$$h = \min(h_1, h_3) \quad (6-59)$$

The present model is validated by comparisons with the experimental data as illustrated in Figure 6-25. In general, the model shows a good prediction of the experimental values with all data included within the lines of 20% error.

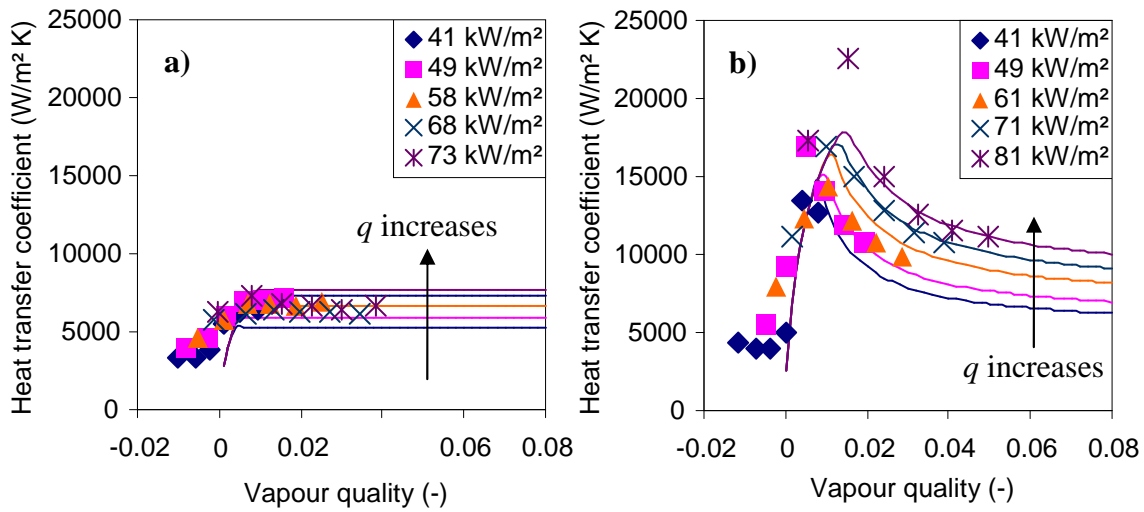


Figure 6-23. Comparison of experimental and predicted heat transfer coefficient for a) SiOx surface and b) Ti surface at 120 kg/m<sup>2</sup> s. For each heat flux, the predicted curve is a continuous line with the same colour as the experimental dots.

The suggested model also gives a good prediction for variation trends of the heat transfer coefficient with vapour quality and heat flux, especially for low-wetted surfaces. However, for highly-wetted surface, experimental data show that the heat transfer coefficient remains nearly constant with change in heat flux, but this behaviour cannot be predicted using the present model. Further works are needed in order to solve this issue as well as to estimate the heat transfer coefficient on unwetted surfaces. Besides, the present model should be validated by a larger set of experimental data from other laboratories worldwide.

## 6.3 Micro-structured surfaces

### 6.3.1 Contact angle

#### Theoretical contact angles

For both structured samples (cf. Section 5.1.1), since the micro-hole diameter is about eight times greater than the micro-hole depth, a water droplet is assumed to be in Wenzel state on these surfaces.

The  $\mu$ -Ti sample is chemically heterogeneous. Indeed, this is a titanium surface containing holes with Pyrex material at the bottom (cf. Figure 6-24a). Therefore, a modified equation of Wenzel model [6.19] is suggested to estimate the contact angle as:

$$\cos \theta = \Phi_{s,Pyrex} \times \cos \theta_{smooth,Pyrex} + (1 - \Phi_{s,Pyrex}) \cos \theta_{smooth,Ti} \quad (6-60)$$

wherein,  $\Phi_{s,Pyrex}$  is the ratio of the Pyrex area to the overall area, and  $\theta_{smooth,Pyrex}$  and  $\theta_{smooth,Ti}$  are the water contact angles on smooth surfaces of Pyrex and titanium, respectively. In the present study,  $\Phi_{s,Pyrex} = 0.3$ ,  $\theta_{smooth,Pyrex} = 74^\circ$  and  $\theta_{smooth,Ti} = 49^\circ$ , hence, Eq. (6-60) gives a contact angle of about  $58^\circ$ .

The  $\mu$ -SiOx sample is chemically homogeneous since SiOx material covers all area of the sample (cf. Figure 6-24b). Thus, for this surface, the contact angle can be approximated using Wenzel equation as:

$$\cos \theta = r \cos \theta_{smooth} \quad (6-61)$$

wherein,  $r$  is the ratio of the actual area to the apparent one of the contact surface and  $\theta_{smooth}$  is the contact angle of water on a smooth surface. For the  $\mu$ -SiOx surface,  $r = 1.03$  and  $\theta_{smooth} = 26^\circ$ , giving a contact angle of about  $22^\circ$ .

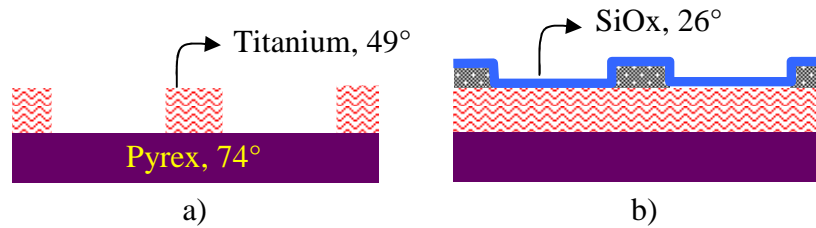


Figure 6-24. Schematic view of topographies of the structured sample surfaces.

### Experimental measurements

The contact angles of water on the structured samples were measured using the sessile drop technique with KRÜSS EasyDrop systems in a cleanroom (cf. 2.2.3). Figure 6-25 illustrates images of water droplets on these surfaces. The obtained contact angles are  $20^\circ$  and  $65^\circ$  for the  $\mu$ -SiOx surface and the  $\mu$ -Ti surface, respectively. These values are close to the theoretical values determined in the above section, with a deviation of about 10%.

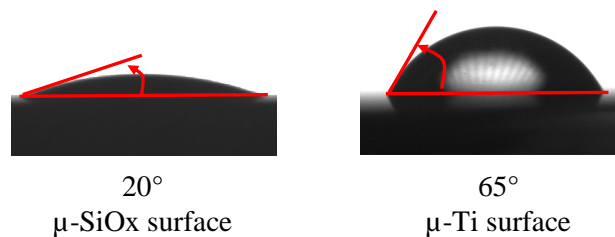


Figure 6-25. Water droplets on the structured sample surfaces at the ambient temperature.

### 6.3.2 Pressure drop

The micro-patterning has a negligible impact on the single-phase pressure drop as shown in Section 5.4.2. However, in boiling conditions, it was observed that the micro-patterning significantly influences the two-phase pressure drop. Figure 6-26 shows the comparisons of the two-phase pressure drops measured on the structured ( $\mu$ -SiOx and  $\mu$ -Ti) surfaces with those measured on the corresponding smooth (SiOx and Ti) surfaces. For both mass fluxes of

100 kg/m<sup>2</sup> s and 120 kg/m<sup>2</sup> s, the two-phase pressure drops of the structured surfaces are significantly lower than the ones of the smooth surfaces, with an average reduction of 40%.

The impact of surface structuring on two-phase pressure drop is related to the superheat needed for onset of nucleate boiling (ONB). Indeed, according to the boiling theory presented in Chapter 1 (cf. Section 1.1), the structured surfaces which contain micro-holes require a lower superheat for ONB compared to the smooth surfaces. This remark is validated by experimental measurements that will be presented in Section 6.3.4. Hence, on the structured surfaces, during the growth of bubbles or slugs, the evaporation rate of liquid would be lower because liquid is superheated at a lower temperature. This leads to a lower friction force at the liquid-vapour interfaces, reducing the two-phase pressure drop.

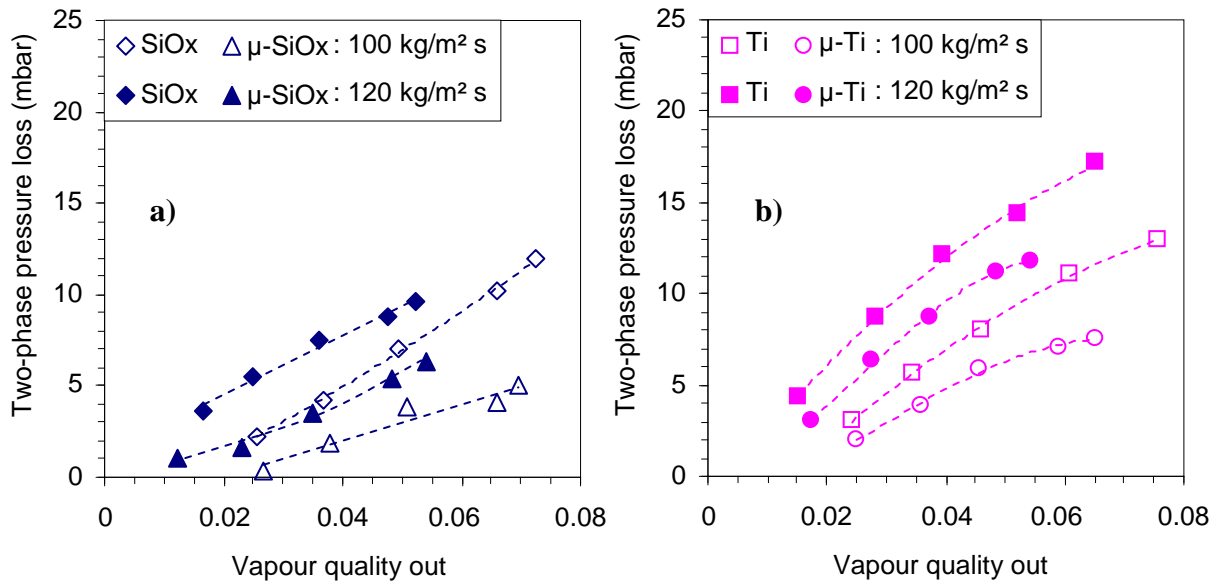


Figure 6-26. Two-phase pressure drop on the smooth (SiOx and Ti) and structured (μ-Ti and μ-SiOx) surfaces at 100 kg/m<sup>2</sup> s and at 120 kg/m<sup>2</sup> s.

In Section 6.2.2, it was observed that the two-phase pressure drop increases when the contact angle increases. However, compared to Ti surface, μ-Ti surface shows a lower two-phase pressure drop even though it has a higher contact angle. This behaviour would be explained by the fact that in the present study, the impact of the superheat for ONB is dominant compared to the impact of contact angle. For μ-SiOx surface, a lower contact angle as well as a lower superheat for ONB would be the main causes for a lower two-phase pressure drop compared to SiOx surface.

### 6.3.3 Flow patterns visualization

The two-phase flows on the structured surfaces were more stable than those on the smooth surfaces. The reduction of flow instabilities can be related to the superheat needed for onset of nucleate boiling which significantly decreases by micro-patterning [6.9]. Unlike SiOx surface, on μ-SiOx surface, the slug-annular flow was observed instead of the churn flow, but bubble generation still occurred in the liquid film of the pre-existing slugs (cf. Figure 6-27).

The flow patterns of μ-Ti surface were similar to those of Ti surface, i.e., they were also identified as: bubbly flow, slug flow and slug-annular flow. However, the back-flow length on μ-Ti surface is significantly lower than the one on Ti surface as illustrated in Figure 6-28. This

would also be a consequence of reduction of the ONB superheat according to the backflow model described in Section 6.2.5. Furthermore, more nucleation sites were activated on the structured surfaces compared to the smooth surfaces.

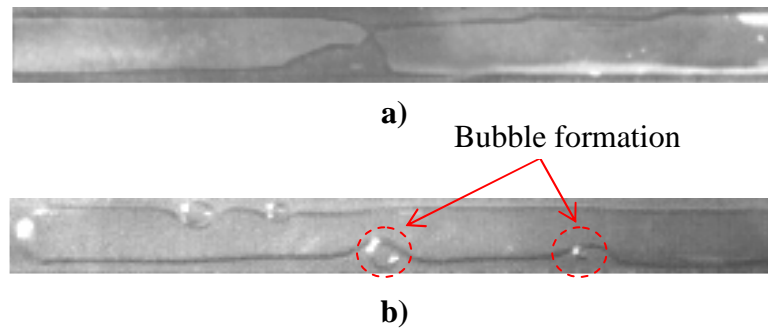


Figure 6-27. Representative images of flow patterns observed on  $\mu$ -SiOx surface: a) slug-annular flow and b) bubble generation in liquid film.

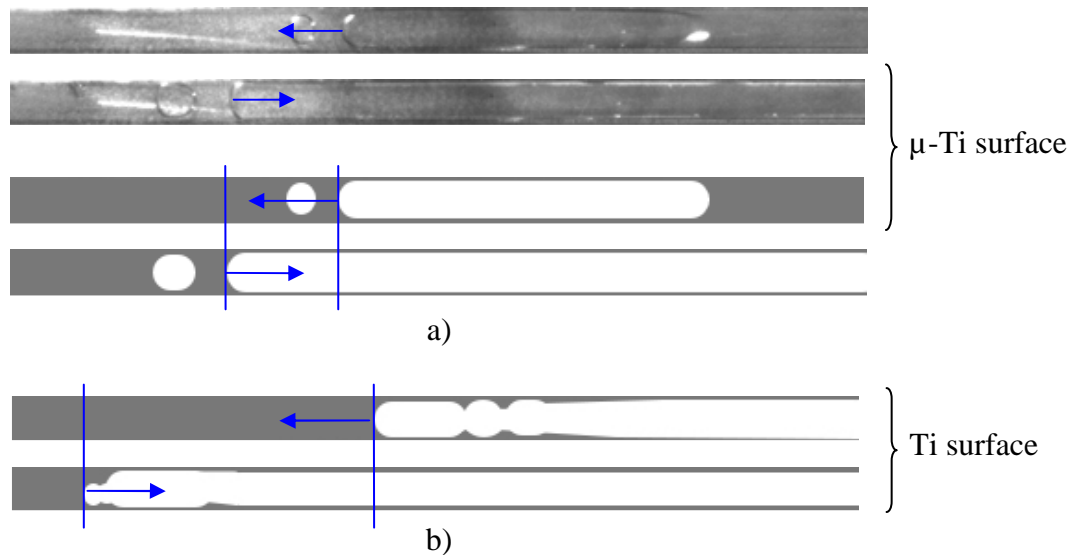


Figure 6-28. Back flow observation: a) on  $\mu$ -Ti surface with original and analysed images and b) on Ti-surface with analysed images.

### 6.3.4 Heat transfer

#### Experimental measurements

Figure 6-29 and Figure 6-30 show comparison of the heat transfer performances of  $\mu$ -SiOx and  $\mu$ -Ti surfaces to those of SiOx and Ti surfaces, respectively. For both operating mass fluxes of  $100 \text{ kg/m}^2 \text{ s}$  and  $120 \text{ kg/m}^2 \text{ s}$ , the structured surfaces exhibit significant enhancements in heat transfer coefficient compared to the smooth surfaces.

In comparison with SiOx surface, the average enhancement in heat transfer coefficient given by SiOx surface is about 73% at  $100 \text{ kg/m}^2 \text{ s}$  and about 67% at  $120 \text{ kg/m}^2 \text{ s}$ . Improvements are obtained with all operating heat fluxes between  $40 \text{ kW/m}^2$  and  $80 \text{ kW/m}^2$ . Furthermore, in average, the mass flux shows a negligible effect on the heat transfer coefficient. It is interesting to notice that on  $\mu$ -SiOx surface, the evolution trend of the heat transfer coefficient with the vapour quality differs from the one on SiOx surface, but is similar to those on Ti and

DLC surfaces. In other words, the heat transfer highly increases and then decreases when the vapour quality increases.

At a given heat flux, the critical vapour quality is defined as the vapour quality at which the maximum heat transfer coefficient is reached. Figure 6-29 shows that the critical vapour qualities of  $\mu$ -SiOx surface are from 0.02 to 0.03 with an average value of 0.025. They are significantly higher than the critical vapour qualities of the other surfaces varying between 0.005 and 0.015. Therefore, using  $\mu$ -SiOx surface, the intermittent dryout is delayed.

In comparison with Ti surface,  $\mu$ -Ti surface shows an average enhancement in heat transfer coefficient of about 85% at  $100 \text{ kg/m}^2 \text{ s}$  and of about 25% at  $120 \text{ kg/m}^2 \text{ s}$ . Among all the sample surfaces,  $\mu$ -Ti surface exhibits the best heat transfer performance. Especially, its heat transfer coefficient can reach to  $50000 \text{ W/m}^2 \text{ s}$  at a mass flux of  $100 \text{ kg/m}^2 \text{ s}$  and at heat flux of  $68 \text{ kW/m}^2$ . Furthermore, unlike the others, for  $\mu$ -Ti surface, the mass flux shows a significant impact on average heat transfer coefficient.

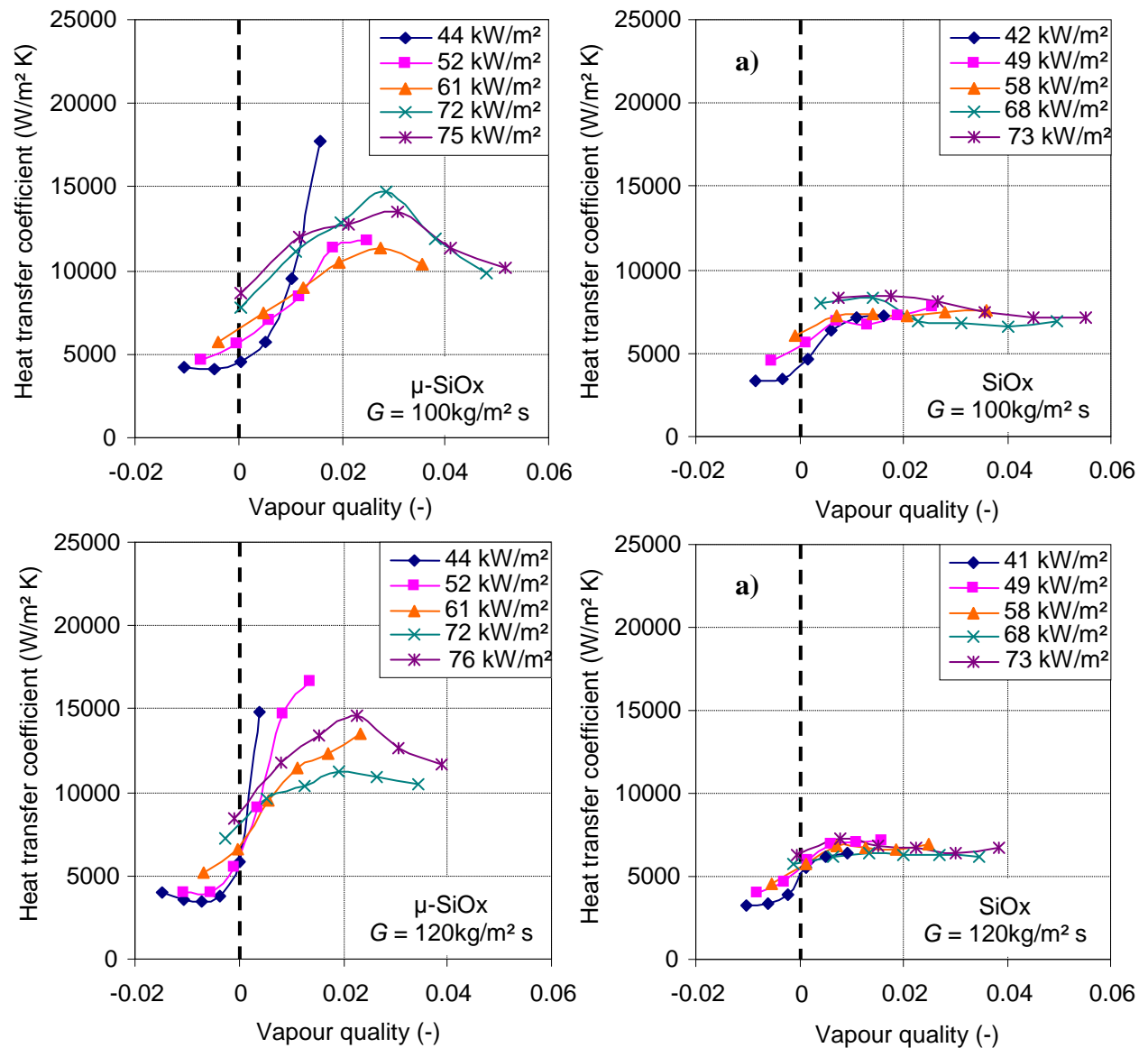


Figure 6-29. Comparison of evolutions of the heat transfer coefficient with the vapour quality for SiOx and  $\mu$ -SiOx surfaces at  $100 \text{ kg/m}^2 \text{ s}$  and  $120 \text{ kg/m}^2 \text{ s}$ .



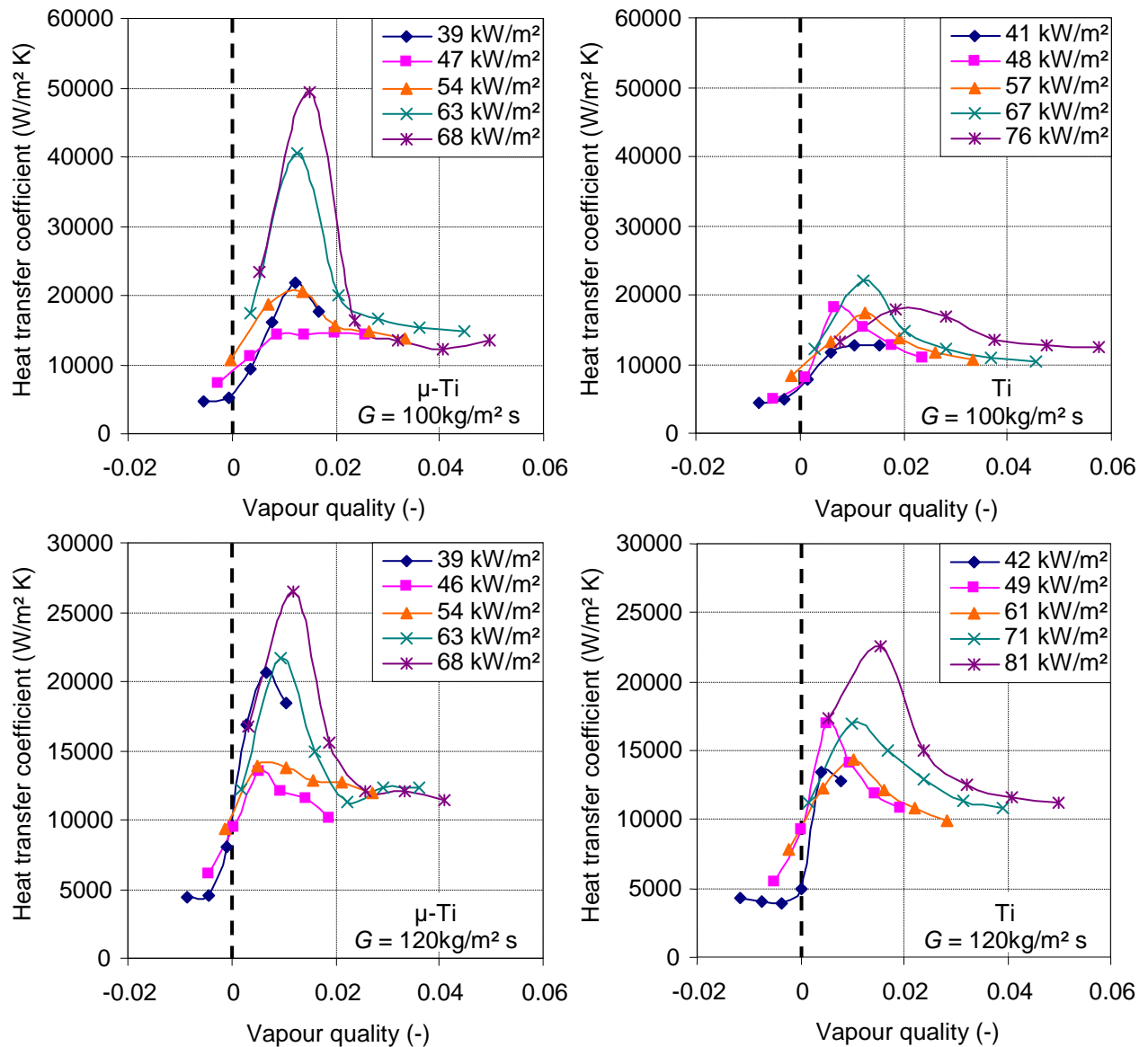


Figure 6-30. Comparison of evolutions of the heat transfer coefficient with the vapour quality for Ti and  $\mu$ -Ti surfaces at  $100 \text{ kg/m}^2 \text{ s}$  and  $120 \text{ kg/m}^2 \text{ s}$ .

### Discussion

For flow boiling in microchannels, the main effect of micro-patterning is identified as the reduction of the superheat for onset of nucleation (ONB). This remark is highlighted by comparisons of the boiling curves for the smooth and structured surfaces, as shown in Figure 6-31 where the wall and saturation temperatures are taken as the average temperatures defined by Eqs. (6-21) and (6-22), respectively.

In comparison with the smooth surfaces, the structured surfaces exhibit lower superheats for ONB. Especially, between SiOx and  $\mu$ -SiOx surfaces, the superheat for ONB is reduced from about  $6^\circ\text{C}$  to about  $2.5^\circ\text{C}$ , which is close to the superheat for ONB of Ti and DLC surfaces. This would be the cause for the change from churn flow to slug-annular flow when SiOx surface is replaced by  $\mu$ -SiOx surface. Indeed, churn flow is related to high liquid superheat that causes rapid evaporation at the liquid-vapour interface and generates thereby flow instabilities.

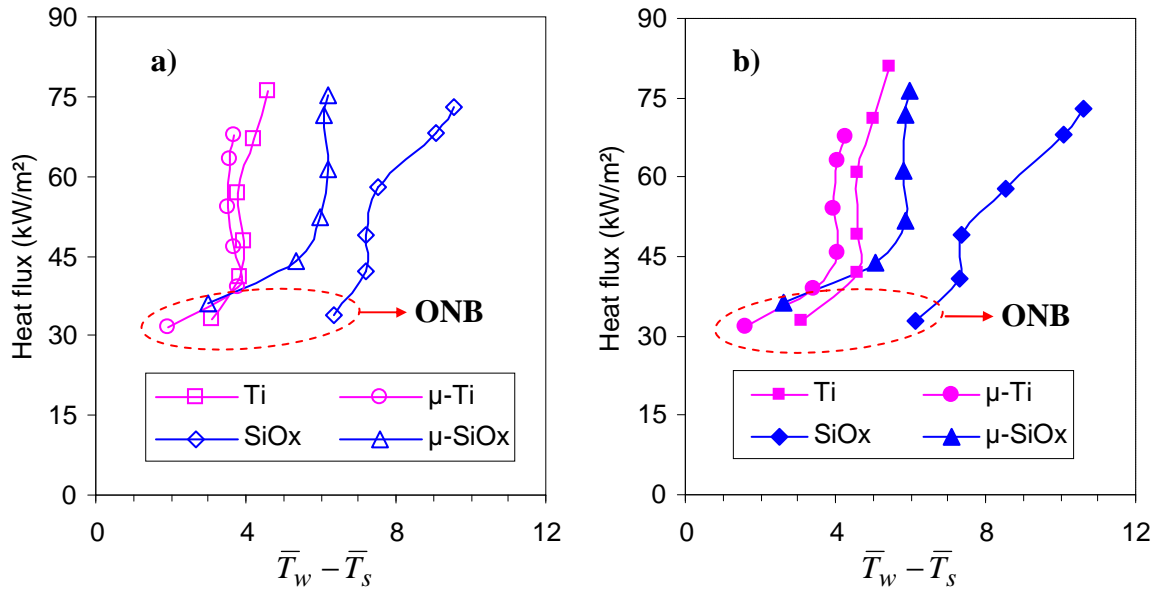


Figure 6-31. Boiling curves of smooth and structured sample surfaces at a) 100 kg/m<sup>2</sup> s and b) 120 kg/m<sup>2</sup> s.

Since the flow patterns on  $\mu$ -SiOx surface are similar to those of Ti and DLC surfaces, the variation tendency of the heat transfer coefficient with the vapour quality on this surface is also similar to the ones on Ti and DLC surfaces. However, because  $\mu$ -SiOx surface is highly wetted, the liquid rewetting rate on this surface is significantly higher than those of Ti and DLC surfaces. As a result, the intermittent dryout occurs on  $\mu$ -SiOx surface at a higher critical vapour quality.

Among all wetted surfaces,  $\mu$ -Ti surface generates the lowest superheat for ONB. This would be a reason for the best heat transfer performance obtained with this surface. The effect of mass flux observed with this surface should be related to the number of the active nucleation sites. Indeed, at a lower mass flux, less number of micro-holes are flooded by liquid penetration and hence, more nucleation sites will be activated in boiling conditions, giving higher heat transfer performance. The impact of the number of nucleation sites is significant at low vapour qualities where nucleate boiling is the dominant heat transfer mode. For  $\mu$ -SiOx surface which is highly wetted, all the nucleation sites are nearly flooded by liquid penetration even at low mass flux. Therefore, from 100 kg/m<sup>2</sup> s to 120 kg/m<sup>2</sup> s, the number of active nucleation sites remains relatively unchanged, leading to the same heat transfer performance.

The differences in boiling behaviours between the structured and smooth surfaces are summarized in Table 6-4 below.

Table 6-4. Comparisons between the smooth and structured samples.

Structured surface versus Smooth surface	Pressure drop	Flow patterns	Heat transfer coefficient
$\mu$ -SiOx versus SiOx	Reduction ( $\approx -40\%$ )	SAF instead of CF	Enhancement ( $\approx +40\%$ )
$\mu$ -Ti versus Ti	Reduction ( $\approx -40\%$ )	Lower backflow length	Enhancement ( $\approx +85\%$ at 100 kg/m <sup>2</sup> and $\approx +25\%$ at 120 kg/m <sup>2</sup> )

## 6.4 Conclusion

The flow boiling heat transfer of water on coated and micro-structured surfaces was determined. The main findings of the present work can be summarized as follows:

- The two-phase pressure drop decreases when the contact angle decreases or when the surfaces are micro-structured. This behaviour was related to the capillary effect and the delay of onset of nucleate boiling. A model was developed to estimate the influence of the contact angle on the two-phase pressure drop.
- Flow patterns were identified for all the sample surfaces. For low-wetted and structured surfaces, confined-bubbly flow, slug flow and slug-annular flow were detected. For highly-wetted and unwetted smooth surfaces, instead of the slug-annular flow, the churn flow was observed. The appearance of churn flow was related to evaporation of highly-superheated liquid and bubble generation around slugs which are the main cause of flow instabilities. In slug-annular or churn flow regimes, intermittent dryout following by liquid rewetting was observed.
- Backflow phenomenon was visualized on all the samples except SiOC hydrophobic surface. A model based on the evaporation of the superheated liquid was suggested to predict the appearance of backflow.
- The general tendency of evolution of the heat transfer coefficient with the vapour quality is as follows: when boiling occurs, the heat transfer coefficient increases with the vapour quality, and then decreases before remaining constant. However, for SiOx highly wetted surface, the heat transfer coefficient changes slightly when the vapour quality or the heat flux increase. For SiOC unwetted surface, nucleate boiling occurs even at a negative vapour quality, i.e. at a fluid temperature lower than the saturation one. A heat transfer model was developed based on three heat transfer modes: conduction through the liquid layer, evaporation of superheated liquid and nucleation boiling. At a first approximation, this model gives a good agreement with the experimental data.
- The micro-structured surfaces show significant enhancements (up to 85%) in heat transfer compared to the smooth surfaces. Especially, using the highly-wetted structured surface, the intermittent dryout is improved, i.e. the critical vapour quality increases.

## 6.5 Reference

- [6.1] S.J. Kline, F.A. McClintock, Describing uncertainties in single-sample experiments, *Mech. Eng.* 75 (1953), 3-8.
- [6.2] R. Revellin, J. R. Thome, Experimental investigation of R-134a and R-245fa two-phase flow in microchannels for different flow conditions, *Int. J. Heat and Fluid Flow* 28 (2007), 63-71.
- [6.3] S.G. Kandlikar, M.E. Steinke, S. Tian, L.A. Campbell, High-speed photographic observation of flow boiling of water in parallel minichannels, 35th Proceedings of National Heat Transfer Conference (2001), Anaheim, CA.

- [6.4] D. Brutin, F. Topin, L. Tadrist, Experimental study of unsteady convective boiling in heated minichannels, *Int. J. Heat and Mass Transfer* 16 (2003), 2957-2965.
- [6.5] C. Choi, C. Huh, D. Kim, M. Kim, Wettability effect on flow boiling in an mems-based single glass microchannel, *The Sixth Int. ASME Conference on Nanochannels, Microchannels and Minichannels ICNMM2008* (2008), Darmstadt, Germany.
- [6.6] J.R. Thome, *Heat Transfer engineering data book III*, Web-based reference book available on web at [www.wlv.com/products](http://www.wlv.com/products) (2010).
- [6.7] K.A. Triplett, S.M. Ghiaasiaan, S.I. Abdel-Khalid, D.L. Sadowski, Gas-liquid two-phase flow in microchannels Part I: two-phase flow patterns, *Int. J. Multiphase Flow* 25 (1999), 377-394.
- [6.8] E. Sobierska, R. Kulenovic, R. Mertz, Heat transfer mechanism and flow pattern during flow boiling of water in a vertical narrow channel- experimental results, *Int. J. Thermal Sciences* 46 (2007), 1172-1181.
- [6.9] S.G. Kandlikar, Nucleation characteristics and stability considerations during flow boiling in microchannels, *Exp. Thermal and Fluid Science* 30 (2006), 441-447.
- [6.10] J.W.G. Tyrrell, P. Attard, Images of nanobubbles on hydrophobic surfaces and their interactions, *Phys. Rev. Letters* 87 (2001), 176104.
- [6.11] R.W. Lockhart, R.C. Martinelli, Proposed correlation data for isothermal two-phase two-component flow in pipes, *Chem. Eng. Progr.* 45 (1949), 39-45.
- [6.12] K. Mishima, T. Hibiki, Some characteristics of air-water two-phase flows in small diameter vertical tubes, *Int. J. Multiphase flow* 22 (1996), 703-712.
- [6.13] L. Friedel, Improved friction pressure drop correlations for horizontal and vertical two-phase pipe flow, *European Two-phase Flow Group Meeting* (1979), Ispra, Italy.
- [6.14] D. Chisholm, Pressure gradients due to friction during the flow of evaporating two-phase mixtures in smooth tubes and channels, *Int. J. Heat and Mass Transfer* 16 (1973), 347-358.
- [6.15] S. G. Bankoff, A variable density single-fluid model for two-phase flow with particular reference to steam-water flow, *J. Heat Transfer* 82 (1960), 265-272.
- [6.16] H. Muller-Steinhagen, K. Heck, A simple pressure drop correlation for two-phase flow in pipes, *Chem. Eng. Process.* 20 (1986), 297-308.
- [6.17] D. Steiner, Heat transfer to boiling saturated liquids, *VDI-Warmeatlas (VDI Heat Atlas)*, Editor: Verein Deutscher Ingenieure, VDI-Gesellschaft Verfahrenstechnik und Chemie-ingenieurwesen (GCV), Translator: J.W. Fullarton, Dusseldorf, 1993.
- [6.18] M.G. Cooper, Heat flows rates in saturated pool boiling – a wide ranging examination using reduced properties, *Advanced in Heat Transfer*, Academic Press (1984), 157-239, Florida, USA.
- [6.19] R.N. Wenzel, Resistance of solid surfaces to wetting by water, *Industrial and Engineering Chemistry* 28 (1936), 7426-7431.



## General conclusions and perspectives

The present study investigated the flow boiling heat transfer in microchannels for the purpose of developing compact cooling systems which can be adapted to miniaturized power components. Surface treatments at nano- and microscales were used as innovative techniques to improve the heat transfer performance as well as to delay the associated intermittent dryout. Before achieving these goals, pool-boiling experiments were performed in order to highlight the impact of nanocoatings on nucleate boiling processes, especially on bubble growth mechanisms.

The interest in nanocoatings was firstly inspired by the emergence of nanofluids for which, recent studies show that during nanofluid boiling, nanoparticles deposit on the heated surface, leading to modifications of the surface wettability, the heat transfer coefficient and the critical heat flux. However, due to controversial results in the literature, the role of nanoparticle deposition on boiling heat transfer is not fully understood yet, and further works is required for a better understanding of the involved mechanisms.

Therefore, in the first part of this work, experiments were performed to explore the mechanism of nanoparticle deposition by nanofluid boiling as well as its impact on pool boiling of a pure fluid. It was observed that the thickness of the deposition layer depends on the initial nanoparticle concentration and the boiling duration. Furthermore, the surfaces with nanoparticle deposition exhibit lower heat transfer coefficients than the uncoated surface. By considering the role of adhesion energy on boiling heat transfer, it was possible to explain the controversial experimental results of the literature.

For a more complete understanding of the impact of surface wettability on the boiling processes, another pool-boiling experiment was conducted where various samples with various contact angles from  $22^\circ$  to  $112^\circ$  were used. It was shown that hydrophobic (unwetted) and hydrophilic (wetted) surfaces exhibit different behaviours under boiling conditions. On hydrophobic surfaces, bubbles appear at lower heat fluxes than on hydrophilic surfaces. However, these bubbles cannot detach from the wall and rapidly coalesce with those formed at neighbouring sites, leading to rapid deterioration of the heated surface.

Moreover, it was observed that the surface wettability has significant impacts on boiling parameters such as bubble departure diameter, bubble emission frequency and heat transfer coefficient. Indeed, by decreasing the contact angle, the bubble departure diameter increases whereas the bubble emission frequency decreases. For low wetted surfaces ( $45^\circ < \theta < 90^\circ$ ), the heat transfer coefficient deteriorates when the contact angle decreases. However, for highly wetted surfaces ( $\theta \leq 45^\circ$ ), the inverse effect was observed: the heat transfer coefficient improves with a decrease in the contact angle. Therefore, the best heat transfer coefficient would be obtained at a contact angle close to  $0^\circ$  or  $90^\circ$ .

For a better understanding of the above observations, an approach to the bubble growth mechanism based on dynamic contact angles was developed. The contact angle hysteresis was showed to play a significant role in a boiling cycle. In particular, the concept of macro- and micro-contact angle was introduced to describe the bubble growth process. Based on this concept, a theoretical model of bubble departure diameter was established. This model next enabled development of new models of pool boiling heat transfer and critical heat flux, which show good agreements with a moderate set of experimental data.

Afterwards, experiments were performed to determine the effects of surface wettability on flow-boiling heat transfer in a microchannel. Thus, a reliable and repeatable method of sample surface fabrication was developed in order to accurately control the surface properties. It consists of a specific surface coating and structuring made in three stages to enable the samples to be used as the heating elements as well as the sensors of local temperature and heat flux. The test channel was a rectangular channel with a hydrodynamic diameter of 0.96 mm and a confinement number of 2.6. Prior to boiling tests, single-phase tests were performed to validate the test facility, measurement techniques and data reduction procedure. The experimental data of single-phase pressure drop and heat transfer coefficient show good agreements with the data predicted by the classical laws.

On boiling conditions, it was observed that the two-phase pressure drop decreases when the contact angle decreases or when the surfaces are micro-structured. For a better understanding of the boiling processes, images taken by a high-speed camera were analysed, giving the flow patterns for all sample surfaces tested. For low-wetted and micro-structured surfaces, confined-bubbly flow, slug flow and slug-annular flow were detected. For highly-wetted and unwetted smooth surfaces, instead of the slug-annular flow, the churn flow was observed. Backflow phenomenon was visualized on all the samples except the unwetted surface.

As a general tendency, the heat transfer coefficient increases with the vapour quality, and then decreases before remaining constant. However, for highly-wetted smooth surface, the heat transfer coefficient changes slightly when the vapour quality or the heat flux increases. For unwetted smooth surface, nucleate boiling occurs even at a negative vapour quality, i.e. at a fluid temperature lower than the saturation one. *In particular, the micro-structured surfaces show significant enhancements (up to 85%) in heat transfer compared to the smooth surfaces. Also, using the highly-wetted structured surface, the intermittent dryout is improved, i.e. the critical vapour quality at which this phenomenon occurs increases.*

The effects of nano- and micro-surface treatments on boiling heat transfer and particularly their impacts on the surface tension force at the triple contact line and the superheat for onset of nucleate boiling were investigated. At a first approximation, some models were developed to predict the effects of surface wettability on the two-phase pressure drop, the heat transfer coefficient as well as the backflow occurrence.

### **Future work**

In the future, it will be definitely interesting to characterize the surfaces with heterogeneous properties of wettability, e.g., a highly-wetted surface containing artificial unwetted nucleation sites. Such surfaces will probably allow a significant reduction of the superheat needed for the onset of nucleate boiling as well as an easy detachment of bubbles. In terms of hydrodynamics, the flow would be more stable, thus, the two-phase pressure drop would be decreased. In terms of heat transfer, the heat transfer coefficient would be enhanced and the intermittent dryout would be delayed.

Furthermore, the flow-boiling experimental loop should be improved for testing larger ranges of mass flux, heat flux and vapour quality. There are also possibilities to perform boiling tests with refrigerants or fluids like HFE-7100 for industrial applications. Finally, further work is needed to optimize the models developed throughout this work. Their predictive abilities should be confirmed by comparison with a larger set of experimental data.

## List of figures

FIGURE 1-1. A VAPOUR EMBRYO FORMED AT THE SOLID SURFACE WITH A CONTACT ANGLE $\theta$ .....	5
FIGURE 1-2. VARIATION OF GIBBS FREE ENERGY WITH BUBBLE RADIUS.....	7
FIGURE 1-3. TIME PERIOD ASSOCIATED WITH THE GROWTH OF EACH BUBBLE IS THE SUM OF THE WAITING TIME AND THE GROWTH TIME.....	7
FIGURE 1-4. SCHEMATIC REPRESENTATION OF THE POOL BOILING CURVE. ....	9
FIGURE 1-5. SCHEMATIC REPRESENTATION OF REGIMES OF FLOW BOILING OBSERVED IN A HORIZONTAL CHANNEL. .....	13
FIGURE 1-6. SCHEMATIC REPRESENTATION OF PRINCIPAL FLOW PATTERNS IN MICROCHANNELS. ....	14
FIGURE 1-7. LOCAL HEAT TRANSFER COEFFICIENT VERSUS LOCAL QUALITY (FROM CANEY <i>ET AL.</i> [1.25] FOR FLOW BOILING OF HFE-7100 IN 40 PARALLEL RECTANGULAR CHANNELS HAVING 0.84 MM HYDRAULIC DIAMETER). .....	15
FIGURE 1-8. LIQUID DROPLETS ON A) WETTED SURFACE AND B) UNWETTED SURFACE. ....	16
FIGURE 1-9. CONTACT ANGLE HYSTERESIS: A) STATIC CONTACT ANGLE $\theta_e$ , B) ADVANCING CONTACT ANGLE $\theta_A$ , C) RECEDING CONTACT ANGLE $\theta_R$ AND D) CONTACT ANGLES OF DROPLET ON INCLINED SURFACE.....	17
FIGURE 1-10. DETERMINATION OF THE SOLID SURFACE TENSION: A) ZISMAN PLOT FOR A LOW DENSITY POLY(ETHYLENE) AND B) OWENS/WENDT PLOT FOR POLY(METHYL METHACRYLATE) (DATA FROM KRÜSS TECHNICAL NOTE [1.33]). ....	20
FIGURE 1-11. ON A HYDROPHOBIC SURFACE, SCHEMATIC VIEW OF A WATER DROPLET IN A) WENZEL STATE AND B) CASSIE STATE.....	21
FIGURE 1-12. CONTACT ANGLE BEHAVIOUR IS ONLY DETERMINED BY SOLID-LIQUID INTERACTIONS AT THE TCL: A) INSIDE THE HYDROPHOBIC ZONE, THE WATER CONTACT ANGLE IS EQUAL TO THAT ON THE HYDROPHOBIC SURFACE AND B) IF THE TCL EXCEEDS THE HYDROPHOBIC ZONE, THE CONTACT ANGLE IS EQUAL TO THAT ON THE HYDROPHILIC SURFACE. ....	21
FIGURE 1-13. ILLUSTRATION OF CROSS SECTION OF: A) POROUS SURFACE, B) ROUGH SURFACE. ....	23
FIGURE 1-14. SCHEMATIC VIEWS OF DIFFERENT INTERIOR SHAPES OF REENTRANT CAVITIES. ....	23
FIGURE 2-1. CEA MAGNETRON SPUTTERING REACTOR: A) EXPERIMENTAL APPARATUS IMAGE AND B) SCHEMATIC DIAGRAM.....	34
FIGURE 2-2. DIAGRAM OF CVD PROCESSES.....	35
FIGURE 2-3. IN-HOUSE BUILT PECVD REACTOR: A) SAMPLE HOLDER AND B) SHOWERHEAD. ....	36
FIGURE 2-4. IN-HOUSE BUILT PECVD REACTOR FOR SILICON OXIDE COATINGS.....	37
FIGURE 2-5. SCHEMATIC VIEW OF ABLATION PROCESS BY LASER BEAM. ....	38
FIGURE 2-6. A) LASER ABLATION TOOL FROM TAMARACK 412 ® AND B) PATTERNED MASK USED TO ABLATE TITANIUM AND DLC COATINGS. ....	39
FIGURE 2-7. INTERACTIONS AT THE SAMPLE SURFACE DUE TO INJECTION OF ELECTRON BEAM. ....	40
FIGURE 2-8. SCHEMATIC VIEW OF A TYPICAL SEM.....	41
FIGURE 2-9. BLOCK DIAGRAM OF ATOMIC FORCE MICROSCOPE. ....	42
FIGURE 2-10. BLOCK DIAGRAM OF THE KRÜSS EASYDROP DSA10 SYSTEM. ....	43
FIGURE 2-11. DIAGRAM OF A LIQUID DROPLET AND ITS BASELINE.....	43
FIGURE 2-12. EXAMPLE OF A CLEAR PICTURE FOR DETERMINATION OF THE CONTACT ANGLE [2.15]. ....	43
FIGURE 2-13. DETERMINATION OF THE CONTACT ANGLE HYSTERESIS: A) INCREASING THE DROPLET VOLUME TO OBTAIN THE ADVANCING ANGLE AND B) DECREASING THE DROPLET VOLUME TO OBTAIN THE RECEDING ANGLE. ....	44
FIGURE 2-14. THEORETICAL CURVE OF EVOLUTION OF THE CONTACT ANGLE WITH THE DROPLET DIAMETER. ....	44
FIGURE 2-15. DIAGRAM OF CIRCUIT FOR RESISTANCE MEASUREMENT BY 2-WIRE TECHNIQUE. ....	45
FIGURE 2-16. DIAGRAM OF CIRCUIT FOR RESISTANCE MEASUREMENT BY 4-WIRE TECHNIQUE. ....	45
FIGURE 2-17. SHUNT OF 0.01 $\Omega$ IS USED TO DETERMINE THE CURRENT.....	46
FIGURE 2-18. SCHEMATIC VIEW OF EXPERIMENTAL SETUP FOR R/T CALIBRATION. ....	47
FIGURE 2-19. EXAMPLE OF T/R CURVE USED FOR TEMPERATURE DETERMINATION FROM MEASUREMENT OF RESISTANCE.....	47
FIGURE 3-1. NANOFLUIDS USED FOR SAMPLE-SURFACE COATING. ....	51
FIGURE 3-2. DIAGRAM OF NANOFLUID NUCLEATE BOILING APPARATUS. ....	52
FIGURE 3-3. FEG-SEM IMAGES OF NANOPARTICLE DEPOSITION LAYER OF A) AU; B) $Al_2O_3$ ; C) $TiO_2$ . ....	53
FIGURE 3-4. DEPOSITION LAYER THICKNESS IN THE CONDITIONS OF: A) 0.0003% V OF AU DURING 600 S, B) 0.01% V OF $Al_2O_3$ DURING 60 S, C) 0.01% V OF $TiO_2$ DURING 250 S AND D) 0.01% V OF $TiO_2$ DURING 500 S.....	55
FIGURE 3-5. EXPERIMENTAL SETUP: (1) SAMPLE HEATER; (2) SAMPLE HOLDER; (3) BOILING VESSEL AND (4) THERMOSTAT.....	56
FIGURE 3-6. BOILING CURVES OF: A) UNCOATED SURFACE WITH UNCERTAINTY BARS AND B) UNCOATED AND COATED SURFACES. ....	58



FIGURE 3-7. EVOLUTION OF THE HEAT TRANSFER COEFFICIENT WITH TIME AT 100 kW/M <sup>2</sup> .....	59
FIGURE 3-8. STATIC CONTACT ANGLES OF 3- $\mu$ L SESSILE WATER-DROPLETS ON THE SAMPLE SURFACES. ....	59
FIGURE 3-9. SCHEMATIC VIEW OF THE CROSS SECTION OF A) UNCOATED SURFACE, B) SURFACE WITH TiO <sub>2</sub> - PARTICLE DEPOSITION AND C) SURFACE WITH TiO <sub>2</sub> -DEPOSITION CLEANED IN ULTRASONIC BATH.....	60
FIGURE 3-10. FEG-SEM IMAGES OF SURFACE COATED BY TiO <sub>2</sub> -NANOPARTICLE DEPOSITION. ....	60
FIGURE 3-11. ADHESION ENERGY OF WATER VERSUS THE CONTACT ANGLE AT 25°C FOR: A) UNCOATED SURFACE, B) SURFACE WITH TiO <sub>2</sub> -PARTICLE DEPOSITION AND C) SURFACE WITH TiO <sub>2</sub> -DEPOSITION CLEANED IN ULTRASONIC BATH. ....	61
FIGURE 4-1. STATIC CONTACT ANGLES OF 2- $\mu$ L SESSILE WATER-DROPLETS ON STAINLESS STEEL SURFACES WITH AND WITHOUT NANOPARTICLE DEPOSITION. ....	65
FIGURE 4-2. AFM TOPOGRAPHY OF THE UNCOATED SURFACE S-REF.....	66
FIGURE 4-3. FEG-SEM IMAGES OF THE TESTED SURFACES (BY MOCVD: S-Pt AND S-Fe <sub>2</sub> O <sub>3</sub> ; BY NNBD: S-TiO <sub>2</sub> AND BY PECVD: S-SiOx, S-SiOC AND S-TEFLON). ....	67
FIGURE 4-4. FOR HYDROPHOBIC SURFACES, BUBBLES ARE CREATED AT LOW SUPERHEATS BUT CANNOT DETACH FROM THE WALL. THERE IS NO BUBBLE EMISSION AND FILM BOILING OCCURS BECAUSE OF BUBBLE COALESCENCE. ....	68
FIGURE 4-5. BUBBLE DEPARTURE ON HYDROPHILIC SURFACES. ....	69
FIGURE 4-6. BUBBLE DEPARTURE DIAMETER (MEASURED AT 200 kW/M <sup>2</sup> ) VERSUS THE STATIC CONTACT ANGLE AT 25 °C. THE CORRELATION OF FRITZ HAS THE OPPOSITE TENDENCY COMPARED TO THE EXPERIMENTAL VALUES. ....	69
FIGURE 4-7. EVOLUTION OF GROWTH TIME (A) AND WAITING TIME (B) AS A FUNCTION OF CONTACT ANGLE. ....	70
FIGURE 4-8. BUBBLE EMISSION FREQUENCY VERSUS THE CONTACT ANGLE.....	70
FIGURE 4-9. HEAT TRANSFER COEFFICIENT OF AN UNTREATED STAINLESS STEEL SURFACE. ....	71
FIGURE 4-10. EFFECTS OF THE SURFACE WETTABILITY ON THE HEAT TRANSFER COEFFICIENT. IN B), THE SAME COLOUR INDICATES THE SAME HEAT FLUX. ....	71
FIGURE 4-11. CONTACT ANGLE CHANGE DURING GROWTH TIME ( $\theta_r \leq \theta_e \leq \theta_d$ ). ....	72
FIGURE 4-12. DYNAMIC CONTACT ANGLE APPROACH FOR NUCLEATE BOILING. ....	73
FIGURE 4-13. CONTACT ANGLE OF A LIQUID DROPLET: A) AT 25° WITHOUT ANY HEAT TRANSFER AND B) AT SATURATION TEMPERATURE ON A HEATED SURFACE: MACRO-CONTACT ANGLE $\theta$ AND MICRO-CONTACT ANGLE $\theta_m$ . ....	74
FIGURE 4-14. MOVEMENT OF THE CONTACT LINE DURING BUBBLE GROWTH: A) THE BUBBLE GROWTH INITIATES, B) THE CONTACT LINE STOPS DISPLACING AT $\theta_m = 90^\circ$ , C) THE CONTACT LINE STARTS MOVING TOWARD THE BUBBLE AXIS, D) THE BUBBLE DETACHES FROM THE WALL AND E) HYSTERESIS OF $\theta$ AND $\theta_m$ . ....	75
FIGURE 4-15. TWO SPHERICAL BUBBLES ARE ASSUMED TO HAVE THE SAME TCL. IF $\theta_2$ IS LOWER THAN $\theta_1$ , THE BUBBLE HAVING THE CONTACT ANGLE $\theta_2$ IS THEN BIGGER THAN THAT HAVING THE CONTACT ANGLE $\theta_1$ . ...	75
FIGURE 4-16. NEW CORRELATION TO ESTIMATE THE BUBBLE DEPARTURE DIAMETER. ....	77
FIGURE 4-17. COMPARISON OF PREDICTED AND MEASURED VAPOUR BUBBLE DEPARTURE DIAMETER. ....	77
FIGURE 4-18. SCHEMATIC VIEW OF THE BASE OF THE BUBBLE WHEN THE MICRO-CONTACT ANGLE IS EQUAL TO 90°. ....	79
FIGURE 4-19. SCHEMATIC VIEW OF A) THE BUBBLE AT ITS MAXIMUM SIZE AND B) THE BUBBLE AT DEPARTURE. ..	81
FIGURE 4-20. COMPARISON OF THE PREDICTED AND EXPERIMENTAL VALUES OF A) DIMENSIONLESS NUMBER DEFINED BY (4-24) AND B) BUBBLE DEPARTURE DIAMETER. ....	83
FIGURE 4-21. PREDICTION OF THE WETTING OF FC-77 ON ALUMINIUM SURFACES.....	83
FIGURE 4-22. HEAT TRANSFER ZONES ON: A) HYDROPHILIC AND B) HYDROPHOBIC SURFACES. ....	84
FIGURE 4-23. COMPARISON BETWEEN THE EXPERIMENTAL DATA AND SOME CORRELATIONS IN LITERATURE. ....	86
FIGURE 4-24. COMPARISON WITH EXPERIMENTAL DATA: A) LINES ARE PREDICTION CURVES AND POINTS ARE EXPERIMENTAL POINTS AND B) PREDICTED HTC VS. EXPERIMENTAL HTC. ....	88
FIGURE 4-25. SCHEMATIC VIEW OF THE MICROLAYER ZONE AT MAXIMUM BUBBLE SIZE. ....	89
FIGURE 4-26. SCHEMATIC VIEW OF EVOLUTION OF LIQUID MASS IN THE MICROLAYER ZONE.....	89
FIGURE 4-27. EVOLUTION OF THE CHF WITH THE CONTACT ANGLE FOR WATER AND WATER-BASED NANOFLUIDS. ....	91
FIGURE 5-1. FABRICATION PROCEDURE OF SMOOTH SURFACES: A) TOP VIEW AND B) PERSPECTIVE VIEW. ....	98
FIGURE 5-2. SIDE VIEW OF FABRICATION PROCEDURE OF STRUCTURED SURFACES: A) $\mu$ -Ti SURFACE AND B) $\mu$ -SiOx SURFACE.....	99
FIGURE 5-3. ACTIVE CAVITY SIZE RANGE FOR SATURATED BOILING OF WATER AT ATMOSPHERIC PRESSURE. ....	99
FIGURE 5-4. SCHEMATIC VIEW OF ELECTRICAL CONNEXIONS. ....	100
FIGURE 5-5. IMAGE OF A TYPICAL WAFER: A) TEST SURFACE WITH ELECTRICAL CONNEXIONS, B) BACKUP SURFACE AND C) AND D) SAMPLES FOR SURFACE CHARACTERISATIONS. ....	100

FIGURE 5-6. FEG-SEM IMAGES OF SiOC SURFACE IN THE PERSPECTIVE VIEW: A) AND B) DEPOSITION LAYERS ON PYREX WAFER, C) NANOPARTICLE LAYER AND D) INTERFACE BETWEEN TITANIUM LAYER AND PYREX WAFER.....	101
FIGURE 5-7. FEG-SEM IMAGES OF THE $\mu$ -Ti SURFACE: A) TOP VIEW, B) SLOPING VIEW AND C) SIDE VIEW.....	102
FIGURE 5-8. FEG-SEM IMAGES OF THE $\mu$ -SiO <sub>x</sub> SURFACE: A) TOP VIEW, B) SLOPING VIEW AND C) SIDE VIEW.....	102
FIGURE 5-9. SCHEMATIC VIEW OF TOPOGRAPHIES OF THE STRUCTURED SAMPLE SURFACES.....	103
FIGURE 5-10. ELECTRICAL RESISTANCE EVOLUTION WITH TEMPERATURE AT DIFFERENT SECTIONS OF THE TITANIUM LAYER.....	103
FIGURE 5-11. ASSEMBLY OF THE TEST SECTION: A) CROSS-SECTION VIEW AND B) TOP VIEW WITHOUT SILICONE COMPOUND AND INSULATION FOAM. ....	104
FIGURE 5-12. SCHEMATIC VIEW OF THE EXPERIMENTAL APPARATUS. ....	105
FIGURE 5-13. SCHEMATIC VIEW OF DISTRIBUTION OF HEAT FLUX GENERATED BY JOULE EFFECT FROM THE TITANIUM LAYER. ....	106
FIGURE 5-14. ELECTRICAL HEAT LOSS VS. ELECTRICAL POWER GENERATED BY JOULE EFFECT AT 120 KG/M <sup>2</sup> S. .	107
FIGURE 5-15. SCHEMATIC VIEW OF THE FLUID FLOW IN THE TEST SECTION. ....	108
FIGURE 5-16. PRESSURE DROPS: A) EXPERIMENTAL PRESSURE DROP AND B) FRICTIONAL AND SINGULAR PRESSURE DROPS.....	110
FIGURE 5-17. TOTAL LIQUID PRESSURE DROP VS. REYNOLDS NUMBER.....	110
FIGURE 5-18. THERMAL ENTRANCE LENGTH VS. REYNOLDS NUMBER AT DIFFERENT FLUID TEMPERATURES. ....	113
FIGURE 5-19. LOCAL NUSSELT NUMBER VS. LOCAL REDUCED LENGTH. ....	114
FIGURE 6-1. STATIC CONTACT ANGLES OF A WATER-DROPLET ON THE SAMPLE SURFACES AT ROOM TEMPERATURE. ....	119
FIGURE 6-2. TWO-PHASE PRESSURE DROPS: A) AT 100 KG/M <sup>2</sup> S AND B) AT 120 KG/M <sup>2</sup> S. ....	120
FIGURE 6-3. REPRESENTATIVE TOP-VIEW IMAGES OF FLOW PATTERNS IN THE TEST CHANNEL FOR ALL THE SAMPLE SURFACES.....	121
FIGURE 6-4. REPRESENTATIVE TOP-VIEW IMAGES OF FLOW PATTERNS ON Ti SURFACE AT DIFFERENT HEAT FLUXES. ....	121
FIGURE 6-5. EVOLUTION OF FLOW PATTERNS ON Ti SURFACE AT 61 kW/M <sup>2</sup> .....	122
FIGURE 6-6. ANALYSED IMAGES OF FLOW PATTERNS ON DLC SURFACE: A) VS. HEAT FLUX AND B) VS. TIME AT 60 kW/M <sup>2</sup> .....	122
FIGURE 6-7. REPRESENTATIVE IMAGE OF CHURN FLOW REGIME (CF) OBSERVED ON SiO <sub>x</sub> SURFACE. ....	123
FIGURE 6-8. REPRESENTATIVE IMAGES OF FLOW PATTERN ON SiOC SURFACE: A) BUBBLES ARE CREATED IN 1°C-SUBCOOLED FLUID AND B) CHURN FLOW REGIME (CF). ....	123
FIGURE 6-9. REPRESENTATIVE IMAGE INTERMITTENT DRYOUT ON DLC SURFACE DETECTED BY CONDENSATION OF VAPOUR.....	124
FIGURE 6-10. FLOW PATTERN MAP: A) OF TRIPLETT <i>ET AL.</i> [6.7] FOR AIR-WATER IN A 1.1 MM HORIZONTAL CHANNEL AND B) GIVEN BY THE PRESENT VISUALIZATION FOR 100 AND 120 KG/M <sup>2</sup> S WHERE THE TRANSITION BOUNDARIES ARE QUALITATIVELY DETERMINED. ....	125
FIGURE 6-11. FOR 100 KG/M <sup>2</sup> S, HEAT TRANSFER COEFFICIENT VS. VAPOUR QUALITY ON A) SiO <sub>x</sub> SURFACE; B) Ti SURFACE; C) DLC SURFACE AND D) SiOC SURFACE.....	126
FIGURE 6-12. FOR 120 KG/M <sup>2</sup> S, HEAT TRANSFER COEFFICIENT VS. VAPOUR QUALITY ON A) SiO <sub>x</sub> SURFACE; B) Ti SURFACE; C) DLC SURFACE AND D) SiOC SURFACE.....	127
FIGURE 6-13. FLOW PATTERNS ON TITANIUM SURFACE AT 120 KG/M <sup>2</sup> S WITH I) ORIGINAL IMAGE AND II) ANALYSED IMAGE. ....	128
FIGURE 6-14. BOILING CURVES FOR VARIOUS SAMPLE SURFACES AT 100 AND 120 KG/M <sup>2</sup> S. ....	128
FIGURE 6-15. COMPARISON BETWEEN EXP. AND THEORETICAL DATA OF TWO-PHASE PRESSURE DROP GRADIENT AT 100 KG/M <sup>2</sup> S.....	132
FIGURE 6-16. COMPARISON BETWEEN EXP. AND THEORETICAL DATA OF TWO-PHASE PRESSURE DROP GRADIENT AT 120 KG/M <sup>2</sup> S.....	133
FIGURE 6-17. SCHEMATICALLY VIEW OF A CONFINED BUBBLE OR SLUG INSIDE A CIRCULAR TUBE.....	133
FIGURE 6-18. GRADIENT OF THE WETTING PRESSURE DROP VS. (1-COS $\theta$ ).....	133
FIGURE 6-19. COMPARISON OF THE PREDICTED AND EXPERIMENTAL VALUES OF THE WETTING PRESSURE-DROP GRADIENT.....	134
FIGURE 6-20. JAKOB NUMBERS FOR ALL SMOOTH SAMPLE SURFACES.....	136
FIGURE 6-21. SCHEMATICALLY VIEW OF THE CROSS SECTION OF THE TEST CHANNEL FOR A) LOW-WETTED SURFACES AND B) HIGHLY-WETTED SURFACES.....	137
FIGURE 6-22. HEAT TRANSFER COEFFICIENT VS. VAPOUR QUALITY FOR THE THREE MODES H <sub>1</sub> , H <sub>2</sub> , H <sub>3</sub> AT 40 kW/M <sup>2</sup> . ....	138

FIGURE 6-23. COMPARISON OF EXPERIMENTAL AND PREDICTED HEAT TRANSFER COEFFICIENT FOR A) SiOX SURFACE AND B) Ti SURFACE AT 120 KG/M <sup>2</sup> S. FOR EACH HEAT FLUX, THE PREDICTED CURVE IS A CONTINUOUS LINE WITH THE SAME COLOUR AS THE EXPERIMENTAL DOTS.....	139
FIGURE 6-24. SCHEMATIC VIEW OF TOPOGRAPHIES OF THE STRUCTURED SAMPLE SURFACES.....	140
FIGURE 6-25. WATER DROPLETS ON THE STRUCTURED SAMPLE SURFACES AT THE AMBIENT TEMPERATURE. ....	140
FIGURE 6-26. TWO-PHASE PRESSURE DROP ON THE SMOOTH (SiOX AND Ti) AND STRUCTURED ( $\mu$ -Ti AND $\mu$ -SiOX) SURFACES AT 100 KG/M <sup>2</sup> S AND AT 120 KG/M <sup>2</sup> S. ....	141
FIGURE 6-27. REPRESENTATIVE IMAGES OF FLOW PATTERNS OBSERVED ON $\mu$ -SiOX SURFACE: A) SLUG-ANNULAR FLOW AND B) BUBBLE GENERATION IN LIQUID FILM. ....	142
FIGURE 6-28. BACK FLOW OBSERVATION: A) ON $\mu$ -Ti SURFACE WITH ORIGINAL AND ANALYSED IMAGES AND B) ON Ti-SURFACE WITH ANALYSED IMAGES. ....	142
FIGURE 6-29. COMPARISON OF EVOLUTIONS OF THE HEAT TRANSFER COEFFICIENT WITH THE VAPOUR QUALITY FOR SiOX AND $\mu$ -SiOX SURFACES AT 100 KG/M <sup>2</sup> S AND 120 KG/M <sup>2</sup> S. ....	143
FIGURE 6-30. COMPARISON OF EVOLUTIONS OF THE HEAT TRANSFER COEFFICIENT WITH THE VAPOUR QUALITY FOR Ti AND $\mu$ -Ti SURFACES AT 100 KG/M <sup>2</sup> S AND 120 KG/M <sup>2</sup> S. ....	144
FIGURE 6-31. BOILING CURVES OF SMOOTH AND STRUCTURED SAMPLE SURFACES AT A) 100 KG/M <sup>2</sup> S AND B) 120 KG/M <sup>2</sup> S.....	145

## List of tables

TABLE 1-1. TECHNIQUES TO FABRICATE ENHANCED SURFACES.....	23
TABLE 1-2. SUMMARY OF STUDIES ON NANOFLUID POOL BOILING.....	25
TABLE 2-1. SUMMARY OF COATING PROCESSES USED IN THIS STUDY. ....	33
TABLE 2-2. PVD PROCESS CONDITIONS FOR DEPOSITING Ti COATINGS.....	35
TABLE 2-3. PECVD PROCESS CONDITIONS FOR DEPOSITING SiCH AND DLC COATINGS.....	36
TABLE 2-4. PVD PROCESS CONDITIONS FOR DEPOSITING PDMS COATINGS. ....	37
TABLE 2-5. MOCVD PROCESS CONDITIONS FOR DEPOSITING $\text{Fe}_2\text{O}_3$ AND Pt COATINGS. ....	38
TABLE 2-6. ABLATION PROCESS CONDITIONS. ....	39
TABLE 3-1. NANOFLUID BOILING CHARACTERISTICS. ....	53
TABLE 3-2. OPERATING CONDITIONS AND UNCERTAINTIES.....	57
TABLE 3-3. THE MODIFIED SURFACES VERSUS THE CLEAN SURFACE.....	61
TABLE 4-1. SAMPLE- SURFACE CHARACTERISTICS.....	66
TABLE 4-2. EXPERIMENTAL DATA OF THE BUBBLE DEPARTURE DIAMETER.....	82
TABLE 4-3. EXPERIMENTAL DATABASE OF HEAT TRANSFER COEFFICIENT. ....	87
TABLE 4-4. EXPERIMENTAL DATABASE COMPARED TO THE PREDICTION METHODS. ....	87
TABLE 5-1. DIMENSIONS OF THE TESTING AREA SECTIONS. ....	100
TABLE 5-2. GLASS LID DIMENSIONS.....	104
TABLE 5-3. HEAT FLUXES BALANCE. ....	107
TABLE 5-4. SINGLE-PHASE PRESSURE DROP CONSTANTS. ....	111
TABLE 6-1. OPERATING PARAMETERS AND UNCERTAINTIES.....	119
TABLE 6-2. CONTACT ANGLE MEASUREMENTS. ....	119
TABLE 6-3. SUMMARY OF FLOW-PATTERN VISUALIZATION. ....	125
TABLE 6-4. COMPARISONS BETWEEN THE SMOOTH AND STRUCTURED SAMPLES. ....	145

## Appendix – Propagation of uncertainty

Giving  $Y$  a parameter depending on  $n$  variables  $x_1, x_2, \dots$  and  $x_n$  as:

$$Y = f(x_1, x_2, \dots, x_n) \quad (\text{A-1})$$

Using the absolute-error method, the uncertainty in determination of this parameter is calculated as:

$$\Delta Y = \left| \frac{df}{dx_1} \right| \Delta x_1 + \left| \frac{df}{dx_2} \right| \Delta x_2 + \dots + \left| \frac{df}{dx_n} \right| \Delta x_n \quad (\text{A-2})$$

wherein  $\Delta x_1, \Delta x_2, \dots$  and  $\Delta x_n$  are the uncertainties in determinations of  $x_1, x_2, \dots$  and  $x_n$ , respectively.

Besides,  $\Delta Y$  can be also determined using the standard-deviation method with a 68% confidence interval as:

$$\Delta Y = \sqrt{\left( \frac{df}{dx_1} \Delta x_1 \right)^2 + \left( \frac{df}{dx_2} \Delta x_2 \right)^2 + \dots + \left( \frac{df}{dx_n} \Delta x_n \right)^2} \quad (\text{A-3})$$

**For pool boiling experiments**, the absolute-error method is used, leading to:

$$\frac{\Delta q}{q} = \frac{\Delta V}{V} + \frac{\Delta I}{I} + \frac{\Delta A_h}{A_h} \quad (\text{A-4})$$

$$\frac{\Delta h}{h} = \frac{\Delta q}{q} + \frac{\Delta T_w + \Delta T_s}{T_w - T_s} \quad (\text{A-5})$$

**For flow boiling experiments**, in order to not overestimate the uncertainties of characteristic parameters, the standard-deviation method is applied. For instance, the uncertainty in determinations of the heat flux and the heat transfer coefficient are calculated as:

$$\frac{\Delta q}{q} = \sqrt{\left( \frac{\Delta V}{V} \right)^2 + \left( \frac{\Delta I}{I} \right)^2 + \left( \frac{\Delta A_h}{A_h} \right)^2} \quad (\text{A-6})$$

$$\frac{\Delta h}{h} = \sqrt{\left( \frac{\Delta q}{q} \right)^2 + \frac{\Delta T_w^2 + \Delta T_s^2}{(T_w - T_s)^2}} \quad (\text{A-7})$$

# Index

## A

Adhesion energy	17, 60
Annular flow	15

## B

Backflow	134
Bubbly flow	14

## C

Cassie	20
Chemical Vapour Deposition	35
Coating	65
Conduction	10, 58
Confinement number	14
Contact angle	42, 65, 72, 119, 139
Cooper	10, 87, 137
Critical heat flux	88

## D

Departure diameter	69, 76
Deposition	97

## E

Emission frequency	69
Enhanced surfaces	22
Enhancement	61, 142

## F

Flow boiling	11
Flow patterns	13, 14, 120, 141
Fritz	8, 22, 69, 76

## G

Gao	21
-----	----

## H

Heat transfer	58, 84, 125, 136, 142
Heat transfer coefficient	70
Hydrophilic	69, 72
Hydrophobic	68, 72
Hysteresis	17, 43

## I

Intermittent dryout	15, 123
---------------------	---------

## L

Laser ablation	38
----------------	----

## M

Macro-contact angle	75
McCarthy	21
Microchannel	95
Micro-contact angle	73, 74
Microlayer heat transfer	10

## N

Nanofluid	24, 51
Nanoparticles	25, 54
Nucleate boiling	9, 29

## O

Owens	18
-------	----

## P

Patterning	39, 98
Physical Vapour Deposition	34

## S

Semi-annular flow	14
Slug flow	14
Superficial velocities	12
Superheated liquid	11
Surface treatment	33
Surface wettability	26, 59, 65

## T

Takata	26, 87
--------	--------

## V

Vapour quality	11
Void fraction	12

## W

Wendt	18
Wenzel	20
Wetting pressure	131

## Y

Young	16
-------	----

## Z

Zisman	18
Zuber	8, 85